

# **MECHANICAL BEHAVIOUR OF TIMBER JOINTS WITH SLOTTED-IN STEEL PLATES**

Proefschrift

ter verkrijging van de graad van doctor  
aan de Technische Universiteit Delft,  
op gezag van de Rector Magnificus prof. ir. K.C.A.M. Luyben,  
voorzitter van het College voor Promoties,  
in het openbaar te verdedigen op vrijdag 1 juni 2012 om 12:30 uur

door

Carmen SANDHAAS  
Diplom-Ingenieurin, Universität Karlsruhe (TH), Duitsland  
Geboren te Bühl (Baden), Duitsland

Dit proefschrift is goedgekeurd door de promotor:

Prof. dr. ir. J.W.G. van de Kuilen                      Technische Universiteit Delft

Samenstelling promotiecommissie:

Rector Magnificus	Voorzitter
Prof. dr. ir. J.W.G. van de Kuilen	Technische Universiteit Delft, promotor
Prof. Dr.-Ing. H.J. Blaß	Karlsruher Institut für Technologie
Prof. dr. ir. L.J. Sluys	Technische Universiteit Delft
Prof. ir. F.S.K. Bijlaard	Technische Universiteit Delft
Prof. dott. ing. A. Ceccotti	IUAV Venezia
Dr. ir. M.A.N. Hendriks	Technische Universiteit Delft
Dr. ir. A.M.P.G. Dias	Universidade de Coimbra

ISBN 978-90-8570-837-7

Copyright © 2012 by Carmen Sandhaas  
All Rights Reserved

Printed by Wöhrmann Print Service, Zutphen, the Netherlands

Für Joost



# ACKNOWLEDGEMENTS

First and foremost, I would like to thank my supervisor Jan-Willem van de Kuilen. His continuous support, motivation and trust helped me through the most difficult periods of the PhD project. Jan-Willem granted me great academic freedom whilst giving me the necessary guidance to not stray off course.

All members of the committee contributed considerably to the work thanks to their questions and input. The long discussions with Max Hendriks and Bert Sluys helped to improve the thesis in the challenging field of computational mechanics.

The PhD thesis comprised also experiments and not only theoretical elaborations. It was a pleasure to be able to work with the people of Stevinlab II, namely Liesbeth Eekhout, Arjan van Rhijn, John Hermsen and Kees van Beek. A thesis on timber joints would not be possible without a carpenter though. Ben Lemmers prepared the test specimens with amazing accuracy and wonderful handicraft. Further thanks go to the people of Holzforschung München who produced the beech glulam, Stefan Torno, Heribert Bergmeier and Bruno Fischer.

In addition to the tests on joints done in Delft, also embedment tests were undertaken. Thanks to Hans Joachim Blaß, I could do these tests in the laboratory of Karlsruhe University. Alex Klein and Michael Deeg did everything to make me feel welcome and they organised everything to enable me to do the experiments efficiently.

The material itself was sponsored by a couple of companies. First of all, Pollmeier Massivholz GmbH & Co. KG did a precious contribution to my thesis by donating beech planks of furniture quality, including even the transport. Groot Lemmer, de Groot Vroomshoop and Ancofer Waldram also sponsored the project by providing material at a favourable price. Groot Lemmer also did a great job in producing the big azobé joints.

As for the theoretical part, there is another person I have to thank. Without Jan Hol from the faculty of Aerospace the modelling would not have taken place because he provided the finite element programme and gave me access to the cluster at Aerospace Engineering.

Furthermore, I want to thank my colleagues, above all Wolfgang Gard, Geert Ravenshorst and Peter de Vries from the timber section whose doors were always open for discussion. Also my roommates made my stay very memorable, we have been a nice team of people with Edi, Nesen, Sofia and Richard in the most beautiful office of TUD.

My last thanks go to my family and friends who were always confident that I took the right decisions whatever happened.

# SUMMARY

Timber joints are a key part of timber structures. Their reliable performance is a prerequisite to successful timber construction. The structural loadbearing behaviour of timber joints is mechanically complex and difficult to predict. Although numerical tools are currently available, these do not consider accurate 3D material models. However, to predict performance of a timber joint with useful accuracy a 3D material model need to be taken into account in the calculation of the global load-slip behaviour.

Most research to date has focused on testing and modelling of timber joints of softwood species whilst knowledge on joints using hardwood species is limited. The use of hardwood as well as higher grade mechanical fixings (i.e. replacing the commonly used mild steel dowels with very high strength steel dowels) can enhance load carrying capacities significantly. This lack of research and consequently the lack of reliable data on hardwood leave the optimisation potentials of hardwood joints with very high strength steel dowels unexploited.

The research reported in this thesis describes the newly developed 3D material model and it describes experiments on hardwood timber joints using dowels with different steel grades. It also compares the calculated mechanical behaviour with the experimental results.

The complex mechanical behaviour of timber joints is mainly related to the highly variable and interdependent properties of the timber members. Wood is a strongly anisotropic material. Moreover, it is ductile in compression but it is brittle in tension and shear. In the area of fasteners in joints these failure modes can overlap, which causes complex 3D stresses to develop. Therefore, the aim of the 3D material model developed in this thesis was to take into account these key issues, strong anisotropy, different failure modes and the combination of ductile and brittle behaviour within one single model.

Continuum damage mechanics (CDM) was chosen to develop the 3D material model. CDM is a nonlinear elastic approach that modifies the stiffness matrix in order to account for nonlinear behaviour. Different failure criteria were determined per stress quadrant in order to identify different failure modes and to assess the damage grade of a model.

Damage was defined as initiated once the failure criteria or damage initiation functions are exceeded. The mechanical behaviour was classified as two main constitutive laws: (i) elastic perfectly plastic for compression loading and (ii) linear softening for tension and shear loading.

A bespoke subroutine was developed which can be supplemented to existing FE software, currently available to timber designers. This subroutine has been tested on simple, theoretical numerical models to verify the 3D material model assumptions and to validate the accuracy and representativeness of the mesh regularisation techniques employed. After the validation, material tests have been simulated under different loading patterns, namely altering the application of load in relation to grain of timber. The modelling outcomes were compared with results from literature and were seen to correlate well. In a final step the behaviour of more complex embedment and joint models including friction and metal fasteners were analysed. The model results were validated with an experimental programme. Embedment strength parallel-to-grain was tested. A further 180 tests were completed on double-shear timber joints with slotted-in steel plates, using one, three and five dowels in row. Three timber species and two dowel steel grades were tested. The timber species were spruce, beech and azobé and the used dowel steel grades were high strength (hss) and very high strength (vhss) steel.

The modelling outcomes were compared with the test results. The reduction of stiffness due to the onset of damage was accurately predicted and damage due to different stress components was successfully identified by the developed model. Ductile behaviour was captured correctly and stable softening curves could be obtained. The importance of accurate mechanical material properties as input parameter has been underlined. Numerical problems were noted specifically in elements directly underneath the dowels where spurious energy modes developed that distorted these elements excessively. The strongly distorted elements could not transfer loads to neighbouring elements that were still intact. In order to optimise the developed model, the spurious energy modes of the highly stressed elements need to be addressed in further research.

In addition to the comparison of modelling outcomes, the tests were also analysed to identify optimisation potential of timber joints using very high strength steel dowels. The embedment tests completed as part of this work have contributed a considerable amount of performance data on high density wood species. The test series on joints has shown that hss dowels can be replaced by vhss dowels. Ductile failure modes with one or two plastic hinges per shear plane could be obtained also with the joints with very high strength steel dowels. The feasibility of joints with high strength steel dowels and hardwood species has been demonstrated in this thesis. Especially the combination of high-density timber with very high strength steel dowels gives promising performance levels and is recommended as an area for further research.

# SAMENVATTING

Het meeste onderzoek naar gedrag en modellering van houtverbindingen is gedaan voor naaldhout. De kennis over loofhoutverbindingen is beperkt. Het gebruik van loofhout en het gebruik van sterkere stalen stiftvormige verbindingsmiddelen (d.w.z. zachte stalen stiften worden vervangen door zeer hoge sterkte stalen (vhss) stiften) kan de sterkte van de verbinding aanzienlijk verhogen. De mogelijke optimalisatie door de combinatie loofhout en zeer hoge sterkte stalen stiften wordt niet vaak toegepast vanwege een gebrek aan kennis en betrouwbare gegevens.

Betrouwbare houtverbindingen zijn essentieel voor houtconstructies. Het mechanisch gedrag van een houtverbinding onder verschillende belastingen is echter complex en laat zich moeilijk voorspellen. De huidige rekenmodellen nemen de anisotropische aspecten van hout niet volledig in beschouwing. Om de sterkte van een houtverbinding te voorspellen is het echter noodzakelijk een 3D materiaalmodel toe te passen in de berekening van het kracht-verplaatsingsgedrag.

In dit proefschrift wordt een 3D materiaalmodel voor toepassing op houtverbindingen beschreven. Daarnaast worden de experimenten beschreven die zijn gedaan op loofhout verbindingen met stalen stiften met verschillende materiaalkwaliteit. Het voorspelde mechanische gedrag (gebaseerd op het ontwikkelde 3D model) wordt vervolgens vergeleken met de resultaten van de experimenten.

Het complexe gedrag van houtverbindingen wordt veroorzaakt door de sterk variërende en onderling afhankelijke eigenschappen van de afzonderlijke houten delen. Hout is een sterk anisotropisch materiaal. Onder druk is hout plastisch en onder trek- en schuifspanningen gedraagt het zich als een bros materiaal. Rondom de verbindingsmiddelen komen al deze spanningstoestanden voor en dit leidt tot een complex driedimensionaal gedrag. Het in dit rapport ontwikkelde materiaalmodel voor hout combineert sterke anisotropie, verschillende bezwijkmechanismen en de combinatie van ductiel en bros gedrag.

De continuum damage mechanics (CDM) methode werd gekozen als basisaanpak voor het 3D materiaalmodel. CDM is een niet-lineaire elastische benadering die de

stijfheidsmatrix aanpast om het niet-lineaire gedrag van het materiaal in rekening te brengen. De bezwijkcriteria zijn gedefinieerd per spanningskwadrant. Hierdoor is het mogelijk om de bezwijkmechanismes te identificeren en om de beschadiging van het materiaal vast te stellen. Beschadiging treedt op wanneer het bezwijkcriterium overschreden is. Het mechanische gedrag wordt gedefinieerd door twee regels: (i) elastisch-perfect plastisch bij druk en (ii) lineaire verslapping bij trek- en schuifspanningen.

Een materiaalsubroutine is ontwikkeld die toegepast kan worden in bestaande FE programma's. De subroutine is getest op simpele, theoretische modellen om de 3D materiaal aannames te verifiëren en om de onafhankelijkheid van de elementgrootte en de mesh vast te stellen. Vervolgens zijn materiaaltests gesimuleerd waarbij de spanningen zijn gevarieerd ten opzichte van de vezelrichting. De uitkomsten zijn in lijn met de gegevens in de literatuur. In de laatste stap is het gedrag van meer complexe stuikproef- en verbindingsmodellen geanalyseerd. De resultaten, berekend op basis van het ontwikkelde model zijn vergeleken met de uitkomsten van experimenten. Stuikproeven waar het hout in de vezelrichting is belast zijn uitgevoerd. Verder zijn er 180 experimenten uitgevoerd op houtverbindingen met één, drie en vijf stiften in een rij. Deze verbindingen zijn getest met drie verschillende houtsoorten (vuren, beuken en azobé). Daarnaast zijn twee sterkten staal (hoge sterkte staal (hss) en vhss) gebruikt.

De uitkomsten uit het model zijn vergeleken met de experimentele resultaten. De reductie van de stijfheid door beginnende beschadiging werd correct voorspeld en de schade vanwege de verschillende spanningscomponenten kon met succes vastgesteld worden in het ontwikkelde model. Het plastische gedrag is goed weergegeven en een stabiele verslapping is aangetoond in de simulatie. Daarbij is vastgesteld dat het belangrijk is de juiste mechanische materiaalparameters te gebruiken. Numerieke problemen ontstaan in die elementen die zich direct onder de stiften bevinden. In deze elementen ontstaan artificiële energie modi die tot excessieve schade van de elementen leiden. Deze zwaar 'beschadigde' elementen dragen geen belasting meer over op de naastliggende elementen die nog wel intact zijn. Om het ontwikkelde materiaalmodel te optimaliseren, moet in het model de afhandeling van de artificiële energie modi worden verbeterd.

Naast de vergelijking tussen model en experimentele uitkomsten zijn deze laatste ook gebruikt om vast te stellen welke optimalisaties van houtverbindingen mogelijk zijn wanneer vhss stiften worden gebruikt. De stuikproeven die in het kader van dit onderzoek zijn uitgevoerd hebben een uitgebreide hoeveelheid data over houtverbindingen met hoge volumieke massa toegevoegd. De verbindingsproeven hebben laten zien dat ook met vhss stiften ductiele bezwijkmechanismes kunnen worden bereikt. Speciaal de combinatie van vhss stiften met hout met hoge volumieke massa toont een aanzienlijke verhoging van de sterkte van houtverbindingen. Het verdient aanbeveling om dit terrein verder te onderzoeken.

# NOMENCLATURE

## Conventions

L longitudinal direction

R radial direction

T tangential direction

Material axes of FE models: 1 = X = L, 2 = Y = R, 3 = Z = T

Order of stresses/strains:  $\sigma_{ij}^T = \{\sigma_{11} \ \sigma_{22} \ \sigma_{33} \ \sigma_{12} \ \sigma_{13} \ \sigma_{23}\}$

## Greek letters

$\alpha$  angle between force direction and grain direction

$\varepsilon_{ij}$  6x6 strain tensor

$\phi$  yield function

$\eta$  fictitious viscous parameter

$\kappa_M$  history parameter

$\mu$  friction coefficient OR mean value

$\Theta$  energy dissipation rate

$\Theta$  strain energy density

$\rho$  density

$\sigma_{ij}$  6x6 stress tensor

$\nu_{ij}$  Poisson's ratios with tension in i-direction and perpendicular contraction in j-direction

## Latin letters

ALLSE	dissipated strain energy
ALLCD	dissipated energy due to viscous regularisation
$\mathbf{C}; C_{ijkl}$	compliance matrix
$\mathbf{D}; D_{ijkl}$	stiffness matrix
$d_M$	damage variable
dt	time increment
$F; F_M$	failure criterion
$f_{max}$	maximum force
$f_{h,0}$	embedment strength parallel-to-grain
$f_M$	material strengths
$f_u$	tension strength of steel
$f_y$	yield strength of steel
$G_f$	fracture energy
$g_f$	characteristic fracture energy
$h$	characteristic element height
$\mathbf{J}$	Jacobian
$K_{ser}$	joint stiffness
$\mathbf{M}$	damage operator
$M_y$	bending moment of steel dowels
$n$	number of fasteners
$n_{ef}$	effective number of fasteners
$R_m$	ultimate strength of steel
$R_{p,0.2}$	proof strength of steel at 0.2% extension
UMAT	subroutine of developed material model (ABAQUS <sup>®</sup> )
$v_{max}$	maximum displacement
$v(F_{max})$	displacement at maximum force
$Y_M$	thermodynamic forces

## Indices

### *Lower indices*

$0$	direction parallel-to-grain
$90$	direction perpendicular-to-grain
$\alpha$	angle to the grain
$c$	compression
$k$	characteristic properties
$roll$	rolling shear
$t$	tension
$V$	viscous stabilisation
$v$	longitudinal shear
Placeholder $M$ :	$X_M = (X_{t,0} \ X_{c,0} \ X_{t,90R} \ X_{c,90R} \ X_{t,90T} \ X_{c,90T} \ X_{vR} \ X_{vT} \ X_{roll})$
If not stated otherwise:	$X_{t,90R} = X_{t,90T} = X_{t,90}$ (tension perpendicular-to-grain) $X_{c,90R} = X_{c,90T} = X_{c,90}$ (compression perpendicular-to-grain) $X_{vR} = X_{vT} = X_v$ (longitudinal shear)

### *Upper indices*

$ef$	effective tensor
$el$	elastic property
$dam$	damaged tensor
$t$	increment
$t-1$	previous increment



# ACRONYMS

CDM	Continuum damage mechanics
COV	Coefficient of variation
CT	Compact tension (test)
EYM	European yield model
FE	Finite element
FM	Failure mode
hss	High strength steel (tension strength = 400-600 MPa)
LEFM	Linear elastic fracture mechanics
m.c.	Moisture content
MoE	Modulus of elasticity
MoR	Modulus of rupture
NLFM	Nonlinear fracture mechanics
RVE	Representative volume element
SENB	Single-edge notched bending (test)
SLA	Sequentially linear analysis
vhss	Very high strength steel (tension strength = 700-1100 MPa)



# TABLE OF CONTENTS

ACKNOWLEDGEMENTS.....	I
SUMMARY .....	III
SAMENVATTING .....	V
NOMENCLATURE .....	VII
ACRONYMS.....	XI
TABLE OF CONTENTS .....	XIII
1 INTRODUCTION.....	1
1.1 Research motivation.....	1
1.1.1 Problem description .....	1
1.1.2 State-of-the-art .....	2
1.1.3 Research questions.....	4
1.1.4 Research programme .....	4
1.2 Structure of thesis .....	5
2 MATERIAL WOOD.....	7
2.1 Introduction .....	7
2.2 Uniaxial tests.....	9
2.2.1 Tensile strength.....	10
2.2.2 Compressive strength.....	13
2.2.3 Shear strength .....	17

2.3	Multiaxial tests .....	20
2.3.1	Combination of normal stresses .....	20
2.3.2	Combination of normal and shear stresses .....	22
2.4	Poisson's ratios .....	24
2.5	Wood anatomy .....	25
2.6	Conclusions .....	27
<b>3</b>	<b>MODELLING TECHNIQUES .....</b>	<b>29</b>
3.1	Introduction .....	29
3.2	Finite element model .....	32
3.2.1	Continuum approaches .....	36
3.2.2	Discrete approaches .....	37
3.3	Failure threshold and development .....	40
3.3.1	Failure criteria .....	40
3.3.2	Post-elastic behaviour .....	47
3.4	Brittle behaviour .....	48
3.4.1	Fracture mechanics .....	48
3.4.2	Continuum damage mechanics .....	49
3.5	Innovative approaches within continuum mechanics .....	51
3.5.1	Hybrid approaches .....	51
3.5.2	Different hierarchical levels .....	53
3.6	From material modelling to joint modelling .....	55
3.7	Conclusions .....	57
<b>4</b>	<b>DEVELOPMENT OF MATERIAL MODEL .....</b>	<b>61</b>
4.1	Introduction .....	61
4.2	Definitions .....	62
4.3	Damage and failure of wood .....	63
4.3.1	Failure mode model .....	63
4.3.2	Failure criteria .....	66
4.3.3	Remarks on failure criteria .....	68

4.4	Methodology .....	69
4.4.1	Thermodynamic framework.....	69
4.4.2	Continuum damage mechanics (CDM).....	70
4.4.3	Physical meaning of Poisson's ratios.....	72
4.4.4	Damage parameters.....	74
4.4.5	Damage evolution functions .....	75
4.4.6	Other computational issues .....	80
4.4.7	Mesh dependency and viscous stabilisation.....	81
4.4.8	Energy calculations.....	86
4.4.9	Increment size dependency .....	87
4.4.10	Tangential formulation.....	88
4.5	Material parameters.....	89
4.6	Subroutine UMAT .....	93
4.6.1	Programming issues.....	93
4.6.2	Verification of UMAT .....	93
4.7	Conclusions .....	103
5	STRUCTURAL MODELS.....	105
5.1	Introduction .....	105
5.2	Material models.....	106
5.2.1	Tension parallel-to-grain.....	106
5.2.2	Compression with different angles to the grain .....	117
5.2.3	Conclusions.....	124
5.3	Embedment models.....	125
5.3.1	Spruce .....	127
5.3.2	Beech .....	134
5.3.3	Azobé.....	134
5.3.4	Conclusions.....	136
5.4	Joint models.....	137
5.4.1	Joints with one dowel.....	139
5.4.2	Joints with three dowels.....	144
5.4.3	Joints with five dowels.....	146
5.5	Conclusions .....	147

6	COMPONENT TESTS.....	149
6.1	Introduction .....	149
6.2	Tension tests on steel dowels .....	150
6.3	Embedment tests .....	155
6.3.1	Literature review .....	155
6.3.2	Test setup and specimens .....	157
6.3.3	Test results .....	159
6.3.4	Ductility of beech.....	164
6.4	Comparison with database .....	166
6.5	Conclusions .....	170
7	JOINT TESTS .....	171
7.1	Introduction .....	171
7.2	Literature review.....	172
7.3	Experimental programme.....	173
7.3.1	Type of joints .....	173
7.3.2	Used materials.....	175
7.3.3	Design of test specimens.....	176
7.3.4	Testing protocol and setup .....	177
7.4	Test results .....	180
7.4.1	General results .....	180
7.4.2	Density versus load carrying capacity.....	185
7.4.3	Influence of wood species – ductility and splitting .....	186
7.4.4	Influence of steel grade.....	189
7.4.5	Effective number $n_{ef}$ of fasteners .....	191
7.4.6	Predictions - Johansen equations .....	195
7.4.7	Stiffness $K_{ser}$ .....	200
7.5	Conclusions .....	203

8	COMPARISON TESTS - MODELS.....	205
8.1	Introduction .....	205
8.2	Embedment specimens.....	206
8.3	Joints.....	209
8.3.1	Spruce joints .....	209
8.3.2	Beech joints.....	212
8.3.3	Azobé joints .....	217
8.4	Conclusions .....	219
9	CLOSURE.....	221
9.1	Conclusions .....	221
9.2	Recommendations .....	223
	REFERENCES.....	225
	CURRICULUM VITAE.....	235
	APPENDIX A: COMPONENT TESTS.....	239
A.1	Tension tests on steel dowels .....	239
A.2	Steel certificates .....	241
A.3	Naming embedment tests .....	243
A.4	Descriptive statistics embedment tests .....	243
A.5	Load-slip graphs of embedment tests .....	245
A.6	Single embedment tests.....	250
	APPENDIX B: JOINT TESTS.....	259
B.1	Naming .....	259
B.2	Descriptive statistics and measured parameters.....	260
B.3	Load-slip graphs.....	268
B.4	Single tests.....	274
	APPENDIX C: MISCELLANEOUS .....	283
C.1	Derivation of damage variables .....	283
C.2	Designation of solution-dependent state variables.....	286
C.3	Needed input material parameters - PROPS .....	287



# 1

## INTRODUCTION

*In this thesis, a 3D material model for wood has been developed. In order to verify the constitutive model, an extensive testing series has been carried out. Apart from the model verification, the tests also serve to prove the suitability and reliability of innovative timber joints using different wood species and very high strength steel dowels. This introduction motivates the research done in the thesis and outlines its structure.*

### 1.1 RESEARCH MOTIVATION

#### 1.1.1 Problem description

Everybody who ever went to the Netherlands for cycling passes hundreds of bridges in order to cross canals and dykes in this incredibly water-rich country. A lot of these bicycle bridges outside cities are made of wood such as the one shown in Figure 1-1. The passing cyclists induce loads on the bridges for which they must be designed. However, wood, or better, structural-size timber, does not make it easy for designers. Wood is anisotropic, heterogeneous and not always durable. Its properties are dependent on moisture content and load duration and usually timber joints are weaker than the timber members.

If non-constructive aspects such as durability are left out and the focus is set on short-term structural issues at a moisture content of 12%, the importance of timber joints as the generally weakest link is clear. It is a prerequisite for successful design that the mechanical performance of timber joints can be predicted reliably. At the same time, designers are interested in obtaining high-performance joints. Especially if they want to build a bridge in the Netherlands that is used by thousands of cyclists every day.

Some cyclists passing the bridge may even realise that the used wood species will most certainly not be spruce or larch, but tropical hardwood. Predictive models should hence be able to cover different wood species and not only commonly used spruce.



**Figure 1-1: Azobé bridge in the Netherlands with detail of joint (fotos: J.W.G. van de Kuilen)**

Therefore, two main tasks have to be achieved, both valid also for other species than softwoods:

- Development of reliable analysis techniques and models to predict the mechanical behaviour of timber joints;
- Development of high-performance joints to improve the versatility and competitiveness of timber in the construction sector.

### **1.1.2 State-of-the-art**

#### Modelling

The modelling of timber joints with dowel-type fasteners presents a major challenge to wood researchers. This challenge is due to several parameters. When modelling, it must be decided whether a 2D model is sufficient or a 3D model needs to be developed. For timber joints failing in a combination of embedment and fastener bending, the mechanical behaviour over the thickness of the timber members cannot be neglected. Furthermore, the fastener bending must be modelled properly. Due to the fastener bending, the stress distributions over the thickness are thought to have an important influence on the global mechanical behaviour. Another challenge is the proper modelling of the timber-steel interface, i.e. friction between the different joint components. However, all parameters mentioned above can be solved with up-to-date Finite Element software. Contact modelling, material modelling of steel and complex 3D models are all implemented in standard software. So why is it still a challenge to model timber joints?

The mechanical behaviour of the last, not yet discussed component timber is the big challenge. Timber with its complex properties cannot be covered by a single approach. Above all, two timber properties are responsible for the difficulties:

- Anisotropy with large differences of the mechanical properties parallel- and perpendicular-to-grain and different properties for tension and compression;
- Ductile and brittle failure modes occurring at the same time, i.e. ductile behaviour in compression and brittle behaviour in tension and shear.

Usually, customised models are developed for different problem classes. Joints, where the timber members are loaded perpendicular-to-grain for instance, can be modelled using fracture mechanics whereas single-dowelled joints having members loaded parallel-to-grain are often modelled applying the flow theory of plasticity. Other models make use of standard Finite Element (FE) programmes and apply cohesive elements to model the splitting planes in joints, all embedded in a plasticity framework.

However, to the author's knowledge no comprehensive models exist that are able to combine the above-mentioned difficulties in one single material model.

#### High-performance joints

A large database of tests on timber joints exists (e.g. Gehri and Fontana, 1983, Ehlbeck and Werner, 1992b, Jorissen, 1998) where a large variability of joints is covered. Different fasteners such as dowels, screws or bolts were used and the layout of the joints ranged from different fastener diameters over different number of fasteners in a row to different number of rows. Timber-to-timber joints and steel-to-timber joints were tested with different numbers of shear planes. Why then is it necessary to carry out more tests?

Only few of these tests have been performed with other species than softwood species and in most cases, mild steel dowels were used. However, a large potential lies in the replacement of mild steel dowels with very high strength steel (vhss) dowels, certainly in combination with high-density wood species. More efficient joints should be possible which require less use of materials (through less dowel diameter, timber cross sections or number of fasteners) while having the same load carrying capacity as equivalent joints with mild steel dowels. However, it must be verified if this type of high-performance joints can be used reliably. In order to do so, tests are indispensable. Also other issues such as effective number of fasteners or joint stiffness can be and need to be investigated for different species and steel grades.

A further main motivation of the tests is the verification of the developed constitutive model of the material wood.

### 1.1.3 Research questions

#### Key question

Which material models are able to reliably simulate the mechanical behaviour of innovative timber joints with very high strength steel dowels using different timber species?

#### Subpart experiments

Is it possible to replace mild steel dowels with very high strength steel dowels and is the load carrying capacity higher?

Can any new information regarding the effective numbers of fasteners  $n_{ef}$  be found or does another viewing point help to further understand the effective numbers of fasteners? What about the joint stiffness?

To what extent do the wood species and the steel grade influence the joint behaviour?

#### Subpart modelling

Is there a novel approach to model wood joints that is able to model ductile and brittle failures?

Is it possible to implement such an approach as material subroutine into commercial finite element programmes such that the material input parameters are clear and easy to identify without the need to programme a complete finite element code? This should lead to a subroutine that can easily be used and optimised also in future.

### 1.1.4 Research programme

In view of the key question, the research programme has been developed. After a thorough literature study presenting comprehensive approaches for timber joint modelling, the continuum damage mechanics (CDM) framework was chosen to develop a 3D material model for wood. This 3D model was then used as constitutive law in numerical simulations with the aim to model and to understand embedment tests and joint behaviour. Material tests, i.e. tension and compression tests were modelled and analysed. The next step involved embedment models where also interaction between timber and fasteners was modelled. Lastly, the most complex models, joint models, were developed. Double-shear timber models with slotted-in steel plates and with one, three and five dowels in a row were simulated.

The numerical models were verified in order to judge the quality of the material model. Literature was used to verify essential model characteristics. Extensive test series were carried out whose outcomes could be compared with the modelling results. High-performance joints were tested where high strength mild steel (hss) dowels were replaced by very high strength steel (vhss) dowels and where other species than softwoods were used. By doing so, it was also possible to analyse the feasibility of high-performance joints. However, the fundamental idea was to replace mild steel dowels with vhss dowels.

This strategy could not be followed as the ordered mild steel dowels did not correspond to S235 or S355, but were high strength steel dowels (hss) with a tension strength above 540 MPa. Further aspects of the mechanical behaviour, i.e. the effective number of fasteners, the influence of wood species, the steel grade and the joint stiffness were discussed. The single scope of model verification was thus broadened by more general investigations into the mechanical performance of joint systems. Preparative component tests, tension tests on steel dowels and embedment tests completed the experimental part. The used wood species for joint tests were spruce, beech and azobé (also known as ekki), and five species for embedment tests, spruce, beech, azobé, cumaru and purpleheart.

## 1.2 STRUCTURE OF THE THESIS

Figure 1-2 shows a flow diagram that outlines the thesis. The thesis can be divided in four parts: reviewing – modelling – testing – comparing.

The **first part** is focused on the material wood and how experimental results can be transferred into input values needed for modelling. The other chapter of part one comprises an extensive review on modelling techniques used to develop numerical joint models. The choice of continuum damage mechanics for developing a material model is motivated.

The **second part** is dedicated to the development of a 3D material model for wood using the concepts of continuum damage mechanics. The theoretical background is explained and the developed routine is verified. The second chapter of part two presents structural models where the developed material model is applied. The structural models range from simulations of uniaxial material tests over embedment tests to joint models.

The **third part** presents the experimental results which covered component tests on the steel dowels and embedment tests. These two testing series served as fundamental tests for the preparation of joint tests. The second chapter of part three shows and analyses joint tests using high strength steel dowels (instead of mild steel dowels) and very high strength steel dowels and three different wood species.

In the **fourth part**, consisting of only one chapter, the modelling outcomes are compared with the experimental outcomes in order to judge the quality of the developed 3D material model. Furthermore, a parameter study is performed matching test results with model prediction capacity.

The closure finally contains conclusions and recommendations for further research.

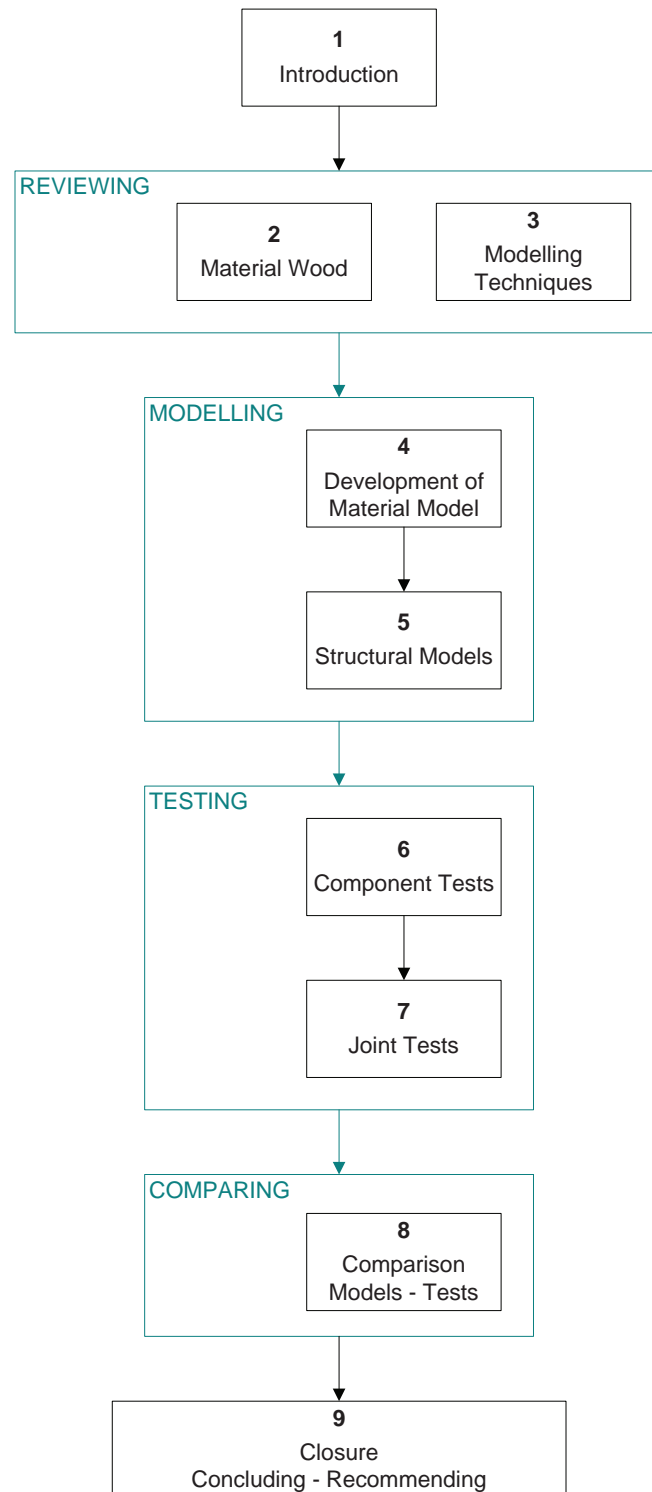


**Figure 1-2: Flow diagram of the thesis**

# 2

## MATERIAL WOOD

*Macroscopic and microscopic failure modes of wood are discussed. The different failure modes of wood are depending on the type and direction of loading as wood is a cellular material composed of longitudinal fibres assembled in annual rings. It is inhomogeneous, anisotropic and has different strengths in tension and compression, showing quasi-brittle failure in tension and shear and ductile failure modes in compression. The focus of this chapter lies on problems connected with the transfer of experimental results into mathematical models. Only short-term loading issues at constant moisture content are treated.*

### 2.1 INTRODUCTION

In order to understand the mechanical behaviour of wood and to develop mathematical models, the anatomy of wood, 3D strength and stiffness properties and the various failure modes under different loadings must be known. Information about these topics can be taken from literature concerning material testing under uniaxial and multiaxial loading. Here, a relevant summary is presented. For more information, the comprehensive literature on these subjects can be consulted. (e.g. Kollmann and Côté, 1984, Grosse, 2005, Persson, 2000, Poulsen, 1998, Keenan, 1973, Eberhardsteiner, 2002, Franke, 2008, Smith et al., 2003). As a preamble it is emphasised that most research is focussing on softwood.

In this chapter, firstly the uniaxial behaviour of wood is presented before multiaxial loading and its effect is discussed. As all mathematical methods rely on test results that are delivering the necessary material properties for the models, the reliability of testing methods and their outcomes are emphasised. Also because in the author's opinion, in the modelling literature the applicability of test results on numerical models is not always adequately discussed. Furthermore, the herein presented results serve to understand the chosen modelling approach presented in chapter 4.

The anatomy of wood with a focus on the differences between different wood species is shortly explained. This section on anatomical issues is considered to be important because here, not only softwood is treated but also European and tropical hardwoods.

Moreover, the natural variability of the mechanical properties will be shortly recalled. For timber, this scatter is significant and has to be considered when deciding for a modelling approach. Too sophisticated approaches requiring precise material parameters do not seem to be relevant if these parameters are not only difficult to establish but are also subject to large scatter.

Material properties such as stiffness and strength are derived from test results. These material properties describe a constitutive model – the relationship between the stress of a material and the associated strain. With the help of such relationships, finite element (FE) programmes can calculate stresses from deformations and thus strains. If simple uniaxial tests are carried out from which uniaxial strengths are derived for mathematical models, in reality multiaxial stresses and strains will already have developed although these phenomena are not measured during the test. The measured values will enter the model, the non-measured will not. With increasing complexity of test setups (biaxial tests, for instance), this problem of measuring certain specified values but neglecting others is getting bigger.

Test outcomes depend also largely on the geometry of the specimen, its moisture content and the boundary conditions. Sometimes, failure modes are developing that are not relevant for practice. Another important factor is the measuring equipment. For instance, when carrying out uniaxial compression tests, some researchers measure the deformations directly on the wood using extensometers or strain gauges whereas others measure the displacement of the testing machine in relation to the test specimen. The resulting load-slip curves will look differently. In the last case, the influence of the supports and the machine's inaccuracies will be included in the test results. Another important factor is the location of measurement. It is not always clearly indicated where experimental results such as load-slip curves were measured on the specimens

Therefore, already at this first crucial step of modelling that is the determination of the constitutive relationship, inaccuracies are becoming a component of the mathematical representation of a structure. A finite element model is just a mere mathematical idealisation of a complex reality where inaccurate datasets enter the modelling at an early stage. This is not a problem per se, but it is crucial to be aware of the limitations in order to produce reliable modelling outcomes for different purposes.

Lastly, the mechanical behaviour of timber used in joints with dowel-type fasteners is discussed. In joints, the loading of the material wood is not as clear as during pure material tests. The dowel diameters and the number of dowels have an influence and they are also rotating inside the wood if a plastic hinge is developing. These more complex actions on wood complicate the investigation of the failure modes. The phenomenological failures on the anatomic scale are combinations of the failures under uniaxial stresses, the stress states causing joint failures are complex. All this illustrates

the challenge of understanding the mechanical behaviour of timber joints in order to properly model it and of the difficulty to determine valuable mechanical properties.

## 2.2 UNIAXIAL TESTS

Modern timber design codes are based on the approach of partial safety factors. The characteristic values for material strength are charged with safety factors and in the case of timber, also with a factor considering the nonlinear viscoelastic moisture-dependent nature of wood. The characteristic values are determined with material tests. However, it is impossible to determine all relevant values such as modulus of elasticity (MoE), modulus of rupture (MoR), compression and tension strength parallel and perpendicular to the grain and shear strength with one single test. Usually, a large number of four-point bending tests deliver regression equations. By means of these equations, a correlation between MoE and MoR can be derived that is needed for the strength-grading of wood. Other properties such as compression, tension and shear strength are derived from the MoR or determined experimentally. (CEN, 2004a, CEN, 2003). The methods mentioned above also mean that no material tests need to be carried out to establish the mechanical properties available in standards, but that empirical relations between density and MoE and a certain property such as compression perpendicular-to-grain define the strength values. In other words, the mechanical properties used for structural modelling and design are not necessarily derived from pure material test results. Furthermore, the test specimens should be of structural size to take the natural variation of timber into account. The natural scatter of material properties cannot be captured by tests on small clear specimens. Furthermore, the measured mechanical properties will be much higher for defect-free wood.

Despite these requirements, most of the available uniaxial testing data are derived from tests carried out on small clear specimens. This, together with the mentioned problems arising from the test setup and difficulties in measuring all occurring phenomena, illustrates how difficult it is to accurately represent the complex nature of wood by means of a mathematical model. Other test series investigate only the mechanical behaviour up to a certain level of deformation which is usually quite low. For instance, compression specimens parallel-to-grain may be loaded only up to the peak stress but not further. On the other hand, the crack growth of specimens loaded in tension must be controlled in order to establish reliable properties such as fracture energy  $G_f$ . Many different values for the fracture energy will be found also due to the difficult test setup. This all complicates the decision which input values to choose to create a good mathematical model.

In the following, typical results for uniaxial tests are shown. Usually, three main directions, longitudinal L, radial R and tangential T, are distinguished as shown in Figure 2-1<sup>1</sup>. For instance, the MoE for softwood in longitudinal direction is approximately 20

---

<sup>1</sup> This definition is consistently used throughout the thesis.

times bigger than the MoE in radial direction which is about 2 times the MoE in tangential direction (Neuhaus, 1994). As a common approach, wood is hence considered as being transversely isotropic. The radial and tangential directions are summed up as the direction perpendicular-to-grain. In fact, many tests in literature do not specify the orientation of the annual rings, but report results parallel and perpendicular to the grain.

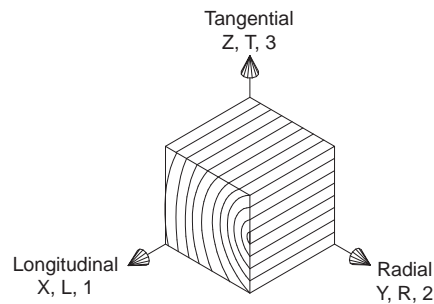


**Figure 2-1: Definition of material directions**

### 2.2.1 Tensile strength

Tension strength parallel-to-grain of wood is usually tested with dog bone shaped specimens. The setup for tension tests perpendicular-to-grain is more complicated. Some researchers used cleavage specimens, but these specimens have predetermined failure planes and the stresses are not uniformly distributed in the stresses section and thus do not represent the ultimate tension stress. More appropriate test specimens are again dog bone shaped specimens that are avoiding predefined failure planes. These specimens are difficult to produce though. For this reason, Poulsen (1998) glued specimens onto a testing rig (reproducing the dog bone shape with glue in order to avoid failure of the glue line). Usually, tests are carried out at 12% moisture content (m.c.) unless defined otherwise.

As shown in Figure 2-1, two different perpendicular planes can be defined, the LT- and the LR-plane. Tension perpendicular-to-grain can thus be applied in the R-direction, but also in the T-direction leading to tension failures in the LT- or the LR-plane respectively. However, henceforth the terminology ‘perpendicular-to-grain’ is used including both directions as often no difference is made between both. (Table 2-2 confirms this. No significant difference can be observed for the LT- or LR-plane) If more information on the material orientation is given in literature, it will be indicated.

Figure 2-2 shows typical load-displacement curves of tension tests parallel-to-grain of spruce (*Picea abies*) carried out on (asymmetric) dog bone shaped specimens 2 x 20 mm in the LR-plane of clear wood (Franke, 2008). Figure 2-3 shows typical test results in terms of stress-strain of uniaxial tension tests in the tangential direction of small (20 x 20 mm) clear Norway spruce (*Picea abies*) specimens (Poulsen, 1998).

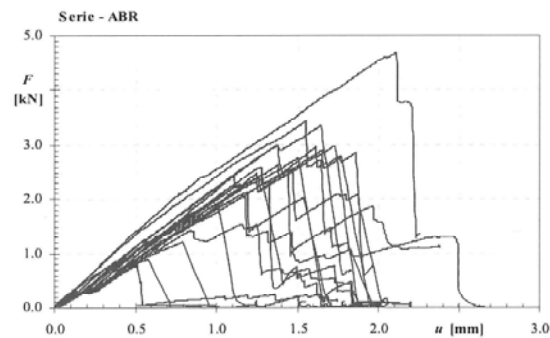


**Figure 2-2: Tension parallel-to-grain of *Picea abies*,  $5\text{kN} \hat{=} 12.5\text{MPa}$  (Franke, 2008, Fig. 4-3)**

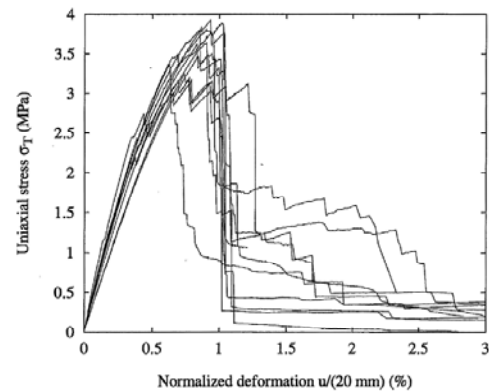


**Figure 2-3: Tension perpendicular-to-grain of *Picea abies* (Poulsen, 1998, Fig. 5.3)**

The brittle failure modes can be clearly seen in Figure 2-2 and Figure 2-3. In tension perpendicular-to-grain, wood is quasi-brittle as can be seen in Figure 2-3. After a slight plastic deformation, the wooden pieces are splitting and a sudden drop in load carrying capacity occurs. The general form of the graph does not differ between tests parallel and perpendicular to the grain, but the ultimate load carrying capacity is different. The tensile strength perpendicular-to-grain is 1%-5% of the tensile strength parallel-to-grain when speaking in terms of characteristic strength values (CEN, 2009). Furthermore, the strength is different between clear and structural-size specimens due to the natural variability (due to knots, grain angle, etc.). Kollmann and Côté (1984) give a table where this can be clearly seen, Table 2-1. Already the presence of a few small knots reduces the tensile strength by 51 percent.

**Table 2-1: Influence of knots on tension strength (Kollmann and Côté, 1984)**

pinewood	density [ $\text{kg/m}^3$ ]	tensile strength	
		[MPa]	reduction
clear	500	76.5	
few, small knots	530	37.7	51%
many, large knots	570	11.7	85%

Figure 2-3 also shows the difficulties associated with tension tests. As the failure mode is brittle, it is nearly impossible to carry out stable tests whose parameters such as fracture energy  $G_f$  are easily transferred into mathematical models. Even more so, the strain is often not measured up to failure. The crack growth is difficult to control even with displacement-controlled test methods.

Another way to analyse the brittle behaviour in tension is to investigate the fracture behaviour by doing mode I tests<sup>2</sup> in terms of fracture mechanics (for instance, compact tension (CT) tests (Boström, 1994) or single-edge notched bending (SENB) tests (Larsen and Gustafsson, 1989)). The aim of these tests is to establish the fracture energy  $G_f$ . Fracture energy is one of the few available parameters to simulate softening behaviour under tension loading if the post-peak behaviour should be modelled. Table 2-2 is taken from Grosse (2005) and reproduces some data from literature for the fracture energy  $G_f$  in mode I in tension perpendicular-to-grain. When looking at Table 2-2, the scatter of the test results is evident.

**Table 2-2: Values for fracture energy  $G_f$  in mode I as cited in Grosse (2005), Tabelle B.6**

Author	test setup	species	$G_f$ [N/m] RL-system	$G_f$ [N/m] TL-system	
Aicher (1997)	SENB	spruce	280	-	
Boström (1987)	notch on one side	pine	m.c.=8%	460	550
			m.c.=10%	445	500
			m.c.=13%	535	460
			m.c.=26%	515	-
			m.c.=?	380	405
	CT		206	-	
Daudeville (1999)	SENB	spruce	220	160	
		fir	210	157	
		spruce	220	164	
		spruce and fir	h=45mm 251	157	
			h=67&100mm	-	160
Frühmann (2002)	splitting test	spruce	180	230	
		beech	540	730	
Reiterer (2002)	splitting test	spruce	337	213	
		pine	422	422	

On the microscopic scale, two different failure modes can be observed when testing parallel-to-grain. The first mode is occurring generally within thin earlywood<sup>3</sup> cells and consist of a net tension failure of the cells whereas thick-walled latewood cells often

<sup>2</sup> There are three possibilities to load a specimen in order to enable crack propagation:

Mode I: Opening mode with a tension load acting perpendicular to the crack plane

Mode II: In-plane shear mode with a shear load acting parallel to the crack plane and perpendicular to the crack front

Mode III: Out-of-plane shear mode with a shear load acting parallel to the crack plane and parallel to the crack front

<sup>3</sup> Please recall that only wood from temperate climate regions has annual rings; tropical hardwoods have growth rings, but no early- or latewood. However, phenomenologically, the failure modes are similar.

rather fail in shear along the cells having no crack running through the cells, but around them.

For tension perpendicular-to-grain, failures can be observed where the cell walls are breaking and the cracks are going through the cells, so-called transversal failures. The other failure mode is independent from the strength of the cell walls, but again is occurring between neighbouring cells. This failure mode is an intercell failure where the middle lamellae is detached or an interwall failure where the S1-layer is being peeled off from the S2-layer (S1 and S2 are layers of the cell wall).

Generally, it must be said that often mixed modes are occurring when a specimen is failing in tension parallel or perpendicular to the grain. The manifold combination possibilities of failure modes underline the difficulties associated with the transfer of test results to mathematical models. The test results need to be smeared over a 'tension strength perpendicular-to-grain with a certain fracture energy  $G_f$ ' in order to make the properties manageable in mathematical models.

### 2.2.2 Compressive strength

A couple of problems concerning the test setup must be resolved before undertaking compression tests. With too small, usually cubic specimens, the boundary conditions, i. e. the fixing of the specimens in the testing rig, have a big influence on the failure mode and ultimate stresses. The specimens must be high enough to ensure a homogeneous stress distribution over the section and at the same time stocky enough to avoid bending and instability. Other researchers also propose dog bone shaped specimens (Dinwoodie, 1968) to overcome these problems. This illustrates how difficult it is to carry out a valid test, even a seemingly simple pure compression test. Analogous to tensile strength, also for compression perpendicular-to-grain different failure planes, LT and LR, can be identified, but are not always recorded.

Figure 2-4 and Figure 2-5 show typical results in terms of stress-strain. Figure 2-4 shows results of compression tests parallel-to-grain done on 25 x 25 x 5 mm specimens. The chosen specimen height by François and Morlier (1993) was small with 5 mm. The reason to choose such a low height was to avoid kink bands (see Figure 2-8) as the authors argued that in presence of kinking, no pure compression tests are carried out because of instability and buckling of the cells. The hardening branch at the end of the test visible in Figure 2-4 indicates however that the test rig was tested rather than the wood. Moreover, compression strength parallel-to-grain should include kink bands in the author's opinion as this is also observable in structures. Other authors use 10 x 10 mm specimens with a height of 20 mm (Reiterer and Stanzl-Tschegg, 2001) to establish the compression strength parallel-to-grain. Also those are small specimens, the results look similar with a yield drop but the hardening branch is missing. Poulsen (1998) tested 20 x 20 mm clear specimens with a height of 70 mm. In his compression tests parallel-to-grain, he also obtained a distinct yield drop with a subsequent steady plateau. His results are shown in Figure 2-5 for clear *Picea abies* specimens with different heights.

Figure 2-6 shows results for compression perpendicular-to-grain done by Franke (2008) on 40 x 40 x 40 mm clear cubes for three different annual ring orientations, in the LT- and LR-plane and with 45° inclined annual rings (= NO-90).

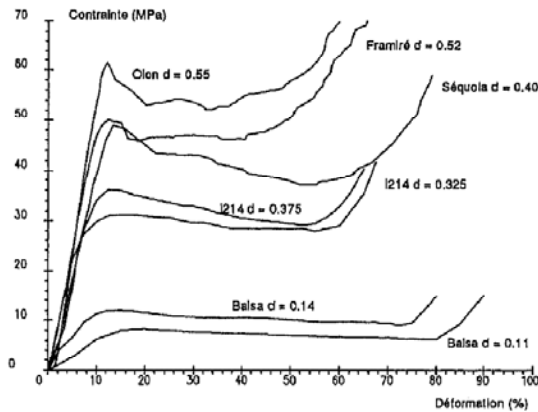


Figure 2-4: Compression parallel-to-grain of different species (François and Morlier, 1993)

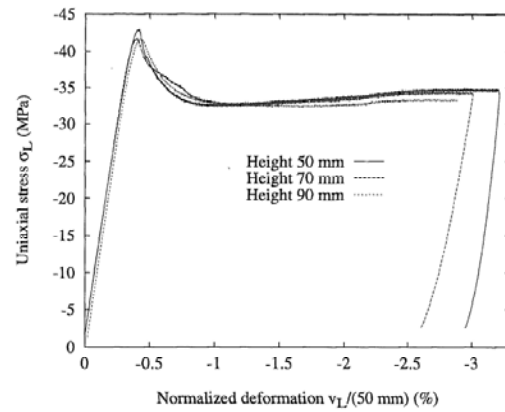


Figure 2-5: Compression parallel-to-grain of *Picea abies* (Poulsen, 1998, Fig. 2.11)

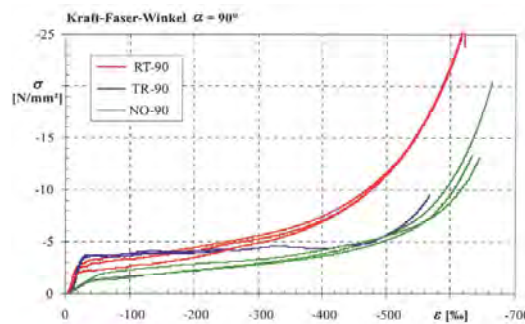


Figure 2-6: Compression perpendicular-to-grain of *Picea abies* (Franke, 2008, Fig. 4-19)

The typical load-slip behaviour in compression parallel-to-grain with a yield drop and subsequent steady plateau is changing when the angles of the grain are modified. At angles to the grain of about 10° to 45°, the failure modes are brittle due to the activated transverse tension and shear. The larger then the angle to the grain ( $\alpha > 45^\circ$ ), the more the failure mode is approaching a pure compression perpendicular-to-grain failure with distinctive densification as shown in Figure 2-6. Tests in compression at different angles to the grain are also well illustrating the creation of multiaxial stress states in formally uniaxial tests as shown in Figure 2-7. The test setup from Figure 2-7 is quite important for researchers who want to investigate into the interaction between shear and transverse compression.

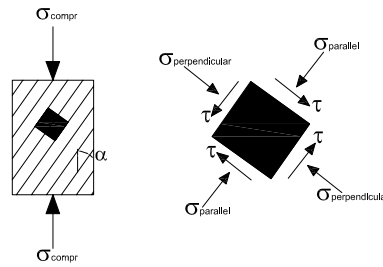


Figure 2-7: Transformation into principal stresses

The failure modes in compression are completely different from the quasi-brittle results in tension. Wood in compression is ductile with a distinct plastic behaviour. In compression parallel-to-grain, the cells are structurally acting as columns which are failing by kinking – a (inclined) kink band is developing, Figure 2-8. In Figure 2-5, the incipient kinking of the fibres is expressed by the yield drop after reaching the maximum stress. The nonlinearity before the decrease in strength is due sliding and microscopic buckling phenomena. After the incipient kinking, a steady plateau is developing where the material is yielding without gaining higher stresses (Poulsen, 1998). Figure 2-8 shows the kink band angle on the tangential face of specimens of different size loaded in compression parallel-to-grain. The cell buckling is usually starting in earlywood, as there the cell walls are thinner and the cells have bigger lumens and thus are more susceptible to stability problems. In reality, the failure mechanism in compression parallel-to-grain is much more complex, first damage occurs in the S2 layer and small slipping is happening between the cells before the buckling starts.

Another possible microscopic failure mode is basically the pushing of the cells into each other, a telescopic-kind of failure as shown in Figure 2-9.

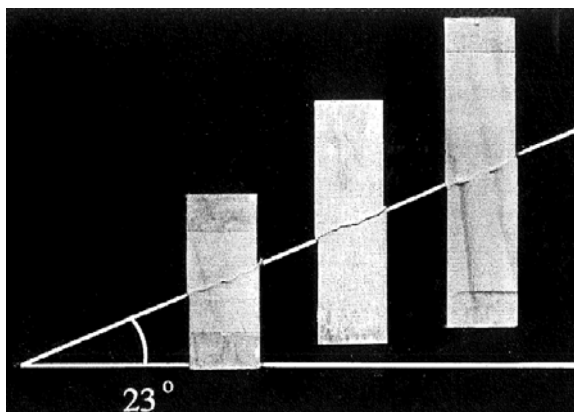


Figure 2-8: Kink band angle,  $\alpha = 23^\circ$   
(Poulsen, 1998, Fig. 2.25)

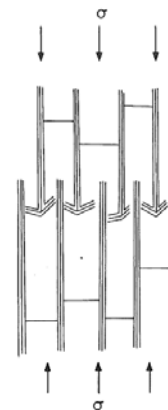


Figure 2-9: Telescopic failure  
(Gibson and Ashby, 1997, Fig. 10.11b)

Figure 2-6 shows results for compression tests perpendicular-to-grain. The onset of plasticity is at a low level of deformation and after a steady yielding without increase in

stress, the densification starts leading to high stresses without increase in deformation. Microscopically, the behaviour in compression perpendicular-to-grain is easily understood when one recalls that the wood cells are hollow and are similar to honeycombs. A compression force on these hollow cells will lead to a folding of the hollow sections (see Figure 2-10). Micromechanically, the failure behaviour in radial compression is different to that in tangential compression. Radially, the wood cells are stacked transferring the forces directly over the walls parallel to the force which are failing in buckling (Figure 2-10). In tangential direction, the cell walls are assembled in a ‘stretcher bond’ leading to a much smoother passage between elastic and plastic region (Figure 2-11). The reason for this smooth transition is the additional bending of the horizontal cell walls that is preceding the buckling of the vertical cell walls. Phenomenologically though, there is no real difference in the load-slip curves of both tests - except for the smoother transition between elastic and plastic region of the tangentially loaded specimens. However, slightly different load carrying capacities are reached as can be seen in Figure 2-6.

In comparison to tensile strength (Table 2-1), compressive strength is certainly much less susceptible to the influence of knots as can be seen in Table 2-3.

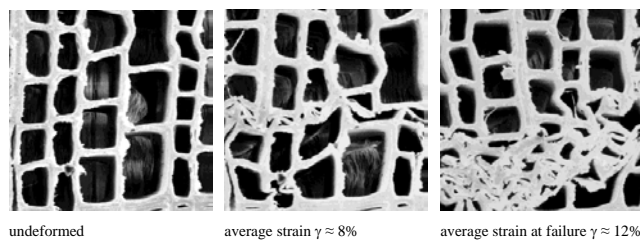


Figure 2-10: Radial compression (Persson, 2000, Fig. 3.19)

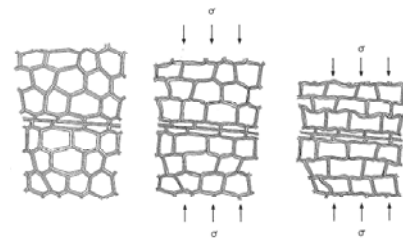


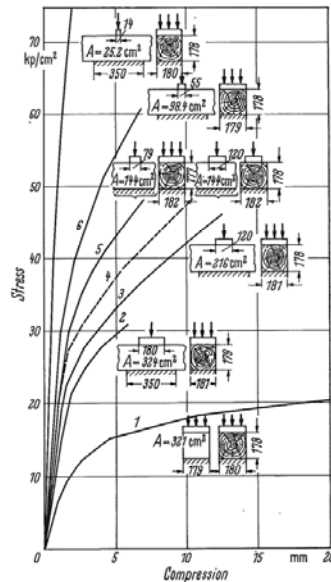
Figure 2-11: Tangential compression (Gibson and Ashby, 1997, Fig. 10.6)

Table 2-3: Influence of knots on compression strength (Kollmann and Côté, 1984)

pinewood	density [kg/m <sup>3</sup> ]	compressive strength	
		[MPa]	reduction
clear	500	39.5	
few, small knots	530	35.4	10%
many, large knots	570	30.8	22%

An interesting testing series is reported in Figure 2-12 taken from Graf (1921) as cited in Kollmann and Côté (1984). Load-slip diagrams of compression tests perpendicular-to-grain carried out on cubes compared to cuboids are shown where only part of the whole surface was loaded. The behaviour of the ‘same’ wood with different geometries is completely different. This can be explained by two mechanisms. Firstly, the load distribution will be different. Secondly, cells have a longitudinal form that could be described as a static system of a beam which can take also tension forces in its axial

direction. When only part of the surface is loaded, the longitudinal cells are even more acting as beams that are increasing the load carrying capacity and at the same time are reducing the deformation.



**Figure 2-12: Load-slip diagrams comparing different compression loadings (Kollmann and Côté, 1984, Fig. 7.73)**

The difficulties associated with the transfer of mechanical properties to constitutive relations are clear. Analogous to failures under tensile loading, also failures under compressive loading are caused by different micromechanical effects and usually, only small clear specimens are tested. The question of what actually should be modelled with a mathematical simulation must be answered carefully knowing about boundary conditions in testing. Also the decision whether localised failure phenomena like buckling of fibres under compression parallel-to-grain shall be modelled or not must be taken carefully.

### 2.2.3 Shear strength

Probably the most difficult uniaxial tests are shear tests, if it is possible at all to properly carry out this type of test. In Grosse (2005), a good review is given of the different testing methods and specimen geometries – the most popular one being the ASTM shear block. Unfortunately, one must be cautious when using shear block test results. As Moses and Prion (2004) could show by means of a numerical model, it may not be the actual shear strength one is measuring. The ASTM shear block suffers from stress peaks causing a premature failure before the actual shear strength is reached. The stress distribution is not uniform. Another problem is that usually, the failure planes are predefined. The material does not have the possibility to follow its own failure plane as it happens in reality.

Another test setup is beams with a low span-to-depth ratio. Keenan (1973) stated that the shear strength of beams is usually much higher than the shear strength of ASTM block specimens. Furthermore, “beam shear strength is not constant but decreases with an increase in the shear span to depth ratio” (Keenan, 1973). Therefore, depending on the test setup, different mechanical properties will be found. In general, it can be said that it is inevitable to introduce parasitic stresses when doing a shear test. It is rather difficult to decide which results are reliable and useable for mathematical models and which are not.

Van de Kuilen and Blaß (2005) carried out shear tests on structural-size I-beams of azobé (*Lophira alata*) and not on small clear wood. The test setup was five-point bending tests with a short span to trigger shear failure, accepting that parasitic stresses were also developing. The same typology of tests were used by Van de Kuilen and Leijten (2002) for other tropical hardwood species and also for spruce.

Discussing the influence of the test setup on shear strength values, it is sufficient to look at three examples for spruce taken from the above-mentioned literature to understand the magnitude of the problem. Van de Kuilen and Leijten (2002) for instance give a mean shear strength of 9.1 MPa. On the other hand, mean values taken from Table B.5 in Grosse (2005) give values of 6.3 MPa (bow-tie shaped, Liu, 1983, as cited in Grosse, 2005), 6.7 MPa and 8.3 MPa (Riberholt, 1991, as cited in Grosse, 2005) or 11.3 MPa (Slip-block, Poulsen, 1997, as cited in Grosse, 2005). Denzler and Glos (2007) carried out tests according to EN 408 (CEN, 2003) with glued-on steel plates. They found mean values between 3.3 and 4.4 MPa. Obviously, the variation of test results is rather high with values ranging between 3.3 MPa and 11.3 MPa.

Generally, shear failures are explosive brittle failures just like tension failures. Shear test results look hence similar to tension tests as shown in Figure 2-3. Shear failure, mode II failure in terms of fracture mechanics (see footnote 2), always happens in the LT- or LR-plane and usually follows the annual rings. Shear failure across cells due to shear stresses in the LR- or LT-plane does not happen. If the failure mechanism is allowed to choose its own failure plane, then it generally follows the annual ring separating earlywood from latewood as this is the weakest part. But, as the tangential shrinking is the highest, typical shrinking flaws are forming in radial direction. These flaws offer a natural path for shear cracks. Accordingly, common shear failures show a zigzag curve, following the tangential plane and then jumping in radial direction to another tangential plane (Figure 2-13). Microscopically, shear failures show the same rupture mechanisms as tension perpendicular to the grain. Interwall (middle lamellae are failing) and intercell failures (S1 layer is detached from S2 layer) can be observed as well as breaking of cell walls – so-called transversal failures.

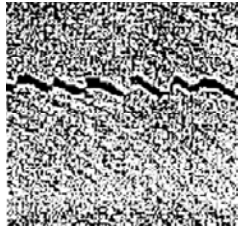


**Figure 2-13: Zigzagging of a shear crack failure, ring angle = 30° (Riyanto and Gupta, 1996)**

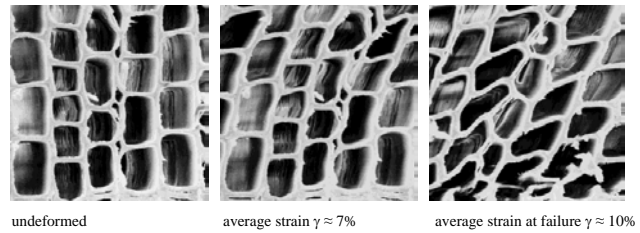


**Figure 2-14: Microscopic shear deformation in RT-plane (Persson, 2000, Fig. 3.21)**

Another shear failure mode is the so-called rolling shear failure – not a longitudinal shear failure, but a failure caused by the shear stresses in the RT-plane. Cell bundles may fail just like a bundle of straws that are rolling off one upon the other – see Figure 2-15. However, rolling shear failure is not relevant for most loading cases as it is not activated easily. Rolling shear usually occurs in cross-laminated timber plates and not often in joints.



**Figure 2-15: Rolling shear failure**

Bocquet (1997) carried out an interesting testing series to investigate the importance of shear strength. He performed an ASTM embedment test (half-hole test on spruce, *Picea abies*, ASTM, 2007) perpendicular-to-grain, drilling a hole directly underneath the bolt leaving just a 1 mm band of wood cells between the hole and the bolt. He additionally cut this band of cells to avoid that the remaining layer of cells will be loaded in tension. As can be seen in Figure 2-17, there is no significant difference between the two tests up to the proportional limit. The only difference is a softer plastic branch of the test with the hole. The importance of shear for the load carrying capacity perpendicular-to-grain was confirmed as no tension forces could develop and no material underneath the bolt was available to give support.

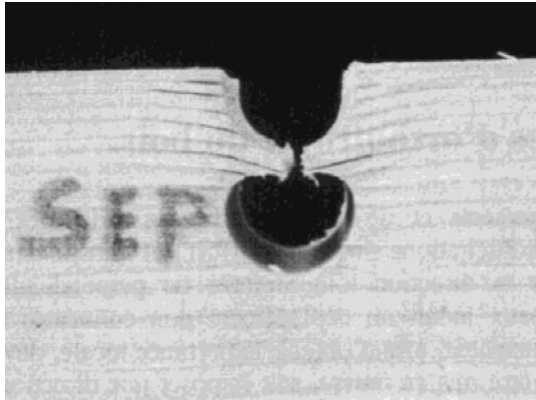


Figure 2-16: Test specimen perpendicular-to-grain (Bocquet, 1997, Fig. 1.23)

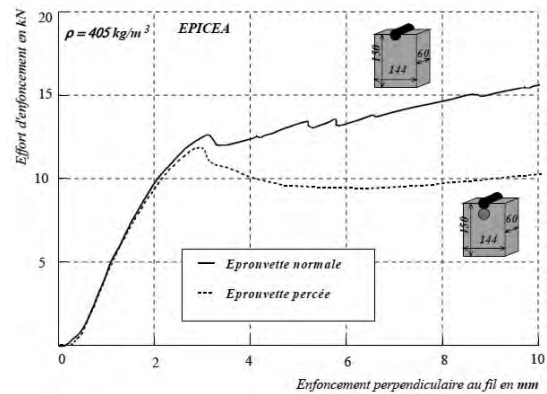


Figure 2-17: Load-displacement curve (Bocquet, 1997, Fig. 1.22a)

## 2.3 MULTIAXIAL TESTS

Multiaxial tests are necessary to investigate in interactions between stresses. Tests applying two (or even three) normal stress components are generally a bit easier to carry out than combinations between normal stresses and shear. However, the last combination, in the form of perpendicular compression combined with shear, has always been of great interest to many researchers because they argue that a high perpendicular compression should activate friction along the cells and thus the longitudinal shear strength should augment. Other researchers decline the contribution of friction, assuming instead an arrest of shear crack propagation due to strong layers (the crack propagation can only occur in longitudinal direction) that leads to an equivalent hardening effect rather than friction (Van der Put, 1993).

In Grosse (2005), a valuable summary is presented which gives a clear overview over most biaxial tests carried out in timber research (Grosse, 2005, Table 5.1). Especially tests on specimens with oblique grain are common (Figure 2-7). Similar to uniaxial tests, most of these tests are carried out on small clear specimens.

### 2.3.1 Combination of normal stresses

An extensive test series on biaxial testing has been carried out by Eberhardsteiner (2002) on cruciform test specimens (LR-plane) of clear spruce wood (*Picea abies*). Also Hemmer (1985) developed tests with combinations of multiaxial stresses on tube-shaped specimens (LT-plane) of white fir (*Abies alba*) that can be also loaded in torsion. Figure 2-18 shows their test results with an angle to the grain  $\alpha = 0^\circ$  in a 2D stress space. It can be seen that material strength is decreasing under multiaxial loads in comparison to uniaxial strength values.

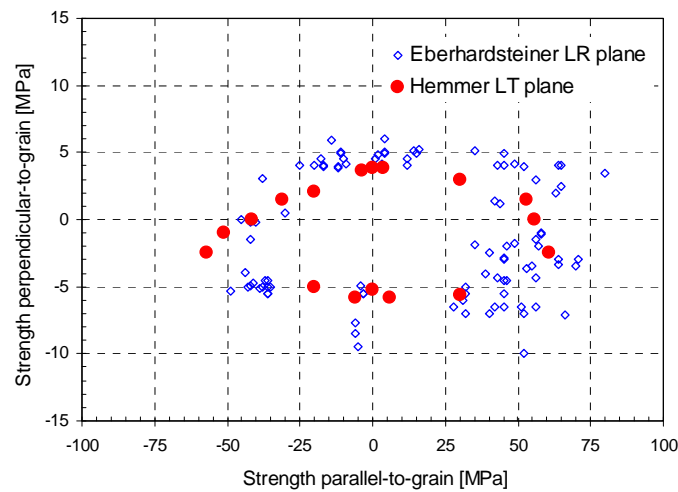


Figure 2-18: Results biaxial tests – combination of normal stresses,  $\alpha = 0^\circ$

Eberhardsteiner (2002) varied the angle to the grain  $\alpha$  of his test specimens. Furthermore, as the specimens were thin, a plane stress situation could be obtained. Fleischmann (2005) extended the testing programme to specimens with knots and the LT-plane. With contact-free measurement methods, they were able to record the resulting 3D strain. Therefore, not only the maximum stresses were measured, but also the evolution of stresses during the test as given in Figure 2-19 (The results are the same as shown in Figure 2-18). Stress evolution was linear up to failure for tension stress combinations (e.g. first quadrant), but nonlinear for compression stress combinations (e.g. third quadrant).

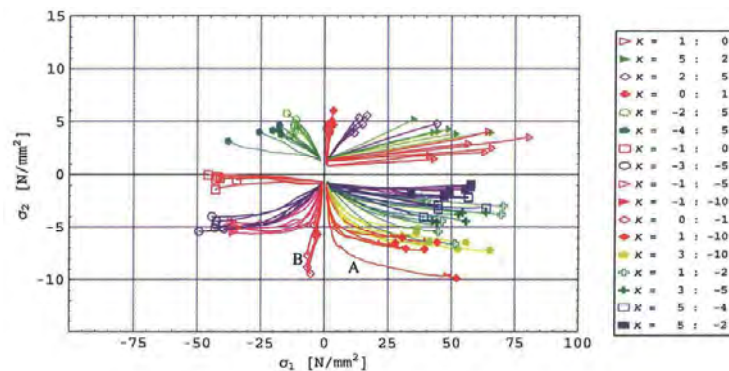


Figure 2-19: Results biaxial tests with stress evolution,  $\alpha = 0^\circ$  (Eberhardsteiner, 2002), Fig. 4.22)

Hemmer (1985) was able to introduce also longitudinal stresses together with torsional and transversal stresses. Therefore, some of his results in Figure 2-18 actually have a third (measured) component that expands the 2D stress space into 3D.

Other biaxial and triaxial compression tests were carried out for instance by Ashkenazi et al. (1973).

### 2.3.2 Combination of normal and shear stresses

In literature, different outcomes on biaxial tests with transversal compression and shear can be found. Mandery (1969) carried out ASTM shear block tests with additionally applied compression perpendicular-to-grain and tests on beams with notches. He found a linear relationship between compression stresses and shear stresses as can be seen in Figure 2-20. Tests carried out by Poulsen (1998) on oblique-grain specimens and Hemmer (1985) on tube-shaped specimens (that can be loaded in torsion) instead show a non-linear relationship where initially, the shear strength is augmenting when transversal compression is present but later, with higher transversal compression, the shear strength is decreasing. Also Franke (2008) carried out tests with oblique angles to the grain. His outcomes however do not confirm the assumption of higher shear strength with higher transversal compression (Figure 2-20). However, considering Figure 2-20, it is evident that not enough test results are available to properly analyse the influence of compression perpendicular-to-grain on the shear strength. It is also possible that the maximum compression level of the tests given in Figure 2-20 was too low with 6 MPa.

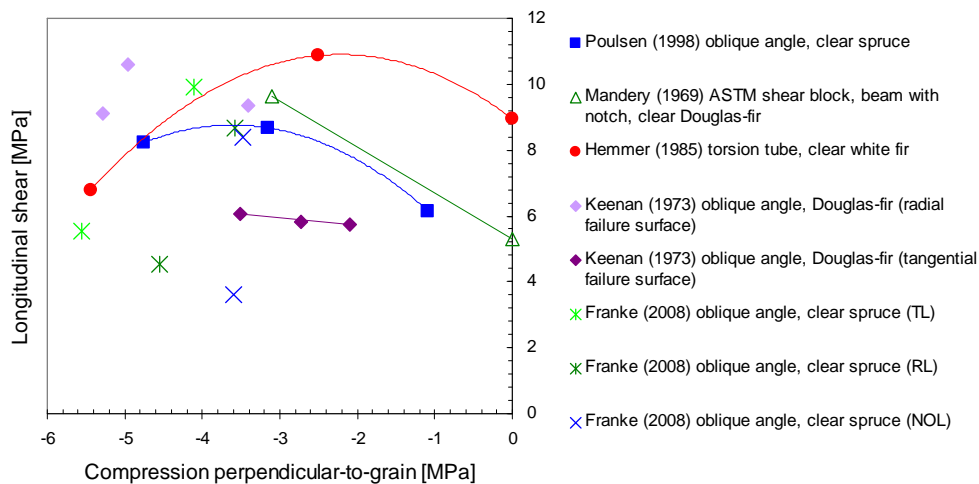


Figure 2-20: Results biaxial tests with transversal compression and shear

Another large testing series was carried out by Keenan (1973). Maybe the most interesting aspect of his work is the fact that he used different test setups to investigate the shear strength of glulam beams. The outcomes on oblique angle specimens are also shown in Figure 2-20. Keenan stated that all his failure modes were shear failures except for a combined shear and transversal compression failure observed when compression perpendicular-to-grain was highest. The results of the two other test series in terms of shear stress versus transversal compression stress are shown in Figure 2-21 and Figure 2-22. When considering the results of the test on ASTM shear block specimens (Figure 2-21), the trend discussed earlier is confirmed. Especially when the failure surface is in the LT-plane (radial failure surface), a hardening of the shear strength due to compression

perpendicular-to-grain is visible. This is different when the failure surface is tangential. Then the trend line is rather horizontal and no hardening can be observed. The data from Mandery (1969) is also inserted. He did however not record the orientation of his specimens.

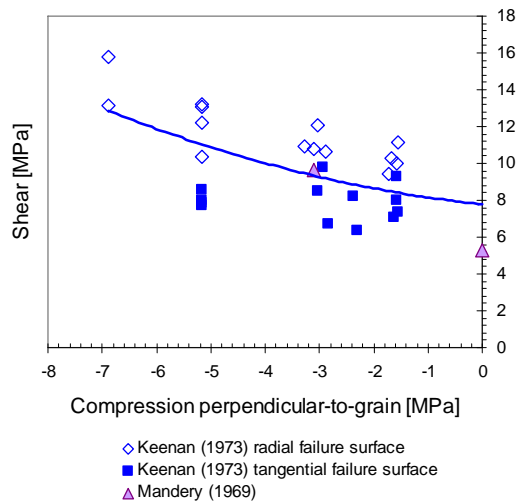


Figure 2-21: ASTM shear block test

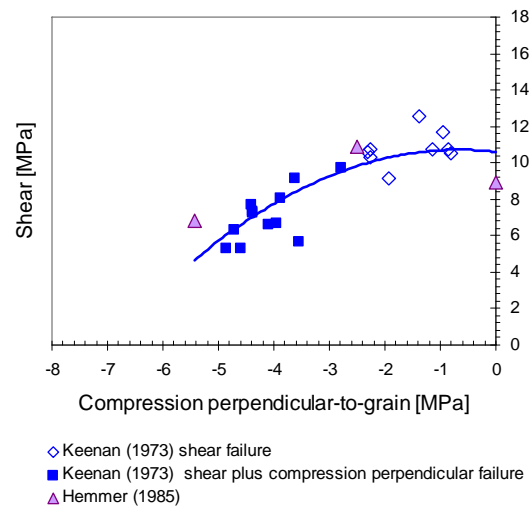


Figure 2-22: Tests on tube-shaped specimens

When considering Figure 2-22 where the results of tests on tube-shaped specimens are shown (Keenan, 1973, Hemmer, 1985), a completely different situation can be observed. Instead of increasing shear strength with increasing transversal compression, a decrease in shear strength after a first short increase can be observed. A possible explanation for this is that the ASTM test defines the failure plane whereas during a torque test on a tube, this shear failure plane is not determined. Keenan (1973) stated that the tests on ASTM shear blocks individuate the tangential plane as the weakest plane as then no increase of shear stress could be seen. In tube-shaped specimens, the shear cracks should happen again in the tangential plane which was however not the case. He concluded that rolling shear failures (hence no longitudinal shear slip, but a shear distortion between earlywood and latewood in an annual ring) were determining the shear strength in his tube-shaped specimens.

Spengler (1982) carried out tests on lamellae of spruce wood he assembled directly from producers of glulam. He glued the lamellae with their long sides on steel plates and then introduced transversal stresses via the steel plates and shear stresses by moving the steel plates in opposite directions. He also found a trend of increasing shear strength with increasing transversal compression, but the scatter of his results was quite high. This was persistent for tests at different moisture contents of the lamellae.

However, all multiaxial testing data, except for the more recent results from Eberhardsteiner (2002), present only ultimate strength values. The load-slip behaviour of

the specimens was generally not measured. This means for numerical methods that the mechanical behaviour before failure under multiaxial stress states is not always known.

## 2.4 POISSON'S RATIOS

Mathematical models always need the Poisson's ratios as input. Otherwise, 2D or 3D stress states cannot be calculated properly. Table 2-4 lists Poisson's ratios for spruce (*Picea abies*) from literature (Wood-Handbook, 1999, Kollmann and Côté, 1984, Neuhaus, 1994) where the first index defines the direction of the tension load and the second index the contraction in perpendicular direction. It is clear that qualitatively, the Poisson's ratios are in line with each other. Usually, experiments to determine the Poisson's ratios are done on small specimens.

**Table 2-4: Poisson's ratios from literature on elastic properties of spruce at 12% m.c.**

source	$\nu_{LR}$	$\nu_{LT}$	$\nu_{RT}$	$\nu_{TR}$	$\nu_{RL}$	$\nu_{TL}$
Wood Handbook (1999) ( <i>Picea sitchensis</i> )	0.372	0.467	0.435	0.245	0.040	0.025
Kollmann and Côté (1984) ( <i>Picea abies</i> )	0.430	0.530	0.420	0.240	0.019	0.013
Neuhaus (1994) ( <i>Picea abies</i> )	0.410	0.554	0.599	0.311	0.056	0.035

In Table 2-5 some actually used Poisson's ratios in modelling literature are shown (Mackenzie-Helnwein et al., 2005, Blaß and Bejtka, 2008, Schmidt and Kaliske, 2006, Franke, 2008). In far most of the papers on modelling, the Poisson's ratios are not given or they are only given incompletely. However, the question remains of how much simulation results are influenced by wrong or confounded Poisson's ratios. In other words how sensitive mathematical models of joints actually are to a change of Poisson's ratios.

**Table 2-5: Poisson's ratios from modelling literature for spruce**

source	$\nu_{LR}$	$\nu_{LT}$	$\nu_{RT}$	$\nu_{TR}$	$\nu_{RL}$	$\nu_{TL}$
Mackenzie-Helnwein et al. (2005)	0.500		0.380			0.013
Blaß and Bejtka (2008)	0.511	0.511	0.203	0.203	0.011	0.011
Schmidt and Kaliske (2006)			0.240		0.450	0.450
Franke (2008)	0.055		0.311			0.035

Another discussion point regarding the Poisson's ratios is the symmetry of the compliance matrix, for instance:

$$\frac{\nu_{TR}}{E_T} = \frac{\nu_{RT}}{E_R} \quad (2-1)$$

where  $\nu_{TR/RT}$  = Poisson's ratio,  $E_T$  = MoE in T-direction,  $E_R$  = MoE in R-direction.

Different researchers (Neuhaus, 1983, Garab et al., 2010) stated, based on experimental results, that the symmetry shown in Equation (2-1) is not the case for wood.

Another relevant question is the evolution of the Poisson's ratios in case of damage. It is unknown if the degradation follows a linear or exponential law. The only experimental results known to the author are given in Franke (2008) and are shown in Figure 2-23. The development of the Poisson's ratio  $\nu_{RT}$  was measured during a compression test perpendicular-to-grain. A degradation of the Poisson ratio can be observed.

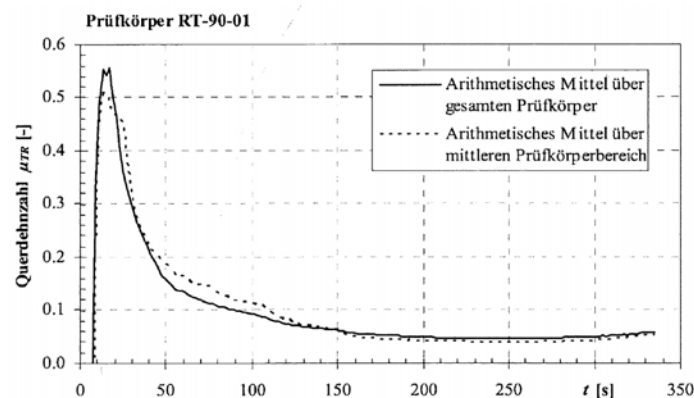


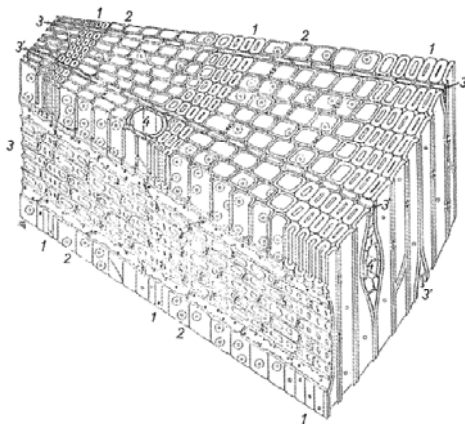
Figure 2-23: Degrading Poisson's ratio  $\nu_{TR}$  (here:  $\mu_{TR}$ ) measured up to failure of a compression test perpendicular-to-grain (Franke, 2008, Figure 4-24)

## 2.5 WOOD ANATOMY

As seen in the previous sections, the anatomy of wood with its cellular structure is determining the mechanical behaviour under different loading cases. Failures will occur on a micromechanical level as transversal wall or interwall failures, but failures can also be observed on the meso-level where failure fronts follow annual rings for instance. Other issues such as the length of the cells will also have an influence on the properties as the 'buckling length' of a cell changes. Inhomogeneities such as density variations are caused by variations in the anatomy. Wood is also inhomogeneous on the macroscopic and mesoscopic scale with knots and issues related to the growing conditions. Furthermore, tropical hardwoods for instance may suffer from interlocked grain which does not occur in species from temperate climates.

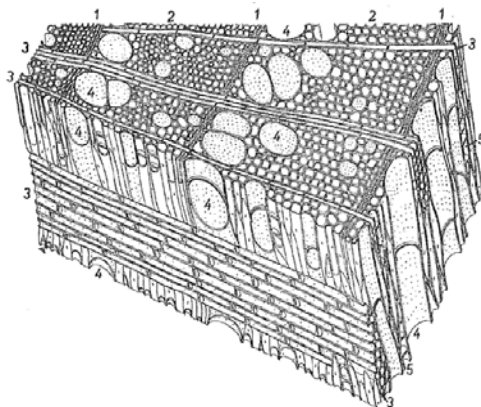
In this thesis, different wood species are used. Differences in anatomy will influence the mechanical behaviour. Therefore, it is important to understand how wood species differ in their anatomic structure. This section has been inserted to underline some major differences in the anatomic structure of various wood species. Again it is referred to the extensive literature for more detailed information than provided here, e.g. (Kollmann and Côté, 1984, Wagenführ, 2007).

All wood species consist of different cell types, namely the tracheids, rays and some species have resin canals. Hardwoods are more evolved and have another cell type called vessels. The tree grow is in rings – in softwoods and non-tropical hardwoods this is expressed by the annual rings. Figure 2-24 shows a drawing of a softwood and Figure 2-25 one of a European hardwood (Nardi-Berti, 1993). The different cell types are indicated.



- 1) latewood tracheids
- 2) earlywood tracheids
- 3) parenchymatic rays
- 4) resin canals

**Figure 2-24: Anatomy of a softwood, pine, *Pinus sylvestris* (Nardi-Berti, 1993, Fig. 44)**



- 1) latewood area
- 2) earlywood area
- 3) parenchymatic rays
- 4) vessels
- 5) axial parenchyma

**Figure 2-25: Anatomy of a hardwood, ash, *Fraxinus excelsior* (Nardi-Berti, 1993, Fig. 48)**

Per wood species, the cells are different in terms of length, width and thickness. Within wood species, these parameters may change as can be seen in Figure 2-24 for earlywood and latewood tracheids where latewood tracheids are thicker than earlywood tracheids. Also the amount and distribution of different cell types may change per wood species. For instance beech has a lot of rays in comparison to other species. The distribution of vessels is also variable. Chestnut for instance has unevenly distributed vessels which are also much bigger than the evenly distributed vessels in beech. Some of these differences

can be well observed when analysing microscopic pictures as shown in Figure 2-26 to Figure 2-29.

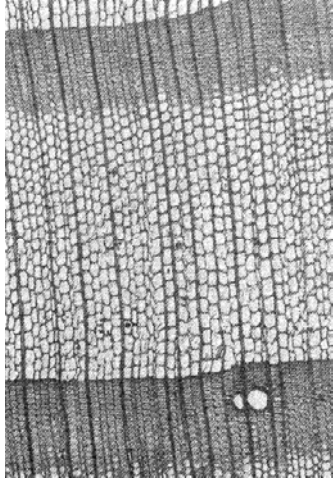


Figure 2-26: Larch *Larix decidua* x51  
(Nardi-Berti, 1993, Fig. 67)



Figure 2-27: Azobé *Lophira alata* x30  
(Wagenführ, 2007)

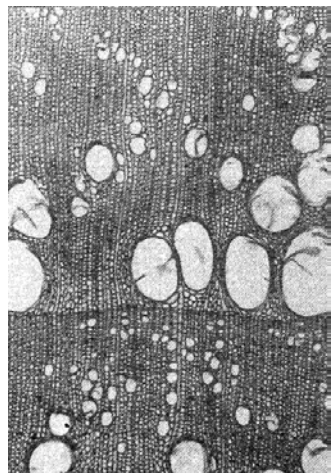


Figure 2-28: Chestnut *Castanea sativa* x51  
(Nardi-Berti, 1993, Fig. 102)

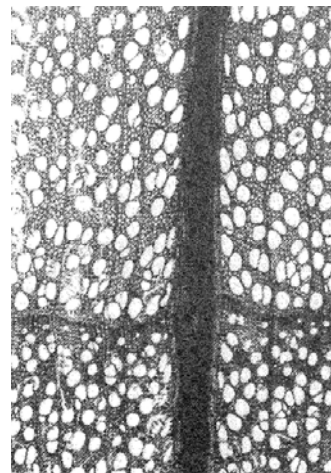


Figure 2-29: Beech *Fagus sylvatica* x51  
(Nardi-Berti, 1993, Fig. 124)

## 2.6 CONCLUSIONS

Issues related with the derivation of material properties for mathematical models were discussed. Two main influence groups could be distinguished, material-related issues such as natural scatter, anisotropy, inhomogeneity or many different available wood species, and test-setup related issues such as geometry and size of specimens, measuring location or choice of measured parameters. Furthermore, most research is based on small

clear (clear = defect-free) specimens of softwood while significantly less information is available for hardwood.

Apart from the availability or reliability of material properties, also failure modes must be identified and failure criteria derived in order to complete a comprehensive mathematical model. However, difficulties connected with different failure modes can easily be illustrated. A wooden piece may already be far in the plastic region in compression perpendicular-to-grain, but still can carry a tension force parallel-to-grain up to its maximum. Also, the failure modes can be progressive. Wood may already be in the nonlinear regime in compression before a shear crack happens. The so-called hypothesis of a 'loose bundle of fibres' may help to understand the concept of independent failure modes. If one splits a wood block along the grain and one is then testing this wood block consisting of loose bundles of cells in tension parallel-to-grain, the ultimate strength in tension will not be affected from the fact that the wood block is split and that therefore, no transverse tension strength is left.

Another straightforward illustration of implementation problems connected with material parameters is the anisotropy of wood that is often not considered. The differentiation into two main material directions, 'parallel-to-grain' and 'perpendicular-to-grain', is already a simplification.

The last point that is important enough to be recalled here is the fact that in timber joints, the mechanical behaviour of wood is more complex. Up to now, the discussed properties were material properties, uniaxial stiffness or strength values assessed by tests or different failure modes of wood caused by clearly defined loading.

However, if timber joints with dowel-type fasteners are tested, the 3D stress states are complex (multiaxial stress states) and system parameters such as dowel diameter are influencing the behaviour of the timber members. Special tests have been developed to assess these system influences, so-called embedment tests where the dowels remain rigid. In joints however, dowels rotate in the timber members if a plastic hinge is developing and additional friction between members is contributing to the mechanical behaviour. In Werner (1993), different influence parameters on joint behaviour are thoroughly discussed.

All this indicates how difficult it is to derive the correct mathematical representation of the mechanical behaviour of wood in general. A first conclusion is to develop not too sophisticated and complex mathematical models. It is not effective to create overly precise models when the input data is sometimes inaccurate and sometimes just best guesses.

# 3

## MODELLING TECHNIQUES

*In the last decades, many different modelling approaches have been developed in order to simulate the behaviour of wood and timber joints. These approaches are presented here to give the reader an overview on modelling techniques, their applicability and basic ideas. Only models considering static and short-term loading are considered. Finally, a promising approach is chosen and the choice is motivated.*

### 3.1 INTRODUCTION

As could be seen in the previous chapter, wood is anisotropic, inhomogeneous and its mechanical properties are subject to large scatter. The development of mathematical models presents thus an interesting challenge in order to establish reliable predictive models. A typical problem in modelling is the need to calibrate mathematical models on test results instead of having ready-to-use material properties. This is related to difficulties in testing and measuring. Furthermore, no constitutive material model and necessary solution strategies seem to be available at the moment that are able to simulate joint behaviour including ductile behaviour in compression and brittle behaviour in tension and shear of the material wood. Usually, different modelling approaches are developed for different problem classes. Models simulating the nonlinear behaviour of timber joints may use classical yield theories such as the one developed by Hill (1948) for orthotropic materials. On the other hand, if brittle behaviour of joints loaded perpendicular-to-grain is to be modelled, for instance fracture mechanics may be used. If it is recalled that also moisture content, duration of load, temperature (to a lesser extent) or macroscopic features such as knots or grain deviation are influencing the mechanical behaviour of timber and subsequently of timber joints - issues not even considered here - then the complexity of modelling is becoming quite clear.

To illustrate the difficulties of predictive modelling, results from embedment tests on different wood species with 16 mm dowels carried out at the TU Delft (Vreeswijk, 2003) are shown in Figure 3-1 to Figure 3-4.

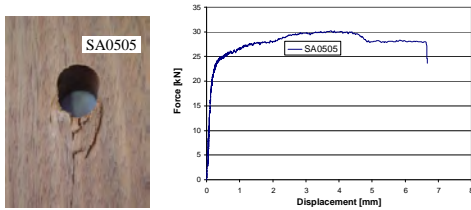


**Figure 3-1: Angelim Vermelho *Dinizia excelsa*,**  
 $\rho_{\text{mean}} = 1106\text{kg/m}^3$ , (Vreeswijk, 2003)

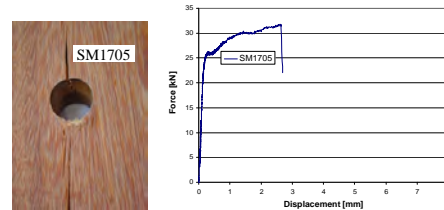


**Figure 3-2: Massaranduba *Manilkara bidentata*,**  $\rho_{\text{mean}} = 972\text{kg/m}^3$ , (Vreeswijk, 2003)

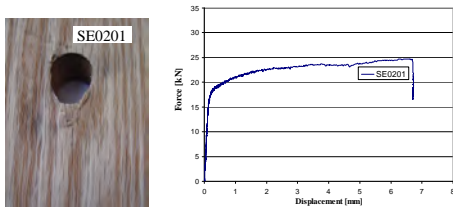


**Figure 3-3: Oak *Quercus rubra*,**  
 $\rho_{\text{mean}} = 716\text{kg/m}^3$ , (Vreeswijk, 2003)

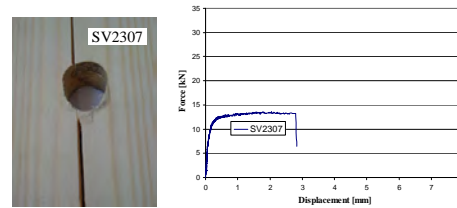


**Figure 3-4: Spruce *Picea abies*,**  
 $\rho_{\text{mean}} = 495\text{kg/m}^3$ , (Vreeswijk, 2003)

It can be seen that, although the only difference of the single tests is the wood species, the specimen behaviour is different. Not only different ultimate loads are reached, but also the ductility differs. In Figure 3-1 and Figure 3-3, the specimens are twice as ductile as the specimens in Figure 3-2 and Figure 3-4.

Generally, reliable mathematical material models are based on four basic concepts:

- valid constitutive model that allows to correctly calculate the stresses from the strains;
- failure/yield<sup>4</sup> criterion that represents the failure mode;
- hardening/softening rule to model nonlinear behaviour;
- good test results that provide the necessary data input for the three items mentioned above.

<sup>4</sup> The concept of plasticity and yield criterion is originally derived for steel. In most cases, steel is isotropic, generally ductile and has a distinct yield stress after which the plastic regime is starting. For wood, this is different. In tension, for instance, no yielding can be observed, the failure mode is quasi-brittle. Therefore, henceforth the expression ‘failure criterion’ is used instead of ‘yield criterion’; the mathematical function is the same. Here, ‘failure’ does not mean that a material has failed and that its strength is zero. A failure criterion identifies the onset of nonlinear behaviour instead.

However, if the task is to model a joint, the problem is more complex. The behaviour of the (in most cases) metallic fasteners and contact between wood and fasteners must be modelled as well. Models able to satisfyingly simulate pure material behaviour may still not be able to simulate joint behaviour.

Generally, nonlinear modelling of steel is easily done and also for contact modelling, i. e. friction, powerful algorithms have been developed. Therefore, as a first conclusion it could be said that the problem of timber joint modelling can be condensed to a problem of wood material modelling. The problems related to reliable numerical modelling of timber joints are presumably due to all problems related to correct modelling of the material wood as mentioned above.

This chapter is hence subdivided. Firstly approaches and problems connected with pure material modelling are discussed. These discussions form the major part of the chapter as a good constitutive model for wood is prerequisite to a good joint model. Secondly, issues related to joint modelling are presented.

Many different approaches are available to simulate the mechanical behaviour of the material wood. The more complex the mathematical models get, the less comprehensible they are for users. Here, the scope lies on numerical Finite Element (FE) models and not on analytical approaches such as the European Yield Model (EYM, Johansen equations (Johansen, 1949)).

A summary of the many various numerical approaches is given. Its aim is to introduce important concepts of finite element modelling to wood engineers in a straightforward and comprehensible way. Many of the concepts and approaches are interwoven. To organise the chapter as good and clear as possible, firstly FE methods in general are briefly discussed with its subparts continuum and discrete approaches. Subsequently, failure criteria are discussed. Failure criteria are necessary for all approaches to describe the onset of failure. These criteria can be derived from classical yield criteria or they can be based on concepts of fracture mechanics. Which one will be chosen is dependent on the problem class. Classical yield criteria are best suited for plastic behaviour whereas brittle behaviour is better modelled with fracture mechanics. Therefore, the choice depends on the post-elastic behaviour of a structure, the behaviour of a material after the proportional limit. Problems related to post-elastic simulations are presented subsequently. After the discussion about proper modelling of softening behaviour, fracture and damage mechanics are introduced which were developed to model softening behaviour. Both approaches can be implemented in continuum and discrete mechanics approaches. Fracture and damage mechanics are theories to analyse brittle problems and are independent from the basic numerical approach chosen.

Subsequently, a section on two different innovative and practicable applications of continuum mechanics using standard FE packages is inserted. The step from material to joints and further issues related to joint modelling are then discussed in section 3.6.

Finally, a summary is given that shows the major application fields, potentials and limitations of the different approaches. For any further information on the FE method, it

is referred to the expert literature, for instance Bathe (2002). Furthermore, additional information can be found in literature where reviews on wood material and timber joint modelling are available (Patton-Mallory, 1997, Kasal and Leichti, 2005, Sandhaas and Van de Kuilen, 2008).

## 3.2 FINITE ELEMENT METHOD

FE methods are nowadays widespread and much-used tools to model the mechanical behaviour of a structure on which a set of known external variables, forces or prescribed displacements, are acting. A set of partial differential equations are solved numerically to determine the values of the unknown internal variables, namely the displacements. From the displacements, the strains can be calculated and, e.g. in the linear elastic domain via Hooke's law, also the stresses. This last step, from strains to stresses is done by applying a valid constitutive law.

The modelled structure is broken down into a system of smaller, finite elements for which the system of equations is approximately solved. Via boundary conditions such as same displacements of some of the nodes, the single smaller elements are connected with each other and a solution for the whole system can be determined:

- The structure as a composition of single elements is modelled;
- The condition of equilibrium of single elements is solved, local solution;
- The system of equations for the whole model by considering boundary conditions between the single elements is built;
- The system of equations for whole model is solved, global solution.

How the structure itself is modelled is up to the engineer who will take a decision looking carefully at the problem type, the ductile or brittle failure mode of the structure and the solution parameters he or she is interested in. Basically there are two different approaches:

- continuum elements (section 3.2.1);
- discrete elements (section 3.2.2).

A discrete approach assigns mechanical behaviour to an assembly of discrete elements. With this approach, structural systems such as a piece of wood can be modelled by describing the system as a grid or lattice where wood fibre properties parallel-to-grain could be assigned to beam elements (e.g. one beam = one fibre) and the perpendicular properties could be modelled by springs connecting the beam elements. The system answer will be calculated exactly solving a system of finite equations. This is different in continuum systems where no discrete elements such as beams model single fibres, but the behaviour of a bundle of fibres is smeared over a continuous system of elements. Then a system of partial differential equations will be solved approximating the system answer. An exact solution of the partial differential equations that fulfils all boundary conditions is only possible for simple systems. Usually, numerical procedures must be used to approximate the system answer. This is especially valid for nonlinear problems. As

always in approximate methods, errors will occur which in our case means that the internal forces will not have exactly the same values as the external forces. Convergence criteria are therefore needed to judge the amount of error and to trigger new iterations in order to minimise the internal error and to finally find a converging solution.

The relationship between strains and stresses in the linear elastic range needed for the local element solution is defined by the stiffness matrix – Hooke's law. In order to obtain a reliable solution for the analysed structure, this relationship, i.e. the parameters of the stiffness matrix, must be defined carefully. The stiffness values and the Poisson's ratios will always derive from experimental results.

However, nearly no structure will have a purely linear behaviour where the system response, i.e. the deformations, is proportional to the load. Usually, structures behave nonlinearly where no proportionality between system response and loading is present. Nonlinearities have a certain impact on the finite element formulation and the solution strategies. Global nonlinearity of a structure not only derives from nonlinear material behaviour, but has basically three sources:

- **Material nonlinearity:**  
Decrease of stiffness of the material (integration point level) with increasing loading (due to yielding, cracking, etc.); element formulation referring to global coordinates.
- **Geometric nonlinearity:**  
Depending on their deformations, stresses are induced in the structures. Element formulation must be in local coordinates and the coordinates must translate and rotate together with the system. Further mathematical simplifications are possible if the strains are small.
- **Contact nonlinearity:**  
Contact nonlinearity occurs, e.g. friction between two bodies of a system. Contact nonlinearity can also be related to material or geometric nonlinearity if for instance, the boundary conditions are dependent on deformations.

Material nonlinearity, if present, is needed for the local element solution and must be evaluated by experiments and implemented in suitable constitutive relations. So-called material yield or failure criteria must be developed to describe the transition zones between elastic behaviour and nonlinear behaviour, the so-called proportional limit.

Before further exploring FE methods, the terms tangent stiffness and secant stiffness are explained as these two expressions will be used extensively. Two levels must be considered. One level is the local integration point level of a finite element where the mechanical behaviour in terms of stresses and strains is calculated. This level requires a constitutive model to calculate the stresses from the strains or better, the stress rate from the strain rate. Such a constitutive model is often given in terms of a stiffness matrix which is the inverse of the compliance matrix. However, mathematically also constants or any type of equation could be given that link the strains to the stresses. The second level is the global level where the global response of the structure is calculated and where

certain convergence criteria must be met, e.g. internal forces equal external forces. In order to calculate the global response, a global stiffness matrix for the whole modelled structure must be assembled.

If considering the local level at an integration point, the constitutive behaviour of a material must be described. This description could be based on damaging elasticity or on (classical) elasto-plasticity. For elastic damage models using the secant stiffness, the path of unloading is going back linearly to the origin as shown in Figure 3-5a. Tangent stiffness is always tangential to the load-displacement curve which means it is equal to the elastic stiffness in the elastic domain. The tangent stiffness is used when describing stress-strain behaviour with classical plasticity as shown in Figure 3-5b. As can be seen in Figure 3-5a, no permanent plastic deformations can be modelled when using secant unloading contrarily to the method using elastic unloading (Figure 3-5b). More advanced coupled elastoplastic damage models aim at combining the two modelling approaches.

Also for the global level, i.e. the assembly of the global stiffness matrix, secant and tangent stiffness are important concepts. The global tangent stiffness matrix (as derivative of the  $\sigma(\varepsilon)$ -function, the so-called Jacobian) may become singular once softening behaviour of the material is developing, i.e. the  $\sigma(\varepsilon)$ -curve has a negative slope. This may cause convergence problems.

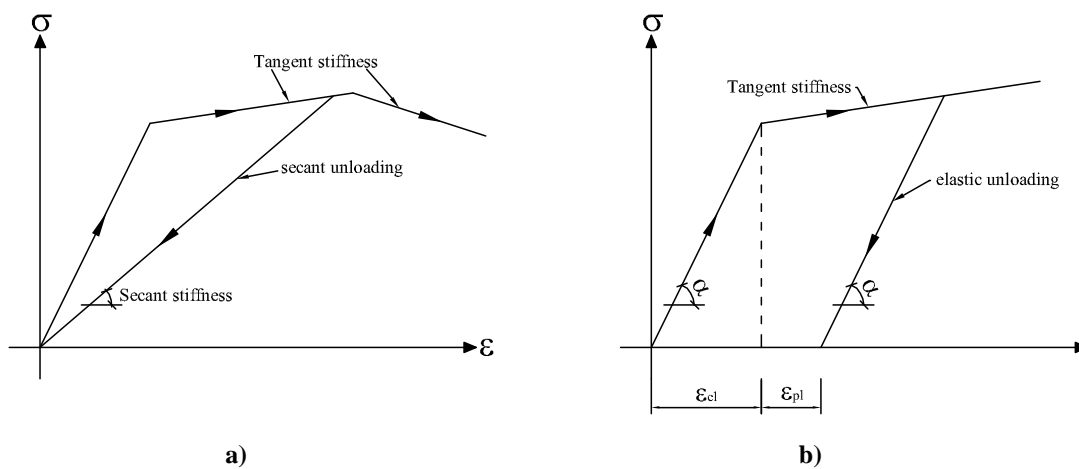


**Figure 3-5: Stress-strain diagrams, a) damage model, b) classical plasticity with elastic unloading**

There are manifold numerical solution algorithms to solve the system of partial differential equations. Having valid constitutive relationships does not mean that models can be solved as also observed in Van der Meer (2010). Van der Meer stated explicitly: “However, carefully constructed kinematic and constitutive models are not all that is needed for successful simulations. When the computer crashes due to non-convergence before the virtual specimen has failed, the model is of no use. And when the computation time is high this does not encourage its use either. In order to get the model working in complex cases, a well-designed solution procedure is indispensable. The key targets in

formulating this procedure are robustness and efficiency.” (Chapter 4 of Van der Meer, 2010).

Usually, a certain problem class needs its own solution strategies and methods. For instance, nonlinear problems are usually solved with incremental-iterative methods (nonlinear problems cannot be solved with non-incremental methods). Incremental methods are subdivided in two classes:

- Non-iterative, single-step or explicit methods (e.g. Euler forward or Runge-Kutta): The differential equations are solved for time  $t^l$ , the state at  $t^{l+1}$  is predicted by solving for state at  $t^l$ . Explicit methods may suffer from numerical instability and may thus require small time steps.
- Iterative implicit methods (e.g. Newton-Raphson (Euler backward)): The differential equations are solved for a still unknown state at time  $t^{l+1}$ , the state at  $t^{l+1}$  is predicted by solving for state at  $t^l$  and  $t^{l+1}$ . Implicit formulations are more complex but larger time steps are possible.

In simple words, explicit methods do not need the assembling of a global stiffness matrix in contrast to implicit methods. Explicit methods are best suited for dynamic problems whereas implicit methods are good for classical continuum mechanics with plasticity. Especially for implicit methods, convergence criteria controlling the equilibrium must be included.

Generally, systems with snapback behaviour (due to instabilities and buckling) lead to problems in an incremental-iterative scheme such as the Newton-Raphson method. This is due to the fact that in snapback problems, especially with geometric instability, the load control algorithm (preferably displacement-control) cannot proceed as the loads/displacements do not grow monotonically anymore. For this classical snapback behaviour other solution algorithms, so-called path-following or arc-length methods (Riks method) were developed that are able to trace the displacement path by choosing a non-fixed load increment. The Riks method thus uses the load magnitude as another unknown variable. The load step is taken as a variable in the solution procedure. New, robust and efficient arc-length methods based on thermodynamic energy principles are available, but they are not implemented in FE packages yet (Van der Meer, 2010).

Softening does not always lead to the problems described above for geometric instabilities. Softening of materials is not always unstable. In this case, standard Newton-Raphson schemes can be used, but then the global Jacobian (= tangent stiffness matrix) may still lead to convergence problems. A new solution strategy developed for continuum mechanics suited for problems with softening is the so-called sequentially linear analysis (SLA). SLA was developed to simulate fracture behaviour for use with continuum elements where single elements may undergo tension softening (Rots and Invernizzi, 2004, Rots et al., 2008). Rots et al. stated that the basic idea was to create an event-by-event strategy where brittle local failures are captured directly instead of “iterating around them” (Rots et al., 2008). The local brittle failures and thus the critical elements are identified by the principal tension stress. If the tensile strength is reached, the stiffness

of the elements will be reduced before starting the next sequence with a secant restart. This secant restart analogously to lattice models (explained in section 3.2.2) is made to capture the next critical element. The resulting graphs have, just like lattice models, a typical saw-tooth shape of the softening as shown in Figure 3-6. SLA is mesh-dependent and mesh regularisation techniques must be used (Rots and Invernizzi, 2004).

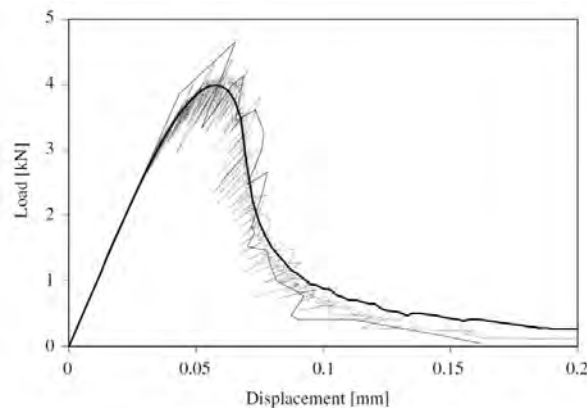


**Figure 3-6: SLA of notched beam (Rots et al., 2008, thick line is nonlinear reference curve)**

As for incremental-iterative schemes, in standard FE programmes, usually the full Newton-Raphson and the modified Newton-Raphson method are available. In full Newton-Raphson, the tangent stiffness matrix is recalculated for every iteration whereas in modified Newton-Raphson, this is the case only for every increment. Therefore, computer time is saved using modified Newton-Raphson, but convergence may be slower.

### 3.2.1 Continuum approaches

For most timber engineering problems, the commonly chosen FE approach is a continuum mechanics approach where a 1D, 2D or 3D structure is subdivided into smaller elements with a certain number of nodes and integration points. The results in terms of stresses and strains are calculated per integration point. Linear or quadratic polynomials are used to interpolate the results in between the integration points. Therefore, depending on the model scale, the results in a sense are averaged over the whole structure. It is usually difficult to model stress concentration phenomena with a continuum mechanics approach. For instance, in order to model splitting in wood, the required model scale and thus mesh size may lead to unmanageable models. In other words, localised failures and ruptures such like buckling of fibres under compression parallel-to-grain or crack propagation under tension perpendicular-to-grain cannot be simulated easily.

The far most common approach to model nonlinear material behaviour is classical elasto-plasticity. Due to the extensive use, also in wood research, the formulation of failure criteria used in plasticity is discussed in section 3.3.1.

Computationally, for time-independent algorithms for nonlinear plastic materials, the difficulties arise from the fact that the load-slip relationship is no longer unique. This means that the assignment of the strains to the stresses is not unequivocal which creates the need of establishing more parameters that can keep track of the loading history. It also means that the tangent stiffness and not the secant stiffness must be used to calculate the stress-strain relationship (see Figure 3-5b) and to account for plastic deformations<sup>5</sup>. Three ingredients are necessary to re-create a clear relationship between the strains and the consequential stresses:

- a yield or failure criterion  $F$  that defines the proportional limit, the transition from the elastic regime to the nonlinear regime;
- a flow rule that links the plastic strain increments to the actual stress state and stress increments (often an associated flow rule is chosen where the failure criterion is used to calculate the plastic strain increments);
- a hardening/softening rule (this is optional and only needed if the material is not elastic perfectly plastic or perfectly brittle). Hardening can be isotropic or kinematic.

Therefore, this so-called flow theory of plasticity uses a relationship between strain rate and stress rate, not between strains and stresses.

Generally, continuum models suffer from mesh dependency if softening material behaviour is prescribed. In section 4.3.7, mesh dependency is discussed.

### 3.2.2 Discrete approaches

Besides continuum approaches, also discrete approaches are possible techniques to simulate material behaviour where the mechanical behaviour is assigned to discrete elements such as springs or beams. Discrete lattice models are an interesting approach traditionally used for brittle materials. Materials are represented by a lattice structure where spring, or more advanced, beam elements (including bending) are used to form a 2D or 3D grid. The elements are calibrated on the properties (stiffness and ultimate strength) of the material that one wants to model. This determination of the element properties is difficult to undertake. The algorithm used to solve these structural models remains linear elastic and at every step, it goes back to the origin (secant stiffness – Figure 3-5a). Elements are switched off (or they are assigned a low stiffness) when their failure strength is reached. Therefore, if no optimisation methods are used, the stiffness matrix must be recomposed after each load step. Afterwards, the next load step is carried out acting on a structure that has fewer members and thus lower stiffness. Like this,

---

<sup>5</sup> If the constitutive model is described via a stiffness matrix. Other possibilities are constants or simple equations that describe the stress-strain relationship.

brittle structures can be modelled by switching off elements. This technique leads to typical saw-tooth shapes of the softening curves as shown in Figure 3-7.

The discrete lattice concept with its beams and springs is well illustrated in Figure 3-8 taken from Wittel et al. (2005) and in Figure 3-9 taken from Reichert (2009).

Most lattice models use the described solution algorithm where the secant stiffness is recalculated from step to step (softening due to element removal) and where no increments are used. Therefore, up to now, lattice models are often perfectly brittle (e.g. Wittel et al., 2005, Snow et al., 2006) and are thus not capable of representing ductile (material) behaviour on the local level. However, the global structural response may still be ductile as shown in Figure 3-7.

Other solution strategies exist however. Reichert (2009) developed a 3D lattice programme trying to include (local) nonlinear material behaviour which proved to be rather hard to implement. Simulation examples taken from Reichert are shown in Figure 3-10 to Figure 3-13. The first two figures show a brittle model simulating a CT test. As can be seen in Figure 3-11, the modelling results are in good agreement with the test results except for the stiffness. This changes if looking at nonlinear behaviour. Figure 3-12 shows a lattice model of a compression test parallel-to-grain. The modelling results of this test are not as good as the results for the CT test as can be seen in Figure 3-13.

Maybe the most important lesson learned from Reichert (2009) is the fact that lattice models are not implemented in general FE codes. As Reichert had to write a complete FE code in order to run his models, also steel properties and contact algorithms had to be inserted in order to model timber joints. This is not a trivial task. Contact algorithms are difficult to develop and have a high computational cost. Reichert stated that his joint models took long to solve and that the algorithm stopped before reaching the maximum displacement.

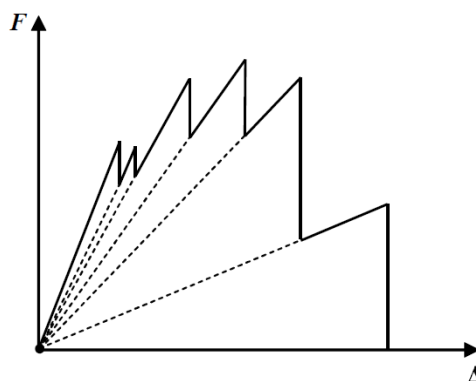


Figure 3-7: Typical saw-tooth load-displacement curve (Reichert, 2009, Fig. 3.12)

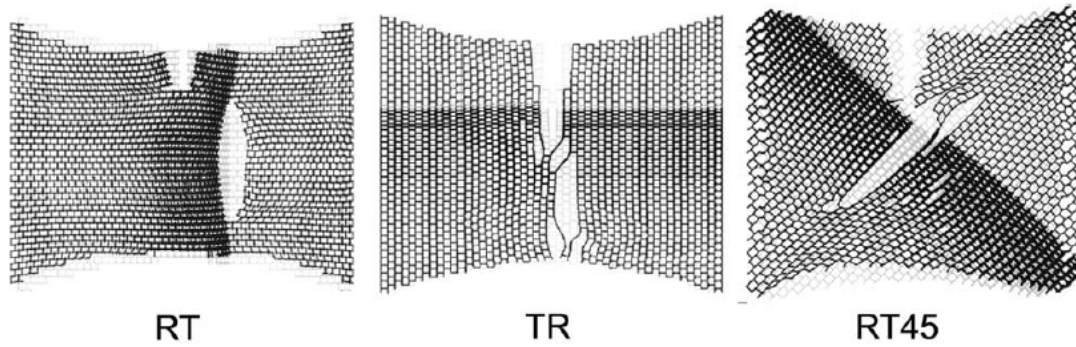


Figure 3-8: Example of lattice models with cracks (Wittel et al., 2005)

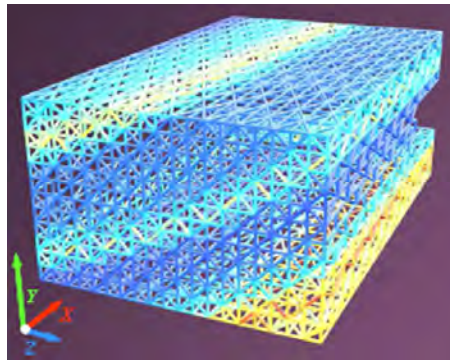


Figure 3-9: Example of lattice model with annual rings (Reichert, 2009, Fig. 5.17)

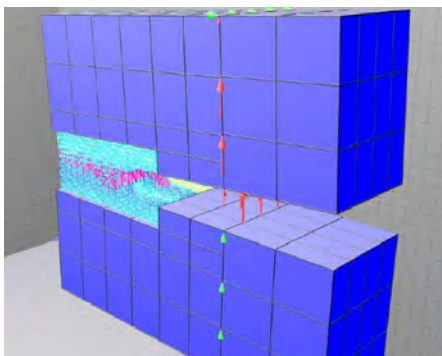


Figure 3-10: CT test model with crack (Reichert, 2009, Fig. 6.8)

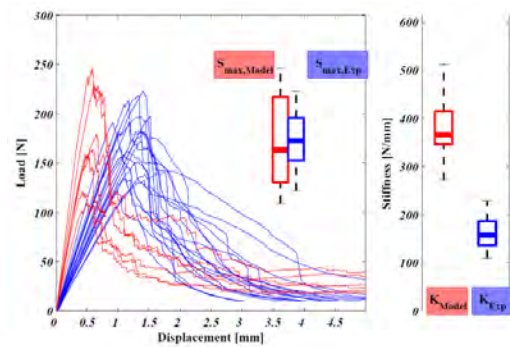


Figure 3-11: Experimental and model results of CT test (Reichert, 2009, Fig. 6.9)

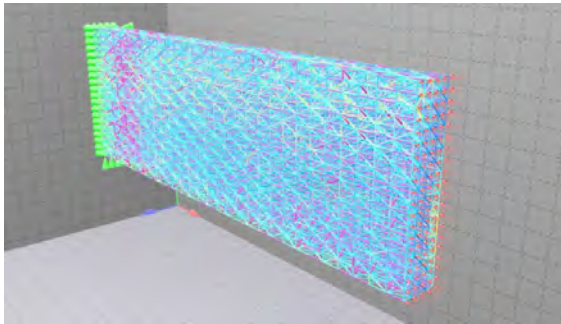


Figure 3-12: Longitudinal compression test mode with failures (Reichert, 2009, Fig. 6.20)

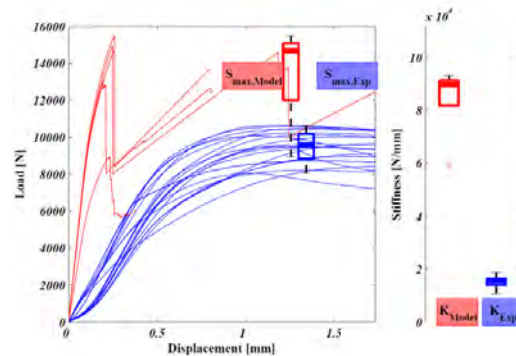


Figure 3-13: Experimental and model results of longitudinal compression test (Reichert, 2009, Fig. 6.22)

Also Schlangen developed a 3D lattice model, the so-called Delft lattice model (Schlangen and Garboczi, 1997). He and his researchers are now extending the software with a user-friendly interface and nonlinear elements. Schlangen developed his models for concrete and rock, but as his software is well developed and advanced it is worth to be mentioned here due to its possible future applicability to wood. Also algorithms for automatic mapping of mesoscopic properties onto the lattice model are available. However, still contact algorithms able to model a fastener-wood system are missing.

### 3.3 FAILURE THRESHOLD AND DEVELOPMENT

In order to correctly identify the onset of failure, a valid failure criterion needs to be defined. This is valid for every kind of nonlinear analysis, be it for example within the framework of continuum mechanics or lattice models. Also the correct description of the post-elastic behaviour is essential for reliable modelling.

#### 3.3.1 Failure criteria

A failure criterion can be expressed as follows:

$$F(\sigma_{ij}, f_M) = 1 \quad (3-1)$$

The failure surface  $F$  is a scalar which is dependent on the 6x6 stress tensor  $\sigma_{ij}$  and material resistances  $f_M$ .  $F$  can be interpreted as a geometric body lying in the 6D stress space. The boundaries of the body indicate the failure stress. Mathematically, all stress vectors inside the boundary of the body are linear elastic. This means that when  $F < 1$ , the material is still linear-elastic. If  $F = 1$ , the material fails.  $F > 1$  is physically not possible. The intersection points of the failure body with the axes are the uniaxial strengths of the described material.

The expression ‘failure surface’ should not be misunderstood. It only indicates the proportional limit and does not mean a material is actually failing. A material may still carry load after having reached the boundary of  $F$ .

Failure criteria can be formulated in terms of strains or in terms of stresses. Both formulations are equivalent as they are connected through a constitutive model. There is one major problem associated with strain-based formulations. That is the difficult execution of tests that determine the material input values in terms of strains as it is nearly impossible to create uniaxial strain conditions. Lateral strains are complicating the issue considerably. Furthermore, it is more difficult to derive clear correlations between strain and failure than between stress and failure, certainly for brittle failures (Puck, 1992). If recalling section 2.1, the difficulties connected with tests carried out in a stress-based or strain-based regime are evident. Usually, tests are carried out measuring uniaxial stresses and displacements. What happens in the other material axes is not measured.

The simplest example for a geometric body representing failure surfaces is a box-type body as shown exemplarily in a 2D stress space in Figure 3-14 for normal stresses. The box-type failure function represents the maximum stress criterion where no interaction between stresses is assumed. The stresses are constant which means that they are generally overestimated. Another problem is that numerically, such a surface is difficult to implement in finite element programmes as it has edges where no clear normal to the surfaces exists. (A normal is necessary to calculate the return mapping of the predictive values in case of an associated flow rule. One advantage of an associated flow rule is the maintenance of a symmetric tangent stiffness matrix which makes numerical solutions efficient.)

A mathematically simple approach to model stress interaction is to choose a linear relationship as shown in Figure 3-14. The linear approach however usually underestimates the stress interactions considerably.

An elegant and still simple approach to describe failure surfaces are quadratic, continuous, closed and convex surfaces such as cylinders, spheres or ellipsoids. They are mathematically simple single surfaces which are able to describe experimental results with a sufficient accuracy without being too demanding mathematically. An example is again given in Figure 3-14. Another advantage is that these surfaces do not suffer from the presence of singular points.

An example of how mechanical behaviour may be represented through an ellipse (a quadratic, convex closed geometrical body) is shown in Figure 3-15, a repetition of Figure 2-18 with a fitting ellipse.

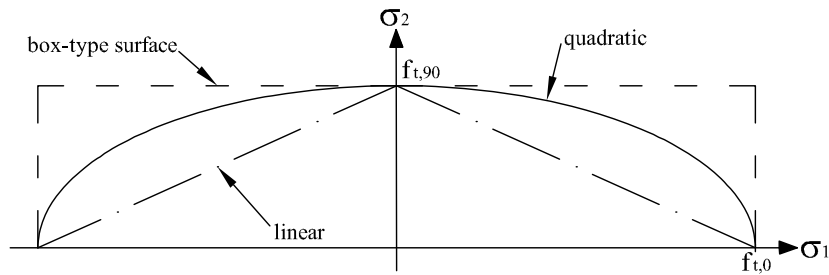


Figure 3-14: Failure surfaces

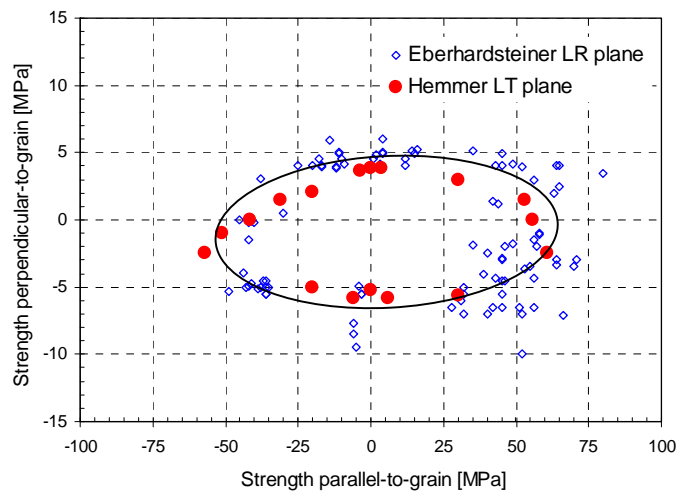
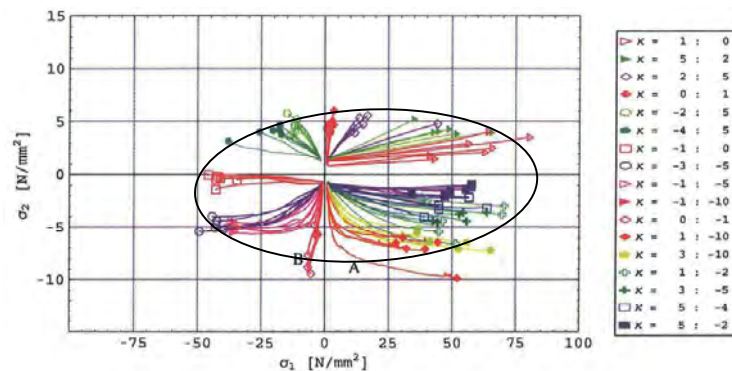


Figure 3-15: Results biaxial tests plus failure surface – combination of normal stresses,  $\alpha = 0^\circ$ . Results from (Eberhardsteiner, 2002, Hemmer, 1985)

There is no physical reason why the stress interactions are modelled with quadratic functions. Already in 1980, Hashin stated that “(the quadratic approximation) is the simplest presentation which can fit the data reasonably well, and in view of the significant scatter of failure test data it hardly seems worthwhile to employ cubic or higher approximations.” (Hashin, 1980). This statement is certainly still valid, especially for wood with its inherent high scatter.

If now also Figure 3-16 (repetition of Figure 2-19) is considered which is showing Eberhardsteiner’s (2002) results together with the load-displacement curves and a fitting ellipse, a first problem of these approaches is evident. The ellipse may not always represent the proportional limit as required mathematically, but the material may already be nonlinear within the ellipse. Wood in compression is indeed nonlinear already at small deformations (second and third quadrant). Only for the combination of tension stresses with their brittle failures the ellipse is correctly describing the onset of failure (first quadrant).



**Figure 3-16: Results biaxial tests with stress evolution,  $\alpha = 0^\circ$**   
(Eberhardsteiner, 2002, Fig. 4.22)

The simplest convex, continuous, regular and closed surface is a cylinder. If one cuts through a cylinder, a circle or an ellipse – depending on the inclination of the cutting surface - is obtained. The von Mises failure criterion for isotropic materials is such a cylinder in the 3D stress space. Von Mises' derivation is based on the assumption that hydrostatic stress states do not lead to failures as it is based on the second deviatoric stress invariant neglecting the first stress invariant of the stress tensor.

The von Mises criterion can be extended for anisotropic materials. This implies mathematically that the failure surface must allow for different axis intercepts as the uniaxial failure strengths are not the same any more. A distorted cylinder, still assuming that a superposition of hydrostatic stresses does not change the failure boundary, is the consequence of such a requirement. Hill (1948) was the first to propose such a failure criterion. In simple words and considering only 2D, Hill extended the von Mises criterion from a circle to an ellipse.

Hill's criterion is in quadratic format. Whether a strength value is positive or negative has no influence on the general form of the criterion. Therefore, the Hill criterion cannot account for different failure strengths in tension and compression.

This was possible with yet another mathematical addition done by Hoffman (1967) and Shih and Lee (1978). They extended Hill's model with linear terms that are odd functions of the normal stresses to include the sign of the stresses. Hence, not only anisotropy can be described by this failure surface, but also different strength values in tension and compression. Mathematically, the ellipse is translating in the 2D stress space.

However, there is still no way to calibrate the interaction between stresses. The uniaxial failure stresses needed to determine the parameters of the failure criteria are independent from each other. In other words the ellipses that can be created with the Hoffman criterion still need to be squeezed and deformed. Tsai and Wu (1971) developed a further extension with again another parameter that accounts for interaction of normal stresses.

Their failure criterion is defined as follows (in short notation<sup>6</sup> –  $F_{ij}$  is a fourth-order tensor) and it can be extended to higher-order polynomials as it has been done by Hemmer (1985):

$$F_i \sigma_i + F_{ij} \sigma_i \sigma_j = 1 \quad \text{with } i, j = 1, 2, \dots, 6 \quad (3-2)$$

The newly introduced interaction term is the second term of the sum ( $F_{ij} \sigma_i \sigma_j$ ) where two stresses can be coupled.

In order to understand the meaning of these failure criteria and that many limitations simply derive from mathematical boundary conditions, the Tsai-Wu criterion is further discussed as a plane problem. Then, it can be notated as follows:

$$F_1 \cdot \sigma_1 + F_2 \cdot \sigma_2 + F_{11} \cdot \sigma_1^2 + F_{22} \cdot \sigma_2^2 + 2F_{12} \cdot \sigma_1 \cdot \sigma_2 + F_{66} \cdot \tau_{12}^2 = 1 \quad (3-3)$$

The next step is the determination of the factors  $F_i$  and  $F_{ij}$ . Uniaxial tests must be done to determine the uniaxial strengths. Firstly, consider  $i = j = 1$ , material axis 1 parallel-to-grain which means strengths  $f_{t,0}$  and  $f_{c,0}$ . Inserting everything in Equation (3-3) delivers:

Compression:

$$-F_1 \cdot f_{c,0} + F_{11} \cdot f_{c,0}^2 = 1 \quad (3-4)$$

Tension:

$$F_1 \cdot f_{t,0} + F_{11} \cdot f_{t,0}^2 = 1 \quad (3-5)$$

Solving for  $F_1$  and  $F_{11}$ :

$$F_1 = \frac{1}{f_{t,0}} - \frac{1}{f_{c,0}} \quad \text{and} \quad F_{11} = \frac{1}{f_{t,0} \cdot f_{c,0}} \quad (3-6)$$

Analogously, the other factors are determined.

---

<sup>6</sup> In literature, short notation is used to avoid complex subscripts as would be required for higher-order tensors. Instead of double indexing, a continuous numbering from 1 to 6 is used: 1-3 indicate the normal stresses and 4-6 the shear stresses. Thus:  $\sigma_1$  equals  $\sigma_{11}$  whereas  $\sigma_4$  in short notation is  $\sigma_{12}$  in normal notation (be careful about the order of the indices in the shear parts of the stress and strain array!).

Furthermore, the factors  $F_i$  and  $F_{ij}$  must hold certain conditions to ensure a closed surface:

$$F_{11} \cdot F_{22} - F_{12}^2 \geq 0 \quad (3-7)$$

The factors  $F_i$  and  $F_{ij}$  shown in Equation (3-6) illustrate nicely some question marks related to these methods. Factor  $F_I$  for instance depends on tensile and compressive strength in the same material direction. Obviously, the failure criterion has no physical meaning.

The mathematical elegance and simplicity explain the popularity of the here presented failure criteria. Furthermore, the criteria are compatible. The most complex Tsai-Wu criterion can be reduced to lower-order criteria such as von Mises, Hill and Hoffman. Moreover, all above-mentioned failure criteria are in tensor formulation, they are symmetric and invariant when the coordinate system in which the elements are described is rotating. Naturally, other criteria do exist. Please refer to e.g. Edlund (1982) or Nahas (1986) for more information.

The parameter  $F_{I2}$  shown in Equation (3-3) was introduced by Tsai and Wu (1971) to account for interaction of normal stresses (no interaction between normal and shear stresses).  $F_{I2}$  must be determined experimentally – although it is not really a phenomenological value, but a mere mathematical trick to distort the form of the failure surface such that interaction between stresses can be controlled. Therefore, the calibration of  $F_{I2}$  is quite difficult as it is not possible to actually test what is mathematically needed (Wu, 1972).

Rahman et al. (1991) were the first to include a multidimensional failure criterion such as the Tsai-Wu theory in timber modelling, assuming  $F_{I2}$  to be zero. They were not able to predict damage and failure with these plastic laws. Bouchaïr and Vergne (1995) reformulated the Tsai-Wu polynomial as a failure surface and a plastic flow rule for orthotropic plasticity. Therewith the regions where the failure criterion is exceeded could be identified and then the material behaviour after failure could be described. The model only considered ductile failures. The brittle splitting failure mode of wood was not described. Their approach was sensitive to numerical problems when choosing a small enough mesh underneath the bolt to simulate the local deformation behaviour of joints. In Grosse (2005), the problems associated with the criterion according to Tsai and Wu (1971) is further discussed and examples are given.

A main problem of the single-surface failure criteria lies in the fact that an ellipsoid or, when considering a 2D stress space, an elliptical closed curve must be determined which marks the transition between the linear-elastic range and the plastic range. As wood has different strength values in different material axes and as these values are also different for tension and compression, it is impossible to really describe an elliptical failure surface or an ellipsoid in 3D that wraps these strength values without leading to unrealistic interaction values. Figure 2-6 illustrates this problem for a 2D case (see also Van der Linden et al., 1994). In order to intersect the axes at the uniaxial strength values, the

ellipse must be of a shape that allows mathematically for even higher strengths parallel-to-grain when some compression perpendicular-to-grain is present.

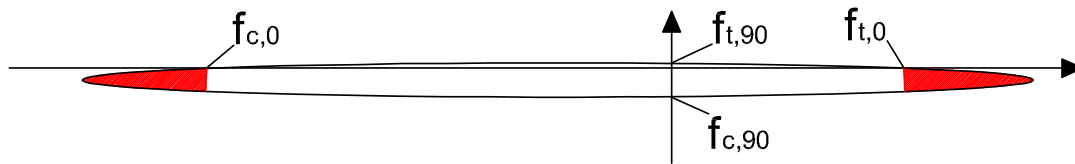


**Figure 3-17: Visualisation of elliptical surface with ‘real’ uniaxial strength values**

Another drawback of single-surface approaches is that usually, they cannot identify the failure mode. The algorithms using single surfaces are only able to determine the onset of failure.

An obvious solution to this problem is to split the single failure surfaces and to develop multiple surfaces per quadrant. With this trick, also different failure modes can be identified which is not possible if one closed surface is used. So-called multi-surface plasticity approaches are already existing (Grosse, 2005, Schmidt and Kaliske, 2006, Mackenzie-Helnwein et al., 2003). They are difficult to implement and have numerical stability problems if the transition from one surface to another is not continuous. Often, their implementation is accompanied by quite sophisticated constitutive laws.

Apart from multi-surface plasticity approaches, there is another possibility to deal with the fact that one single surface may not be the best representation of experiments. In the field of fibre composites, many approaches exist that define piecewise convex and continuously differentiable surfaces for the single failure modes. Mathematically this means that no single closed surface exists in the 6D stress space but that a case by case distinction must be done to assign the correct failure surface to the correct stress combinations. (Hashin, 1980, Puck, 1996, Juhasz, 2003). In composites for instance, two failure modes are distinguished, fibre failure and matrix failure. Most criteria are based on the invariants of the stress tensor as these invariants are not susceptible to coordinate changes (Hashin, 1980). As can be seen nicely in Hashin (1980) and Matzenmiller et al. (1995), the concept is straightforward and physically meaningful. A simple example is given for a plane stress case (see Matzenmiller et al., 1995):

$$\begin{array}{lll}
\text{Tension in 1-direction:} & \sigma_{11} \geq 0: & \frac{\sigma_{11}^2}{f_{1,t}^2} = 1 \\
\text{Compression in 1-direction:} & \sigma_{11} < 0: & \frac{\sigma_{11}^2}{f_{1,c}^2} = 1 \\
\text{Tension in 2-direction:} & \sigma_{22} \geq 0: & \frac{\sigma_{22}^2}{f_{2,t}^2} + \frac{\sigma_{12}^2}{f_v^2} = 1 \\
\text{Compression in 2-direction:} & \sigma_{22} < 0: & \frac{\sigma_{22}^2}{f_{2,c}^2} + \frac{\sigma_{12}^2}{f_v^2} = 1
\end{array} \tag{3-8}$$

Per stress component or combination of components, a failure criterion can be formulated. This criterion may be a simple maximum stress criterion or a quadratic criterion. Also the complex Tsai-Wu criterion could be chosen. As tension or compression stresses are identified, different failure criteria for tension and compression can be applied. Therefore, failure modes can be identified using piecewise defined failure criteria. Smooth transitions between the single surfaces analogously to multi-surface approaches are not needed. The piecewise definition of failure modes is a valid approach to develop more physically meaningful failure criteria.

### 3.3.2 Post-elastic behaviour

It is often not sufficient to simply establish the maximum stress values in order to accurately describe the mechanical behaviour of a material. The post-elastic behaviour, i.e. the mechanical behaviour after reaching the proportional limit, must be described also. As seen in chapter 2, the mechanical behaviour for wood is ductile for compressive loads, but quasi-brittle for tension or shear loads. The plastic behaviour in compression is thus rather easy to model. Most FE codes already contain algorithms for classical elasto-plasticity where it is sufficient to implement the shape of the post-elastic curve into hardening routines. The FE programme carries out an elastic calculation until the failure value is reached (which lies on the boundary of the failure surface).

If the constitutive law of the material is elastic-perfectly plastic, the algorithm will first predict the stresses assuming that the material is still elastic. The predicted elastic stress will be too high and has to be re-projected onto the failure surface. Therefore, the stresses are constant whereas the deformations increase, elastic-perfectly plastic behaviour.

If isotropic hardening is assumed instead, the failure surface is expanding (Figure 3-18). Subsequently, also the stresses and not only the deformations increase, elastic-plastic behaviour with isotropic hardening.

Another possibility to model hardening is kinematic hardening. As shown in Figure 3-18, the surface does not change, but it can translate in the stress space. Kinematic hardening

was developed to model cyclic loading of metals to capture the effect that the material strength will be smaller when reloading in the alternate direction (Bauschinger effect).

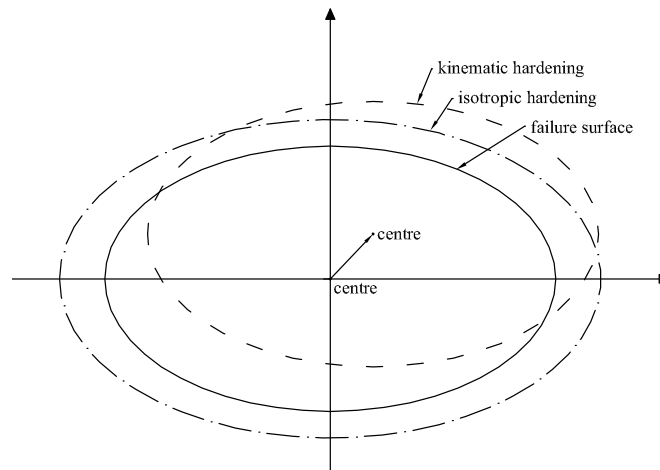


**Figure 3-18: Isotropic and kinematic hardening**

### 3.4 BRITTLE BEHAVIOUR

Three approaches that have been developed to simulate brittle behaviour are shortly presented: fracture mechanics, damage mechanics and lattice models. The last concept, lattice models, has been already discussed in section 3.2.2 as it is a discrete modelling technique contrary to continuum mechanics.

#### 3.4.1 Fracture mechanics

Fracture mechanics were developed to analyse the phenomenon of stress concentrations and subsequent cracking failure modes. These modes with high stress concentrations are difficult to model with continuum mechanics. However, principles from fracture mechanics are often applied within continuum mechanics to simulate brittle behaviour.

In these cases, usually the failure criterion is based on a fracture mechanics approach. Schmid (2002) investigated in the applicability of fracture mechanics on wood whereas Sjödin et al. (2008) looked into the contribution of friction between dowel and wood using a linear elastic fracture mechanics (LEFM) failure criterion. Also Ballerini and Rizzi (2005) carried out extensive research using Wu's criterion (1967) to investigate in the splitting strength of wood loaded perpendicular-to-grain. Wu's criterion (1967) is a mixed-mode fracture criterion developed for a mixed crack opening and shear failure (mixed mode I and II, see Footnote 2).

Fracture mechanics analyse the stress and strain field at the crack tip. To describe these fields, linear-elastic fracture mechanics (LEFM) assume that all strain energy goes into the propagation of cracks. Within LEFM, stress intensity factors (evaluated for the three different crack opening modes I, II or III) or the strain energy release rate must be determined. Both are material constants and must be established with tests. Nonlinear fracture mechanics (NLFM) must be applied if some of the available strain energy is dissipated through micro-mechanisms around the crack tip, such as for instance fibre bridging in wood, and thus not all available strain energy goes into crack propagation. Vasic et al. (2005) stated that wood is rather poorly represented by LEFM and NLFM should be applied instead. Popular methods within NLFM are the crack tip opening displacement (CTOD method), R-curves or the J-integral (Smith et al., 2003). Fracture mechanics are mathematically complex and hence computationally expensive.

Fracture mechanics are used to describe softening curves in classical plasticity approaches and they deliver failure criteria within continuum mechanics. Often, the strain energy release rate, or simpler fracture energy  $G_f$ , is used (see for instance Grosse, 2005). As the fracture energy  $G_f$  is often applied, some important specifications in view of computational implementation must be given. Fracture energy is the energy that is needed for crack formation or, differently said, fracture energy is the energy needed to create new crack surfaces. If material tests are given in terms of traction-separation curves, then the fracture energy is the area underneath the curve. If however only the stress-strain curve (resp. force-displacement) is known, then the fracture energy as the area underneath the curve has the unit 'energy per volume' and must be transformed into a surface value by multiplying the area by the width (resp. the area).

### 3.4.2 Continuum damage mechanics

A simple and straightforward approach to model softening (or hardening) in materials are continuum damage mechanics (CDM). CDM is a nonlinear-elastic method where the nonlinear behaviour is obtained by modifying the stiffness matrix or its inverse, the compliance matrix. This is analogous to lattice models as presented in section 3.2.2. However, CDM can be implemented in an incremental-iterative framework. The stress increments are calculated from strain increments via a variable stiffness matrix. Therefore and as opposed to classical plasticity, damage mechanics unloads with the secant stiffness and not with the elastic stiffness. This approach can hence not model permanent plastic deformations. Figure 3-19 and Equation (3-9) show the basic idea of CDM.

One drawback of continuum damage mechanics as of any continuum approach is that the models are mesh dependent when softening is modelled. Furthermore, as CDM are implemented in a continuum mechanics approach, problems with local failures or instabilities will still be persistent if the model scale is not small enough to capture these localised effects.

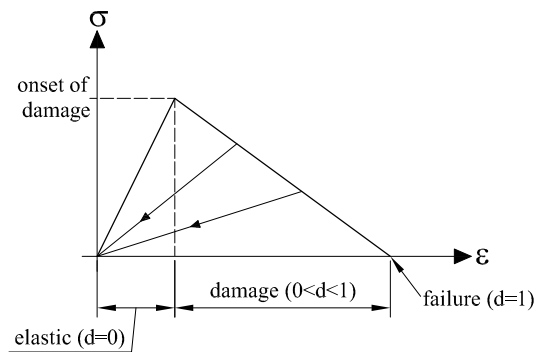


**Figure 3-19: Basic idea of damage mechanics, linear damage function**

In CDM, a damage variable  $d$ ,  $0 \leq d \leq 1$ , is determined and inserted into the fundamental Hooke equation as follows:

$$\sigma_{ij} = (1-d)D_{ijkl}\varepsilon_{kl} \quad (3-9)$$

If  $d = 0$ , no damage is present; if  $d = 1$ , the material has failed.

In case of anisotropic damage, several damage variables need to be defined.

In comparison to plasticity, damage is much easier to implement. No flow rules or hardening rules are needed. The material behaviour is completely defined by the damage variables. However, failure surfaces still need to be formulated to identify the onset of damage and a function must be developed that describes the evolution of the damage variable  $d$ . The models are stress - or strain-based, depending on whether they compare the onset of damage ( $d > 0$ ) to a strain or a stress criterion.

However, CDM are often formulated in terms of strains as this is more straightforward in computational mechanics. The damage variable  $d$  starts to develop after a certain strain threshold has been passed. Damage develops with increasing strain and is not reversible. As for stress-based formulations, stress is no unequivocal parameter in softening as a certain elastic stress level will be reached again when strain-softening develops. Therefore, not only a damage parameter is needed, but analogously to the flow theory of plasticity also a history parameter that takes the loading history into account.

Furthermore, at every new increment  $t$ , the input values in constitutive material subroutines are the strains  $\varepsilon^t$  at increment  $t$ , but the stresses  $\sigma^{t-1}$  at increment  $t-1$ . Within the subroutine, the stresses  $\sigma^t$  at increment  $t$  are updated. If now the onset of damage is formulated in terms of stress, a prediction of the stresses  $\sigma^t$  for the actual increment  $t$  must be evaluated with which the failure criteria can be compared. This explains why usually strain-based formulations are preferred.

However, recalling the issues discussed in section 3.3.1 (stress- or strain-based failure criteria), it is evident that it is not trivial to obtain correct input values in terms of strain.

Some researchers used the concepts of damage mechanics to simulate the mechanical behaviour of wood. Cofer et al. (1999) used an anisotropic damage model. Unfortunately, it was only a preliminary study with simple assumptions to investigate into the potential of this approach. Also in a research project of the U.S. Federal Highway Administration (2007), a material model for wood using concepts from damage mechanics has been developed for dynamic problems. The developed model applies classical flow theory of plasticity to formulate ductile failure of wood in compression and damage mechanics for the brittle failure modes. They consider wood being transverse isotropic and the chosen failure criterion is the Hashin criterion. Even visco-plastic rate effects were included. In a special report of the U.S. Federal Highway Administration (2005), the wood material model was evaluated.

Damage mechanics are widespread and well developed in the field of fibre composites (for instance Maimí et al., 2007, Lopes, 2009, Matzenmiller et al., 1995, Maimí, 2006, Feih and Shercliff, 2005b).

### **3.5 INNOVATIVE APPROACHES WITHIN CONTINUUM MECHANICS**

Modern FE packages offer many tools for material modelling. Two hybrid approaches using these tools without the need of user subroutine programming are shown in section 3.5.1. In section 3.5.2, an innovative hierarchical model is presented.

#### **3.5.1 Hybrid approaches**

A hybrid model was developed by Bocquet in 2D (Bocquet, 1997, Racher and Bocquet, 2005) by merging two approaches, beam on foundation models and standard 2D FE models with elasto-plasticity. Bocquet superimposed two different element types around the bolt hole as can be seen in Figure 3-20 and Figure 3-21. A simple isotropic bar element reproduced the material behaviour parallel-to-grain. The other isotropic element called JOINT reproduced the behaviour perpendicular-to-grain and represented the typical behaviour of wood in transverse compression with plastic hardening and transverse tension with a cut-off criterion (Figure 3-20). Also the shear behaviour was modelled with the JOINT elements. If for example the capacity in tension perpendicular-to-grain was reached, the wood split and the JOINT elements dropped out, the beam elements were still able to transfer load parallel-to-grain. The outer wood was modelled as an elastic orthotropic material.

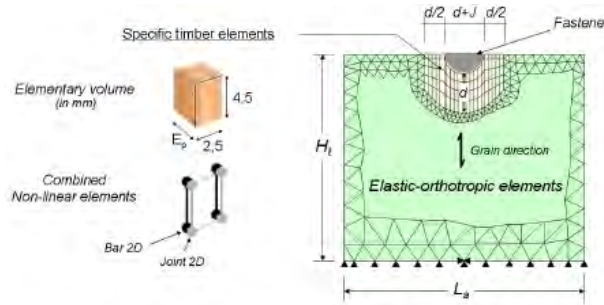


**Figure 3-20: Superimposed FE element and model (Racher and Bocquet, 2005)**

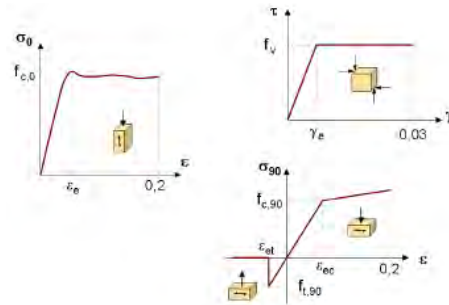


**Figure 3-21: Properties of FE element (Racher and Bocquet, 2005)**

This means that the close-up range of the bolt has been partly discretised and modelled with specific timber elements (Figure 3-20). With this, Bocquet was able to represent the nonlinear embedding behaviour of wood and joint behaviour including brittle splitting phenomena due to stresses perpendicular-to-grain or shear.

Toussaint (2009) together with Bocquet further developed the idea of superimposing two element types. Toussaint used a commercial FE package with two already implemented material models, orthotropic plastic beam elements for mechanical behaviour parallel-to-grain and 3D solids of crushable foam that simulated the behaviour perpendicular-to-grain (Figure 3-22).

The main scope of this approach was to model the densification of wood under compression perpendicular-to-grain together with brittle failure in tension perpendicular-to-grain. Toussaint found good agreements between models and experimental results.

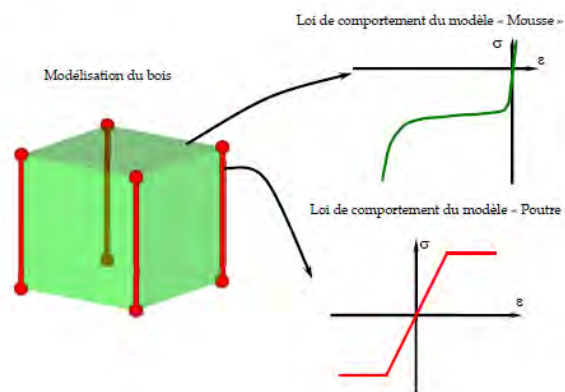


**Figure 3-22: Toussaint's superposed elements to model wood (Toussaint, 2009, Fig 175)**

Another hybrid approach is also using different element formulations. Besides standard continuum elements, most FE packages offer so-called cohesive or interface elements. These element types are similar to contact elements and can separate after a specified threshold has been passed. The separation process itself can be defined as well. It can

follow exponential laws for instance. The interface elements must be calibrated on test results, often compact tension (CT) tests which is rather cumbersome. In Figure 3-23 and Figure 3-24, a model loaded in tension parallel-to-grain with interface elements is shown (Franke, 2008).

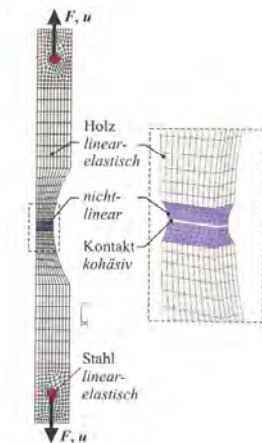


Figure 3-23: FE model with cohesive elements as splitting plane (Franke, 2008, Fig. 5-1)

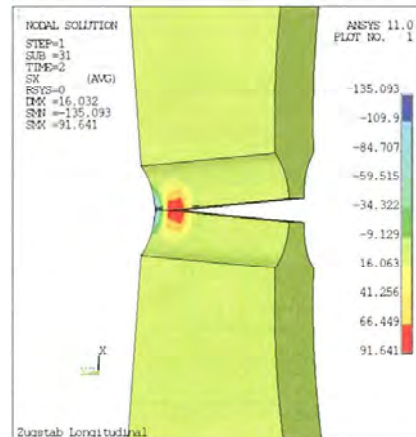


Figure 3-24: FE model after splitting (Franke, 2008, Fig. 5-4)

The cohesive or interface elements must be inserted in model regions where splitting is expected. This is a drawback as the splitting planes are pre-defined. However, as seen in chapter 2, wood has preferred splitting planes and in most cases it is known beforehand where splitting will occur. Therefore, these approaches are well-working practical methods to simulate ductile and brittle behaviour of wood in an efficient way (Blaß and Bejtka, 2008, Campilho et al., 2009, Franke, 2008) although considerable test data is necessary to calibrate the cohesive elements. One challenge still is to simulate shear splitting. It would be especially interesting to model the phenomenon of plug and block shear-out in multiple-dowelled joints with these elements.

### 3.5.2 Different hierarchical levels

An important question to be answered when dealing with wood modelling is which hierarchical level of wood should be chosen. Different levels are for instance:

- Chemical level modelling cellulose and lignin;
- Microscopic level modelling cells;
- Mesoscale where the annual rings are modelled;
- Macroscale with clear wood;
- Megascale of structural wood including knots and grain deviations.

The microscopic features of wood as a structure are modelled when starting the modelling at the microscopic level. However, existing microscopic models are not yet

able to be used on an engineering scale. Nearly all microscopic structural models have a preliminary need to determine the failure mode. It must be known whether the wood structure fails under parallel or transverse tension or compression, under shear or combinations of those. Only then a model can be developed that allows for the identified failure modes. The model's setup typically represents the microstructure of wood. It has a cellular structure geometrically similar to wood. Material properties are assigned to the model's different components. Stupnicki (1968) for example assumed that failure occurs in the intercellular layer. Therefore, he developed a cell frame system made of middle lamellae including rectangular cells with thick walls as latewood and hexagonal cells with thinner walls as earlywood. The cell walls themselves were assumed to be made of weaker material. The model was loaded in compression parallel-to-grain. Stupnicki's numerical results were 10-15 times higher than the crushing strength of wood which he explained with the fact that the model assumed perfectly straight middle lamellae whereas in reality, they are corrugated and have cavities producing stress concentrations.

More recent multi-scale models were presented by Persson (2000) and Hofstetter et al. (2005). Persson used homogenising techniques scaling up different hierarchy levels of wood. The first level was the microfibrils level with lignin, hemicellulose and cellulose as homogeneous material. This homogenised level was then used to represent wall layers with microfibrils as homogeneous material. Persson (2000) undertook 3D FE analysis in uniaxial (radial and tangential) compression in the plastic range choosing Hill's criterion as a failure surface. A 3D analysis in the sense that he assigned a thickness to the cell walls before assembling the walls to represent a piece of wood. Also the stiffness and hygroexpansion properties were investigated. Simulation results were given for single cells or small wooden pieces and effects due to moisture changes were included. Density, properties of the chemical constituents and microfibril angle of the S2-layer were found to govern the macroscopic mechanical properties. Persson stated that numerical problems were encountered when simulating the compression behaviour of small clear wooden pieces. This means that such a modelling is hardly suitable for engineering purposes at the current state-of-the-art.

Hofstetter et al. (2005) developed a micromechanical, even chemical model starting with the properties of lignin, hemicellulose and water and then carrying out a homogenisation scaling up the hierarchy levels of wood. At each hierarchy level, a homogenised stiffness tensor (composed of the material properties of the single constituents – such as at the first hierarchy level lignin, hemicellulose and water) was determined. In other words, every constituent's properties were represented through so-called representative volume elements (RVEs), the merging of the different RVEs established then the necessary boundary conditions in terms of deformation and stresses to create a higher organised element. This multistep homogenisation or determination of a homogenised mechanical behaviour from low organisation levels of the material up to higher levels was accomplished through four levels:

- First hierarchy level ‘polymer network’ with RVEs up to a length of 8-20 nm; lignin, hemicellulose, water;
- Second hierarchy level ‘cell walls’ with RVEs up to a length of 0.5-1  $\mu\text{m}$ ; adding crystalline and amorphous cellulose;
- Third hierarchy level ‘softwood’ with RVEs up to a length of 100-150  $\mu\text{m}$ ; adding lumen;
- Fourth hierarchy level ‘hardwood’ with RVEs up to 2-4 mm; adding vessels.

The model assumed ideal material, dealt only with elasticity and was dependent on the correct material input of the first two levels – a field for which many different values can be found in literature depending for instance on the extraction method of lignin or cellulose. A continuum micromechanical approach may in future be promising for e. g. wood drying simulations, but seems to be too complicated and generalising to be a reasonable approach for structural wood at the current state-of-the-art.

As stated in section 3.2.2, also approaches to model the mesoscopic scale (e.g. annual rings) exist. Bigorgne et al. (2010) developed a subroutine to assign different mechanical properties to earlywood and latewood in a continuum mechanics context and Reichert (2009) did the same for lattice models.

In a sense, also the natural scatter of wood properties could be interpreted as being dependent on the modelling scale. On any scale larger than the microscopic scale, the influence of growth can be observed – this ranging from annual rings to knots and grain deviation. Therefore, Clouston and Lam (2001) included Monte Carlo algorithms to randomly model a certain bandwidth of material properties in a continuum mechanics model. Landis et al. (2002) again did the same for lattice models.

### 3.6 FROM MATERIAL MODELLING TO JOINT MODELLING

With few exceptions, all reviewed literature up to now dealt with material modelling of clear wood in most cases and not with timber joint modelling. The issues related to timber joint modelling are additional issues to material modelling issues.

Failure of timber joints relates to local processes around the loaded areas. A fundamental work to understand these localised phenomena was done by Rodd (1973). He and, based on his idea, Werner (1993) developed a mathematical model predicting the lateral resistance of a bolt that is composed of the force necessary to crush the fibres in the direction of the movement parallel-to-grain (embedment) and the perpendicular component of the force necessary to displace the fibres around the bolt. It is this component that causes tension perpendicular-to-grain which is related to splitting. Furthermore, Rodd (1973) assessed the influence of rough or smooth bolt surfaces on the failure modes and ultimate strength values of timber joints: The rougher the bolt, the higher the load carrying capacity due to the better stress distribution. This underlines the importance of friction and contact modelling in FE analyses. Werner’s work (1993) also

includes a thorough discussion of the parameters that influence the embedment strength and hence also the joint behaviour.

First mathematical models of timber joints started with plane problems modelling wood as orthotropic linear elastic and the fastener as rigid (Rowlands et al., 1982). These models were slowly extended by refining the contact modelling and by inserting plasticity laws (Rahman et al., 1991) maintaining a rigid fastener. Already Rowlands et al. (1982) underlined that even though they used linear elastic material properties, the joint behaviour is nonlinear due to the changing contact stresses at various load levels and deformation states. Rahman et al. (1991) stated that using plastic material properties in compression, the contact stresses were reduced by 20% which may well affect the failure mode beneath the fastener. However, to predict damage and failure, only linear elastic material properties were considered. Due to computational limitations, it was not possible to consider 3D stress states.

Another approach is to use a piecewise incremental method to describe nonlinear material behaviour instead of plasticity laws. Patton-Mallory et al. (1997) developed a 3D model of a single fastener joint loaded parallel-to-grain where the plastic behaviour in compression was approximated with a trilinear curve with lower stiffness values for increasing compressive strains. Also trilinear shear stiffness degradation was implemented in order to model the softening due to local fractures resulting from brittle shear failures. Tension perpendicular-to-grain was assumed to be linear because it was impossible to implement brittle nonlinear behaviour in the numerical programme. The bolt was modelled as elastic-perfectly plastic. Interaction of stresses was not considered. Patton-Mallory stated that the model is valid up to a joint displacement below 1 mm which only represents the initial stage of the load-slip curve. This is probably due to convergence problems. Further 3D models were developed by Cofer et al. (1999) and Moses and Prion (2003). Cofer et al. (1999) further developed the model by Patton-Mallory et al. (1997) by adding a continuum damage mechanics approach to describe brittle failure in tension. Another 3D model was proposed by Moses and Prion (2003). They used the Hill criterion to simulate joint performance using bilinear stress-strain curves. A subroutine was written to include the size effect to account for brittle behaviour. The maximum stress criterion was used as a failure surface for the brittle cases which means that the three tension and the three shear stresses were independently compared against maximum strength values. The simulation did not model the complete ductile behaviour of the tested joints up to failure, but stopped at about 2-3 mm of displacement.

Dias (2005) developed a 3D Finite Element model to simulate embedment tests using the Hill criterion to define plasticity of timber. His outcomes could trace the load-slip behaviour of the tested specimens of spruce, chestnut and maritime pine up to failure by modelling the stiffness, maximum load as well as the maximum slip correctly. Especially the ability of simulating joint behaviour also at higher displacement stages is a fundamental step in joint modelling. In view of the problem of availability of mechanical input parameters, Dias et al. (2010) further developed the 3D model. They developed a practical approach to transfer test data into material input parameters for numerical

models. Dias used Hill's theory whose anisotropic parameters are all calculated as ratios between uniaxial yield stresses and equivalent tensile yield stress of an isotropic material. Therefore, apart from elastic properties and possible strain hardening parameters, three parameters are sufficient to sufficiently define the plastic behaviour of wood as a transverse isotropic material: the equivalent yield stress and two ratios to define the perpendicular normal stresses and the shear stresses. Dias derived an equation to determine the equivalent stress  $\sigma_0$  as a function of the embedment strength. Through a comparative study with embedment test results, Dias calibrated also the transverse isotropic yield stress ratios. He used a trilinear law to model isotropic strain hardening with a low initial equivalent yield stress (16% of  $\sigma_0$ ). Further comparisons of experimental results with models confirmed the validity of his approach. The model's major advantage is that its material input can be based on a huge database of embedment test results.

Many other joint models exist that combine linear elastic material properties with sophisticated contact modelling. Bickerdicke and Quenneville (2006) give a recent example where the load transmission from bolt to wood is achieved with calibrated nonlinear springs. Their approach is a variation of beam on foundation models which are genuine phenomenological models. Beam on foundation models are extensively used for modelling due to their simplicity and valid outcomes (Foschi, 1974, Sawata and Yasumura, 2003). The models are close to the actual global system behaviour, but due to their simplified structure it is never possible to consider all variables that are influencing the wood behaviour.

As a conclusion, the statement from section 3.1 can be repeated - the problems related to reliable numerical modelling of timber joints are presumably due to problems related to correct modelling of the material wood as the mechanical behaviour of steel and, to a certain grade, friction effects are better represented in actual joint models.

### 3.7 CONCLUSIONS

Modelling wood is a challenging task. An anisotropic, inhomogeneous material, different failure modes for different loadings, large variability and scale dependency to name some of the properties that turn wood into a difficult material to describe with mathematical models. Many numerical approaches exist that describe various aspects of wood behaviour, models focussing on ductile behaviour or others describing splitting. Table 3-1 shows some possible examples and chosen approaches to solve structural problems.

**Table 3-1: Examples for different modelling approaches**

<b>Problem type</b>	<b>Ductile problems</b>	<b>Brittle problems</b>	<b>Mixed problems</b>
<b>Example</b>	support - local compression perpendicular- to-grain	tension members	connections loaded parallel-to-grain
<b>Possible approaches</b>	continuum mechanics with classical plasticity	continuum mechanics with fracture mechanics	continuum mechanics with plasticity and interface elements
<b>Possible failure criteria</b>	Hill	Wu's criterion for mixed mode failure	1. Hill criterion for plasticity 2. Max. tension strength before separation
<b>Other possibilities</b>	-	lattice model or damage mechanics	continuum mechanics with plasticity and no modelling of splitting

The situation is even more complex if timber joints are modelled. Then additional effects from the fasteners and necessary contact modelling complicate matters. The main problem however remains the same. Firstly, a valid and reliable material model must be available to simulate the mechanical behaviour. To the author's knowledge, there is no single approach able to simulate the complete mechanical behaviour of timber joints, including ductile and brittle behaviour and correct stiffness, load carrying capacity and ultimate displacement predictions.

As hence the development of a constitutive model is the main focus of this thesis and as other researchers should be able to use and further develop this work, the first decision was to use a commercial FE package. Thereby, necessary modelling tools such as element definition, contact algorithms or solution methods are already implemented. The following list gives some more points that were considered when deciding on how to approach the task of developing a constitutive model:

1. Comprehensibility of approach
2. Transparency of input values
3. Robustness
4. Visualisation of results
5. Speed
6. Usability for others
7. Least programming needs

Focussing on the need to develop reliable numerical models to predict the mechanical behaviour of timber joints, the most important arguments of the main discussed approaches in this chapter are briefly presented in the following. This should help to motivate a choice for an approach with which a novel constitutive material model for wood is developed.

**Classical continuum mechanics**

<b>advantage</b>	<b>disadvantage</b>
Extensive FE packages available Integral approach Widely used tools  Simple implementation of constitutive models	Averaged results No localised failures Multisurface plasticity implemented – no innovative character Softening difficult – convergence problems

**Fracture mechanics**

<b>advantage</b>	<b>disadvantage</b>
Combination with plasticity within FE code possible Good modelling of brittle failures	Only for brittle failures Complex formulations – high computational costs

**Hybrid approaches**

<b>advantage</b>	<b>disadvantage</b>
Descriptive and simple models Interface elements available for brittle failures  Use of standard FE packages	No innovative character of work Limited by FE formulation (e.g. cohesive elements only with exponential laws) No stress interactions

**Lattice models**

<b>advantage</b>	<b>disadvantage</b>
Discrete model - wood at meso-scale Descriptive structural model (wood fibres) Densification possible Beam lattice models available that include bending and shear Property scatter easily implementable	Beam parameters difficult to determine Up to now, ideally brittle only High computational cost No simple software package available  Only material models, no system models (such as joints) that include contact formulations

**Sequentially linear analysis (SLA)**

<b>advantage</b>	<b>disadvantage</b>
No convergence problems when softening Straightforward approach and implementation	New solution algorithm, no Newton-Raphson 2D, new method with no added functions Not implemented yet in standard packages

**Continuum damage mechanics (CDM)**

<b>advantage</b>	<b>disadvantage</b>
Implementable in standard FE packages	No permanent deformations
Few material parameters needed	Mesh dependent
Material model easily implementable	Convergence problems when used in implicit code

Out of the many available methods to define constitutive models, continuum damage mechanics were chosen as this approach is mathematically simple and the combination of ductile and brittle failure modes is possible. The innovative character for wood research is seen to be high. Also the possibility to visualise different failure modes seems to be promising. Furthermore, a material model based on continuum damage mechanics can be implemented as a subroutine in existing FE programmes.

# 4

## DEVELOPMENT OF MATERIAL MODEL

*Applying the principles of continuum damage mechanics (CDM), a 3D material model is developed. CDM is a simple straightforward approach that can model ductility and softening. Failure modes can be identified and the deformation behaviour can be described. The material model should be able to describe not only the load carrying capacity but also the deformation behaviour and failure modes of timber joints. The developed model is thoroughly explained, the subroutine and further programming issues are evaluated. Furthermore, model verifications are carried out.*

### 4.1 INTRODUCTION

The purpose of this thesis is to develop a material model that is able to simulate the mechanical behaviour of wood. The material model should be suitable also for joint models. Furthermore, not only the load carrying capacity of the modelled joints should be satisfactorily predicted, but also the failure modes and deformation behaviour after the elastic regime.

A promising approach is the methodology of continuum damage mechanics (CDM) which is a widespread method used in fibre-reinforced composites (e.g. Matzenmiller et al., 1995, Maimí, 2006, Lopes, 2009). It is computationally simple as it manipulates the stiffness matrix in order to account for nonlinear behaviour, thus being a nonlinear elastic approach. It can be implemented in commercial FE packages by programming a material user subroutine that defines the constitutive relations. All other needed FE tools (such as element definition, contact algorithms and solution procedures) are already implemented and can be used for modelling purposes. This reduces the programming work to the constitutive material model. No complete FE programme needs to be developed.

This chapter introduces the material model. Failure modes and corresponding failure criteria are defined followed by some fundamentals of continuum damage mechanics. Subsequently, the damage evolution laws are discussed. Lastly, the model is verified. The source code of the material model is given in Sandhaas (2011).

## 4.2 DEFINITIONS

Material orientations and other conventions must be clearly defined before introducing the material model. Figure 4-1 shows the definition of the material directions and stress components. The direction ‘X, L, 1’ for instance can be found back in the index notation of the stresses in Equation (4-1). Strains are analogously defined. Therefore, e.g. normal stresses parallel-to-grain are expressed as stress components  $\sigma_{11}$  and shear stresses in the LT-plane are expressed as stress components  $\sigma_{13}$ . The definition and order of the stress array as defined in Equation (4-1) is consistently used throughout the thesis and is the same as used in the finite element package ABAQUS®.

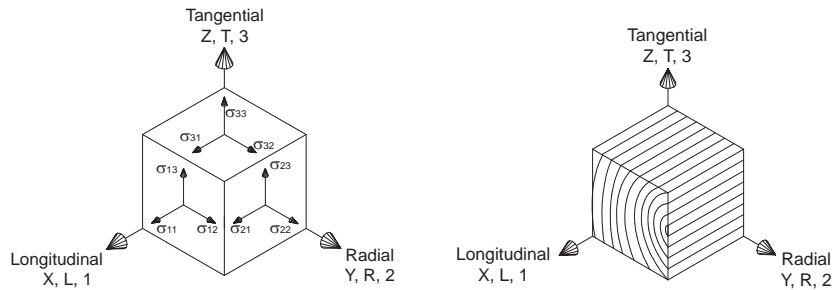


**Figure 4-1: Definition of stress components and material directions**

$$\begin{aligned} \boldsymbol{\sigma} &= [\sigma_{11} \quad \sigma_{22} \quad \sigma_{33} \quad \sigma_{12} \quad \sigma_{13} \quad \sigma_{23}]^T = [\sigma_L \quad \sigma_R \quad \sigma_T \quad \sigma_{LR} \quad \sigma_{LT} \quad \sigma_{RT}]^T = \\ &= [\sigma_0 \quad \sigma_{90R} \quad \sigma_{90T} \quad \sigma_{vR} \quad \sigma_{vT} \quad \sigma_{roll}]^T \end{aligned} \quad (4-1)$$

Stresses, e.g. normal stresses parallel-to-grain  $\sigma_{11}$ , can be positive or negative. By means of the Macaulay operator given in Equation (4-2), short notation is possible if a distinction between tension and compression is necessary. The Macaulay operator is very useful to define damage variables as will be seen in the next section.

$$\langle a \rangle := \frac{(a + |a|)}{2} \quad (4-2)$$

Lastly, stresses, failure modes or damage variables must be identified which is done by means of the placeholder M used as index (similarly used in Equation (4-1)):

$$M = \{t, 0 \quad c, 0 \quad t, 90R \quad c, 90R \quad t, 90T \quad c, 90T \quad vR \quad vT \quad roll\} \quad (4-3)$$

Where first index:  $t$  = tension,  $c$  = compression,  $v$  = longitudinal shear,  $roll$  = rolling shear;  
 second index:  $0$  = parallel-to-grain,  $90$  = perpendicular-to-grain;  
 third index:  $R$  = radial direction,  $T$  = tangential direction.

### 4.3 DAMAGE AND FAILURE OF WOOD

A constitutive damage model suitable for wood cannot be of isotropic nature. It must be, in its simplest version, a transverse isotropic model as discussed previously. Transverse isotropy has five independent constants. From a mathematical point of view however, five independent constants are not sufficient to model an orthotropic material such as wood. In transverse isotropy, the shear modulus  $G_{23}$  (= rolling shear modulus) is not an independent constant, but it is a function of the perpendicular Young's modulus  $E_{22}$  and the Poisson's ratio  $\nu_{23}$ . For wood, this is a wrong assumption which leads to a highly wrong shear modulus  $G_{23}$ .

Therefore, an orthotropic material model with nine independent constants was chosen. The single components  $D_{ijkl}$  of the stiffness matrix (through its inverse  $C_{ijkl}$ ) are changed according to the degree of damage. The first question when deciding for an orthotropic damage model is thus which damage should be modelled and how many failure modes and damage parameters are needed. The effect of these parameters on the compliance matrix is defined afterwards.

#### 4.3.1 Failure mode model

Accordingly to the discussions in chapter 2, the mechanical behaviour of wood can be categorised in the following failure modes I – VIII (FM I – VIII):

- *FM I: Tension parallel-to-grain*

Failure in tension parallel-to-grain is a brittle failure mode of wood which is caused by tensile stresses  $\sigma_{11}$  parallel-to-grain. It is assumed that other stress components do not influence the tension strength parallel-to-grain. Damage in tension parallel-to-grain is supposed to have no effect on other material properties. Also in the case of subsequent loading in compression parallel-to-grain, the tension cracks close and a compression force parallel-to-grain can be transmitted with the virgin elastic stiffness  $E_{11}$ . In other words, reduced tension strength does not lead to reduced compression strength.

- *FM II: Compression parallel-to-grain*

Failure in compression parallel-to-grain is a ductile failure mode of wood which is caused by compression stresses  $\sigma_{11}$  parallel-to-grain. It is assumed that other stress components do not influence the compression strength parallel-to-grain. Damage in compression parallel-to-grain is supposed to have no effect on other material properties. However, once a wooden piece has been loaded in compression parallel-to-grain up to damage through buckling of fibres, it could be supposed that the elastic tension stiffness parallel-to-grain as well as the tension strength have been degraded due to compression damage. Therefore, stiffness  $E_{11}$  in tension parallel-to-grain could be dependent on the damage history in

compression parallel-to-grain. Due to not enough experimental evidence, this was not implemented<sup>7</sup>.

The transverse tension modes and shear modes have to be combined as for instance splitting parallel to the LR-plane can be caused by tension perpendicular-to-grain (mode I), shear (mode II) or a combination of both (mixed mode). It is not possible to define separate failure modes for each stress component as degradation of one component also leads to degradation of the other components. This means that damage due to longitudinal shear also leads to damage in tension perpendicular-to-grain even though the actual normal tension stress component perpendicular-to-grain may still be lower than the transverse tension strength.

The transverse compression modes are more complex. A valid assumption for compression failure perpendicular-to-grain is to consider only normal compressive stress contributions without contributions of shear stresses. Considering ongoing discussions about the influence of transverse compression on shear strength (section 2.3.2), rather an increase in shear strength under increasing transverse compression may be observed. Therefore, an assumption of no interaction between transverse compression and shear may be on the conservative side. Considering the fibrous nature of wood, damage in shear should still allow wood to take load in compression via contact of the cell walls. However, shear failures can occur also under compressive stresses perpendicular-to-grain, i.e. if the compression load is applied under an angle to the grain creating thus high shear stress components. Therefore, for transverse compression, two failure modes can be identified. Firstly, ductile failure in compression that does not lead to shear damage and secondly, brittle failure due to high shear stress components.

- *FM III: Tension perpendicular-to-grain, tangential splitting (in LT-plane)*

Failure in tension perpendicular-to-grain with splitting in LT-plane is a brittle failure mode of wood which is caused by tensile stresses  $\sigma_{22}$  in the radial direction, longitudinal shear stresses  $\sigma_{12}$  in the LT-plane and rolling shear stresses  $\sigma_{23}$ . Once FM III is activated, all three contributing stiffness components  $E_{22}$ ,  $G_{12}$  and  $G_{23}$  must degrade although not all uniaxial strengths may be reached. For instance, FM III may be activated through longitudinal shear stresses that are higher than the shear strength. The positive stress component  $\sigma_{22}$  may still be lower than the value for tensile strength. However, also damage in tension perpendicular-to-grain must develop in this case.

- *FM IV and FM V: Compression perpendicular-to-grain, radial direction*

Two failure modes ‘FM IV: pure transverse compression’ and ‘FM V: shear’, both occurring under compression perpendicular-to-grain, can be distinguished. Failure in compression perpendicular-to-grain is a ductile failure mode of wood which is caused only by compression stresses  $\sigma_{22}$  in radial direction. Brittle shear

---

<sup>7</sup> How this supposed effect could be implemented is shown in Equation (4-33).

failure can also occur if for instance the compression load is applied with an angle to the grain creating high shear stress components.

- *FM VI: Tension perpendicular-to-grain, radial splitting (in LR-plane)*

Failure in tension perpendicular-to-grain with splitting in LR-plane is a brittle failure mode of wood which is caused by tensile stresses  $\sigma_{33}$  in the tangential direction, longitudinal shear stresses  $\sigma_{13}$  in the LR-plane and rolling shear stresses  $\sigma_{23}$ . Furthermore the same observations as for FM III are valid.

- *FM VII and FM VIII: Compression perpendicular-to-grain, tangential direction*  
FM VII / FM VIII are analogous to FM IV / FM V.

After having identified the failure modes, the damage variables must be defined. Therefore, the next question to be answered is about the type of damage that should be modelled and the number of damage variables.

#### What type of damage?

The main conclusion from chapter 2 is that wood is ductile in compression parallel and perpendicular to the grain and quasi-brittle in tension and shear. Therefore, two distinctive mechanical behaviours must be modelled:

- nonlinear **ductile** behaviour in compression parallel and perpendicular to the grain;
- nonlinear **brittle softening** behaviour in tension and shear where the shear is independent of the sign.

#### How many damage parameters?

A logical consequence from the above conclusions is to define nine damage parameters:

1.  $d_{t,0}$  = damage in tension parallel-to-grain;
2.  $d_{c,0}$  = damage in compression parallel-to-grain;
3.  $d_{t,90R}$  = damage in tension perpendicular-to-grain, radial direction (LT-plane);
4.  $d_{c,90R}$  = damage in compression perpendicular-to-grain, radial direction;
5.  $d_{t,90T}$  = damage in tension perpendicular-to-grain, tangential direction (LR-plane);
6.  $d_{c,90T}$  = damage in compression perpendicular-to-grain, tangential direction;
7.  $d_{vR}$  = damage in longitudinal shear, LT-plane;
8.  $d_{vT}$  = damage in longitudinal shear, LR-plane;
9.  $d_{roll}$  = damage in rolling shear, RT-plane.

The first two damage variables  $d_{t,0}$  and  $d_{c,0}$  are activated by the same normal stress component,  $\sigma_{11}$  parallel-to-grain. However, the damage variables differ depending on the sign of the stress component. In damage mechanics, a distinction in tension (index 't') and compression (index 'c') can easily be made as shown in Equation (4-4) using the

Macaulay operator of Equation (4-2). The two damage variables for a normal stress component can be combined. Damage variables  $d_{t,0}$  and  $d_{c,0}$  can thus be expressed as damage variable  $d_0$ .

$$\begin{aligned}
 d_0 &= d_{t,0} \frac{\langle \sigma_{11} \rangle}{|\sigma_{11}|} + d_{c,0} \frac{\langle -\sigma_{11} \rangle}{|\sigma_{11}|} \\
 d_{90R} &= d_{t,90R} \frac{\langle \sigma_{22} \rangle}{|\sigma_{22}|} + d_{c,90R} \frac{\langle -\sigma_{22} \rangle}{|\sigma_{22}|} \\
 d_{90T} &= d_{t,90T} \frac{\langle \sigma_{33} \rangle}{|\sigma_{33}|} + d_{c,90T} \frac{\langle -\sigma_{33} \rangle}{|\sigma_{33}|}
 \end{aligned} \tag{4-4}$$

### 4.3.2 Failure criteria

Wood is usually considered a transverse isotropic material (FM III = FM VI; FM IV = FM VII; FM V = FM VIII) which would reduce the number of failure modes to four. However, mathematically wood cannot be considered as a transverse isotropic material as discussed above. Apart from a wrong rolling shear modulus, the description of wood as a transverse isotropic material would presumably lead to wrong locations of the failure planes. In transverse isotropy, assumptions (i. e. rolling shear deformation  $\gamma_{23} = 0$ ) must be taken to identify the failure plane for failures perpendicular-to-grain. This failure plane may thus be lying somewhere in the perpendicular planes, rotating around the longitudinal axis which is not realistic for wood with its clearly defined failure planes.

In section 3.3.1, different classical failure criteria are discussed and the advantages and disadvantages of different criteria were assessed. It was shown that based on experimental evidence, the use of sophisticated criteria cannot be motivated. Therefore, within the scope of this thesis, the simplest approaches are chosen to show the potential of the CDM approach. Van der Meer (2010) further motivates the choice of simple criteria as he argued that the “difference between available formulations is small as far as failure initiation is concerned.” A minimum number of eight failure modes is established. For parallel failures, no interactions are assumed and maximum stress criteria are chosen. For the perpendicular cases however, a case distinction is made. Purely elliptic criteria are chosen for the tensile modes considering normal and shear stresses. Under transverse compression, a maximum stress criterion for the normal stress component is defined and a quadratic criterion for the combination of shear stress components. In Equations (4-5) to (4-12), the failure criteria FM I to VIII are shown (the respective damage variables that are triggered by the failure criteria are given in parenthesis).

*FM I – if  $\sigma_{11} \geq 0$  (damage variable  $d_{t,0}$ ):*

$$F_{t,0}(\sigma) = \frac{\sigma_{11}}{f_{t,0}} \leq 1 \quad (4-5)$$

*FM II – if  $\sigma_{11} < 0$  (damage variable  $d_{c,0}$ ):*

$$F_{c,0}(\sigma) = \frac{-\sigma_{11}}{f_{c,0}} \leq 1 \quad (4-6)$$

*FM III – if  $\sigma_{22} \geq 0$  (damage variables  $d_{t,90R}$ ,  $d_{vR}$  and  $d_{roll}$ ):*

$$F_{t,90R}(\sigma) = \frac{\sigma_{22}^2}{f_{t,90}^2} + \frac{\sigma_{12}^2}{f_v^2} + \frac{\sigma_{23}^2}{f_{roll}^2} \leq 1 \quad (4-7)$$

*FM IV – if  $\sigma_{22} < 0$  (damage variable  $d_{c,90R}$ ):*

$$F_{c,90R}(\sigma) = \frac{-\sigma_{22}}{f_{c,90}} \leq 1 \quad (4-8)$$

*FM V – if  $\sigma_{22} < 0$  (damage variables  $d_{vR}$  and  $d_{roll}$ ):*

$$F_{vR}(\sigma) = \frac{\sigma_{12}^2}{f_v^2} + \frac{\sigma_{23}^2}{f_{roll}^2} \leq 1 \quad (4-9)$$

*FM VI – if  $\sigma_{33} \geq 0$  (damage variables  $d_{t,90T}$ ,  $d_{vT}$  and  $d_{roll}$ ):*

$$F_{t,90T}(\sigma) = \frac{\sigma_{33}^2}{f_{t,90}^2} + \frac{\sigma_{13}^2}{f_v^2} + \frac{\sigma_{23}^2}{f_{roll}^2} \leq 1 \quad (4-10)$$

*FM VII – if  $\sigma_{33} < 0$  (damage variable  $d_{c,90T}$ ):*

$$F_{c,90T}(\sigma) = \frac{-\sigma_{33}}{f_{c,90}} \leq 1 \quad (4-11)$$

*FM VIII – if  $\sigma_{33} < 0$  (damage variables  $d_{vT}$  and  $d_{roll}$ ):*

$$F_{vT}(\sigma) = \frac{\sigma_{13}^2}{f_v^2} + \frac{\sigma_{23}^2}{f_{roll}^2} \leq 1 \quad (4-12)$$

Shear failure is considered in the failure modes for normal stresses perpendicular-to-grain. However, separate shear damage variables, based on shear strength and mode II fracture energy, are formulated. Therefore, no equivalent perpendicular damage is formulated, but the shear damage variables develop according to their fracture energies.

Figure 4-2 shows FM I to IV with typical values for the wood species spruce for a plane stress case. The quadratic form of FM III nearly vanishes due to the low tension strength perpendicular-to-grain.

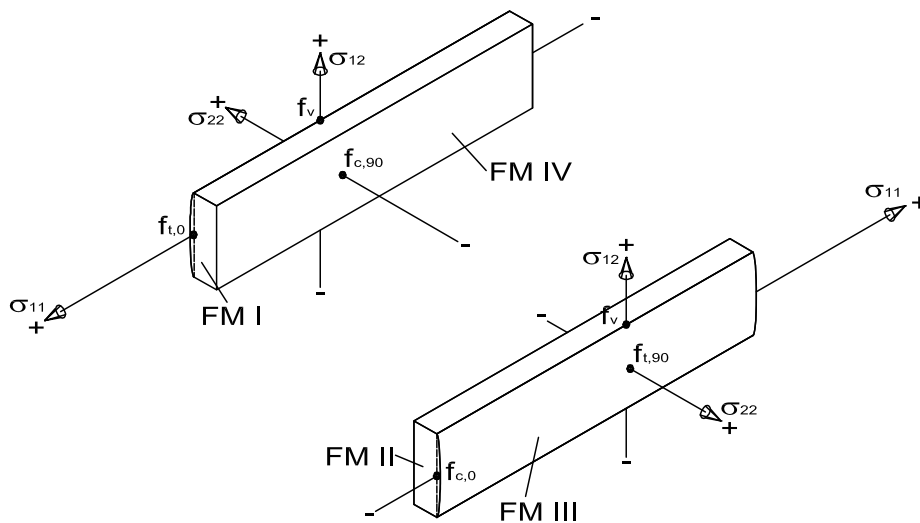


Figure 4-2: Graphical representation of failure modes FM I, II, III, IV, plane stress

### 4.3.3 Remarks on failure criteria

No single-surface failure criterion is chosen due to the inability of such a criterion to identify failure modes as discussed in section 3.3.1. Instead, separate criteria per failure mode according to Hashin (1980) are used which are defined per quadrant of the stress space. This requires a more complex programming as case distinctions must be defined.

Other, especially transverse, failure criteria used within the framework of continuum damage mechanics are for instance given in Maimí (2006) where the LaCR04 criterion (Pinho et al., 2005) was used. The LaCR04 criterion focusses on the effect of transverse compression on the shear strength. Many other criteria used in composite mechanics are dealing with a possible hardening of the shear stresses under increasing compression stresses perpendicular-to-grain. The literature (e.g. Juhasz, 2003) gives more examples for the interested reader. The Hashin criteria (Hashin, 1980) based on stress invariants instead can be considered as classical criteria for this type of material model approach.

Another remark is on the physical meaning of separated failure criteria and subsequent separation of damage parameters. The volume is not considered being constant contrarily

to the von Mises or Hill models as the derivation of the failure criteria is not based on the second deviatoric invariant of the stress tensor.

## 4.4 METHODOLOGY

### 4.4.1 Thermodynamic framework

Following Allix et al. (2003) and Maimí (2006), neglecting differences in temperature and moisture content and assuming a constant density, a possible function  $\theta$  for the strain energy density is as follows:

$$\begin{aligned} \theta = & \frac{\sigma_{11}^2}{2(1-d_0)E_{11}} + \frac{\sigma_{22}^2}{2(1-d_{90R})E_{22}} + \frac{\sigma_{33}^2}{2(1-d_{90T})E_{33}} \\ & + \frac{\sigma_{12}^2}{2(1-d_{vR})E_{12}} + \frac{\sigma_{13}^2}{2(1-d_{vT})E_{13}} + \frac{\sigma_{23}^2}{2(1-d_{roll})E_{23}} \\ & - \frac{\nu_{12}}{E_{11}}\sigma_{11}\sigma_{22} - \frac{\nu_{13}}{E_{11}}\sigma_{11}\sigma_{33} - \frac{\nu_{23}}{E_{22}}\sigma_{22}\sigma_{33} \end{aligned} \quad (4-13)$$

From the above shown function  $\theta$  for the strain energy density per unit volume, the strain tensor can be calculated through partial differentiation:

$$\boldsymbol{\varepsilon} = \frac{\partial \theta}{\partial \boldsymbol{\sigma}} = \mathbf{C} : \boldsymbol{\sigma} \quad \text{with} \quad \mathbf{C} = \frac{\partial^2 \theta}{\partial \boldsymbol{\sigma}_{ij} \otimes \partial \boldsymbol{\sigma}_{ij}} \quad (4-14)$$

with

$$\partial \boldsymbol{\sigma}_{ij} \otimes \partial \boldsymbol{\sigma}_{ij} = \begin{bmatrix} \partial \sigma_{11} \partial \sigma_{11} & \partial \sigma_{11} \partial \sigma_{22} & \cdot & \cdot \\ \partial \sigma_{22} \partial \sigma_{11} & \partial \sigma_{22} \partial \sigma_{22} & & \\ \cdot & & \cdot & \\ \cdot & & & \cdot \end{bmatrix} \quad (4-15)$$

The compliance tensor  $C$  is known from Hooke's law and describes the linear elastic relationship between strains  $\boldsymbol{\varepsilon}$  and stresses  $\boldsymbol{\sigma}$ . (see also Equation (4-20))

Subsequently, the thermodynamic forces (= release rates of damage energy) can be calculated as:

$$\begin{aligned}
Y_0 &= \frac{\partial \theta}{\partial d_0} = \frac{\sigma_{11}^2}{2(1-d_0)^2 E_{11}} \\
Y_{90R/90T} &= \frac{\partial \theta}{\partial d_{90R/90T}} = \frac{\sigma_{22/33}^2}{2(1-d_{90R/90T})^2 E_{22/33}} \\
Y_{vR/vT} &= \frac{\partial \theta}{\partial d_{vR/vT}} = \frac{\sigma_{12/13}^2}{2(1-d_{vR/vT})^2 E_{12/13}} \\
Y_{roll} &= \frac{\partial \theta}{\partial d_{roll}} = \frac{\sigma_{23}^2}{2(1-d_{roll})^2 E_{23}}
\end{aligned} \tag{4-16}$$

The dissipation rate follows from the thermodynamic forces:

$$\Theta = Y_0 \dot{d}_0 + Y_{90R/90T} \dot{d}_{90R/90T} + Y_{vR/vT} \dot{d}_{vR/vT} + Y_{roll} \dot{d}_{roll} \tag{4-17}$$

The thermodynamic forces are always positive as can be seen in Equation (4-16). Therefore, the dissipation rate  $\Theta$  is positive if the evolution of the damage variables is always positive:

$$\dot{d} > 0 \tag{4-18}$$

The positiveness of the energy dissipation rate is a fundamental requirement of continuum mechanics models in order to avoid spurious energy dissipation that leads to wrong results.

#### 4.4.2 Continuum damage mechanics (CDM)

In section 3.4.2, the basics of CDM were shortly presented to introduce the concept. Here, the fundamentals will again be explained based on a damaged compliance matrix and not on a damaged stiffness matrix as done in section 3.4.2.

CDM describes nonlinear material behaviour, especially softening behaviour, as caused by voids, defects or microcracks which reduce the area or volume of the material that can transmit forces. The effective stress  $\sigma^{ef}$  is the stress acting on the non-damaged material. A simple relationship between effective stresses  $\sigma^{ef}$  and nominal stresses  $\sigma$  is shown in Equation (4-19) with  $M$  being the damage operator which is composed by nine damage parameters  $d_M$  (with index  $M$  of Equation (4-3)). As defined in Equation (4-4), the distinction in tension and compression is made by the Macaulay operator. Therefore, entries  $d_0$ ,  $d_{90R}$  and  $d_{90T}$  define two damage variables each.

$$\begin{aligned}
 \boldsymbol{\sigma}^{ef} &= \mathbf{M}\boldsymbol{\sigma} \\
 \boldsymbol{\sigma}^{ef} &= [\sigma_{11}^{ef} \quad \sigma_{22}^{ef} \quad \sigma_{33}^{ef} \quad \sigma_{12}^{ef} \quad \sigma_{13}^{ef} \quad \sigma_{23}^{ef}]^T \\
 \boldsymbol{\sigma} &= [\sigma_{11} \quad \sigma_{22} \quad \sigma_{33} \quad \sigma_{12} \quad \sigma_{13} \quad \sigma_{23}]^T \\
 \mathbf{d} &= [d_0 \quad d_{90R} \quad d_{90T} \quad d_{vR} \quad d_{vT} \quad d_{roll}]^T \\
 \mathbf{M}_{ij} &= \begin{cases} \left[ \frac{1}{1-d_0} \quad \frac{1}{1-d_{90R}} \quad \frac{1}{1-d_{90T}} \quad \frac{1}{1-d_{vR}} \quad \frac{1}{1-d_{vT}} \quad \frac{1}{1-d_{roll}} \right] & \text{if } i=j \\ 0 & \text{if } i \neq j \end{cases}
 \end{aligned} \tag{4-19}$$

The relationships of Equation (4-19) show a simple way to model nonlinear behaviour by manipulating the elastic stiffness in Hooke's law. It is obvious that the introduction of orthotropic damage parameters  $d_M$  ranging from 0 to 1 are able to straightforwardly reduce the elastic stresses in order to represent effective stresses acting on the remaining intact volume of the material.

As the effective stress  $\boldsymbol{\sigma}^{ef}$  is the stress acting on the (remaining) undamaged material, it can also be formulated as shown in Equation (4-20) for a Hookean material with  $D^{el}$  the elastic stiffness matrix. Or, in the inverse formulation with the elastic compliance matrix  $C^{el}$ :

$$\boldsymbol{\sigma}^{ef} = \mathbf{D}^{el} \boldsymbol{\varepsilon} \quad \text{OR} \quad \boldsymbol{\varepsilon} = \mathbf{C}^{el} \boldsymbol{\sigma}^{ef} \tag{4-20}$$

with

$$\mathbf{D}^{el} = D_{ijkl}^{el} = \begin{bmatrix} (1-\nu_{23}\nu_{32})\Delta E_{11} & (\nu_{12} + \nu_{13}\nu_{32})\Delta E_{22} & (\nu_{13} + \nu_{12}\nu_{23})\Delta E_{33} & 0 & 0 & 0 \\ (\nu_{12} + \nu_{13}\nu_{32})\Delta E_{22} & (1-\nu_{13}\nu_{31})\Delta E_{22} & (\nu_{23} + \nu_{21}\nu_{13})\Delta E_{33} & 0 & 0 & 0 \\ (\nu_{13} + \nu_{12}\nu_{23})\Delta E_{33} & (\nu_{23} + \nu_{21}\nu_{13})\Delta E_{33} & (1-\nu_{12}\nu_{21})\Delta E_{33} & 0 & 0 & 0 \\ 0 & 0 & 0 & G_{12} & 0 & 0 \\ 0 & 0 & 0 & 0 & G_{13} & 0 \\ 0 & 0 & 0 & 0 & 0 & G_{23} \end{bmatrix} \tag{4-21}$$

$$\text{with } \Delta = \frac{1}{(1-\nu_{12}\nu_{21} - \nu_{13}\nu_{31} - \nu_{23}\nu_{32} - 2\nu_{13}\nu_{21}\nu_{32})}$$

Now, the damaged compliance matrix  $C$  for an orthotropic material can be modelled according to Equation (4-14) with the nominal stresses  $\boldsymbol{\sigma}$ :

$$\boldsymbol{\varepsilon} = \mathbf{C}^{dam} \boldsymbol{\sigma} \tag{4-22}$$

with

$$\mathbf{C}^{dam} = \begin{bmatrix} \frac{1}{(1-d_0)E_{11}} & -\frac{\nu_{21}}{E_{22}} & -\frac{\nu_{31}}{E_{33}} & 0 & 0 & 0 \\ -\frac{\nu_{12}}{E_{11}} & \frac{1}{(1-d_{90R})E_{22}} & -\frac{\nu_{32}}{E_{33}} & 0 & 0 & 0 \\ -\frac{\nu_{13}}{E_{11}} & -\frac{\nu_{23}}{E_{22}} & \frac{1}{(1-d_{90T})E_{33}} & 0 & 0 & 0 \\ 0 & 0 & 0 & \frac{1}{(1-d_{vR})G_{12}} & 0 & 0 \\ 0 & 0 & 0 & 0 & \frac{1}{(1-d_{vT})G_{13}} & 0 \\ 0 & 0 & 0 & 0 & 0 & \frac{1}{(1-d_{roll})G_{23}} \end{bmatrix} \quad (4-23)$$

Equation (4-22) can be reformulated for the damaged elastic compliance matrix  $\mathbf{C}^{dam}$  (see Matzenmiller et al. (1995)) which leads to the same tensor as given in Equation (4-23):

$$\boldsymbol{\varepsilon} = \mathbf{C}^{el} \boldsymbol{\sigma}^{ef} = \mathbf{C}^{el} \mathbf{M} \boldsymbol{\sigma} = \mathbf{C}^{dam} \boldsymbol{\sigma} \quad (4-24)$$

In finite element programmes, the inverse of the compliance matrix, the stiffness matrix  $\mathbf{D}$  is needed in order to update the stresses:

$$\mathbf{D}^{dam} = (\mathbf{C}^{dam})^{-1} \Rightarrow \boldsymbol{\sigma} = \mathbf{D}^{dam} \boldsymbol{\varepsilon} \quad (4-25)$$

If the compliance matrix is positive definite and the damage variables  $\mathbf{d}$  are less than 1, this inverse exists.

However, when calculating the inverse of the damaged compliance matrix as given in Equation (4-23), non-diagonal, non-zero entries of the form  $\nu_{ij}(\mathbf{d})$  containing Poisson's ratios and damage parameters will be obtained. The influence of the non-diagonal, non-zero entries is discussed in the following section.

#### 4.4.3 Physical meaning of Poisson's ratios

The non-diagonal, non-zero entries of the inversed damaged compliance matrix contain Poisson's ratios. By means of the Poisson's ratios, the relationship between the normal stresses resp. strains is defined. Subsequently, these non-diagonal entries must also be adjusted taking damage into account:  $\nu_{ij} = \nu_{ij}(\mathbf{d})$ .

An example is given to clarify the need of adjusting also the non-diagonal components. Entry (1, 2) of the compliance matrix determines the contribution of  $\sigma_{22}$  to the strain  $\varepsilon_{11}$ . On the other hand, its inverse correspondent, entry (1, 2) of the stiffness matrix,

determines the contribution of  $\varepsilon_{22}$  to the stress  $\sigma_{11}$ . If for instance damage in entry (1, 1) in tension parallel-to-grain is considered, entry (1, 2) translates the effect of damage in 1-direction on the properties in the 2-direction. If damage  $d_0$  approaches 1, stress and stiffness in 1-direction approach 0 and the Poisson effect on the 2- and 3-direction in entries (1, 2) and (1, 3) must disappear. Then the failure in tension parallel-to-grain does not affect the mechanical properties in the 2- and 3-direction. Physically this means that a wooden piece that has failed in tension parallel-to-grain still takes load in the perpendicular directions, may even be undamaged in the perpendicular directions. If the Poisson effect does not disappear, damage in 1-direction causes damage also in the 2-direction.

The same reasoning can be followed for the perpendicular directions. For instance, damage  $d_{t,90R}$  in 2-direction with failure in tension perpendicular-to-grain does not degrade the mechanical properties parallel-to-grain. The analogy of a 'loose bundle of fibres' illustrates this. A wooden piece failed in tension perpendicular-to-grain (reduced to bundles of fibres) can still be loaded in tension parallel-to-grain. The damage effects in tension parallel and perpendicular to the grain are decoupled.

However, there is no experimental evidence. Usually, specimens tested up to failure in tension perpendicular-to-grain are not retested under tension parallel-to-grain. Assumptions are taken on the influence of damage in one direction on the mechanical properties in the other directions. Also, nearly no research is known that investigates in the degradation of the Poisson's ratios (except Figure 2-23).

Furthermore, the whole discussion is more complex. Entry (1, 2) of the stiffness matrix as inverse of the compliance matrix for instance contains contributions of all three normal damage parameters  $d_0$ ,  $d_{90R}$  and  $d_{90T}$ . The following is valid: parameter  $d_0$  assesses the influence of damage parallel-to-grain on the properties perpendicular-to-grain. Parameter  $d_{90R}$  determines the effect of damage perpendicular-to-grain on the properties parallel-to-grain. To conclude, the combined effect of all these constituents on the perpendicular direction to the loading direction is rather undecipherable. Additionally, the symmetry of the constitutive tensor must be guaranteed also in the damaged state ((1, 2) = (2, 1)).

The shear damage parameters are automatically decoupled when calculating the inverse of the compliance matrix. Entry (4, 4) of the stiffness matrix contains only parameters  $G_{12}$  and  $d_{vR}$ . However, as seen in section 4.2, damage in normal direction, i.e. transverse tension or compression, influences also the shear stiffness.

All above discussed issues are especially important for wood. The large differences in mechanical properties parallel and perpendicular to the grain emphasise the influence of the Poisson's ratios. If a wooden piece is loaded in its strong direction parallel-to-grain, any parallel damage will have a prominent effect on the weak directions perpendicular-to-grain.

As a conclusion to the discussion on the influence of the Poisson's ratios onto stresses and strains, the normal damage parameters  $d_0$ ,  $d_{90R}$  and  $d_{90T}$  are considered to be

decoupled. A pragmatic solution is to choose low Poisson's ratios in order to minimise their influence – the chosen Poisson's ratios have the value of the damaged Poisson's ratios already at the beginning of the modelling (Figure 4-3). A further improvement of the material model would be to insert a linear degradation of the Poisson's ratios instead as shown in Figure 4-3<sup>8</sup>.

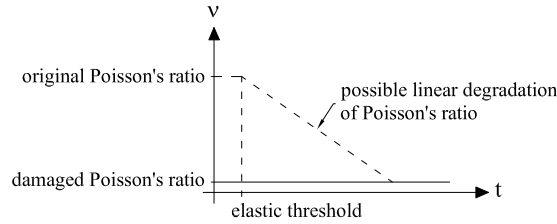


**Figure 4-3: Degradation of Poisson's ratios**

#### 4.4.4 Damage parameters

The nine damage parameters  $d_M$  as defined in section 4.3.1 evolve once the damage within the material has initiated. Mathematically, the damage process is irreversible. This irreversibility is also one of the theoretical requirements within the framework of thermodynamics. It must be guaranteed that damage can only grow (Equation (4-18)):

$$\dot{d}_M \geq 0 \quad (4-18)$$

The condition of Equation (4-18) can be easily fulfilled by demanding that

$$\mathbf{d}^t = \max \left\{ 0, \max_{incr=0,t} \{ \mathbf{d}^{incr} \} \right\} \quad (4-26)$$

which means that every damage parameter  $d$  is a solution dependent state variable that must be saved at every increment  $t$ .

As mentioned, the range of the damage parameters is between zero and one as defined in Equation (4-27). If the parameters  $d_M$  are equal to zero, no damage is present. During the damage process, the parameters  $d_M$  increase until complete failure is reached. Complete failure is reached when the parameters  $d_M$  have the value one. However, the damage parameters should never reach a value of one as then the stresses are equal to zero which

<sup>8</sup> As a first approach, degradation of the Poisson's ratios, i.e. of the form  $\nu_{12}^{dam} = (1-d_0)\nu_{12}$ , was implemented, but the degradation evolution coupled to the damage parameters is not strong enough to avoid a wrong Poisson effect. Therefore, it was decided to choose constantly low Poisson's ratios.

may lead to numerical instabilities. Therefore, a threshold value very close to one is set as maximum value for  $d_M$ <sup>9</sup>.

$$0 \leq d_M < 1 \quad (4-27)$$

#### 4.4.5 Damage evolution functions

If the failure criteria  $F_M(\sigma) > 1$ , the damage parameters start to grow. Two linear damage evolution laws are considered. One law is for elastic perfectly plastic behaviour, Figure 4-4, and the second one for brittle behaviour, Figure 4-5.

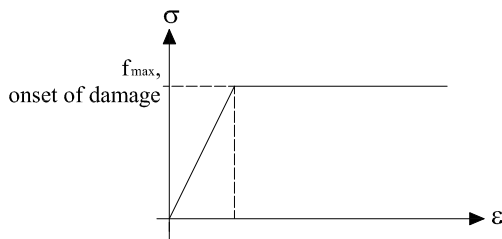


Figure 4-4: Stress-strain graph for elastic-perfectly plastic behaviour

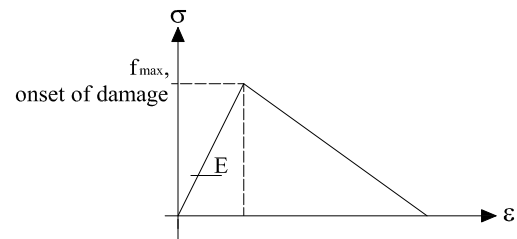


Figure 4-5: Stress-strain graph for softening behaviour

In order to define the damage evolution functions, a history parameter or state variable  $\kappa_M$  must be defined that keeps track of the loading history. Damage initiation functions (= failure criteria) trigger the onset of damage. A material is not damaged if Equation (4-28) holds.

$$F_M \leq 1 \quad (4-28)$$

Equation (4-28) can be reformulated introducing a state variable  $\kappa_M$ . Speaking in terms of yield, the yield function  $\phi$  becomes a function of the yield surface  $F_M$  and the state variable  $\kappa_M \geq 1$ :

$$\phi(F_M, \kappa_M) = F_M - \kappa_M \leq 0 \quad (4-29)$$

<sup>9</sup> This threshold value is chosen to 0.9999995.

This principle is analogous to the flow theory of plasticity. The yield surface  $F_M$  is the damage initiation function or failure criterion. As in classical plasticity and following Maimí (2006), the so-called Kuhn-Tucker conditions must hold:

$$\phi_M \leq 0, \quad \dot{\kappa}_M \geq 0, \quad \dot{\kappa}_M \phi = 0 \quad (4-30)$$

In the elastic range,  $F_M$  is smaller than 1 and therefore, as  $\kappa_M \geq 1$ , Equation (4-29) is negative,  $\phi_M < 0$ . When  $\phi_M = 0$ , the yield function is activated and the rate of the failure criterion  $\dot{F}_M$  must be established in order to decide whether the response is unloading ( $\dot{F}_M < 0$ ), neutral ( $\dot{F}_M = 0$ ) or loading ( $\dot{F}_M > 0$ ). If indeed  $\dot{F}_M$  is growing monotonically, the state variable  $\kappa_M$  also grows and with it the damage parameter  $d_M(\kappa_M)$ . Therefore, the damage parameter  $d_M$  depends on the state variable  $\kappa_M$  as only then the correct damage evolution can develop once the failure criterion  $F_M$  is exceeded. Analogously to damage, the state variable can only remain constant or grow (second Kuhn-Tucker condition).

In the case of loading ( $\dot{F}_M > 0$ ), the consistency criterion must be fulfilled which follows from the last Kuhn-Tucker condition:

$$\dot{\phi}_M = \dot{F}_M - \dot{\kappa}_M = 0 \quad (4-31)$$

According to Maimí (2006), Equation (4-31) can be integrated explicitly leading to the following final requirements for the state variable  $\kappa_M$ :

$$F_M = \kappa_M : \quad \kappa^t = \max \left\{ 1, \max_{incr=0,t} \{ \mathbf{F}^{incr} \} \right\} \quad (4-32)$$

A possible further definition could be following Equation (4-33) which was not implemented at the current state of research as there is not enough experimental evidence. Equation (4-33) means that damage in compression parallel-to-grain causes damage in tension parallel-to-grain. This could be a correct physical assumption for wood as one could state that buckling of fibres under compression parallel-to-grain leads to a lower tension strength parallel-to-grain.

$$\text{Tension parallel-to-grain: } \kappa_{t,0}^t = \max \left\{ 1, \max_{incr=0,t} \{ F_{t,0}^{incr} \}, \max_{incr=0,t} \{ F_{c,0}^{incr} \} \right\} \quad (4-33)$$

Finally, to sum up the mathematical requirements discussed above:

- State variable  $\kappa_M$  keeps track of the loading history;
- $\kappa_M = F_M$ , but is always bigger than 1 which means that as long as  $F_M$  is smaller than 1, the material is elastic;
- Once  $F_M \geq 1$ , damage starts and as long as the material is loaded,  $F_M$  and subsequently  $\kappa_M$  grows. At unloading, the last maximum state of  $\kappa_M$  at increment  $t-1$  is saved and further loading continues at this saved level of  $\kappa_M$ ;
- As long as  $\kappa_M$  grows, the damage parameter  $d_M(\kappa_M)$  grows.

The damage parameter  $d$  cannot be a function of the strains  $\varepsilon$ . For instance, once FM III ( $= F_{t,90R}$ , splitting parallel to LT-plane) is activated due to high longitudinal shear stresses, the stiffnesses of all other contributing stress components ( $E_{22}$  and  $E_{23}$ ) must degrade as well although the resp. uniaxial stresses  $\sigma_{22}$  and  $\sigma_{23}$  may still be below the uniaxial strengths  $f_{t,90}$  and  $f_{roll}$ . In such a case, a dependency of the damage parameters  $d_{t,90R}$  and  $d_{roll}$  on the strains  $\varepsilon_{22}$  and  $\varepsilon_{23}$  may not trigger the evolution of damage in these secondary directions. A dependency on the history parameters  $\kappa_{t,90R}$  and  $\kappa_{roll}$  will enforce the evolution of the damage parameters  $d_{t,90R}$  and  $d_{roll}$  instead.

The physical reason behind the enforcing of damage although the uniaxial strengths may not be exceeded is obvious: once a wooden piece has failed in shear parallel to the LT-plane, it will not be able to take any loads in tension perpendicular to the LT-plane. Of course another assumption is implicitly made by enforcing damage as described above if no separate damage evolution functions are defined. It is assumed that the mechanical behaviour under pure tension perpendicular-to-grain is the same as when failure in tension perpendicular-to-grain is only a secondary effect of failure in longitudinal shear. In other words, if wood fails in longitudinal shear, the degradation of the strength in tension perpendicular-to-grain is caused by shear failure but develops in the same way if it would be caused by tension stresses perpendicular-to-grain.

A last remark is done on another possibility to define the damage parameters. The above explained methodology models a continuous degradation whereas also constant degradation could be modelled (Feih and Shercliff, 2005a). In this second approach, constant damage factors are defined that are not dependent on the strains (or equivalent strain for isotropic damage). These factors fully describe the stiffness degradation of the material in every direction. They are applied as soon as damage starts to develop. This approach needs less solution dependent state variables as for instance the history parameter  $\kappa_M$  does not need to be saved at every increment. However, a continuous damage approach was favoured as this approach is physically more meaningful than one single constant factor for each component of the stiffness tensor. For instance, the damage rate can depend on the fracture energy and evolve accordingly whereas this is not possible with constant factors.

Within the scope of this thesis, the simplest approaches, i.e. linear damage evolution functions, have been chosen. In literature, many more complex damage evolution laws

can be found (e.g. Maimí, 2006, Federal Highway Administration, 2007). The linear laws shown in Figure 4-4 and Figure 4-5 are expressed as mathematical equations in terms of the state variables  $\kappa_M$ . The derivation of the damage functions is given in Appendix C.

The boundary conditions of the equations are known:

$$\begin{aligned} d(\kappa_M \leq 1) &= 0 \\ d(\kappa_M \rightarrow \infty) &= 1 \end{aligned} \quad (4-34)$$

$$\text{Brittle behaviour: } d(\kappa_M) = 1 \Leftrightarrow \int \sigma A \cdot du = G_f$$

Equation (4-35) shows the linear damage evolution function for the brittle case (Figure 4-5).

$$d(\kappa_M) = 1 - \frac{1}{f_{\max}^2 - 2g_f E} \left( f_{\max}^2 - \frac{2g_f E}{\kappa_M} \right) \quad (4-35)$$

Equation (4-35) includes the characteristic fracture energies  $g_f$  of the different modes related to the characteristic element size (Equation (4-41)). For instance, for the damage parameters  $d_{t,90R}$  and  $d_{t,90T}$ , the characteristic fracture energy perpendicular-to-grain (mode I)  $g_{f,90}$  is used. By replacing  $g_f$  with  $G_f$ , the crack band model used to alleviate mesh dependency (section 4.4.7) can be deactivated. (see also Sandhaas, 2011)

Equation (4-36) shows the law for the elastic perfectly plastic case (Figure 4-4).

$$d(\kappa_M) = 1 - \frac{1}{\kappa_M} \quad (4-36)$$

Shear damage parameters  $d_{vRT}$  and  $d_{roll}$

Shear damage variables can be triggered by different failure criteria and must be superposed. For instance, rolling shear damage  $d_{roll}$  may be caused by splitting in the LT-plane (FM III) and compression in tangential direction (FM VIII). Both components to the rolling shear damage must be added according to Equation (4-37):

$$d_{roll} = 1 - [1 - d_{roll,FMIII}] [1 - d_{roll,FMVIII}] \quad (4-37)$$

For the longitudinal shear parameters, the development is analogous. If for instance radial shear damage  $d_{vR}$  developed due to a tension component  $\sigma_{22}$  perpendicular-to-grain (FM III), subsequent loading in transverse compression  $\sigma_{22}$  (FM V) may again trigger radial shear damage  $d_{vR}$  where the damage variable must have memorised the previous damage due to transverse tension:

$$d_{vR} = 1 - [1 - d_{vR,FMIII}] [1 - d_{vR,FMV}] \quad (4-38)$$

Further possibilities could be to couple degradation of the shear stiffness with damage parallel-to-grain as shown in Equation (4-39). It could be assumed that the shear stiffness decreases proportionally to the stiffness parallel-to-grain as the shear stiffness depends on the damage in parallel and in perpendicular direction. If the material is damaged only in tension parallel-to-grain, the shear damage parameter  $d_v$  could be equal to the tension damage parameter parallel-to-grain  $d_{t,0}$ . If instead the material is damaged in tension perpendicular-to-grain, the additional shear damage parameter  $d^*$  could be calculated according to Equation (4-35).

$$d_v = 1 - [1 - d_{t,0}] [1 - d^*] \quad (4-39)$$

with

$$d^* = d(\kappa_{t,90R}) = d_{vR} \quad \text{resp.} \quad d^* = d(\kappa_{t,90T}) = d_{vT} \quad (4-40)$$

This coupling of shear damage to damage parallel-to-grain is not activated in the current subroutine as it leads to fast degradation of elements which is not physically admissible.

The flow diagram in Figure 4-6 summarises the approach and shows the flow of a material subroutine that can be implemented in commercial FE codes.

The other parameter apart from the stresses that must be updated in the subroutine is the secant stiffness matrix (see section 4.4.10).

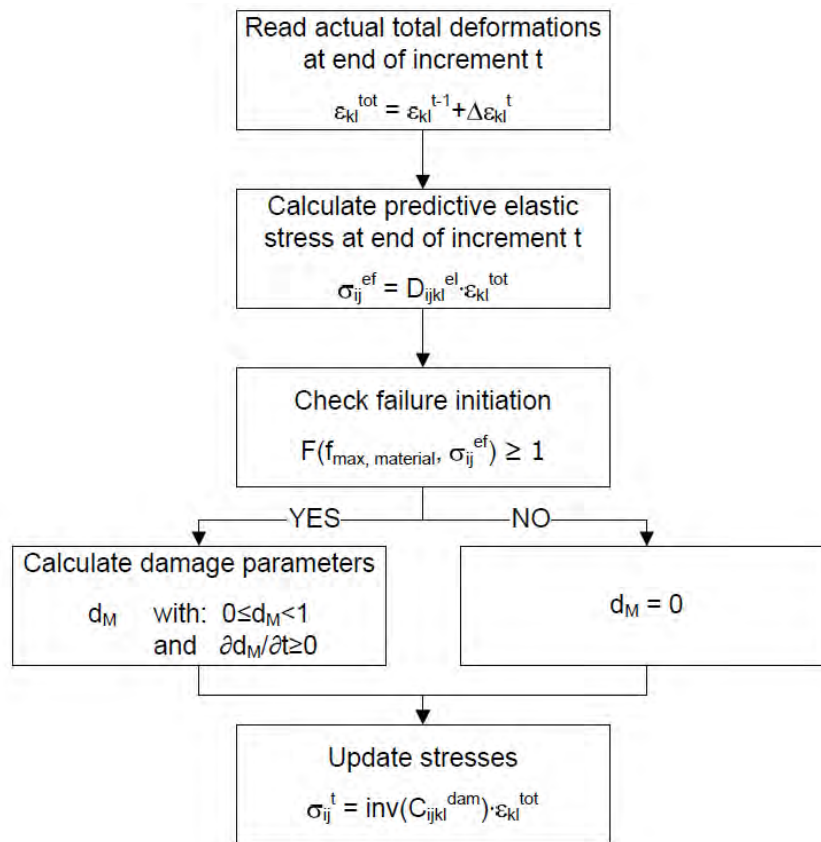


Figure 4-6: Flow diagram of damage model

#### 4.4.6 Other computational issues

This short section summarises some computational issues which were not mentioned yet.

##### Load Application

All load is applied in displacement-control.

##### Nonlinear Geometry Option

Both small displacement and large displacement theory can be used. Large displacement theory takes nonlinearities deriving from large deformations into account. If not indicated otherwise, the large-displacement option is enabled.

##### Material Orientation

Local material orientations must always be defined in order to assign the directions of the wood, resp. parallel and perpendicular to the grain. The numbering system is established as shown in Figure 4-1.

#### Mesh Dependency (section 4.4.7)

If not indicated otherwise, for verification and material models, the crack band option is activated to avoid a dependence on the finite element discretisation. However, all embedment and joint models are run without the crack band model. Further information is given in the subroutine verification section and chapter 5.

#### Solution Algorithm

The implicit full Newton-Raphson algorithm was selected. As in this thesis a commercially available FE package was used, it was not possible to choose more innovative solution procedures such as dissipation-based arc-length methods (Van der Meer, 2010).

#### **4.4.7 Mesh dependency and viscous stabilisation**

A major problem of continuum damage mechanics as of any other continuum approach modelling softening behaviour is the strong mesh dependency of the results. The source of mesh dependency is of mathematical nature as with the onset of softening, the previously well-posed problem has turned into an ill-posed problem. In computations, this results in a stiffness matrix which is no longer positive definite. The mathematical solution is a localisation zone of zero width without energy dissipation. The numerical solution tries to capture this physically inadmissible mathematical solution which yields a localised zone of smallest possible width, i.e. a single element in most cases.

In Figure 4-7, the numerical development of mesh dependency is explained by means of a one-dimensional example. As long as the material is elastic, the stress-strain relationship is unique and all elements, i.e. their integration points, follow the same stress-strain curve ( $d\sigma d\varepsilon > 0$ ). However, any type of softening behaviour involves a maximum of the  $\sigma(\varepsilon)$ -curve where the derivative, the gradient of  $\sigma(\varepsilon)$  is zero:  $d\sigma d\varepsilon = 0$ . From this point on, the solution problem is mathematically ill-posed which may result in loss of uniqueness, more than one solution is possible. A bifurcation problem arises as shown schematically in Figure 4-7. The element solution can follow the stress-strain curve and increase the element's strains with decreasing stresses whereas a second option is to decrease stresses as well as strains by following the secant stiffness back to origin. A special point is the maximum of the stress-strain curve. There,  $d\sigma = 0$  which means that  $d\varepsilon$  can assume any value.

The bifurcation problem is consistent for increased loading and thus a stress-strain curve that has entered the softening branch with negative stiffness:  $d\sigma d\varepsilon < 0$ . Integration points can choose between two options, i.e. increase strains and follow the  $\sigma(\varepsilon)$ -curve or unload elastically to the origin. Energetically, the solution will always try to dissipate the least amount of energy possible (by trying to follow the mathematical solution of zero width with no energy dissipation). This will lead to localisation as softening behaviour will be concentrated in few elements. Only those few elements will have increased strains

whereas all other elements choose the secant stiffness and unload or cannot even enter the descending branch. The global answer shows softening although most elements unload along the secant branch.

Energy considerations explain this localisation effect. When unloading along the secant stiffness, only the energy between the secant stiffness and  $\sigma(\varepsilon)$  is dissipated which corresponds to the material input value fracture energy  $G_f^{10}$ . The dissipated energy is indicated by the grey-shaded area in Figure 4-7. All energy below the secant stiffness remains available instead. The total work done by the elements is the complete area underneath the  $\sigma(\varepsilon)$ -curve where only the part of the elastic energy remains available.

Therefore, localisation will occur as the dissipation will be concentrated in few elements due to energetical optimisation. Localisation is energetically the less costly option as less energy is dissipated when more elements unload instead of dissipating energy by following the  $\sigma(\varepsilon)$ -curve. Energy optimisation will be best if the energy dissipation concentration is possible in infinitely small elements as then the least energy will be dissipated. In other words, the smaller the elements, the closer the softening curve to the elastic secant unloading as illustrated in Figure 4-8. Therefore, numerical results will depend on the mesh size. (see also Needleman, 1988, Gross and Seelig, 2011).

Figure 4-7 illustrates also another issue connected with softening behaviour which is the unloading of all elements except the ones that follow the global load-slip curve. This may lead to problems with the load transfer of damage elements to neighbouring elements.

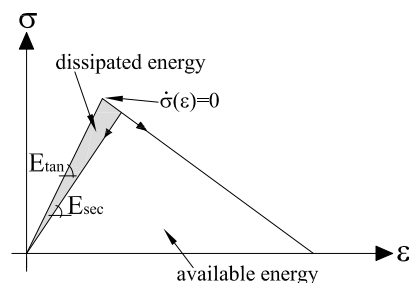


Figure 4-7: Graphical representation of a bifurcation problem

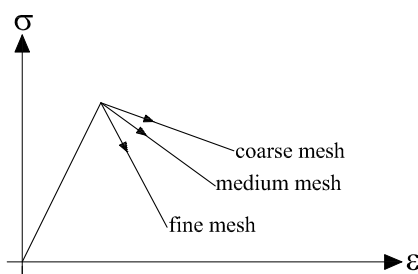


Figure 4-8: Influence of mesh size on numerical results

<sup>10</sup> Please note, the fracture energy  $G_f$  is a surface value.

Different algorithms have been developed in order to regularise models and to deliver mesh-independent results. One is shortly presented in the following. In literature, more regularisation techniques are available (e.g. Sluys, 1992).

#### Crack band method

Bažant and Oh's crack band model (1983) used in literature was developed to alleviate mesh dependency. Basically, the fracture energy is expressed in terms of characteristic element length  $h$  where  $h$  is a geometrical value in [length] containing information on a characteristic element size. Generally,  $h$  is a typical length of a line across an element for a first-order element (see ABAQUS<sup>®</sup>).

$$g_f = \frac{G_f}{h} \quad (4-41)$$

The introduction of a characteristic fracture energy  $g_f$  that is correlated to the element size provides the transformation of the fracture energy  $G_f$  into a 'mesh-dependent' value. For instance, in a coarse mesh,  $h$  will be large and leads hence to a small characteristic fracture energy  $g_f$  in comparison to the large  $g_f$  of a fine mesh with a small characteristic element length  $h$ . This adjustment of the fracture energy considering the mesh size compensates for the trend of continuum softening models to dissipate as less energy as possible. Fine meshes that dissipate less energy (Figure 4-8) will have a larger value for the fracture energy than coarse meshes. This larger fracture energy produces a less steep softening curve and therefore compensates for lesser energy dissipation of fine meshes.

However, Bažant and Oh's model only works when one failure mode is dominating and when a localised solution occurs. It is valid when damage develops only in a band of elements and not in all elements homogeneously. A crack band can be identified with the following: imagine a tension beam as shown in Figure 4-9 (here with ten 3D linear brick elements with full integration, section 1 x 1 mm, 10 mm long). If this beam model has the same material properties in every element and is loaded in pure tension, no localised damage will be observed. The damage will develop in all elements simultaneously.

However, a crack band can develop if one of the elements of the tension model is weakened, for instance by choosing a slightly lower strength for a single element as shown in Figure 4-9. Then, the damage will localise in this element and will not propagate to the other neighbouring elements – the single weakened element is the weakest link in the chain (Figure 4-10). If such a type of structure is modelled, mesh dependency can be observed which will be shown after having introduced the method of viscous stabilisation.

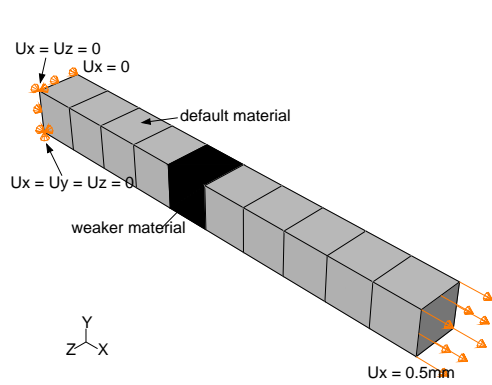


Figure 4-9: Tension beam with weaker material

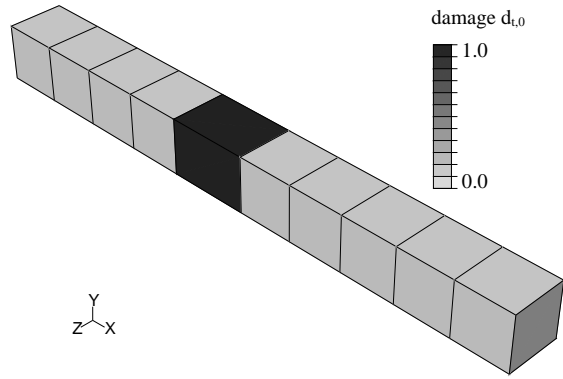


Figure 4-10: Localised damage component  $d_{t,0}$  at 0.5 mm maximum deformation

### Viscous stabilisation

Viscous stabilisation is used in order to improve the convergence characteristics of the developed material model (Duvaut and Lions, 1972, as cited in Maimí, 2006). A fictitious viscous parameter  $\eta$  is introduced in the model. The bifurcation problem as described in Figure 4-7 vanishes when introducing this parameter. Due to the additional viscous component, the stiffness matrix remains generally positive definite. Therefore, viscous stabilisation leads to a more robust solution process with less convergence problems. Indeed, other researchers (Maimí, 2006) used this method purely to stabilise the solution, but not to alleviate mesh dependency (crack band method was used instead).

As viscosity is a time-dependent material parameter, viscous stabilisation must be a function of the rate of damage. The rate of the damage variable or of the damage threshold (= failure criteria) may be used. Equation (4-42) shows the stabilisation as a function of rate of damage variables:

$$\dot{d} = \frac{(d - d_v)}{\eta} \quad (4-42)$$

In Equation (4-42), the viscous parameter  $\eta$  defines the rate at which the true damage  $d$  and the stabilised damage  $d_v$  as defined in Equation (4-43) approach each other. Equation (4-42) can now be discretised in time. Equation (4-43) shows the discretised equation based on the backward Euler algorithm to insert an artificial viscosity  $\eta$  that is acting on the damage variables (Maimí, 2006). The fictitious viscosity acts on integration point level. It can be seen that if  $\eta = 0$ , the damage variable is the same as in Equation (4-26).

$$d_v^t = \max \left\{ 0, d_v^{t-1}, \frac{\eta}{\eta + dt} d_v^{t-1} + \frac{dt}{\eta + dt} d^t \right\} \quad (4-43)$$

Similar to the crack band model, also viscous stabilisation introduces a characteristic element length. However, this length scale is not inserted explicitly as in the crack band model (characteristic element length  $h$ ), but implicitly (Needleman, 1988, Sluys, 1992). Therefore, viscous stabilisation can be also used as a regularisation method. Here, the viscous formulation only leads to stabilisation, but the effect is too small to regularise the problem.

On a simple tension beam model with different meshes (the model with ten elements is shown in Figure 4-9), a mesh dependency study is carried out. The same model of Figure 4-9 has been run also with 80 and 640 elements, see Figure 4-11 (Material parameters spruce see Table 4-1). As in Figure 4-9, a lower tension strength parallel-to-grain (23 MPa instead of 24 MPa) was assigned to one slice of elements. The large displacement theory was used. The finite elements are linear 3D brick elements with full numerical integration (eight integration points).

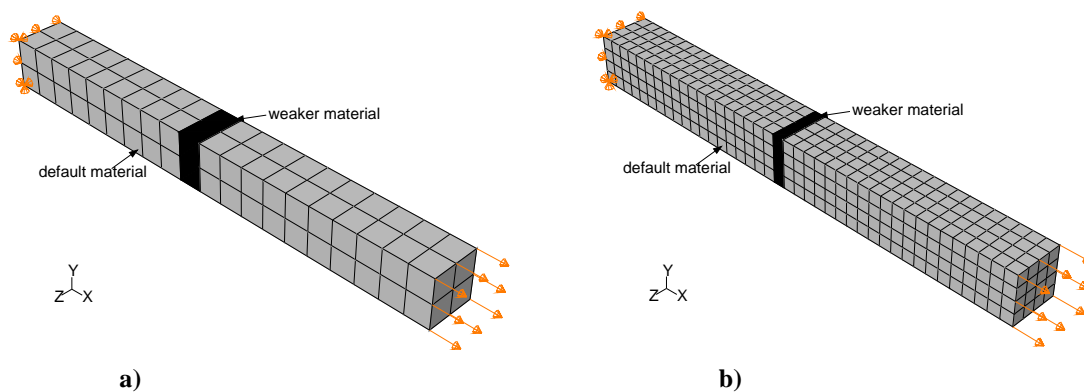
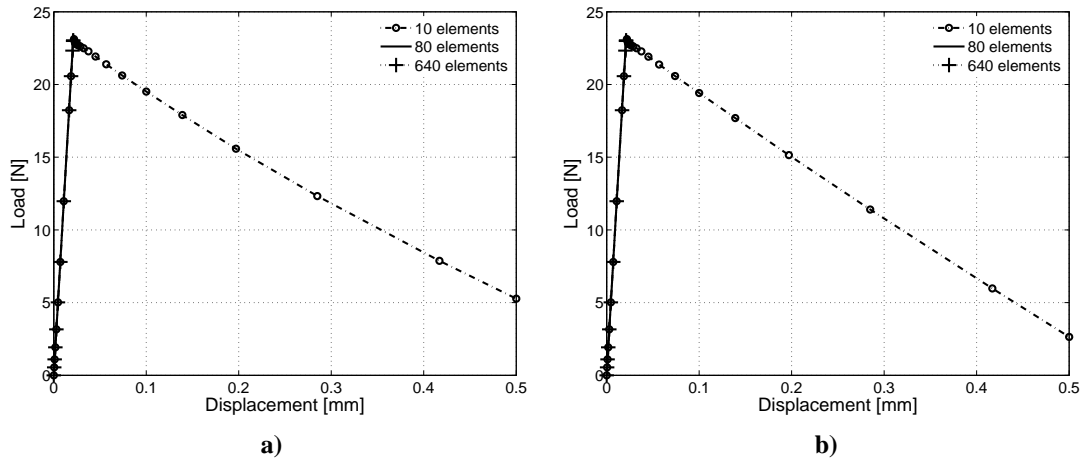


Figure 4-11: Tension beam of Figure 4-9; a) 80 elements, b) 640 elements

Figure 4-12 and Figure 4-13 show the results for the two techniques in terms of load-slip data (sum of reaction forces in X-direction versus displacement in X-direction). In Figure 4-12a, no regularisation technique was used. Due to convergence problems, the models with 80 and 640 elements did not enter the softening branch, but stopped at maximum load. The same was valid for Figure 4-12b where only the crack band method was used. However, when activating viscous stabilisation with  $\eta = 0.0001$ , the numerical calculations could finish as shown in Figure 4-13. Only viscous stabilisation was used in Figure 4-13a where a strong mesh dependency can be observed. As shown qualitatively in Figure 4-8, the coarser mesh results in more ductile behaviour. The results confirm that here, viscous stabilisation is purely stabilising the numerical algorithm. It is ineffective for alleviation of mesh dependency.

Finally, load-slip results activating both methods are given in Figure 4-13b. It can be seen that mesh dependency improves considerably although it does not vanish completely.

As a conclusion to the findings, Bažant and Oh's crack band model (1983) is used to alleviate mesh dependency whereas viscous stabilisation is always activated in order to improve convergence.



**Figure 4-12: Load-slip graph of tension beams with different mesh size, please note: the models with 80 and 640 elements did not enter the decending branch;**  
**a) no regularisation method, b) crack band model**

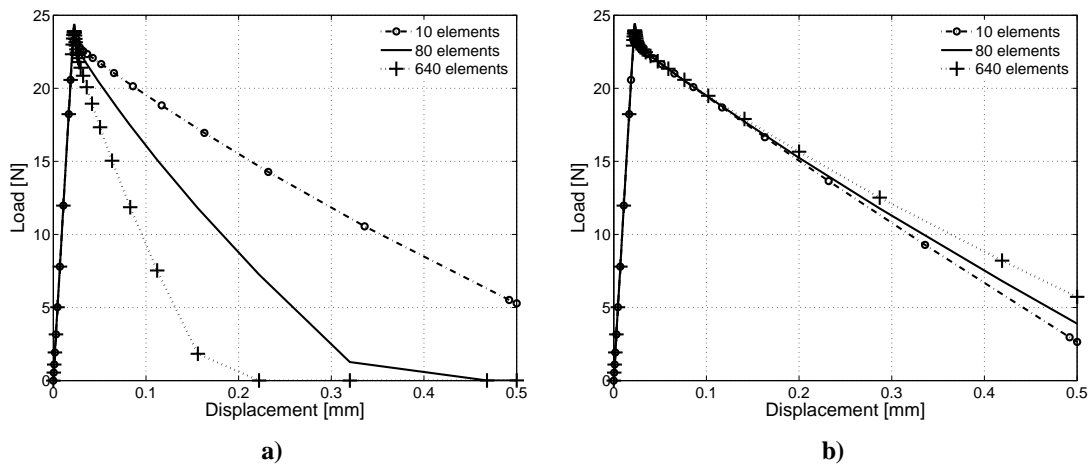


**Figure 4-13: Load-slip graph of tension beams with different mesh size;**  
**a) viscous stabilisation, b) both methods**

#### 4.4.8 Energy calculations

As viscous stabilisation is applied to improve convergence, the energy output must be checked in order to judge the model performance and reliability, i.e. to check that fictitious viscosity is not influencing modelling results. To this scope, the internal energy

parameters *ALLSE* (specific elastic strain energy) and *ALLCD* (creep dissipation<sup>11</sup>) are established. The two parameters are integrated at every increment – *ALLSE* as the total dissipated energy and *ALLCD* as the dissipated energy associated with viscous regularisation. Both parameters do not have any influence on the solution. They are merely used for energy output, checks and postprocessing.

The total dissipated strain energy *ALLSE* is calculated according to Equation (4-44). As the FE programme uses engineering strains, the equation for the shear components is different.

$$\begin{aligned} \text{For normal stress components:} \quad & \text{ALLSE}_{ij} = \frac{1}{2} (\sigma'_{ij,V} + \sigma'^{t-1}_{ij,V}) d\varepsilon_{ij} \\ \text{For shear stress components:} \quad & \text{ALLSE}_{ij} = (\sigma'_{ij,V} + \sigma'^{t-1}_{ij,V}) d\varepsilon_{ij} \end{aligned} \quad (4-44)$$

The dissipated energy due to viscous regularisation *ALLCD* should be small and is calculated according to Equation (4-45).

$$\begin{aligned} \text{For normal stress components:} \quad & \text{ALLCD}_{ij} = \frac{1}{2} (\sigma'_{ij,V} + \sigma'^{t-1}_{ij,V} - \sigma'_t - \sigma'^{t-1}_{ij}) d\varepsilon_{ij} \\ \text{For shear stress components:} \quad & \text{ALLCD}_{ij} = (\sigma'_{ij,V} + \sigma'^{t-1}_{ij,V} - \sigma'_t - \sigma'^{t-1}_{ij}) d\varepsilon_{ij} \end{aligned} \quad (4-45)$$

#### 4.4.9 Increment size dependency

Increment size dependency as illustrated in Figure 4-14 may occur when applying the described material model. The upper figure gives the displacement history of a single element model of 1 x 1 x 1 mm loaded firstly in compression and then in tension. The figures below show the modelling results for three different maximum increment sizes. Obviously, when loading in tension, a maximum increment size of 0.1 is too large leading to an overestimation of the tension strength. A maximum increment size of 0.01 instead leads to a wrong stiffness in the first part of the reloading as the chosen increment is too big. However, in the following increment, the correct stiffness is found. A maximum increment of 0.001 does not exhibit errors, but is more costly. To illustrate the time requirements between different increments: increment 0.1 needs 23 s to terminate the simulation, increment 0.01 81 s and increment 0.001 1421 s. The increment size must be chosen carefully in order to get a perfect combination of computational efficiency and accuracy.

---

<sup>11</sup> *ALLCD* is defined as ‘creep energy’ in ABAQUS®. Here, it is re-defined and is used to control the influence of viscous regularisation on the amount of dissipated strain energy. The resp. parameter ‘creep energy’ can be analysed in the postprocessing. *ALLCD* is called *SCD* in *UMAT*; *ALLSE* is called *SSE* in *UMAT*.

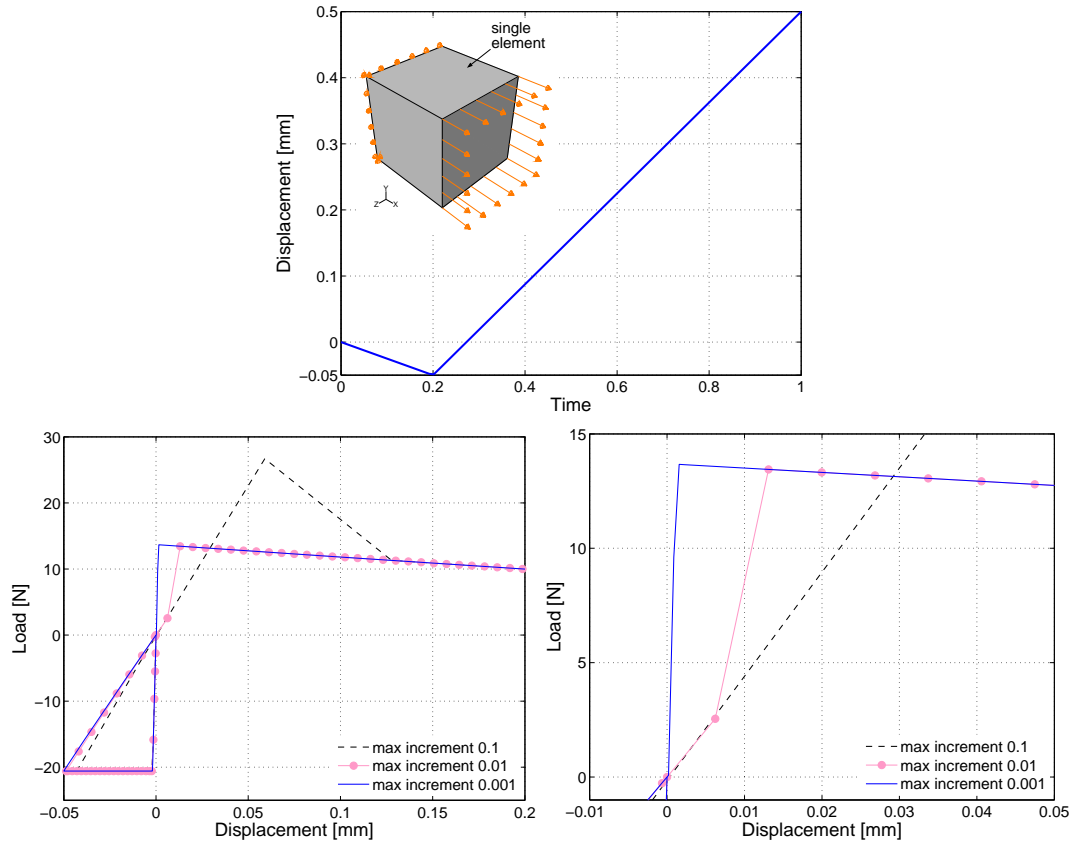


Figure 4-14: Increment size dependency, calculation with  $f_{c,0} = 21\text{MPa}$ ,  $f_{t,0} = 14\text{MPa}$

#### 4.4.10 Tangential formulation

Generally, the Jacobian  $J$  as defined in Equation (4-46) is used as tangential formulation. The Jacobian is easily implementable in strain-based formulations but not as straightforward in stress-based formulations (last partial differentiation is on strains).

$$\mathbf{J} = \mathbf{D} : \dot{\boldsymbol{\varepsilon}} = \mathbf{D} + \frac{d\mathbf{D}}{d\boldsymbol{\varepsilon}} = \mathbf{D} + \frac{\partial \mathbf{D}}{\partial \mathbf{d}} \frac{\partial \mathbf{d}}{\partial \boldsymbol{\kappa}} \frac{\partial \boldsymbol{\kappa}}{\partial \boldsymbol{\varepsilon}} \quad (4-46)$$

Here however, the secant stiffness is considered to assemble the global stiffness matrix:

$$\mathbf{J} = \mathbf{D}^{dam} = \text{inv}(\mathbf{C}_{ijkl}^{dam}) \quad (4-47)$$

This leads to a slower convergence rate.

## 4.5 MATERIAL PARAMETERS

As discussed in chapter 2, it is difficult to obtain useable mechanical properties to completely describe the 3D material model for wood – in total 17 properties are needed as can be seen in Table 4-1. Before focusing on the issues concerning availability of material parameters, other conclusions from chapter 2 concerning computational implementation and significance are discussed. This is considered to be important in order to understand the difference between phenomenological test results and mathematical models.

### Stiffness and strength

Stiffness and strength properties seem to be the most straightforward and easily established material parameters that are needed for constitutive modelling. However, it is, certainly for shear strength, difficult to carry out pure uniaxial tests without secondary stress components. Stress interactions may occur which are even more difficult to assess. At this stage of the material model, an increase of shear strength with increasing compression perpendicular-to-grain is not considered by the material model. Especially for wood in compression, it is difficult to establish a ‘yield’ strength as the stress-strain curve is already nonlinear at an early stage. Therefore, the proportional limit is difficult to determine. Furthermore, the question remains whether the strength properties have been assessed on small clear wood specimens or on large scale specimens taking a size-effect into account. As for mathematical efficiency, a typical problem for wood is that the parallel, perpendicular and shear strength values are different from each other.

### Poisson’s ratios

In literature, there is a rather high scatter of Poisson’s ratios and they are usually measured on small clear specimens. The evolution of the Poisson’s ratios in the nonlinear regime is unknown (see section 2.4). Any further discussion of the Poisson’s ratios is excluded as the values for the Poisson’s ratios are fictitious (see section 4.4.3).

### Fracture energy

Fracture energy is needed to create new crack surfaces and is difficult to determine. A prerequisite is stable crack growth in tests. If fracture energy is established as the area underneath a stress-strain curve, then it is a volume-related parameter instead of a surface-related parameter. Most tests that establish fracture energy are tests on small clear wood, influences from heterogeneity of the material are thus not considered. Furthermore, fracture energy is generally assumed to be constant whereas a valid hypothesis for heterogeneous materials would be a non-constant fracture energy. In areas with knots for instance, the energy needed to create new fracture planes will certainly be different to areas with no knots. Furthermore, the fracture energy will be different for different modes.

As stated above, material parameters are difficult to obtain and are subject to large scatter. For softwood, extensive literature exists (e.g. thorough discussions for spruce in Franke, 2008, and Grosse, 2005). In fact, only for softwood, all 17 parameters can be determined, for instance based on information given in Franke (2008). It is considerably more difficult to obtain necessary mechanical properties for European and tropical hardwoods. Especially rolling shear properties and fracture energies are not available in literature. However, many more data for all wood species are available from four-point bending tests used for strength-grading and from embedment tests.

In view of these problems, the approach by Dias et al. (2010) discussed in section 3.6 to transfer test data into material input parameters for numerical models is recalled here. Dias et al. used the Hill criterion. They derived an equation to determine the equivalent stress  $\sigma_0$  as a function of the embedment strength and could hence derive all necessary post-elastic material parameters from one single value, the embedment strength, of which a large database is available.

Similar investigations into the transfer of test results on structural timber into useable material properties for mathematical modelling hence seem to be necessary to obtain reliable material parameters. However, fracture energies needed to model softening will not be obtained with such a procedure.

The arising question is if the developed material model is already too sophisticated considering the difficulties connected with the derivation of the necessary 17 material parameters. In the author's opinion this is not the case. Wood shows huge differences in strength parameters, i.e. parallel and perpendicular to the grain, longitudinal and rolling shear. Furthermore, wood is ductile in compression and quasi-brittle in tension and shear. In order to model softening, a parameter quantifying the softening rate is needed. Therefore, the chosen 17 parameters of the orthogonal material model are the minimum number of parameters in order to describe the main features of wood. The 17 parameters are also well-defined mechanical parameters and no smeared values whose origins are not clear.

Generally, standards as EN 338 (CEN, 2009) are sources for characteristic properties of stiffness and strength of structural-size timber. Information on rolling shear properties and fracture energies are not given in EN 338. A possibility is to derive mean properties from the characteristic properties given in EN 338 according to Equation (4-48) assuming a Gaussian normal distribution:

$$\mu(f_k) = e^{\left[\ln(f_k) + 0.54\right]} \quad (4-48)$$

where  $\mu$  = mean value;  $f_k$  = characteristic value

The used species in this research were spruce, beech and azobé. The mean densities of the test specimens were  $\rho_{mean} = 445 \text{ kg/m}^3$  for spruce,  $\rho_{mean} = 715 \text{ kg/m}^3$  for beech and  $\rho_{mean} = 1120 \text{ kg/m}^3$  for azobé (see chapter 7). These densities result in strength classes

C24, D40 and D70 according to EN 338. Hence these three strength classes were chosen to derive the material properties.

Analogies were applied to derive the missing parameters rolling shear and fracture energy:

#### Rolling shear modulus and strength

Information on rolling shear modulus and strength is needed for instance for certain wood products as cross-laminated timber. In technical approvals of these products, values are given for rolling shear modulus (mean value) and strength (characteristic value). All approvals give the same values,  $G_{roll} = 50$  MPa and  $f_{roll} = 0.5$  MPa. These values are used for spruce.

The ratio of longitudinal shear values over rolling shear values is calculated for spruce and subsequently kept constant for beech and azobé. (example:  $G_v/G_{roll}(\text{spruce}) = 690/50 = 13.8$ .  $G_{roll}(\text{beech}) = G_v(\text{beech})/13.8 = 810/13.8 = 59$  MPa) Interesting to note is that for spruce, the ratio of longitudinal shear modulus over rolling shear modulus and the ratio of longitudinal shear strength over rolling shear strength have the same value.

#### Fracture energies

Some simplified assumptions were made. As initial parameters for spruce, the values given by Franke (2008, Table C-2) were used. As it was observed that his high fracture energy for tension parallel-to-grain of  $G_{f,0} = 60$  N/mm in combination with the low fracture energy for tension perpendicular-to-grain of  $G_{f,90} = 0.18$  N/mm could cause instabilities, these two values were adjusted to the values shown in Table 4-1.

For beech and azobé, the resulting ratios for spruce of fracture energy and respective strength were kept constant. (example:  $f_{t,0}/G_{f,0}(\text{spruce}) = 24/6 = 4$ .  $G_{f,0}(\text{beech}) = 41/4 = 10$ )

The reference species was spruce because most information is available for this wood species. The ratios of certain material properties such as rolling shear values and fracture energies were extrapolated to hardwood – this is an analogous approach to EN 384 (CEN, 2004a) where all mechanical properties are defined as ratios of easily available values as density, MoE parallel-to-grain and bending strength. EN 384 however is valid for softwood. Here, it is assumed that at the current state-of-the-art an analogous approach can be applied to hardwoods. Hardwoods are with their vessels, different vessel distributions and fibre lengths much less homogeneous than softwoods. Of course this leads to rough engineering estimations of material properties, but seems to be one of the few available approaches in order to obtain all needed mechanical properties. It cannot be expected that all properties, especially valid shear properties and fracture energies, will be established by tests in near future for all used wood species. Other ways to solve the problem of non-available mechanical properties must be found. Further research must also assess the influence of for instance the different anatomies on important issues such as ductility.

The chosen approach is consistent. However, it must be clear that the chosen material properties are derived from characteristic values where only the longitudinal MoE and the bending strength are properties derived from tests. The necessary values for the material model such as the transverse tension strength are only proportional values with a specific relation to the bending strength. For instance, Van de Kuilen and Blaß (2005) found an experimental mean shear strength value for azobé (*Lophira alata*) of 17.7 MPa which is much higher than the value of 8.6 MPa given in Table 4-1. Also the tension strength perpendicular-to-grain is rather low. For instance, Blaß and Schmid (2001) give a mean transverse tension strength derived from tests for spruce of 1.89 MPa which is nearly three times the value given in Table 4-1.

Table 4-1 summarises the material properties used for modelling. The value of fictitious viscosity is chosen to be  $\eta = 0.0001$ . A conclusion to the discussion in this chapter is to carry out a well-defined parameter study changing the material properties given in Table 4-1.

**Table 4-1: Material input values for all 3 wood species**

Parameter	Units	Spruce ( <i>Picea abies</i> )	Beech ( <i>Fagus sylvatica</i> )	Azobé ( <i>Lophira alata</i> )	Source
$E_{11}$		11000	13000	20000	
$E_{22} = E_{33}$		370	860	1330	EN 338
$G_{12} = G_{13}$		690	810	1250	
$G_{23}$		50	59	91	analogies, see above
$f_{t,0}$	MPa	24 (14)	41 (24)	72 (42)	Equation (4-46); $f_k$ from EN 338 ( $f_k$ in parenthesis)
$f_{c,0}$		36 (21)	45 (26)	58 (34)	
$f_{t,90}$		0.7 (0.4)	1.0 (0.6)	1.0 (0.6)	
$f_{c,90}$		4.3 (2.5)	14.2 (8.3)	23.2 (13.5)	
$f_v$		6.9 (4.0)	6.9 (4.0)	8.6 (5.0)	
$f_{roll}$		0.5	0.5	0.6	analogies, see above
$G_{f,0}$	N/mm	6	10	18	analogies, see above
$G_{f,90}$		0.5	0.71	0.71	
$G_{f,v}$		1.2	1.2	1.5	
$G_{f,roll}$		0.6	0.6	0.7	
$\eta$	-	0.0001	0.0001	0.0001	estimation

## 4.6 SUBROUTINE UMAT

### 4.6.1 Programming issues

For all modelling tasks, the finite element package ABAQUS<sup>®</sup> was used. Within ABAQUS<sup>®</sup>, it is possible to programme so-called user subroutines. For this thesis, a material user subroutine (called UMAT in ABAQUS<sup>®</sup>) was developed. The UMAT was programmed in FORTRAN. During the programming process, some main programming issues were identified which are mentioned here to support the future programmer. The UMAT is given in Sandhaas (2011).

- Use the PARAMETER function to define constants (such as 0.5, 1 or 2);
- Always define variables as REAL or INTEGER;
- Most of the non-identified bugs derive from wrong equations such as impossible division through ZERO, non-defined variables and mismatches in the arguments. Other bugs and compiling/linking problems are usually described in the log file of ABAQUS<sup>®</sup>;
- Use the write command to write intermediate steps to the log file such as certain stress or strain components or internal variables as this facilitates the verification of the UMAT.

### 4.6.2 Verification of UMAT

Every developed material model must be checked thoroughly before applying it on complex models such as joint models. The verifications are carried out on fictitious models where the model response can be checked easily. Verifications comprise different steps. The variable settings are for instance different loading cases in tension, compression, monotonic or cyclic loading, multiaxial loading and changing material orientations where not the elements are rotated but the material orientation within the elements.

Furthermore, the verifications shown in this section illustrate the available tools to investigate the numerical results. Manifold methods from load-slip graphs over integration point results and contour plots exist to check numerical outputs.

Figure 4-15 shows a cubic model with 3D linear brick elements (1 x 1 x 1 mm) with full integration, thus with eight integration points and linear interpolation between integration points. The boundary conditions are also shown in Figure 4-15. If verification results are given in terms of load-slip, then the indicated nodal results were used. The mesh varied between one, eight and 125 elements without changing the geometry or boundary conditions. All used material properties including the viscous parameter  $\eta$  are given in Table 4-1. For the verifications, only the properties for spruce are considered.

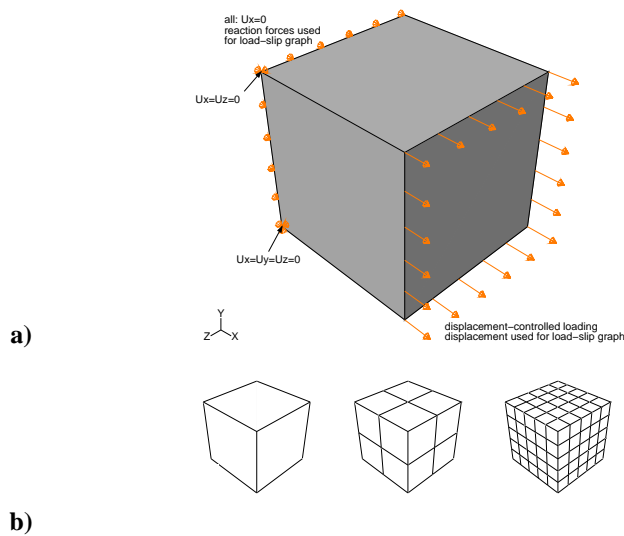


**Figure 4-15: a) 1 x 1 x 1 mm model, 3D linear brick elements with full integration;  
b) different meshes of model – one element, eight elements, 125 elements**

### Monotonic and cyclic loading

First verifications were carried out simulating loading parallel and perpendicular to the grain under monotonic (tension and compression) and cyclic loading. The crack band model was not activated as no localisation was expected. The monotonic loading was an increasing deformation up to 0.5 mm whereas the cyclic loading was tension up to 0.02 mm (to trigger nonlinearity) with subsequent compression up to 0.5 mm. Figure 4-16 to Figure 4-19 show the load-slip graphs. The simulation results are correct:

- Both tension parallel and perpendicular to the grain are calculated correctly ( $f_{t,0} = 24 \text{ MPa}$ ,  $f_{t,90} = 0.7 \text{ MPa}$ )
- Compression parallel and perpendicular to the grain is perfectly plastic at the resp. maximum strength values ( $f_{c,0} = 36 \text{ MPa}$ ,  $f_{c,90} = 4.3 \text{ MPa}$ ).
- The two cyclic loadings also properly simulate the implemented material behaviour. After initiation of damage in tension, unloading is along the secant stiffness and the original MoE is taken when entering the compression region.

It is interesting to note that the maximum increment size of the models with monotonic loading was 1 whereas the maximum increment size of the models with cyclic loading was 0.01. This has to do with the increment size dependency as discussed in section 4.4.9.

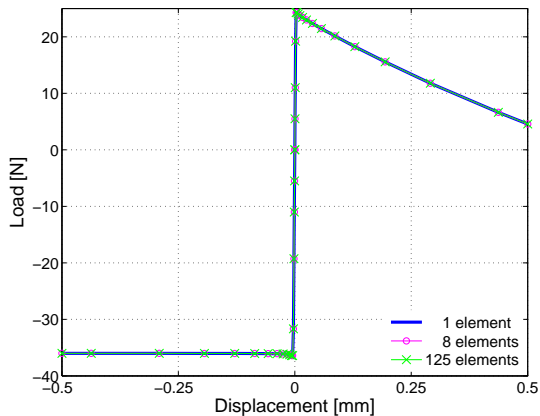


Figure 4-16: Monotonic loading parallel-to-grain, tension and compression

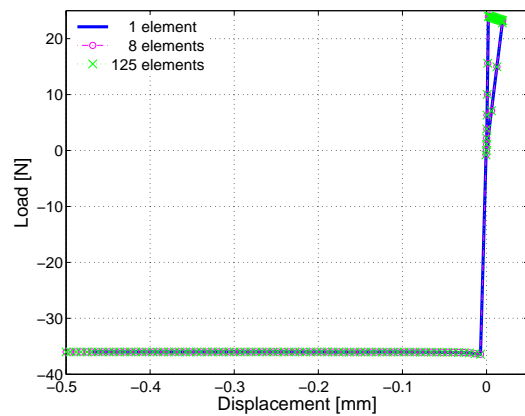


Figure 4-17: Cyclic loading parallel-to-grain

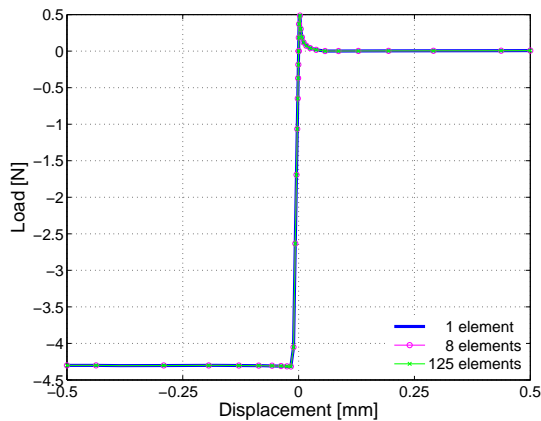


Figure 4-18: Monotonic loading perpendicular-to-grain (radial direction), tension and compression

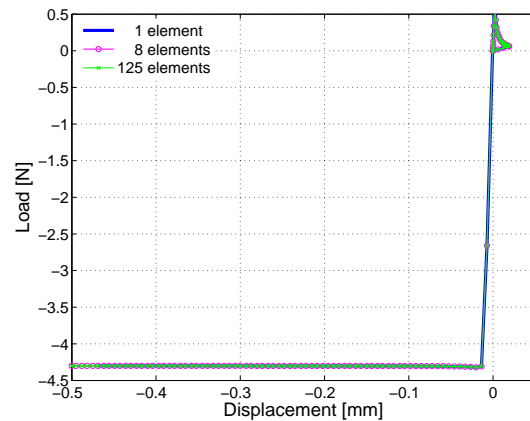


Figure 4-19: Cyclic loading perpendicular-to-grain (radial direction)

An important note on these first verifications is on the mesh dependency and the crack band method which was discussed in section 4.4.7. As already stated, the crack band model was not activated. Considering the model shown in Figure 4-15, it becomes clear that damage can be expected to develop in all elements simultaneously as the same material properties are assigned to all elements. This means, no crack band or localised solution is expected. Then the crack band method is not valid as discussed in section 4.4.7. Therefore, the fracture energy  $G_f$  was used in the damage formulations of Equation (4-35) instead of the characteristic damage energy  $g_f$ , see Equation (4-41).

The verifications shown in Figure 4-16 were repeated using the characteristic fracture energy  $g_f$  (Equation (4-41)), activating the crack band method. Then, an artificial mesh dependency is created. In Figure 4-20, the results can be seen. An opposite mesh dependency can be observed where the inclination of the single element model is approximately five times the inclination of the model with five elements in a row. The more elements (i.e. smaller elements) are used, the more ductile the system is. This is due

to the definition of  $g_f$ . The smaller the elements, the smaller is  $h$  and therefore, the more fracture energy remains available which leads to a more ductile answer.

The conclusion of section 4.4.7 is confirmed. The crack band method should not be used in models where no local crack band can develop and the response is homogeneous. Therefore, continuum FE models that show material softening (related to the integration points) must be examined with regards to localised deformation bands in order to decide if the crack band method can be used to alleviate mesh dependency. Otherwise the crack band method cannot be used.

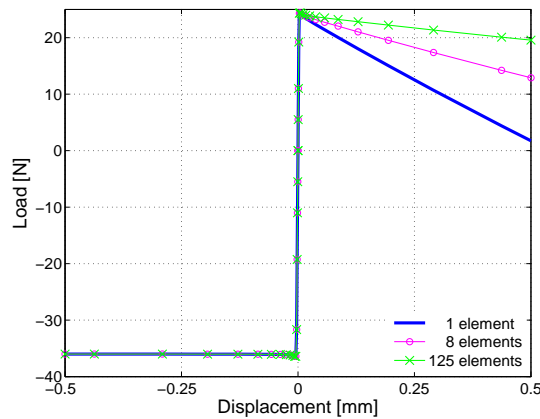


**Figure 4-20: Monotonic loading parallel-to-grain with characteristic fracture energy  $g_f$ , tension and compression with opposite mesh dependency**

#### Different perpendicular failure criteria

The next verifications show the influence of different failure criteria continuing the discussion of section 4.3. The influence of three different formulations for the case of transverse compression with an angle to the grain of  $\alpha = 20^\circ$  is investigated. This loading scheme means that in the model, transverse compression and shear evolves.

- Figure 4-21: Failure criteria as implemented (Equations (4-8) and (4-9) resp. (4-11) and (4-12)), with maximum stress criteria for transverse compression and quadratic interaction between longitudinal and rolling shear.
- Figure 4-22: Smearred failure criteria of transverse compression and shear analogous to the transverse tension criteria according to Equation (4-49):

$$\sigma_{22/33} < 0: \quad F_{c,90R/T}(\sigma) = \frac{-\sigma_{22/33}}{f_{c,90}} + \frac{\sigma_{12/13}^2}{f_v^2} + \frac{\sigma_{23}^2}{f_{roll}^2} \leq 1 \quad (4-49)$$

- Figure 4-23: Maximum stress criterion for transverse compression (= Equations (4-8) and (4-11)), no consideration of shear in loading case transverse compression ( $\sigma_{22/33} < 0$ ).

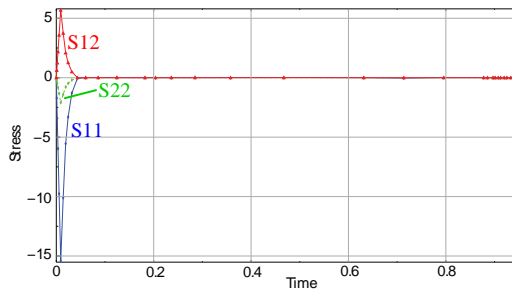


Figure 4-21: Failure criteria as implemented

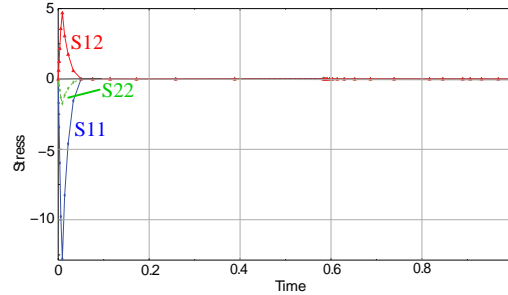


Figure 4-22: Failure criteria according to Equation (4-49)

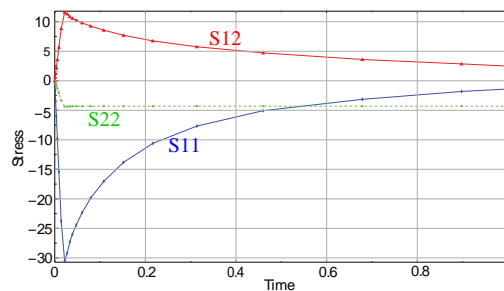


Figure 4-23: Failure criteria with no transverse compression – shear interaction

Two main points can be observed:

- Figure 4-21 and Figure 4-22 do not differ much and show correct stress distributions with the transverse compression  $\sigma_{22}$  developing analogously to the shear stress  $\sigma_{12}$ . However, Figure 4-22 with the smeared failure criterion indicates lower shear stresses which is logic considering the assumed interaction between transverse compression and shear. Subsequently, the global load-slip behaviour should show lower forces;
- Figure 4-23 shows a shear stress  $\sigma_{12}$  that exceeds the shear strength which is not realistic. The failure surface is defined by the transverse compression strength. Only when  $f_{c,90}$  is reached, failure occurs and the model starts to soften due to brittle longitudinal shear.

Figure 4-24 shows the results in terms of load-slip data of the three models. The results for the smeared failure criterion, Equation (4-49), are lower than for the criteria as is. The results for the simulation with no failure criterion for shear loading under simultaneous transverse compression loading are wrong as can be expected after Figure 4-23.

However, the smeared failure criterion defined in Equation (4-49) gives wrong results for loading with compression under an angle to the grain. Then, the combined effect of ductile compression stresses and brittle shear stresses lead to mixed failures between ductile and brittle which cannot be modelled with Equation (4-49). Using Equation (4-49),

these mixed failures cannot be modelled and apart from pure compression parallel and perpendicular to the grain, the material behaviour will be brittle (see also Figure 4-27).

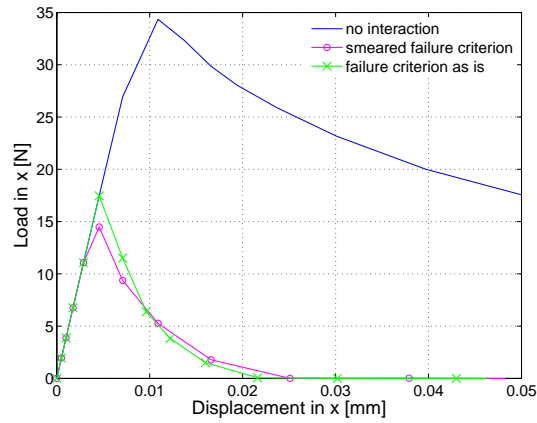


Figure 4-24: Load-slip results with three different failure modes,  $\alpha = 20^\circ$

#### Different element types

To investigate the influence of different element types, the bricks from Figure 4-15 have been replaced by tetrahedrons as shown in Figure 4-25. The boundary conditions have not been changed and the loading scheme is cyclic loading. As can be seen in Figure 4-26, the results are the same as for the model with brick elements (Figure 4-19).

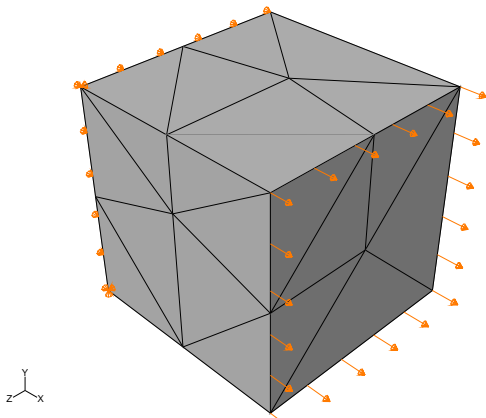


Figure 4-25: Cube model with tetrahedrons

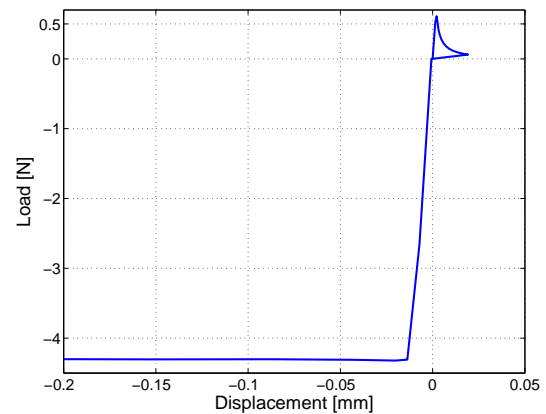
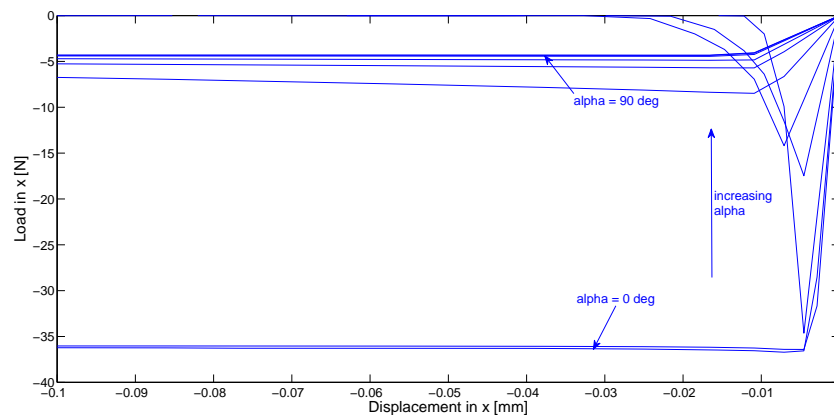


Figure 4-26: Load-slip graph under cyclic loading perpendicular-to-grain of model with tetrahedrons

### Different material orientations

The following verification involved varying material orientations and was carried out on the single element model of Figure 4-15. Radial stress  $\sigma_{22}$  and longitudinal shear  $\sigma_{12}$  were gradually activated with increasing rotation angle  $\alpha$  of the material orientation (with  $\alpha = 0^\circ = \text{parallel-to-grain}$ ,  $\alpha = 90^\circ = \text{perpendicular-to-grain}$ ). The results in terms of load-slip are shown in Figure 4-27. The calculation results are correct, namely

- With  $\alpha = 0^\circ$  resp.  $\alpha = 90^\circ$ , the results are perfectly plastic obtaining the uniaxial strengths;
- With small rotation angles  $\alpha$  ( $20^\circ < \alpha < 45^\circ$ ), the results are brittle as the brittle behaviour of shear is dominating;
- The more the rotation angle  $\alpha$  is increasing, the more ductile the behaviour becomes (which is not the case if the smeared failure criterion shown in Equation (4-49) is used. Then the behaviour is brittle except for pure parallel or perpendicular stress. This is due to the effect of the brittle shear which develops simultaneously to the transverse compression in a smeared approach);
- With large rotation angles  $\alpha$  ( $\alpha > 60^\circ$ ), the results are close to the results with compression loading perpendicular-to-grain.



**Figure 4-27: Different material orientations ( $\alpha = 5, 10, 20, 30, 45, 60, 70, 80, 85$  degrees) with monotonic compression load**

A classical check when having different angles  $\alpha$  to the grain is the comparison of the modelling results with the Hankinson equation<sup>12</sup> (Hankinson, 1921). This comparison is visualised in Figure 4-28. The prediction quality is good. Major differences are observed

<sup>12</sup> Hankinson equation: 
$$f_{c,\alpha} = \frac{f_{c,0} \cdot f_{c,90}}{f_{c,0} \sin^2 \alpha + f_{c,90} \cos^2 \alpha}$$

for material orientations of 5 to 30 degrees. Especially the inflexion point between angles 20° and 30° is remarkable. However, the maximum error is only 15% for an angle of 10°.

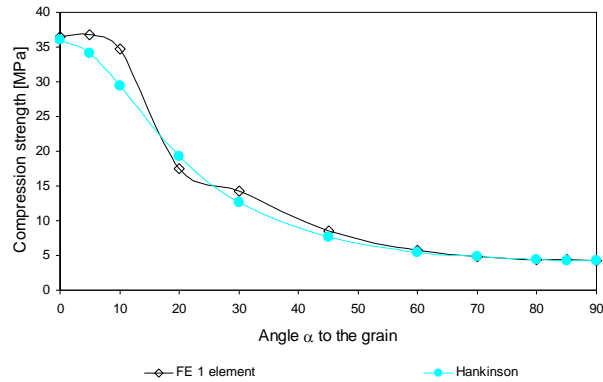


Figure 4-28: Superposition of FE results and Hankinson equation

### Different fracture energies

The influence of the fracture energies is investigated on the single-element model. Three different values for the fracture energy  $G_{f,0}$  were chosen and the loading was tension parallel-to-grain.

Figure 4-29 shows the results in terms of load-slip for the chosen fracture energies  $G_{f,0} = 6, 0.6$  and  $60$  N/mm. The softening branch changes correctly depending on the chosen value for the fracture energy. The general trend is correct: the smaller the fracture energy, the more brittle the behaviour<sup>13</sup>.

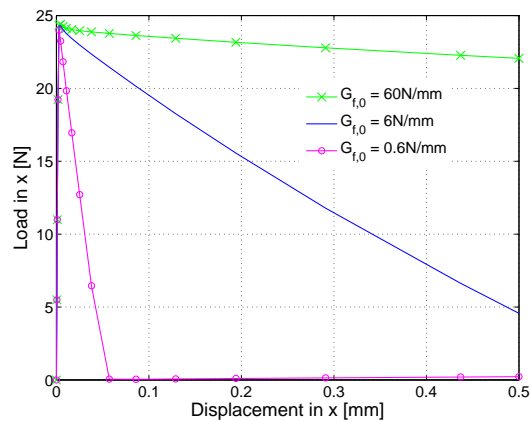


Figure 4-29: Load-slip graphs for three different fracture energies  $G_{f,0}$

<sup>13</sup> A nice check can be done for  $G_{f,0} = 0.6$  N/mm: The integral of the load-slip curve is  $\frac{1}{2} \cdot 0.05 \text{ mm} \cdot 24 \text{ MPa} = 0.6 \text{ N/mm}$ . This is exactly the amount of fracture energy  $G_{f,0}$ .

### Compression loading and subsequent shear loading

The model from Figure 4-15 with 125 elements was loaded in compression perpendicular-to-grain (up to 0.015 mm in order to trigger damage) with subsequent loading in shear (up to 0.1 mm). The boundary conditions were changed for the case of shear loading: then the cube was simply clamped.

Figure 4-30 and Figure 4-31 show typical integration point results in the time domain where the time step 1.0 indicates the transition from compression loading to shear loading. The development of the damage variables is correct. First, the damage variable  $d_{c,90}$  for compression perpendicular-to-grain develops.  $d_{c,90}$  is constant when the damage variable  $d_{vR}$  (together with  $d_{t,90R}$  and  $d_{roll}$ ) develops under shear loading. The corresponding stress components are shown in Figure 4-31 and are also correct. The 1 x 1 mm cube starts to accumulate damage at 4.3 MPa which is the transverse compression strength and reaches its tension peak at less than 0.7 MPa, the transverse tension strength (it must be less as also shear components are present).

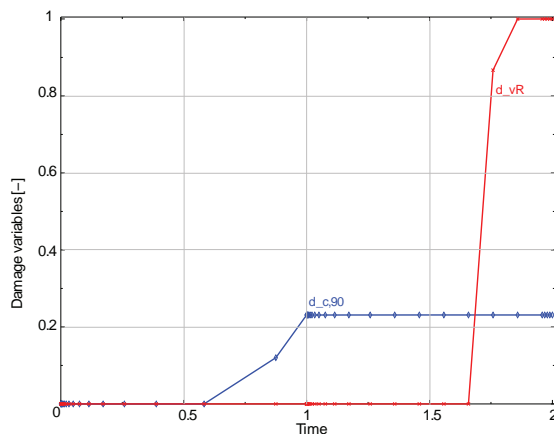


Figure 4-30: Damage variables  $d_{c,90}$  and  $d_{vR}$

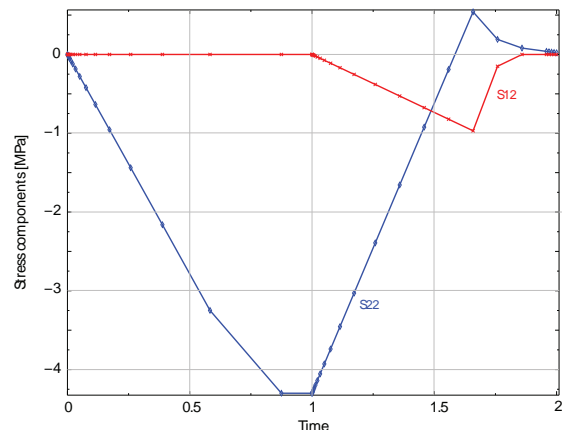


Figure 4-31: Stress components  $\sigma_{22}$  and  $\sigma_{12}$

### Tapered beam

The last verifications included a tapered beam model as shown in Figure 4-32 where the boundary conditions and the mesh can be seen. In this model, a crack band develops and therefore, the crack band method must be activated. The loading scheme was monotonic tension loading. The tapered area in the centre of the model is shaded and consists of two elements.

The results at the integration points of the two elements in the tapered area are shown in Figure 4-33 to Figure 4-37. The maximum tension stress parallel-to-grain  $\sigma_{11}$  shown in Figure 4-33 is 24 MPa with subsequent softening (see also the damage variable in tension parallel-to-grain of Figure 4-34) which is correct. The modulus of elasticity  $E_{11}$  is decreasing correctly as shown in Figure 4-35 while the strain components  $\varepsilon_{11}$  are increasing monotonously as shown in Figure 4-36. The plot of the energies of Figure 4-37

show that the energy of the viscous stabilisation (ALLCD) is very small compared with the total strain energy (ALLSE) which indicates that the calculation results are not influenced by the fictitious viscosity of  $\eta = 0.0001$ . The peak of ALLCD when damage initiates indicates the need of fictitious viscosity in order to facilitate convergence.

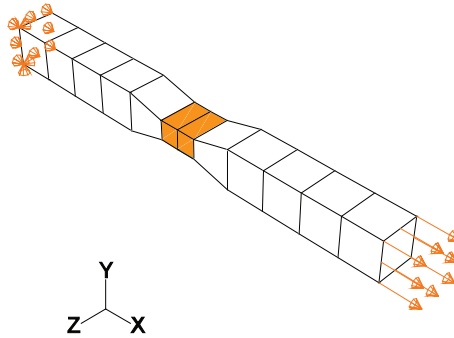


**Figure 4-32: Mesh and boundary conditions (analogous to cube model from Figure 4-15), monotonic tension load parallel-to-grain, shaded area in the centre is tapered**

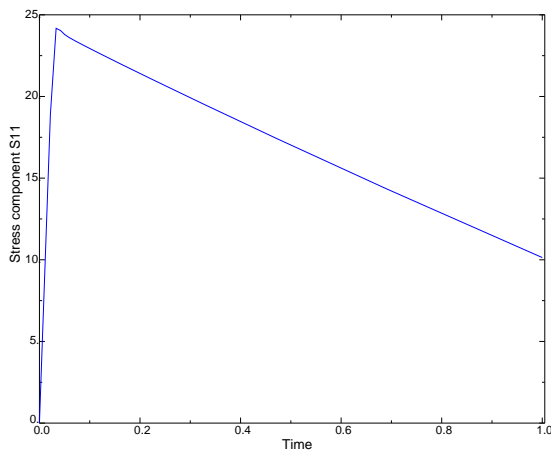


**Figure 4-33: Normal stress component  $\sigma_{11}$  [MPa]**

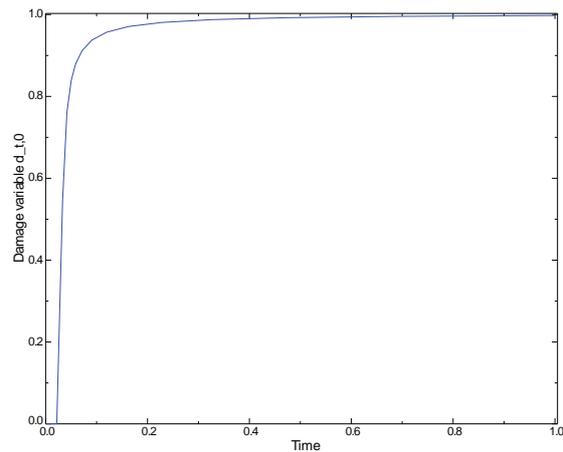


**Figure 4-34: Damage variable  $d_{t,0}$  [-]**

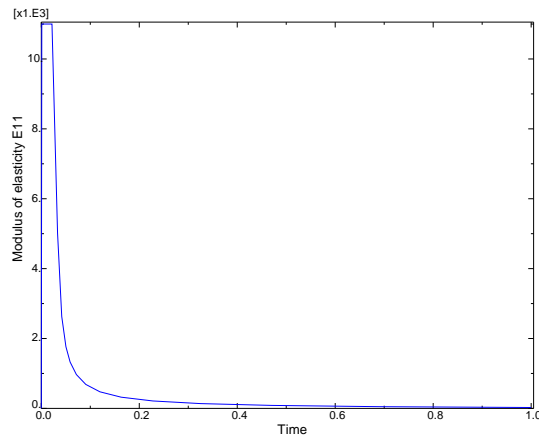
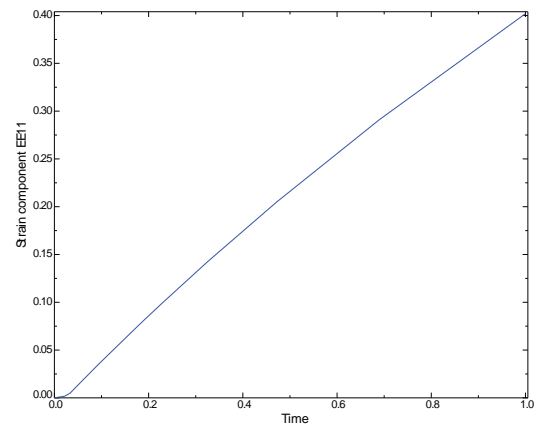
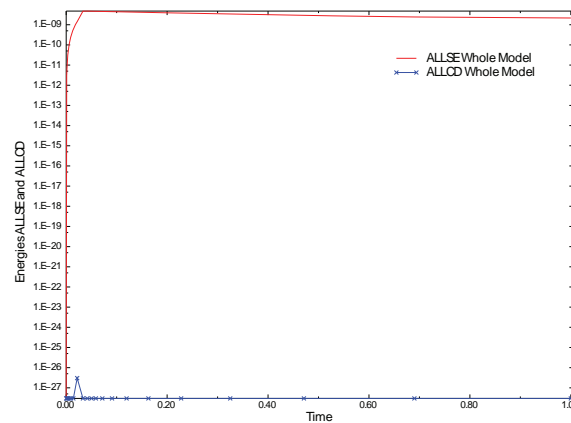
Figure 4-35: Modulus of elasticity  $E_{II}$  [MPa]Figure 4-36: Elastic strains  $\epsilon_{II}$  [ - ]

Figure 4-37: Elastic strain energy ALLSE and viscous regularisation energy ALLCD (logarithmic scale)

## 4.7 CONCLUSIONS

A material model for wood was developed that can be combined with commercially available FE software packages. The model proved to be promising for timber modelling as in comparison to many available FE tools, ductile and brittle behaviour can be simulated within a holistic 3D orthotropic model. The failure ellipsoid is piecewise defined in the 6D stress space which makes it possible to model strongly orthotropic material with large strength differences in the single material directions. Interactions of stresses are considered for the failure modes ‘splitting perpendicular-to-grain’. However, no hardening of the shear strength under increasing transverse compression is considered. The failure modes can be identified as every single damage parameter can be visualised. No plastic deformations can be modelled as CDM is nonlinear elastic and unloading follows the secant stiffness.

The necessary material properties are immediate stiffness, strength and fracture properties. If the input values must be changed for calibration purposes, physically possible ‘new’ values for stiffness and strength can be chosen without the need to introduce artificial parameters. For instance, fracture energies can be adapted to calibrate the strength loss at increasing strains.

As to mesh dependency, it could be shown that regularised results can be obtained by using the crack band method if models show localised solutions (see models in section 5.2.1). But the crack band model should not be used in cases where the deformation is not localised in a small domain of a structure (see models in section 5.3 and 5.4). Viscous stabilisation has no influence on mesh regularisation, but it improves convergence considerably. Furthermore, the increment size must be chosen small enough in order to avoid wrong results even if the used FE software uses adaptive incrementing.

# 5

## STRUCTURAL MODELS

*The developed material model presented in chapter 4 is applied to predict the mechanical performance of wood and of timber joints. Material tests taken from literature are simulated. Embedment tests and double-shear timber joints with slotted-in steel plates and one, three and five dowels in a row are modelled. Three different wood species, spruce, beech and azobé, are considered. Major results as load-slip graphs, stress distributions and influence of dowel number and wood species are discussed. Modelling-related issues such as mesh dependency are assessed.*

### 5.1 INTRODUCTION

The material model developed in chapter 4 proposed a unified approach in order to cover ductile and brittle modes within an implicit continuum mechanics framework. The developed material model was implemented in the FE software ABAQUS® via a subroutine called UMAT. In this chapter, the outcomes for a variety of models (from pure material models over embedment models to joint models) are presented.

Firstly, pure material tests using spruce taken from literature were modelled in order to verify the applicability of the developed material model. Compression tests under different angles to the grain and tension tests parallel-to-grain were simulated. Material models without steel parts and contact are easier to interpret and therefore, issues related to the material model can be more thoroughly evaluated on these ‘simple’ examples.

Afterwards, embedment models are simulated which are less complex models than joint models as dowel-bending and other contact than steel dowel - timber does not occur. A certain calibration of predictive joint models (i.e. calibration of the material parameters such as stiffness or strength values) will be always required. This calibration is usually carried out comparing FE models with test results. The most complex suitable test results on which material parameters for joint models can be calibrated are in fact embedment tests. Therefore, the second part of this chapter contains embedment modelling results using 12 mm and 24 mm steel dowels and different wood species.

In the third part of this chapter, timber joint models are presented. All joints were double-shear timber joints with slotted-in steel plates. The used 12 mm and 24 mm dowels were high strength steel (hss) dowels and very high strength steel (vhss) dowels. The used wood species were spruce (*Picea abies*), beech (*Fagus sylvatica*) and azobé (*Lophira alata*). The number of steel dowels in a row was one, three and five.

Contrarily to the material test results, the embedment and joint test results were not taken from literature, but from own experiments which will be presented in chapters 6 and 7. In chapter 8 finally, the experimental results on embedment specimens and joints will be compared with the FE prediction results.

## 5.2 MATERIAL MODELS

In order to verify the capability of the models to predict the mechanical behaviour of wood, available material tests from literature were modelled. The chosen tests were undertaken by Franke (2008) and comprise tension tests parallel-to-grain and compression tests with different angles to the grain. All tests were carried out on small clear spruce specimens. However, the material parameters for spruce used in the FE models were derived for structural-size wood and are given in Table 4-1. Steel was modelled as being linear elastic with a MoE of 210000 MPa and a Poisson's coefficient of 0.3. The used 3D solid elements were linear bricks with full integration.

### 5.2.1 Tension parallel-to-grain

The FE model loaded in tension parallel-to-grain was modelled after Franke's test specimens (Franke, 2008). Due to the asymmetric specimen, it is rather difficult to assign boundary conditions that do not trigger secondary stresses. If the specimen is loaded parallel-to-grain and secondary stresses develop due to restraints, these secondary stresses in the much weaker perpendicular directions can cause damage and material degradation before reaching the tension strength parallel-to-grain. The locally overstrained elements collapse completely when they are fully damaged. Collapsed elements lead to large element distortions, so-called spurious energy modes. Locally, convergence can be impeded or even impossible.

Spurious energy modes of elements are an issue for all models. As soon as complex 3D stress and strain states occur, local distortions due to 3D element collapse lead to sudden large strains in one (or more) direction. Large strains lead to large stresses and subsequently, equilibrium in the 3D space is not easily obtained.

In view of these issues, two different models were developed as can be seen in Figure 5-1. In the first model, called model A, Figure 5-1a, the steel dowels needed to load the test specimens have been modelled as well because the model should be able to rotate in order to avoid secondary stresses. The friction coefficient between steel and wood was assumed to be 0.5 (stick-slip model). The boundary conditions were applied on the steel dowels where the lower dowel was fixed in all three directions and the upper dowel was

loaded in displacement-control and did not allow for movements in Z- and X-direction. Analogously to the tests, the load-slip graphs were derived from the reaction forces in Y-direction of the lower steel dowel and the deformation in Y-direction of the upper dowel.

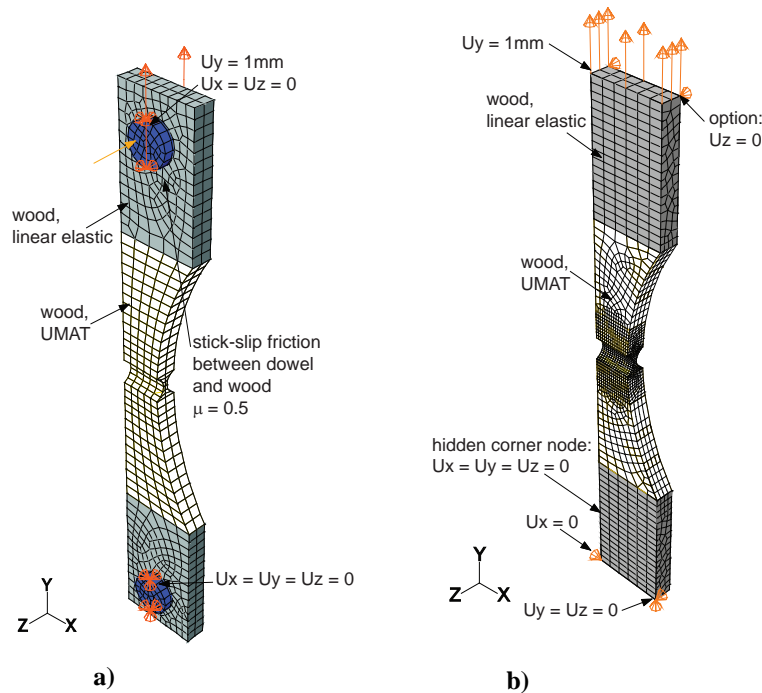


**Figure 5-1: Tension parallel-to-grain, a) model A, b) model B**

The second model, called model B, was simpler (see Figure 5-1b). The steel dowels were not modelled and the boundary conditions and loading were directly applied on the wood specimen. The boundary conditions did not correspond to Franke's test setup. The load-slip graphs of the simulations were derived from the displacement of the upper part of the model whereas the reaction forces in Y-direction of the lower part provided the force component of the load-slip graph. The size of the tapered region in both models is 2 x 20 mm.

Model A was the more accurate model. Model B served to evaluate the influence of different boundary conditions. The geometry of both models corresponded to Franke's tension test specimens. The material model was used only in the central part of the model, purely linear elastic behaviour was assumed for the outer wood and for the steel. Models A and B are typical examples where local material orientations must be defined because otherwise the models are loaded perpendicular-to-grain<sup>14</sup>. The loading was displacement-

<sup>14</sup> In the developed material model (subroutine UMAT), the longitudinal direction is defined in X-direction, the radial material direction is the Y-direction and the tangential direction corresponds to the Z-direction. Here however, the longitudinal direction is in global Y.

controlled up to a deformation of 1 mm. The default material properties of the UMAT were given in Table 4-1. If not indicated otherwise, the large displacement theory was used. The crack band model was activated.

The following modelling parameters were varied:

- Material properties;
- Boundary conditions;
- Large and small displacement theory;
- Mesh.

Firstly, model B (without the optional boundary condition  $U_z = 0$  on top) was run. Figure 5-2 shows the development of the damage variable  $d_{t,0}$ <sup>15</sup>. The crack propagation can be clearly seen. In Figure 5-3, the load-slip graph is shown where also the increments of Figure 5-2 are indicated. When comparing Figure 5-2 with Figure 5-3, it can be observed that the nonlinear part starts approximately at increment 100 where crack initiation can be seen. At increment 300, the maximum load is reached where the damage already covers more than half of the width of the notch. Increments 350 and 400 are on the softening branch and at the last increment, the crack is completed and no residual load carrying capacity is available. A stable numerical crack growth can thus be achieved with the developed material model. However, many increments are needed.

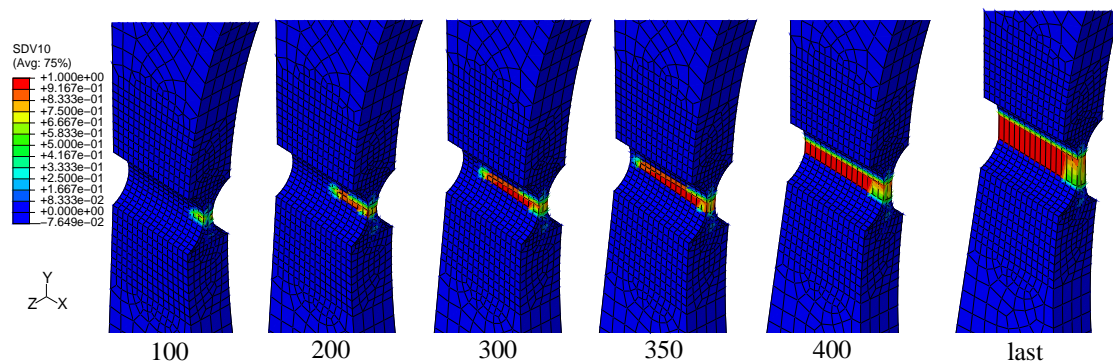


Figure 5-2: Model B, damage variable  $d_{t,0}$  – at increments 100, 200, 300, 350, 400 and last

<sup>15</sup> As the damage variables are solution dependent state variables, they are identified in the postprocessing via the abbreviation SDV with the following assignments:

$$\begin{aligned} \text{SDV10} &= d_{t,0}; & \text{SDV11} &= d_{c,0}; & \text{SDV12} &= d_{t,90R}; & \text{SDV13} &= d_{c,90R}; & \text{SDV14} &= d_{t,90T}; & \text{SDV15} &= d_{c,90T}; \\ \text{SDV16} &= d_{vR}; & \text{SDV17} &= d_{vT}; & \text{SDV18} &= d_{roll} \end{aligned}$$

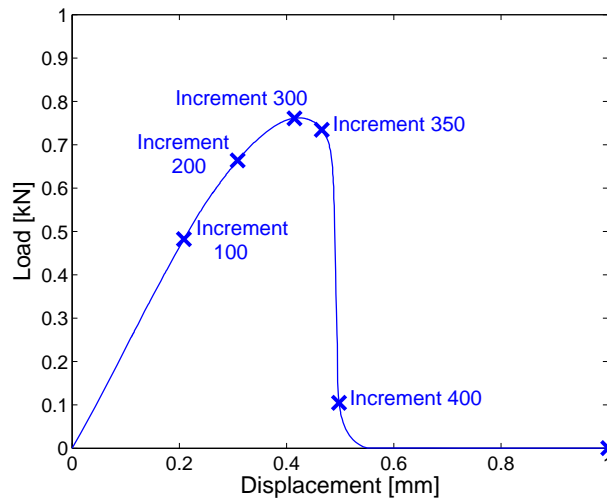


Figure 5-3: Load-slip graph of model B

Figure 5-4 shows the simulation results in terms of the strain component  $\varepsilon_{11}$  at the last increment, this time the deformations are 10x exaggerated. As the specimen displaced considerably in Z-direction (see Figure 5-4a), additional boundary conditions to restrain the movement in Z-direction were applied (see Figure 5-1b optional boundary condition  $U_z = 0$  on top). Figure 5-5b shows the result of this modified model in terms of  $\varepsilon_{11}$ . No displacement in Z-direction occurred, but the rear elements, where the crack reaches last, distorted considerably as can be also seen in Figure 5-6a which shows the rear side of the model. In Figure 5-6b, the distorted elements were removed. As can be seen, only the outermost elements distorted excessively. As only the boundary conditions changed, this must be due to secondary stresses due to the additional restraint. The reason for the excessive distortion and subsequent convergence problems becomes clear when looking at Figure 5-7 where the strain components for one of the distorted elements are shown. When reaching the final deformation, the strain components change significantly. It seems indeed as if the elements collapse in all directions as discussed in the beginning of this section. Spurious energy modes develop. The elements are completely damaged when high enough secondary stresses develop that cause failure also in other directions than the main loading direction. Possible improvements could be to not allow for complete damage or excessive strains. For instance, a threshold value could be set to limit damage or strains. However, such a solution would not be ideal; a smeared parameter without physical meaning would be introduced.

Another drawback is that the stresses are not transferred to the next, not yet completely collapsed row of elements. This effect was already discussed in section 4.4.7.

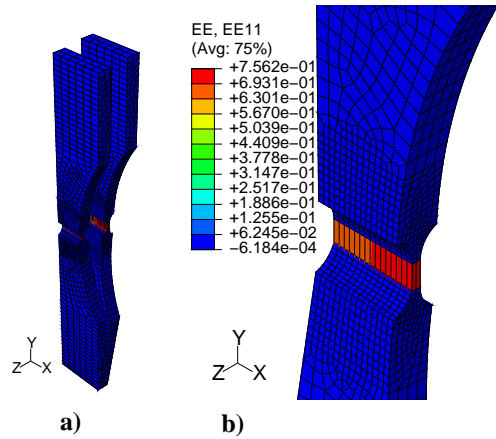


Figure 5-4: a) Overview of deformed and undeformed model B; b) strain component  $\epsilon_{11}$  of model B, last increment; deformations 5x exaggerated

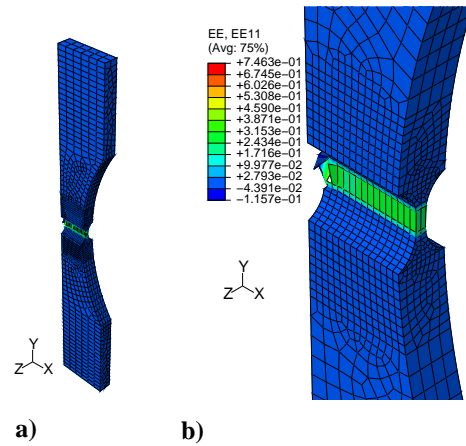


Figure 5-5: a) Overview of deformed and undeformed model B with option 'Uz = 0' (see Figure 5-1b); b) strain component  $\epsilon_{11}$ , last increment; deformations 10x exaggerated

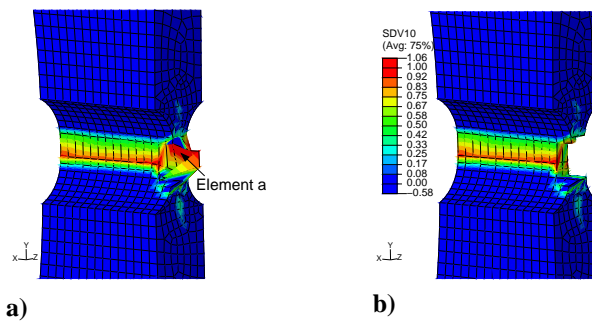


Figure 5-6: Damage variable  $d_{t,0}$  at last increment at compression side of model B with option 'Uz = 0', deformations 10x exaggerated; a) Figure 5-5 turned by 180°, b) distorted elements deleted

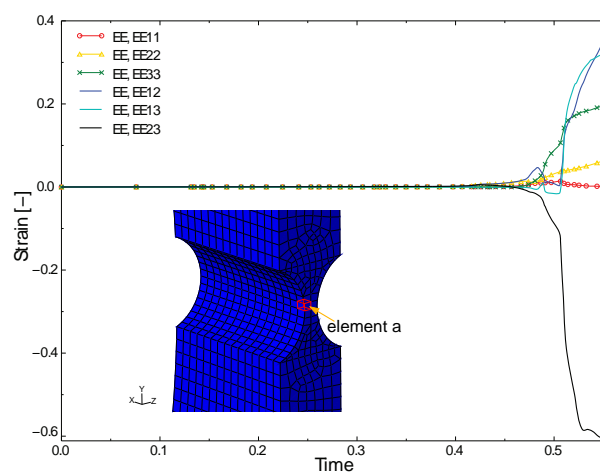
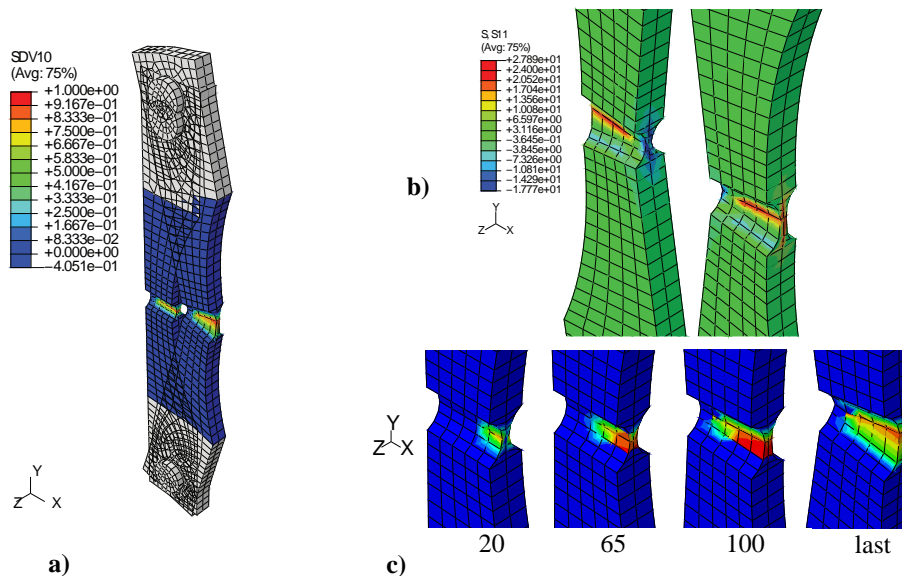


Figure 5-7: Typical strain components of indicated element a, integration point 6

Figure 5-8 shows the simulation result for model A including the steel dowels. In Figure 5-8a, it can be seen how the model is rotating due to the asymmetry. The compression stresses on the rear of the model that are created due to the asymmetry can be observed in Figure 5-8b. Figure 5-8c shows the damage variable  $d_{t,0}$  at various increments that are also indicated in the load-slip graph of the model in Figure 5-9. Analogously to model B, the crack initiation around increment 20 indicates the start of the nonlinear regime. Increments 100 and 122 (last increment) are part of the softening branch. Figure 5-9 shows that model A does not fail completely what may be due to the asymmetry and compression stresses on the rear side which are still observable in the last increment 122. For comparison reasons, Figure 5-9 shows also the load-slip graph of model B. Three main remarks can be done:

- The stiffness is different for both models;
- Model A is less brittle than model B;
- The maximum load carrying capacity is comparable (713N for model A versus 762N for model B).

The simulation results of models A and B underline the thoroughly discussed issues connected with test setups. It is difficult to design a good specimen geometry that triggers only the failure mode it was designed for. Secondary stresses can develop that are not measured, maybe not even observable, but they will be part of the real 3D stress field of the tests.



**Figure 5-8: Model A at last increment, deformation 5x exaggerated;**  
**a) deformed model at last increment, b) stress component  $\sigma_{11}$  at increment 65,**  
**c) damage variable  $d_{t,0}$  at increments 20, 40, 70 and last**

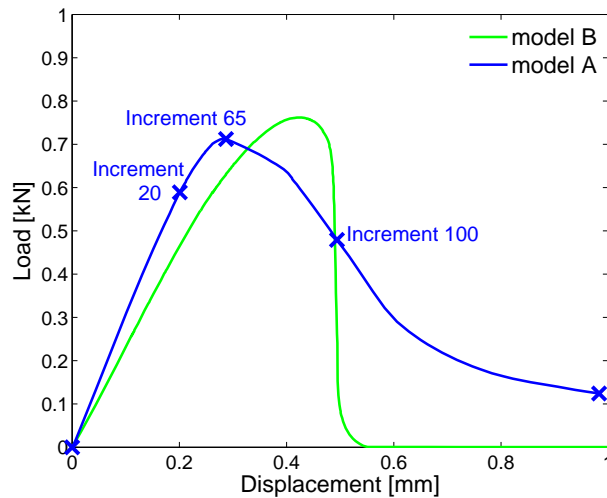


Figure 5-9: Load-slip graph of model A and model B

Table 5-1: Material input values for spruce, default values and Franke's values

Parameter	Units	Table 4-1	Franke (2008), means Tabelle 5-3, 5-4 and C-2
$E_{11}$		11000	7000
$E_{22} = E_{33}$		370	620
$G_{12} = G_{13}$		690	680
$G_{23}$		50	42
$f_{t,0}$	MPa	24	130
$f_{c,0}$		36	50
$f_{t,90}$		0.7	3.0
$f_{c,90}$		4.3	3.2
$f_v$		6.9	4.6
$f_{roll}$		0.5	1.0
$G_{f,0}$	N/mm	6	60
$G_{f,90}$		0.5	0.18
$G_{f,v}$		1.2	1.2
$G_{f,roll}$		0.6	0.6
$\nu$	-	0.0001	0.0001

Figure 5-10 shows load-slip graphs for model A where different parameters were varied. The mesh was changed. Furthermore, large and small displacement theory were used and the fracture energy  $G_{f,0}$  was increased by a factor of 10 and of 100. Especially the fracture energy  $G_{f,0}$  used for mode I failure parallel-to-grain is an important parameter as it should define the softening grade of the model. Furthermore, Franke's (2008) properties for small clear spruce specimens were used as given in Table 5-1.

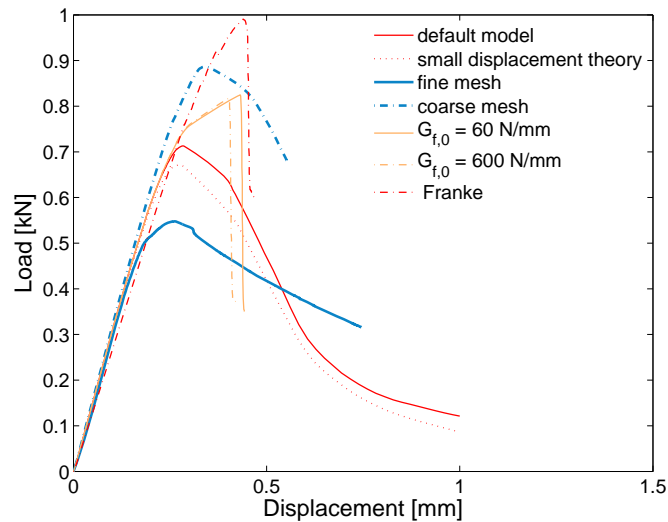


Figure 5-10: Load-slip graphs of model A with varied parameters

A small difference in ultimate load carrying capacity for small and large displacement theory can be observed. As long as no closer look in the cause of this difference is taken, it is recommended to apply the theory of large displacements for further models. It is computationally more demanding, but it is expected that the theory of large displacements delivers better results.

The models with different fracture energies in mode I parallel-to-grain  $G_{f,0}$  show much stronger brittle behaviour than the default model A. A higher fracture energy value than 6 N/mm should be chosen to obtain brittle failure. For  $G_{f,0} = 60$  N/mm and 600 N/mm, the ultimate load carrying capacity is higher than for the default model with  $G_{f,0} = 6$  N/mm. Both models with higher fracture energies do not differ much from each other.

Furthermore, the value of the fictitious viscosity was changed to  $\eta = 0.0002$ . No difference could be observed between the default model ( $\eta = 0.0001$ ) and the model with  $\eta = 0.0002$ . (The perfect overlap of the two models is not shown in Figure 5-10.)

When the numerical results are compared with Franke's experimental results shown in Figure 5-11, it can be seen that the numerical models cover the lower bound of test results. If the two test results with the lowest load carrying capacity are considered, the prediction quality is satisfactory. The maximum load and the brittle behaviour are correctly modelled when applying Franke's (higher) material properties for small spruce specimens. As for the failure modes, especially the model with Franke's properties did not fail in tension parallel-to-grain, but due to high shear and tension stresses perpendicular-to-grain in the roundings of the notches as shown later (Figure 5-19). It is difficult to compare tests and models in order to judge the quality of the failure mode prediction. Due to the short notch of the test specimens, it is possible that high shear stresses developed that initiated splitting.

A mesh dependency can be seen although the crack band model was activated. This was not expected as the validation of section 4.37 showed that mesh dependency could be alleviated using the crack band model. In Figure 5-12 and Figure 5-13, the mesh and the results at the resp. last increments in terms of stress component  $\sigma_{11}$  and damage variable  $d_{t,0}$  are given for model A. The model with the finest mesh shows again strong distortion patterns of the elements. It is the author's opinion that the observed mesh dependency is strongly correlated to the problems with element distortions due to complex 3D stress fields rather than to problems connected with the applied regularisation method. The spurious energy modes are the most important problem to deal with in further research. Interesting for this discussion is again a closer look in the strongly distorting elements.

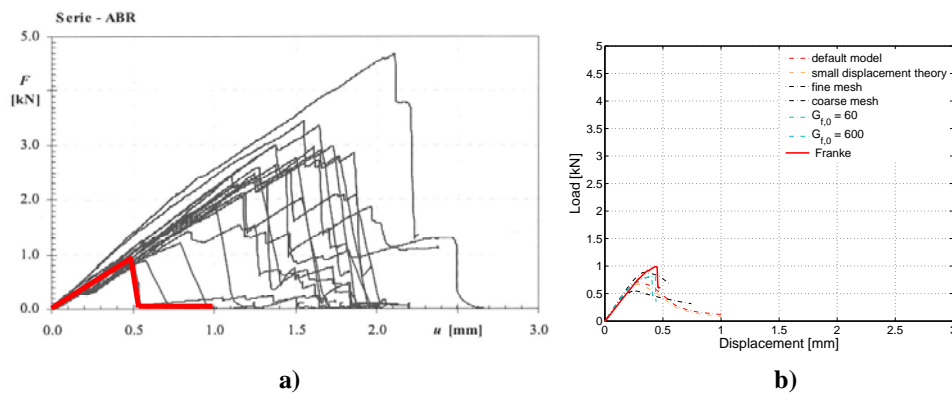


Figure 5-11: a) Test results from Franke ((2008), Abb. 4-3) on small clear spruce wood; one test result highlighted; b) modelling results of Figure 5-10 on same scale as test results

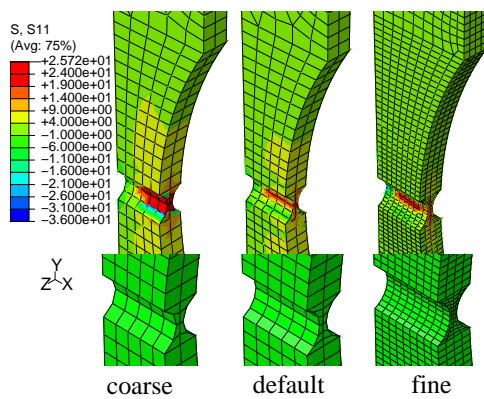


Figure 5-12: Model A, stress component  $\sigma_{11}$  for three meshes at respective maximum load carrying capacity

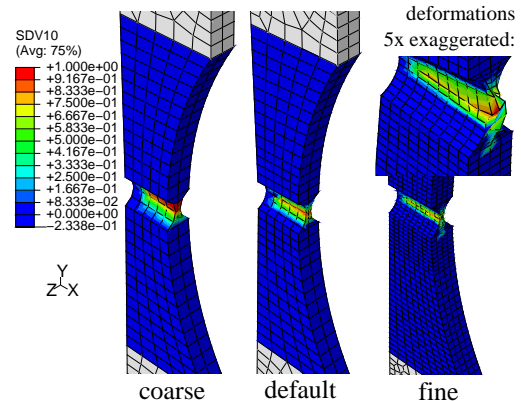


Figure 5-13: Model A, damage variable  $d_{t,0}$  for three meshes; detail of fine mesh with deformed elements

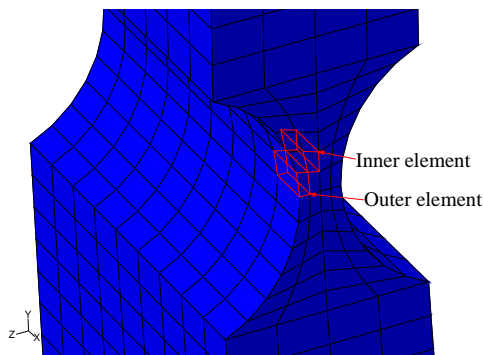


Figure 5-14: Model B, detail of fine mesh

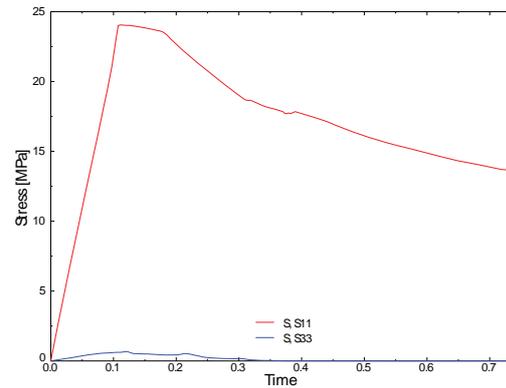


Figure 5-15: Outer element indicated in Figure 5-14, stress components  $\sigma_{11}$  and  $\sigma_{33}$

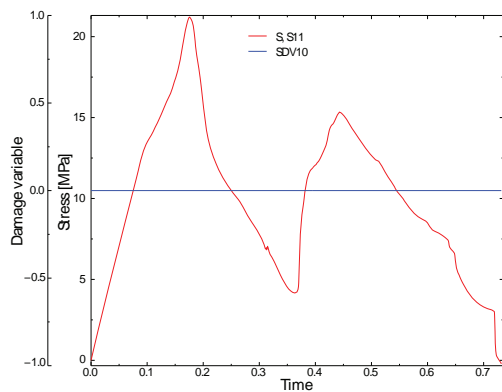


Figure 5-16: Inner element (Figure 5-14) stress component  $\sigma_{11}$  and damage variable  $d_{t,0}$

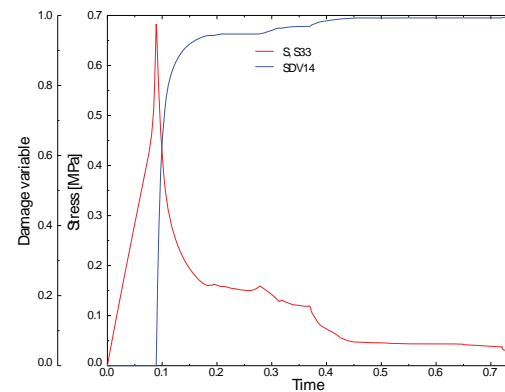


Figure 5-17: Inner element (Figure 5-14) stress component  $\sigma_{33}$  and damage variable  $d_{t,90}$

Figure 5-14 shows a detail of model B with the fine mesh. Two elements are highlighted. One inner element of the curved part of the notch and an outer element on the ‘straight’ part of the notch. In Figure 5-15, the results for an integration point of the outer element is given. The element failed in tension parallel-to-grain. This is completely different for the inner element as can be seen in Figure 5-16 and Figure 5-17. The inner element did not fail in tension parallel-to-grain, but in tension perpendicular-to-grain. This was due to the perpendicular stress component caused by the rounded notch. The stress fields were complicated already at an early stage of the numerical calculations. Some elements had no perpendicular and shear stiffness left before the parallel damage could start properly.

Another observation can be made for model A with Franke’s material parameters. Franke used higher mechanical properties for small test pieces of clear wood where the ratio of tension strength parallel-to-grain over shear strength was much higher than for structural-size wood, see Table 5-1. Indeed the ultimate load carrying capacity was the highest of all models. However, the numerical model did not fail in tension parallel-to-grain at all, but

in shear and tension perpendicular-to-grain in the rounded region of the notch. Figure 5-18 shows damage variable  $d_{t,0}$  at increment 70. Figure 5-19 shows damage variable  $d_v$  at the same increment. The specimen started to fail in shear. Longitudinal tension stresses never reached the strength threshold at which damage in tension parallel-to-grain would have started. This is a realistic prediction as the notched region was rather short which triggered firstly shear failure before actually failing in tension parallel-to-grain.

Finally, typical energies ALLSE and ALLCD for the default model B are shown in Figure 5-20 (the other models show similar relationships between ALLSE and ALLCD). ALLCD represents the dissipated energy due to viscous regularisation whereas ALLSE gives the total dissipated energy. Logically, ALLCD must be much smaller than ALLSE (see also section 4.4.8). Figure 5-20 proves that the chosen viscosity for regularisation  $\eta = 0.001$  is not too high as ALLCD is considerably smaller than ALLSE.

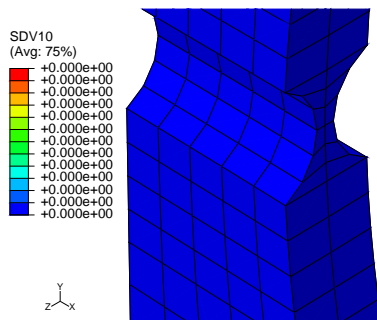


Figure 5-18: Model B, Franke's properties, damage variable  $d_{t,0}$ , increment 70

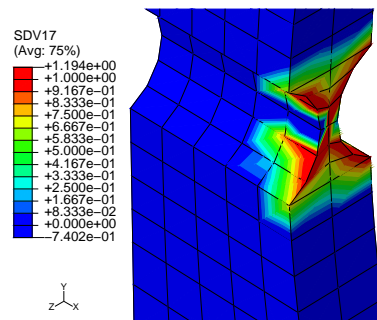


Figure 5-19: Model B, Franke's properties, damage variable  $d_v$ , increment 70

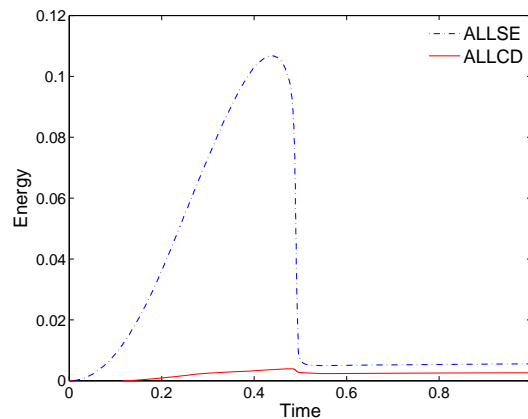


Figure 5-20: Energies for model B, default parameters

## 5.2.2 Compression with different angles to the grain

The next models simulated compression tests with different angles to the grain again taken from Franke (2008). The tests were carried out by placing the test specimen of 40 x 40 x 40 mm between two steel plates that transmitted the loading. These steel plates need to be modelled to include the effect of friction on the test results. Friction between wood and steel was modelled with a stick-slip model ( $\mu = 0.5$ ). This friction is restraining the lateral deformation of the wood block. The specimens were tested and simulated parallel-to-grain, perpendicular-to-grain and at angles to the grain of 22.5° and 45° respectively.

Franke (2008) discussed the influence of friction between the wood block and steel plates on the modelling results for compression parallel-to-grain. He used the Hoffman (1967) criterion and stated that the lateral constraint led to a localised plastic region directly underneath the steel plates which he stated was not realistic. The model could not describe kinking as observed in tests and therefore, the global load-slip curve could not be simulated satisfyingly according to Franke. Franke stated that the mechanical behaviour was not sensitive to changes of the material properties. Franke's conclusion was that more precise material models, which are able to define all regions of the experimental load-slip curves, should be used. Therefore, Franke used also Grosse's (2005) multi-surface plasticity material model in order to simulate compression tests parallel-to-grain. However, this proved not to be possible in combination with friction. Franke stated that problems with friction were observed only for the case parallel-to-grain. The compression tests perpendicular-to-grain and at angles to the grain of 22.5° and 45° respectively showed more homogeneous failures. This led to less numerical problems with both the Hoffman criteria and Grosse's model. As for the quality of Franke's numerical simulations using Grosse's model, the prediction of the load-slip curves for the perpendicular-to-grain loading was a perfect overlap of the test results. The simulations for compression with an angle to the grain did not result in satisfying load-slip curves.

In the following it will be investigated if similar problems can be observed for analogous models that are run with the developed material model. It is expected that the elements directly underneath the steel plates cause problems. Due to the complex 3D stress and strain states of these elements, the FE programme could have problems with convergence in this localised band of elements due to spurious energy modes as discussed previously. These will be important observations because also in embedment and joint models, similarly strained elements (in compression) will occur directly underneath the dowel.

Figure 5-21 shows the compression model where local material orientations must be assigned in order to simulate tests parallel-to-grain, perpendicular-to-grain and at angles to the grain of 45° and 22.5°. The following model variations will be undertaken:

- Mesh (64, 512 and 3375 elements where 512 elements is the default mesh);
- Small and large displacement theory;
- Different material properties (fracture energies).

The default material properties of the UMAT were given in Table 4-1. If not indicated otherwise, the large displacement theory was used. The load-slip graphs were evaluated with the reaction forces in X-direction and the loading (= displacement) in X-direction. The crack band model was activated.

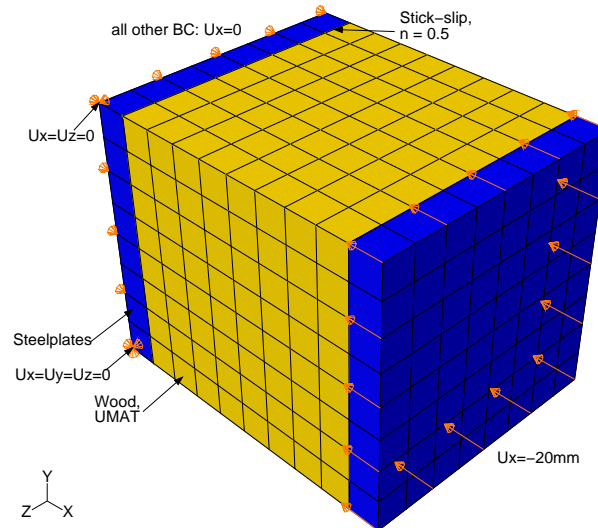


**Figure 5-21: Compression with an angle to the grain, model with boundary conditions, materials and mesh; here with 512 elements**

### Compression parallel-to-grain

The model parallel-to-grain did not show the same problems with friction as discussed by Franke (2008). This can be seen in Figure 5-22b. Because the material model does not model constant volume, the elements are simply squeezed together and the correspondent load-slip graphs are elastic perfectly plastic as seen in Figure 5-22a. No difference can be seen for different meshes and for small and large displacement theory as can be expected.

Specimens loaded in compression parallel-to-grain develop kink bands as discussed in section 2.2.2. The developed material model does not represent these localised failures. However, it is in the author's opinion that proper modelling of kink bands is not relevant for embedment and joint models. Only material models that aim at accurately reproducing test results on wood pieces need to be able to simulate kinking.

The reached ultimate load carrying capacity of 57.6 kN is correct. Divided by the surface area of 40 x 40 mm, an ultimate compression stress of 36 MPa can be calculated.

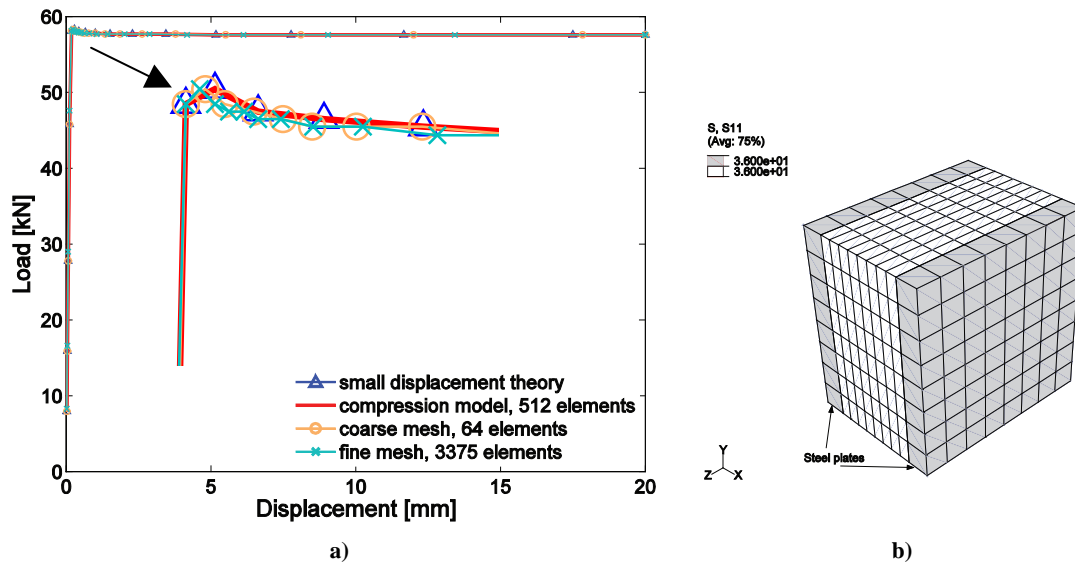


Figure 5-22: Compression model parallel-to-grain; a) load-slip graphs, b) stress component  $\sigma_{11}$

#### Compression perpendicular-to-grain

Also compression perpendicular-to-grain did not cause any major problem. The results were exactly the same as for compression parallel-to-grain – except that an ultimate stress of 4.3 MPa was reached (see also Figure 5-23). In comparison to test results, no densification with an increase in stress at large deformations can be modelled as the constitutive law implemented in the material model is elastic perfectly plastic.

#### Compression with different angles to the grain (22.5°, 45°)

More interesting are the results for compression with an angle to the grain of 22.5° and 45°. Complex 3D stress states develop due to the activation of shear and tension perpendicular-to-grain together with friction between wood block and steel plates.

Figure 5-23 shows the load-slip graphs of all four models, tests in compression parallel- and perpendicular-to-grain and with an angle to the grain of 22.5° and 45°. The different global constitutive behaviour of the wood blocks is evident. For 22.5°, the wood block is more brittle than for 45°. The ultimate load carrying capacity also shows logic differences with 22.5° having a higher capacity than 45°. In order to understand the influence of the fracture energies on the mechanical behaviour, two more models were run with an angle to the grain of 22.5°. Different fracture energies for shear failure were used as shown in Figure 5-24. When using half the default fracture energy, the numerical results do not differ much. The models are not sensitive to minor changes of the fracture energies. A change of a magnitude of 10x changes the material behaviour completely. No brittle failure can be observed. In Figure 5-25, the modelling results using large and small displacement theory are shown. No significant difference can be observed. The need for small increments in the softening part can be observed as well.

Finally, the mesh size was varied. Figure 5-26 shows the results for an angle to the grain of  $22.5^\circ$  and  $45^\circ$ . Similar to the tension test results, also here a mesh dependency can be observed. However, the single results differ much less from each other than the ones shown in Figure 5-10.

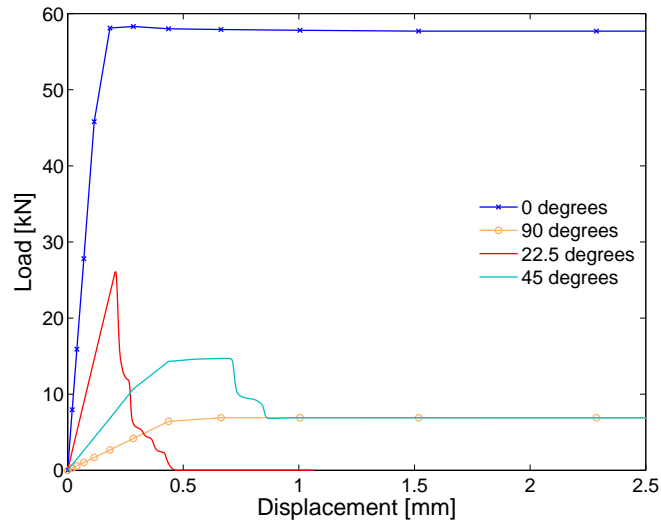


Figure 5-23: Load-slip graphs for  $\alpha = 0^\circ, 90^\circ, 22.5^\circ, 45^\circ$

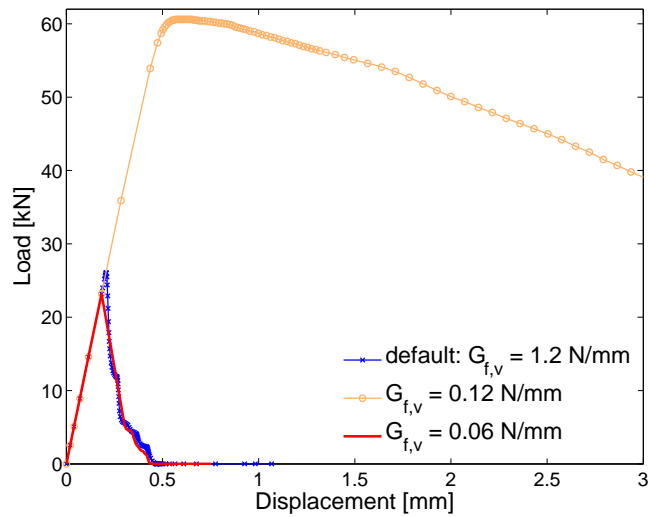


Figure 5-24: Load-slip graphs for  $\alpha = 22.5^\circ$ , different fracture energies  $G_{f,v}$

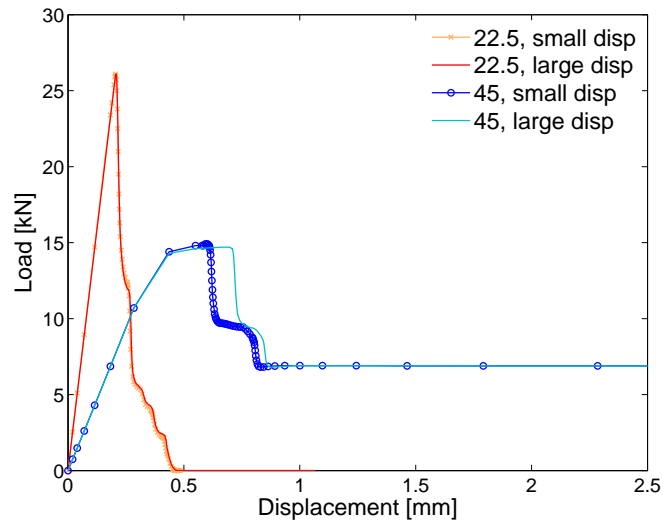


Figure 5-25: Load-slip graphs for  $\alpha = 22.5^\circ$  and  $45^\circ$ , small and large displacement theory

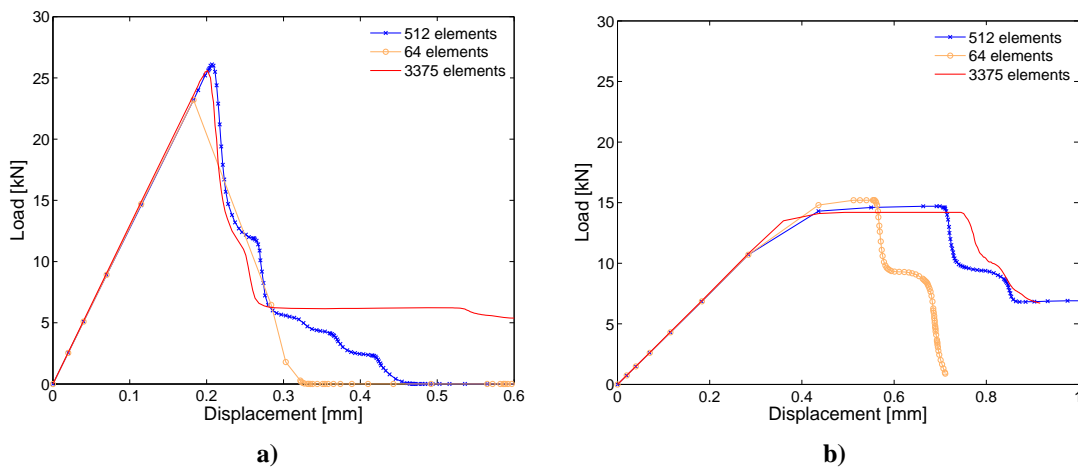


Figure 5-26: Load-slip graphs for three different mesh sizes; a)  $\alpha = 22.5^\circ$ , b)  $\alpha = 45^\circ$

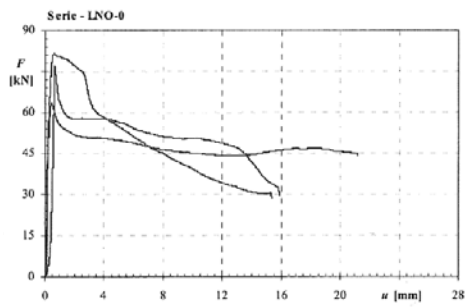


Figure 5-27: Results from Franke (2008) for  $\alpha = 0^\circ$

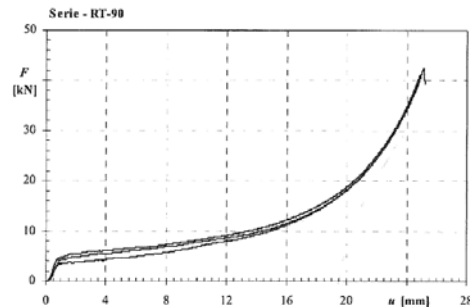
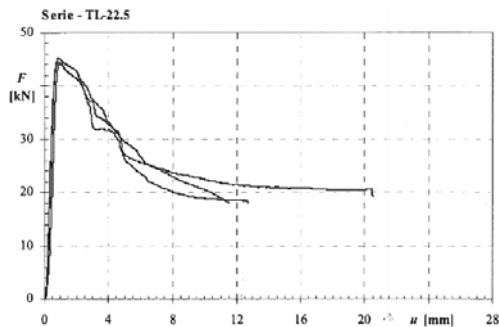
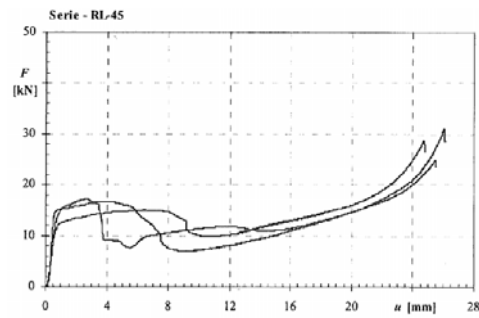


Figure 5-28: Results from Franke (2008) for  $\alpha = 90^\circ$



**Figure 5-29: Results from Franke (2008)  
for  $\alpha = 22.5^\circ$**



**Figure 5-30: Results from Franke (2008)  
for  $\alpha = 45^\circ$**

Before discussing numerical issues, the modelling results are compared with test results. Figure 5-27 to Figure 5-30 show Franke's (2008) test results for an angle to the grain of  $\alpha = 0^\circ, 22.5^\circ, 45^\circ, 90^\circ$ . The respective modelling results were shown in Figure 5-23 (please note that the scale of the x-axis is different from the test results). The qualitative constitutive behaviour could be captured.

#### Comparison compression parallel-to-grain

The constitutive relationship of the material subroutine models elastic perfectly plastic behaviour. This could be found back in the numerical results. The load carrying capacity was with 60 kN smaller than the experimental results. This could be expected as the tests were done on small clear wood with higher mechanical properties than the ones considered for the models. The experimental load-slip graph as shown in Figure 5-27 could not be reproduced. However, other test results look different from Figure 5-27 – see for instance Figure 2-5 where the wood block continued yielding after the yield drop and no softening could be observed. Therefore, the numerical post-elastic behaviour agreed better with the experimental results shown in Figure 2-5. However, additional modelling of kinking is not expected to increase the prediction quality of joint models.

#### Comparison compression perpendicular-to-grain

The mechanical material model for compression perpendicular-to-grain is the same as for compression parallel-to-grain. The predicted load carrying capacity of 7 kN is higher but still a good fit to the test results. This is obvious when considering the governing material property  $f_{c,90}$  which was assumed to be 4.3 MPa for the numerical model whereas Franke (2008) found a mean value from the tests of 3.2 MPa. As for the prediction quality of the load-slip curve, densification at high deformations cannot be modelled. However, again it is discussable whether densification is an important effect for joint models.

#### Comparison compression with an angle to the grain of $22.5^\circ$ and $45^\circ$

The qualitative load-slip behaviour could be satisfyingly predicted with the numerical models. The models with an angle to the grain of  $22.5^\circ$  are more brittle in comparison to the test results. The load carrying capacity of the specimen with an angle to the grain of

45° could be predicted well. For the specimens with an angle to the grain of 22.5°, the predicted load carrying capacity is lower which is due to the chosen lower mechanical properties for structural-size wood. Localised failures observed in tests such as buckling of fibres cannot be modelled. Furthermore, the predicted stiffness is too high.

The strong element distortion observed in the tension models was also observable in the compression models under an angle to the grain as then, brittle failures due to transverse tension and shear were activated in the elements directly underneath the steel plates. Figure 5-31 shows exemplarily the numerical results for the model with compression under 45° at different increments. The collapse of the element rows directly underneath the steel plates can be seen. The load slip graph with the increments is given in Figure 5-32a. Figure 5-32b shows the stress components  $\sigma_{22}$  and  $\sigma_{12}$  and the corresponding damage variables  $d_{c,90}$  and  $d_v$ . The elements lost rapidly their shear stiffness with subsequent collapse. Instead of continuing the load transfer to the next row of elements, the calculation stopped. With the unloading of the first row of elements underneath the steel plates due to shear stiffness degradation<sup>16</sup>, also the second row was unloaded and did not take any more loading (see also Figure 5-42). The reason for this was already explained in section 4.3.7, Figure 4-7. However, the obtained global load-slip curve was satisfying at the current state-of-the-art. The difference between tests with an angle to the grain of 22.5° and 45° can be clearly seen. With an angle to the grain of 22.5°, the global load-slip behaviour is more brittle than with 45°.

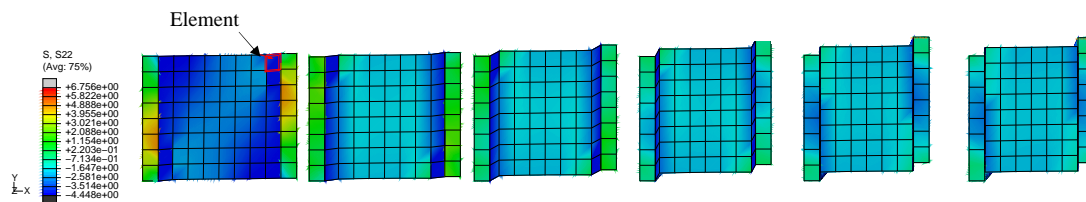


Figure 5-31: Compression with  $\alpha = 45^\circ$ , at increments 50, 70, 75, 77, 80 and last

<sup>16</sup>Shear damage is coupled to transverse tension damage; a degradation of shear stiffness also leads to a degradation of the perpendicular MoE. Therefore, the element loses not only shear stiffness, but also perpendicular MoE.

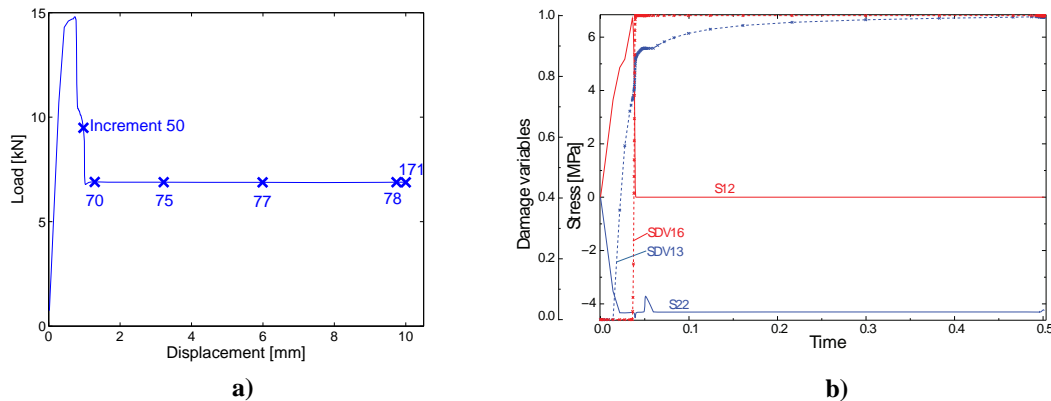


Figure 5-32: Compression with  $\alpha = 45^\circ$ ; a) load-slip graph, b) stress components  $\sigma_{22}$ ,  $\sigma_{12}$  and conjugated damage variables  $d_{c,90}$  (SDV13) and  $d_v$  (SDV16)

### 5.2.3 Conclusions

The examples described above have shown that the material model is able to identify different failure modes. Stable softening curves are possible and also ductile behaviour is modelled properly within one single material model.

From the modelling outcomes and numerical problems, the following conclusions for the next step of modelling, embedment modelling, can be drawn:

- Take  $G_{f,0} = 60$  N/mm for spruce as 6 N/mm leads to too ductile material behaviour.
- Elements are susceptible to spurious energy modes due to 3D collapse. Especially directly underneath the bolt, element distortion and subsequent convergence problems can be expected which may lead to a calculation stop.
- Unloading of elements leads to secant unloading of neighbouring elements. Therefore, if one row of elements fails (and distorts excessively), the neighbouring elements do not take over the load as they are already unloading.
- Further research must take a closer look into the problems connected with element distortion, subsequent mesh sensitivity and the unloading of neighbouring elements.

However, generally it can be said that observed problems such as the sensitivity to different meshes and boundary conditions are not expected to be as prominent in more complex models such as embedment models. In that sense, embedment models should be easier to handle as secondary stresses are less probably introduced.

For clarity reasons, Table 5-2 gives again all used material parameters that are used by default in all following models. The issues discussed in section 4.5 concerning the reliability of the chosen material properties are still valid.

**Table 5-2: Default material properties, all wood species**

Parameter	Units	spruce	beech	azobé
$E_{11}$		11000	13000	20000
$E_{22}=E_{33}$		370	860	1330
$G_{12}=G_{13}$		690	810	1250
$G_{23}$		50	59	91
$f_{t,0}$	MPa	24	41	72
$f_{c,0}$		36	45	58
$f_{t,90}$		0.7	1.0	1.0
$f_{c,90}$		4.3	14.2	23.2
$f_v$		6.9	6.9	8.6
$f_{roll}$		0.5	0.5	0.6
$G_{r,0}$	N/mm	60	100	180
$G_{f,90}$		0.5	0.71	0.71
$G_{f,v}$		1.2	1.2	1.5
$G_{f,roll}$		0.6	0.6	0.7
$\eta$	-	0.0001	0.0001	0.0001

### 5.3 EMBEDMENT MODELS

The extensive discussion of material models was necessary to understand the innovative contribution of the material model developed in this thesis. This model is able to model stable crack growth while at the same time developing elastic perfectly plastic stress curves for compression loads. It was also important to clarify the problems still connected with the material model, especially the spurious energy modes and the lack of load transfer from fully damaged element to neighbouring elements.

After the material tests, embedment tests were modelled. Numerical models using three species, spruce, beech and azobé, and two different steel dowel diameters were simulated<sup>17</sup>. The material properties were given in Table 5-2. Figure 5-33 shows the embedment models with the most relevant information. The friction coefficient between timber and steel dowel was assumed to be 0.5. The symmetry of the model with regards to the width and the thickness is used and only a quarter is modelled. All models were run with the theory of large displacements. The used 3D elements were linear Gaussian bricks with eight integration points and full integration.

As for mesh regularisation techniques, it was decided to deactivate the crack band model as no localisation is expected. The crack band model could lead to opposite mesh dependency as discussed in section 4.6.2, Figure 4-20. However, the effect of the crack

<sup>17</sup> As the developed material model is a homogenised continuum model, no difference for different dowel diameters is expected.

band method on the model results was checked. No difference could be observed for the models with and without crack band method, see exemplarily Figure 5-34.

Other model variations than wood species and dowel diameter were carried out:

- Mesh:  
The default mesh was refined or coarser in order to get an idea on how mesh sensitive the models are.
- Different material properties (only section spruce):  
The values for the fracture energies are changed to investigate their influence on the modelling result. This also because it is assumed that the fracture energies are the major calibration values of the models. Other values such as the MoE are not changed.
- Different threshold value for damage variables in UMAT<sup>18</sup> (only section spruce):  
In the previous section, the problems of collapsing elements was discussed. One idea to improve the element behaviour is to increase the damage threshold in order to avoid a complete 3D stiffness reduction. By doing so, a residual stiffness in all directions is maintained which should reduce the uncontrolled collapse of elements<sup>19</sup>. However, this is not an ideal solution as it introduces a non-controlable parameter into the material model that has no physical meaning. It is done here anyway to investigate the causes of artificial softening.
- High strength and very high strength steel dowels<sup>20</sup> (only section beech):  
This should not have any influence on the modelling results as the dowels are not bending in this test setup.
- Different friction coefficient (only section azobé).

The load-slip data were derived from the displacement of the dowel and the reaction forces of the timber piece.

All geometrical data of the models such as thickness and width can be taken from chapter 6 where the experimental results will be presented.

---

<sup>18</sup> A threshold value for the damage variables is given in order to avoid that the variables assume values equal or even lower than zero. This threshold value is put to 0.9999995 being the maximum value of the damage variables  $d_M$  (thus never  $d_M = 1$ ). The variations carried out here assumed threshold values of 0.99 and 0.8.

<sup>19</sup> Another approach could be to introduce a maximum value of the strain components to avoid the sudden increase of strains once a material direction is completely damaged. However, this is probably difficult due to equilibrium requirements.

<sup>20</sup> Young's modulus and strength properties see Table 6-1; Poisson's ratio  $\nu = 0.3$ .

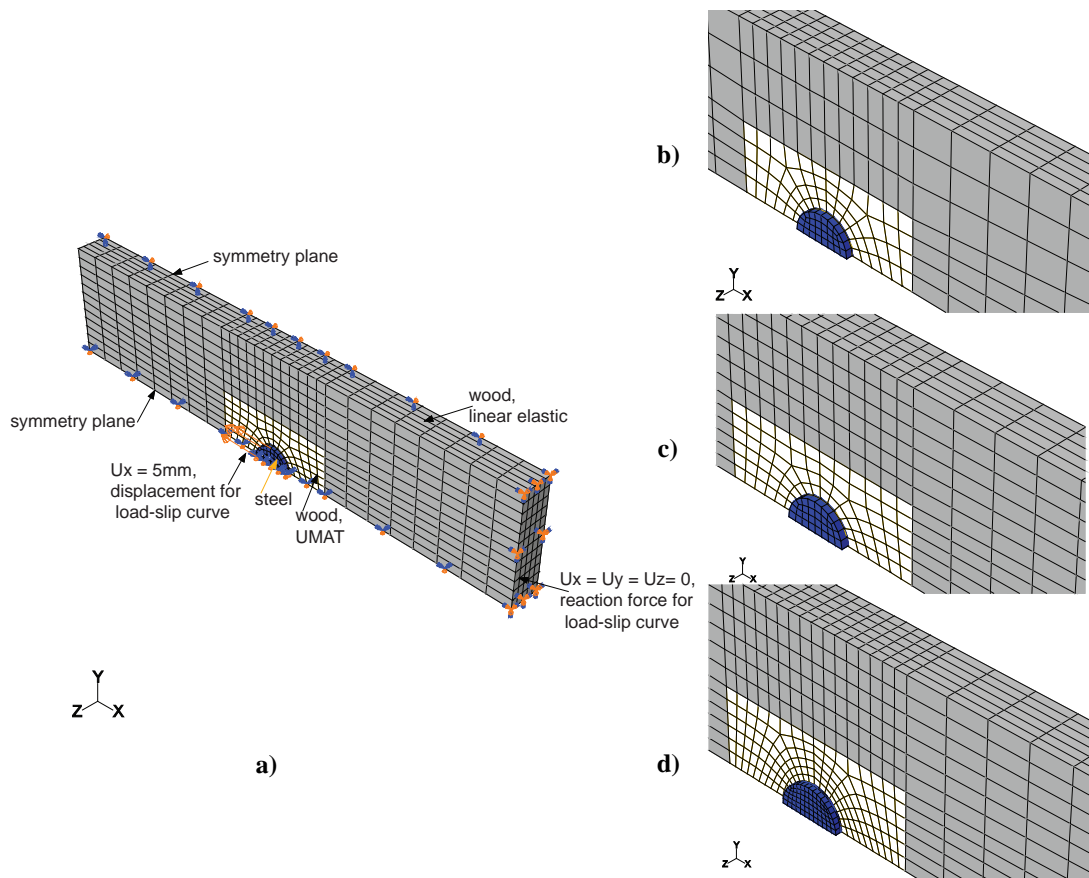


**Figure 5-33: Quarter of embedment model; a) with boundary conditions, materials and default mesh, b) detail coarse mesh, c) detail default mesh, d) detail fine mesh**

### 5.3.1 Spruce

Firstly, the simulations were run with the material properties of spruce – just as the verification models in chapter 4 and the material models of the previous section. Embedment models with 12 mm and 24 mm dowels were developed. Figure 5-35 shows simulation results in terms of embedment strength versus displacement. Different model variations were overlapped to the default spruce model (with default mesh and material properties as indicated in Table 5-2). Generally it could be observed that the models are too brittle which however is a purely artificial brittleness. A higher deformation capacity than 1 mm can be expected. This unloading was due to excessive distortion of the first row of elements directly underneath the dowel and the fact that the second row of elements started to unload simultaneously to the first row. Once the first row of elements collapsed completely, the second row was not able to take over the load and continue the ‘yielding’ of the specimen. A realistic outcome of the models is the yield drop that can be seen in Figure 5-35.

### Different material properties

The model was not susceptible to major changes of fracture energies. No difference could be observed between the default model and a model with  $G_{f,0} = 6$  N/mm. The model with  $G_{f,90} = 0.05$  N/mm and  $G_{f,v} = 0.12$  N/mm showed a slightly lower load carrying capacity, but the same deformation behaviour inclusive the yield drop.

### Different mesh

The fine mesh showed a slightly lower load carrying capacity than the default mesh, but with similar post-peak behaviour. As expected, the numerical problems with embedment models were less prominent than with material models (Figure 5-10 shows a much stronger mesh dependency than Figure 5-35). The coarse mesh showed more ductile behaviour than the default mesh.

### Different threshold values for damage variables

An increase of the threshold value influenced the collapsing behaviour of the elements directly underneath the dowel considerably. Even more, with a threshold value of 0.8, the fixed damage variables that kept a residual constant stiffness of 20% led to a hardening with increasing strains which is a similar behaviour as densification. This densification was so strong that no ductile behaviour could be observed anymore. A threshold value of 0.8 is not realistic. Interestingly enough, with a threshold value of 0.8, the numerical model finished the calculation up to the required displacement of 5 mm in one third of the calculation time.

A threshold value of 0.99 confirmed the assumption that the observed softening of the models is a numerical effect of the excessive distortion of the first row of elements underneath the dowel and the unloading of the second row of elements. This second row of elements could not take higher loads once the first row collapsed. Through a threshold value for the damage variables and a resulting constant residual value of all stiffness properties, the first row of elements did not collapse completely. The softening was less strong than with the default model. For instance, the strain components  $\varepsilon_{33}$  were smaller than with the default model as shown in Figure 5-36. Furthermore, the deformations of the model with a threshold value of 0.99 were different from the default model.

However, the insertion of such an uncontrollable artificial parameter with no physical meaning is not wished in the final subroutine. As already stated, it is done here anyway to investigate the causes of the discussed artificial softening. A higher threshold value will not be used in further modelling.

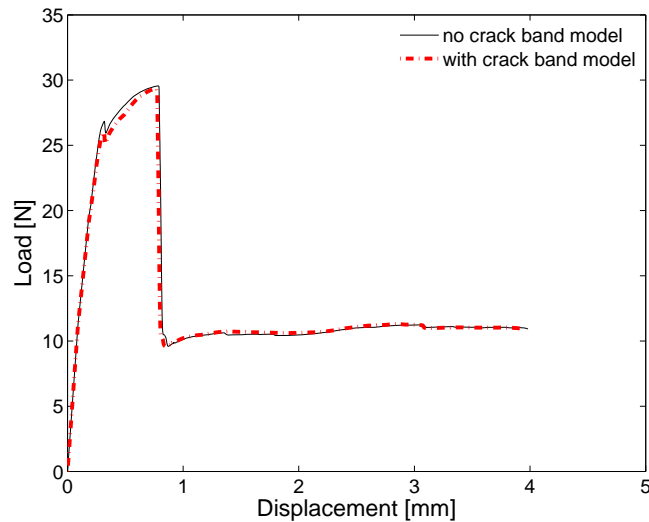


**Figure 5-34: Embedment model spruce with 24 mm dowels; default model with and without crack band model**

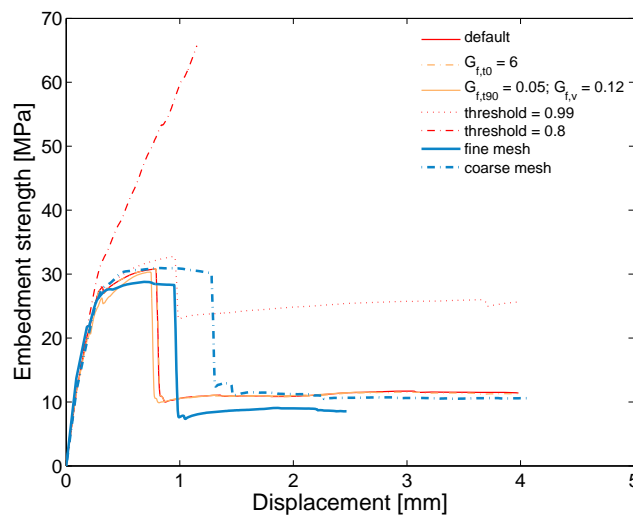


**Figure 5-35: Embedment model spruce with 24 mm dowels; stress-slip graphs with varied parameters, overlap of default model and model with  $G_{t,t0} = 6$  N/mm**

A closer look is taken into the default model spruce with 24 mm hss dowels. Figure 5-37 shows the damage variable  $d_{c,0}$  and  $d_{t,90}$  at the last increment. The timber underneath the dowel was completely crushed (Figure 5-37a) and splitting was initiated (Figure 5-37b). The stress components  $\sigma_{11}$  at different increments are shown in Figure 5-39 (increments see Figure 5-40). The stress components  $\sigma_{11}$  developed correctly. Directly underneath the dowel, compression stresses developed which were evenly distributed over the thickness. Also the damage development in transverse tension and shear is correct as can be seen in Figure 5-38: element a as indicated in Figure 5-37b starts to fail in longitudinal shear whereas element b starts to fail due to high tension stresses perpendicular-to-grain.

For the element directly underneath the dowel identified in Figure 5-39, strain components and some damage variables are shown in Figure 5-41. The reason for the unrealistic stress development was extensive element distortion as can be seen in Figure 5-41a. This is analogous to the material models (Figure 5-7). For instance, the damage variable in compression parallel-to-grain, SDV11, developed realistically until the element distortion started that caused a sudden increase in damage perpendicular-to-grain and in shear. Another unrealistic development was that the element was later also failing in tension parallel-to-grain, SDV10, although it had already failed in all other directions and in compression parallel-to-grain.

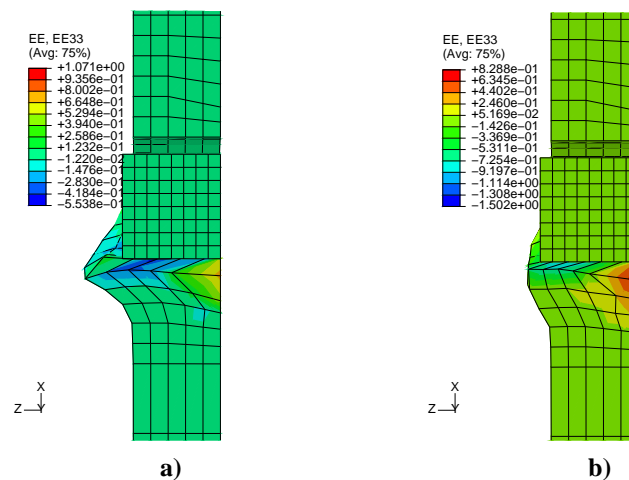


Figure 5-36: Strain component  $\epsilon_{33}$ ; a) default model, b) model with threshold value of 0.99

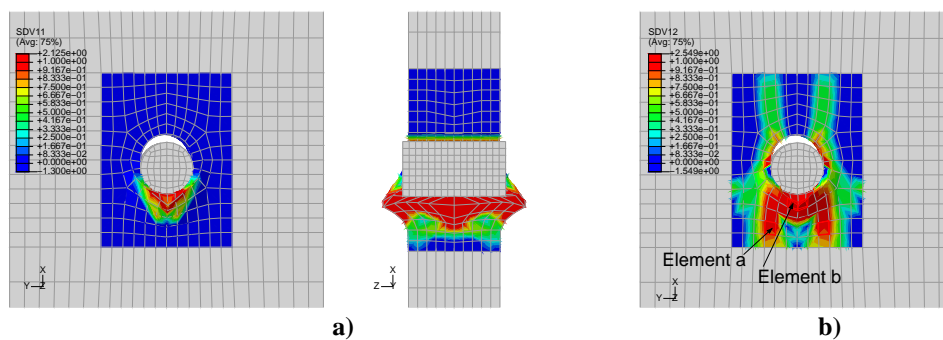


Figure 5-37: Embedment model spruce with 24 mm dowels; a) damage variable  $d_{c,0}$ ; b) damage variable  $d_{t,90}$  and indication of elements a and b

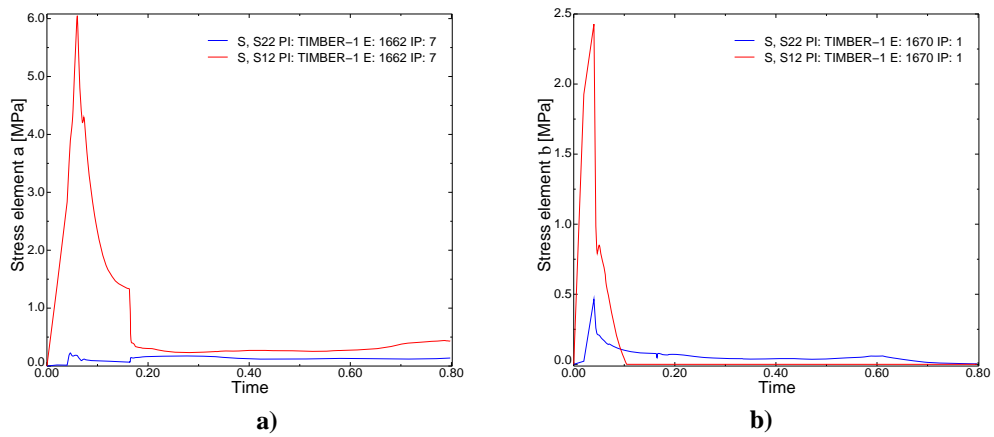


Figure 5-38: Stress components  $\sigma_{22}$  and  $\sigma_{12}$ ; a) element a; b) element b (see Figure 5-37)

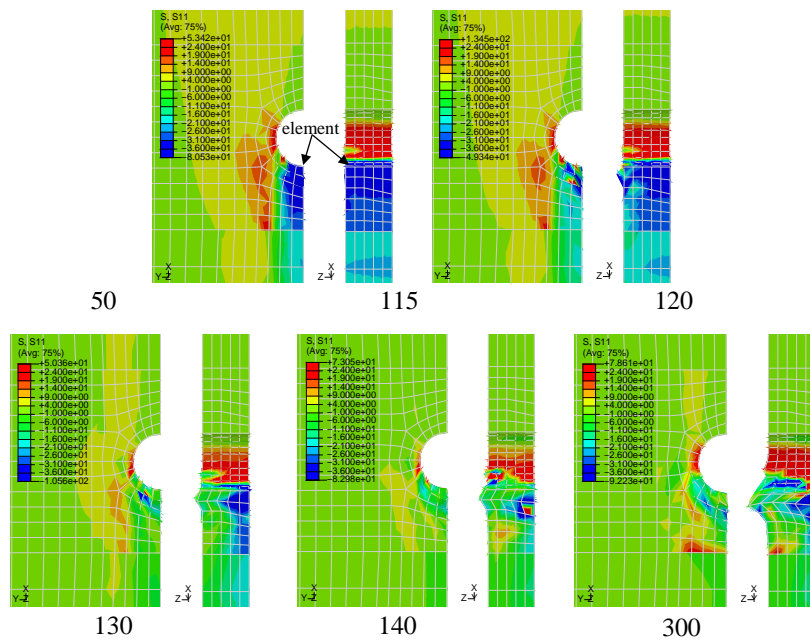


Figure 5-39: Embedment model spruce with 24 mm dowels (quarter); stress component  $\sigma_{11}$ ; at increments 50 (with indication of element), 115, 120, 130, 140, 300

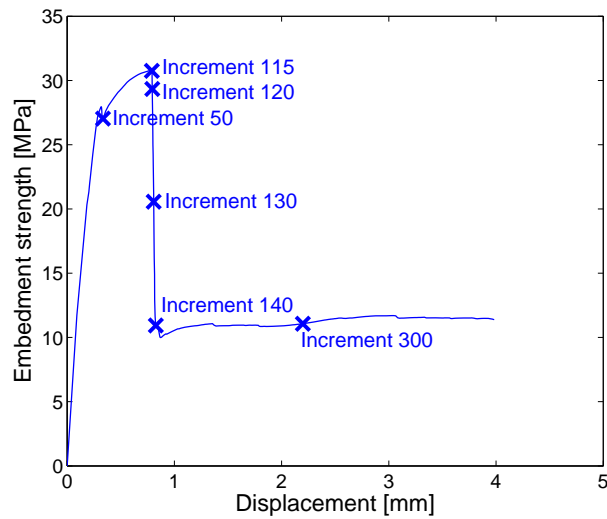


Figure 5-40: Embedment strength – displacement of embedment model spruce with 24 mm dowels

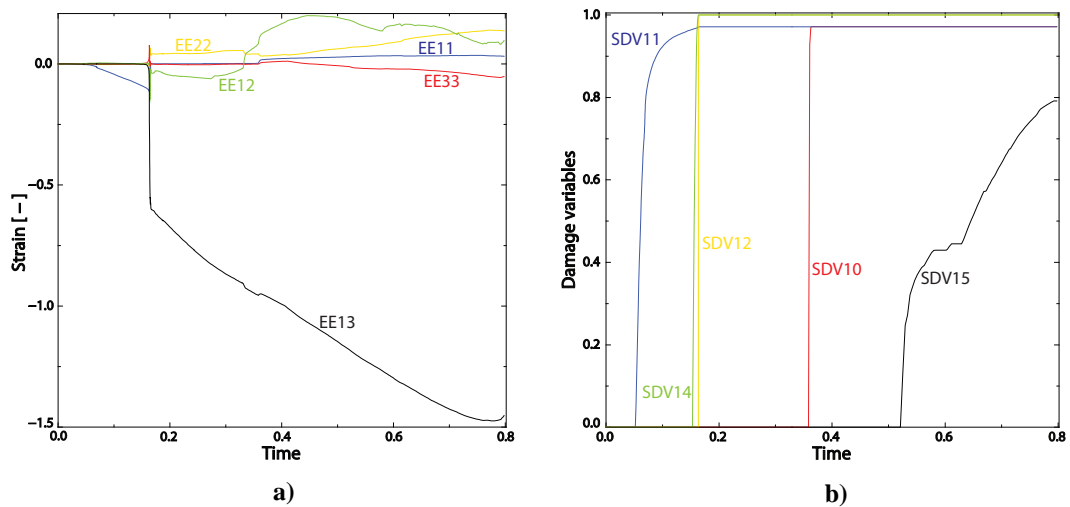
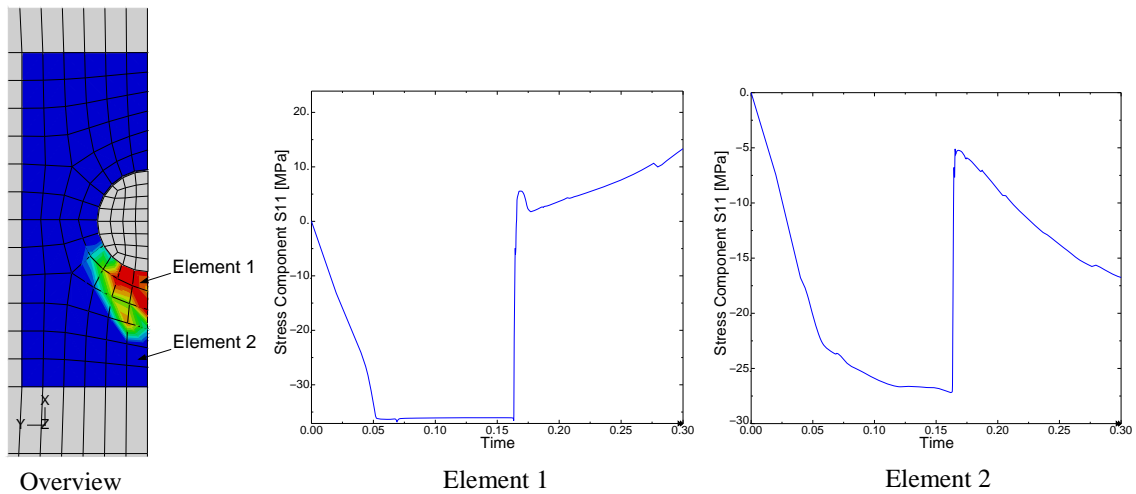


Figure 5-41: a) Strain components of indicated element in Figure 5-39 (increment 50)  
b) damage variables of indicated element in Figure 5-39 (increment 50)

To illustrate the incapability of the model to transfer stresses to the next row of elements once one row has collapsed and distorted excessively, integration point results in terms of stress component  $\sigma_{11}$  are shown in Figure 5-42 for elements in different rows underneath the dowel. It can be seen that once element 1 directly underneath the dowel has failed, element 2 does not take over the load. The stress component  $\sigma_{11}$  of element 2 does not reach the compression strength parallel-to-grain.

Figure 5-43 finally shows the overlap of the default model for 12 mm and 24 mm dowels. The number of elements was the same for both models. As expected, no difference in load carrying capacity can be observed. The different load-slip behaviour is due to the different element size which start to distort excessively at smaller deformations for the models with 12 mm dowels which has smaller elements.



**Figure 5-42: Spruce with 24 mm dowel, typical development of stress component  $\sigma_{II}$  (compression parallel-to-grain) for indicated elements**

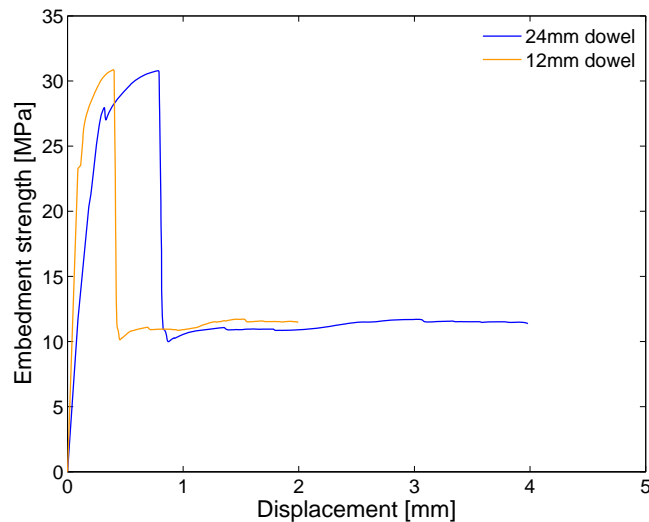


**Figure 5-43: Stress-slip graph of embedment model spruce with 12 mm and 24 mm dowels**

### 5.3.2 Beech

The next models were run with the material properties for beech (Table 5-2). Two meshes were run, the default and the coarse mesh from Figure 5-33. Additionally, two different dowel steel grades, high strength steel (hss) and very high strength steel (vhss), were modelled<sup>21</sup>. Young's modulus and strength properties of the steel were taken from Table 6-1 and the Poisson's ratio was assumed to be 0.3. No difference in load carrying capacity and load-slip behaviour is expected for the different steel grades as the dowels do not bend in embedment models. Figure 5-44 confirms this assumption. Indeed no difference can be observed for the models with hss and vhss. Additionally, the models with coarse mesh can be seen also in Figure 5-44. The same trend as with the spruce models can be observed (see Figure 5-35. For azobé, see Figure 5-45). All deformations of the default models stop at around 1 mm which is not due to failure of the timber, but to local failure of the elements directly underneath the dowel. The failures represent numerical failures that have no physical meaning. Analogously to spruce, also here higher deformations can be reached for the coarse mesh.

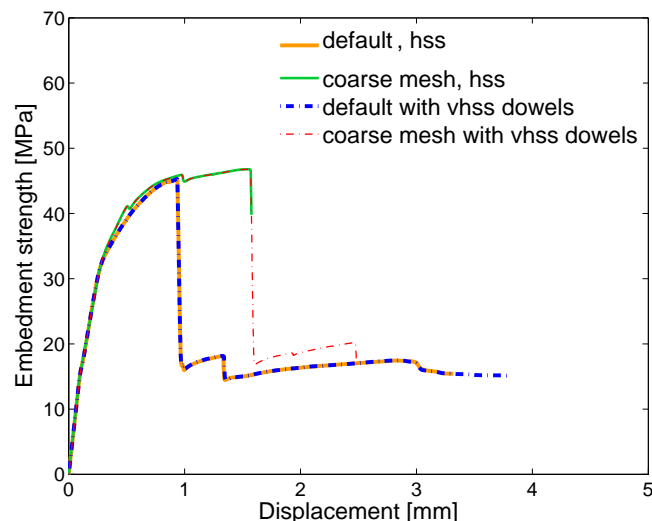


Figure 5-44: Stress-slip graph of embedment model beech with 24 mm dowels, hss and vhss dowels, default and coarse mesh

### 5.3.3 Azobé

Finally, default embedment models (Figure 5-35 with default mesh c) with the material properties for azobé from Table 5-2 were run. This time, the friction coefficient between timber and dowel was changed: the default coefficient  $\mu = 0.5$  was used together with

<sup>21</sup> Instead of hss, mild steel (S235) was ordered. However, tension tests proved that the steel grades corresponded to S520 or S610 and thus to hss instead.

values of  $\mu = 0.1$  and  $\mu = 0.7$ . Figure 5-45 shows the results. As expected, a higher friction coefficient leads to higher embedment strength whereas a lower friction coefficient leads to lower embedment strength.

The overlap of the default model for all three wood species is shown in Figure 5-46. Although the mesh was the same for all species, the beech models reached a higher deformation before the numerical collapse. This indicates that the chosen mechanical properties influence the numerical behaviour and the excessive element distortion. Another interesting finding is the ratio of embedment strengths of the three species. The ratios of embedment strengths reached in modelling do not reflect the ratios of the mechanical properties used for modelling. If considering the mechanical properties used in the models, especially the compression strength parallel-to-grain, then the beech model should show an embedment strength closer to the capacity of spruce. Instead, the embedment strength of beech is considerably closer to the result for azobé. Furthermore, yield drops can be seen for spruce and azobé, but not for beech.

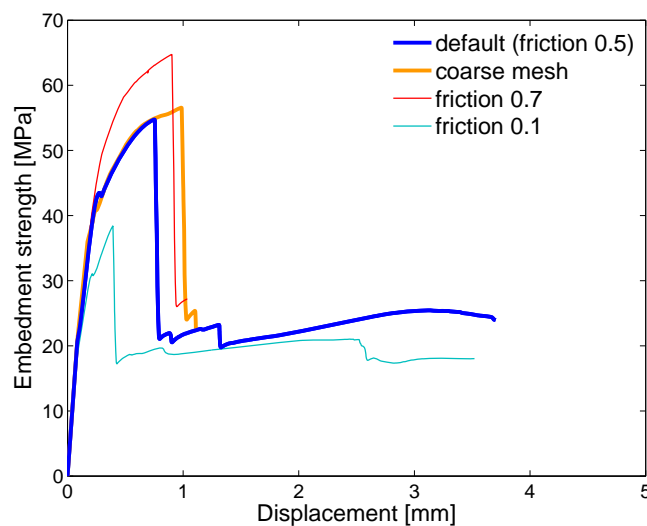


**Figure 5-45: Stress-slip graph of embedment model azobé with 24 mm dowels, three different friction coefficients**

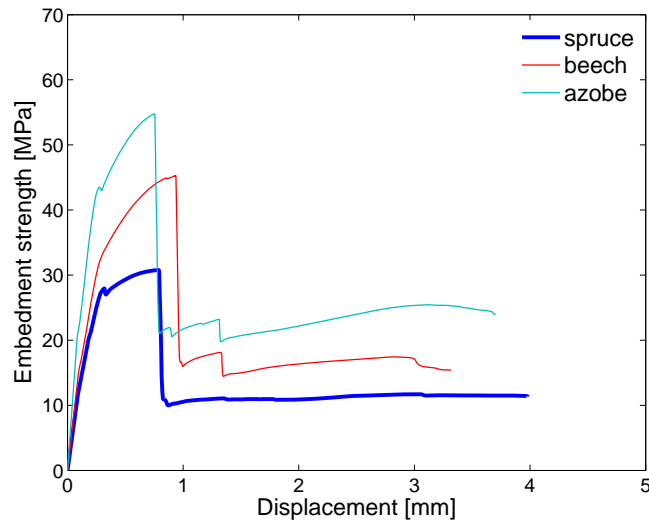


**Figure 5-46: Stress-slip graph of default embedment models spruce, beech and azobé, all 24 mm dowels**

### 5.3.4 Conclusions

The developed material model is able to properly simulate the (initial) nonlinear ductile behaviour of embedment models which is caused by crushing of fibres underneath the dowel. Also initiation of splitting is indicated correctly by perpendicular and shear damage. Different wood species reach different ultimate loads.

However, numerical problems are persistent. The most important issues from the material tests were observed again. All load-slip graphs of the embedment models show initial ductile behaviour. When the first row of elements underneath the dowel distorts excessively, a sudden drop in load carrying capacity occurs after which the models continue to ‘yield’. This brittle softening is not due to material failure, but due to failure of a localised band of elements. It represents a numerical failure with no physical meaning other than that the wood underneath the dowel is collapsed completely being thus an artificial softening. When the elements directly underneath the dowel reach their ultimate 3D load carrying capacity and fail in all material directions, they start to distort excessively leading to a calculation stop. One fundamental problem connected to the excessive distortions is the fact that once the first row of elements is unloading, also all other elements are unloading. These unloading elements do not take higher loads after the collapse of the first row of elements although they did not yet reach their ultimate capacity. In a certain sense the loading is not transferred to the next row of elements, no stress redistribution takes place. Therefore, the localised band of elements directly underneath the dowel governs the global load-slip behaviour.

Mesh dependency seems to be a direct result of this behaviour. Element distortion could be considered as being a ‘geometrical’ effect depending on the element size. The bigger the elements, the bigger the sustainable displacements before collapse. This could be also

observed for the tension models of section 5.2.1 where the models with coarse mesh failed later than the models with fine mesh thus reaching a higher load carrying capacity (Figure 5-10).

The most urgent further research effort must be put into element distortion control and a proper transfer of loads once one band of elements has failed. This transfer of loads is expected to lead to a more ductile behaviour.

## 5.4 JOINT MODELS

The final modelling steps are 3D joint models. Double-shear timber joints with slotted-in steel plates and with one, three and five dowels in a row were modelled. Three different wood species, spruce, beech and azobé, and two different dowel diameters, 12 mm and 24 mm, were simulated. Symmetry planes were used and only a quarter was modelled. The model for a joint with one dowel is shown in Figure 5-47. The models for joints with three and five dowels are analogous and are shown in Figure 5-48. The crack band model was deactivated.

Sensitivity studies with different mesh and problem analyses have been done with the previous material and embedment models. Therefore, the focus of the joint models lies in running all chosen variations as indicated in Figure 5-49. This was done with view of the experimental programme carried out later and whose outcomes can then be compared with the predictions presented here.

The mesh was kept constant for all models and was the same as for the default embedment models<sup>22</sup>. Also the models with 12 mm and 24 mm dowels had the same number of elements which means that the elements of the models with 12 mm dowels were half the size of the elements of the models with 24 mm dowels.

The load-slip graphs of the models are derived as indicated in Figure 5-47a with the force being the sum of the reaction forces in X-direction of the model and the displacement being the displacement in X-direction of the indicated node on the upper outer end of the slotted-in steel plate.

The nomination is as follows:

- First letter indicates wood species: S = spruce, B = beech, A = azobé;
- First number indicates dowel diameter: 12 = 12 mm dowel, 24 = 24 mm dowel;
- Second letter indicates steel grade: C = hss, no C = vhss;
- Second number after dash indicates number of dowels:  
1 = 1 dowel, 3 = 3 dowels, 5 = 5 dowels.

---

<sup>22</sup> Of course, the number of elements over the thickness was different.

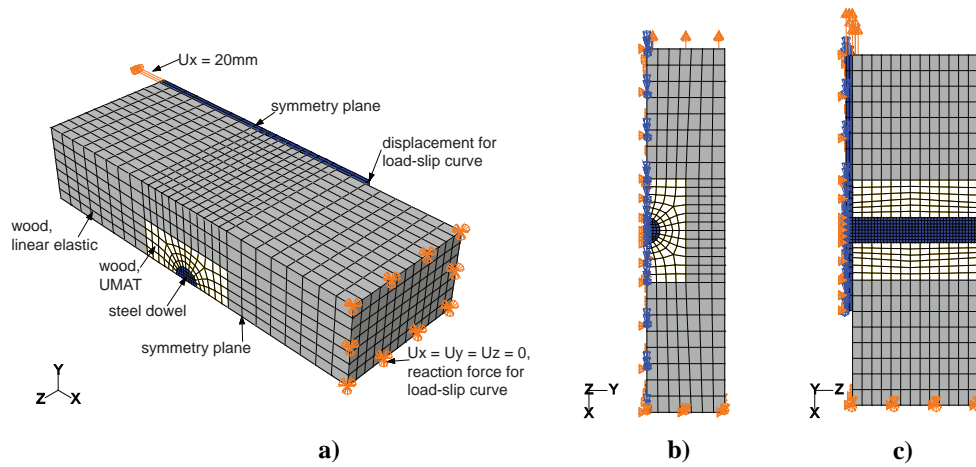


**Figure 5-47: Typical model with one dowel, default mesh and boundary conditions; a) overview, b) symmetry plane in width, c) symmetry plane in thickness**

**Table 5-3: Number of elements of wood specimen around dowels**

	Number of elements in quarter model
dowel diameter	12
in thickness, Z-direction	13
in width, Y-direction	4
in length, X-direction	12

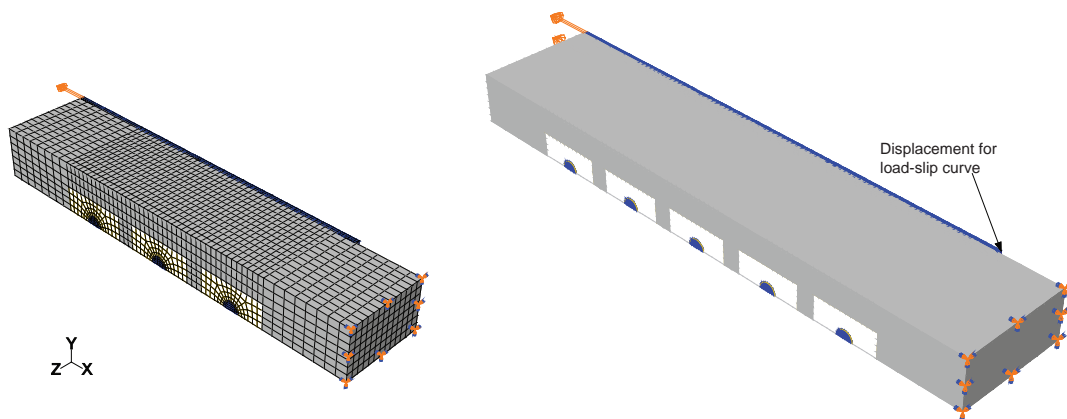


**Figure 5-48: Typical models for joints with three (A24-3) and five dowels (B24C-5)**

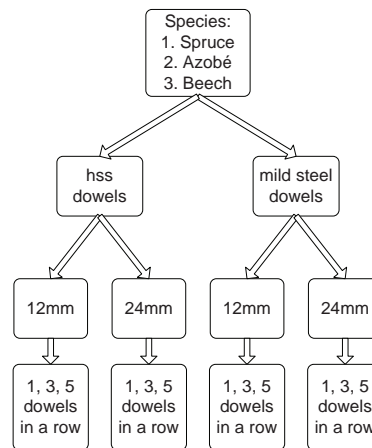


**Figure 5-49: Flowchart of model variations**

The main modelling parameters are summarised below:

- **Steel:**  
Von Mises plasticity with properties from Table 6-1 for high strength steel and very high strength steel, Poisson's ratio  $\nu = 0.3$ .
- **Wood:**  
Only an inner region around the dowel (with half the width of the timber specimen and a height of 3 times the dowel diameter) is modelled applying the developed material model. The outer timber is modelled as linear elastic. Material input values are given in Table 5-2.
- **Friction:**  
Between timber and steel parts  $\mu = 0.5$ ; between steel parts  $\mu = 0.3$ . The stick-slip model with penalty formulation was used.
- **Element type:**  
3D linear blocks with eight integration points were used.

The theory of large displacements was activated. The initial increment size was chosen to 0.001 and automatic incrementation was used. The number of increments was limited to 500.

All geometrical data such as height, dowel spacing or timber member thickness can be taken from chapter 7 where the experimental results will be presented.

#### 5.4.1 Joints with one dowel

Figure 5-50 and Figure 5-51 show the results for all joint models with one dowel where the hss dowels are represented with dotted lines. The increase in load carrying capacity between hss and vhs dowels can be seen. The transition between the elastic and the

plastic regime occurred slower for vhss dowels. Until the initiation of plastification of the hss dowels, the stiffness was the same and increased from spruce over beech to azobé – according to the higher elastic properties of the hardwoods. The load carrying capacity differed for the wood species as expected with azobé reaching the highest load carrying capacity. The observed ‘artificial softening’ started at different displacements which could be assigned to the effect of the different mechanical properties on element collapse. The mesh remained the same for all models.

Representatively for all joint with hss, the results in terms of damage variable  $d_{c,0}$  of the spruce model with one 24 mm hss dowel are shown in Figure 5-52a where the fibre crushing underneath the dowel can be observed. Figure 5-52b shows the stress component  $\sigma_{33}$  to visualise the dowel bending.

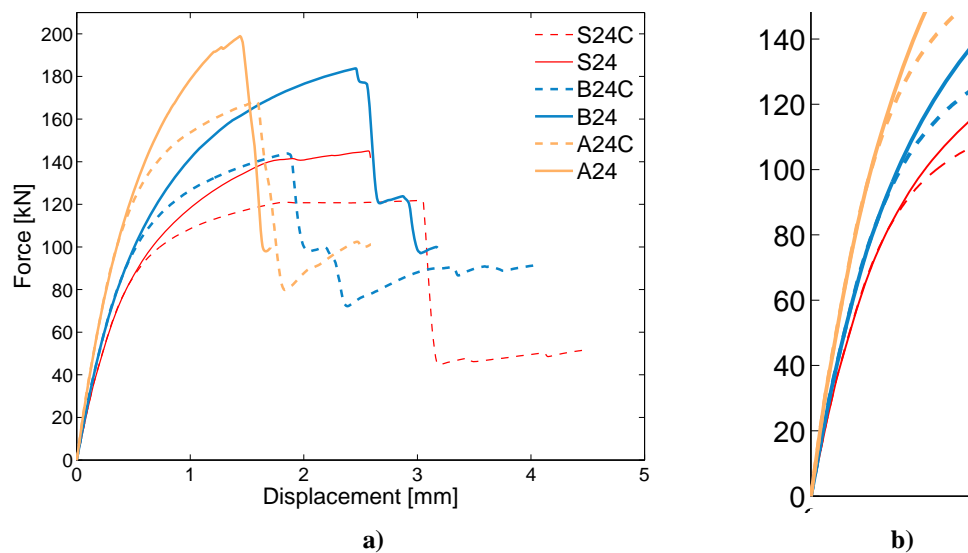


Figure 5-50: a) Load-slip graphs for all models with one 24 mm dowel;  
b) detail of graph

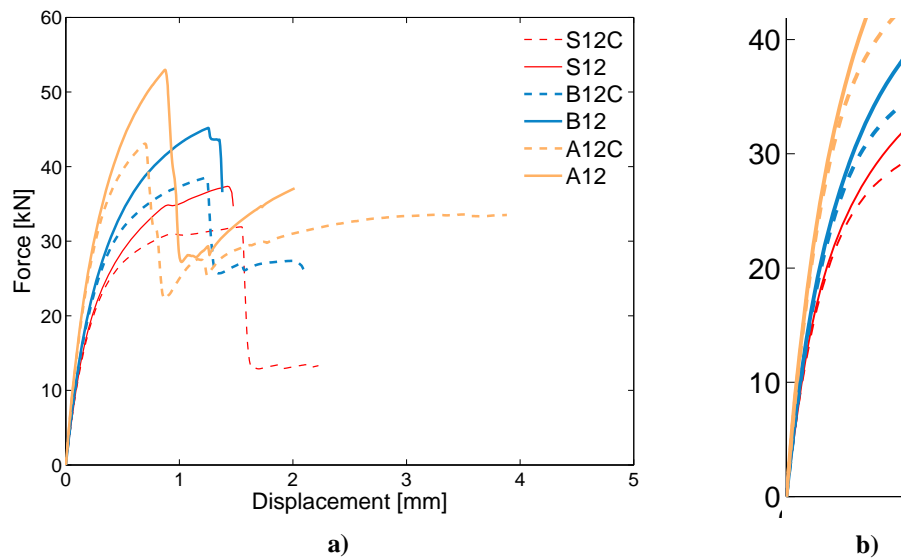


Figure 5-51: a) Load-slip graphs for all models with one 12 mm dowel;  
b) detail of graph

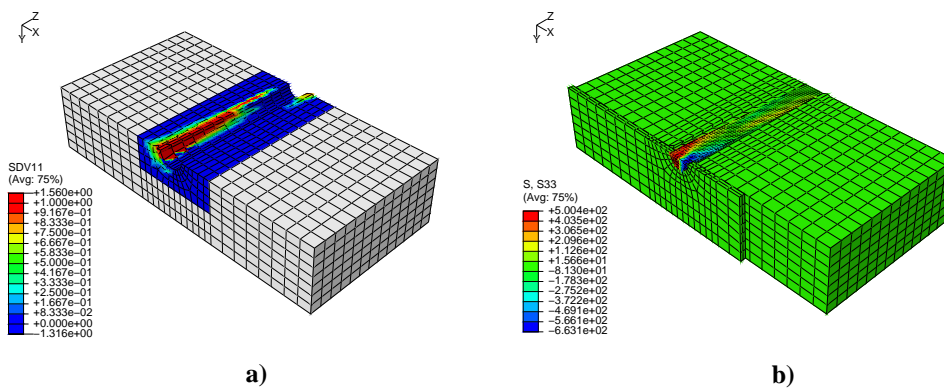
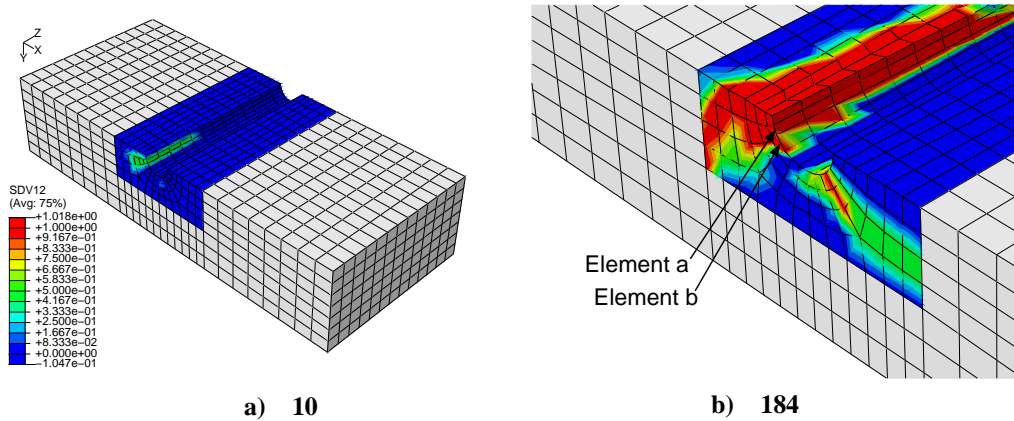


Figure 5-52: Spruce joint with one 24 mm hss dowel at last increment;  
a) damage variable  $d_{c,0}$ , b) Stress component  $\sigma_{33}$

The damage variable  $d_{t,90}$  for the beech joint with one 12 mm v hss steel dowel is shown in Figure 5-53. The stress components  $\sigma_{22}$  and  $\sigma_{12}$  of the indicated elements are given in Figure 5-54 and Figure 5-56. The damage variable  $d_{t,90}$  is coupled to  $d_v$  and  $d_{roll}$ . The shown damage is thus a smeared damage that can be triggered by high transverse tension stresses or high shear stresses. The indicated elements started to fail due to high transverse tension or shear, depending on their location. Element a started to fail in transverse tension whereas element b failed in longitudinal shear. These are correct predictions. Element b which is located on the side of the dowel developed high transverse compression stresses at higher dowel displacements. Also this is correct. The dowel induces compression stresses perpendicular-to-grain when it is embedding in the timber member. In Figure 5-53, also the initiation of splitting can be observed. For

instance, at increment 10, damage  $d_{t,90}$  (and, coupled,  $d_v$ ) started whereas no damage due to compression parallel-to-grain,  $d_{c,0}$ , was observed yet.



**Figure 5-53: Beech joint with one 12 mm vhs dowel at a) increment 10 and b) last increment 184; damage variable  $d_{t,90}$ ; elements a and b indicated**

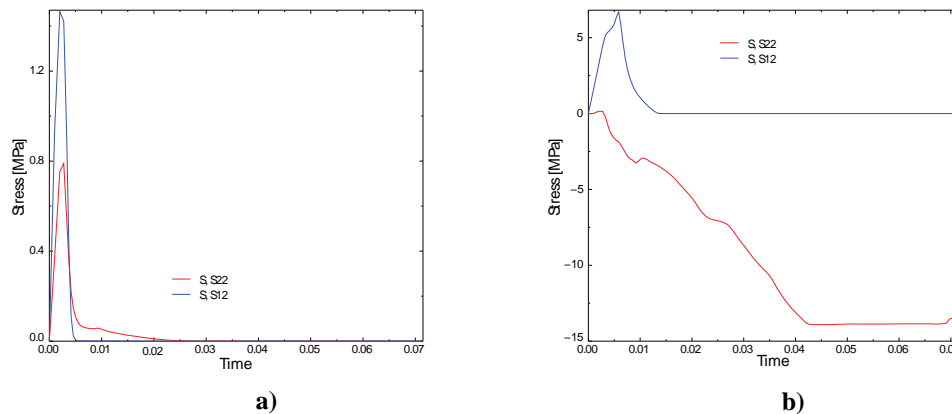


**Figure 5-54: Stress components  $\sigma_{22}$  and  $\sigma_{12}$  of beech joint with one 12 mm vhs dowel; a) element a -  $\sigma_{22}$  governs, b) element b -  $\sigma_{12}$  governs, elements indicated in Figure 5-53**

Joints with one dowel are more ductile than joints with more than one dowel in a row. The global load-slip behaviour can be influenced tremendously by the chosen material parameters. Especially the fracture energies should have a considerable influence on the joint behaviour. A change in material properties should also change the distortion behaviour of the weakest row of elements. A short study modifying material properties for beech joints was done to investigate the sensitivity of the joint models on certain material parameters. A joint with beech was chosen because usually, beech splits later and therefore, beech joints are usually more ductile than spruce or azobé joints (see also section 6.3.4). Figure 5-55 shows the results for a beech joint with one 24 mm hss dowel and different material properties as given in Table 5-4 where the modified material properties are highlighted. It can be seen how fundamentally the joint behaviour was

changing. The model 'iso' with approximately isotropic properties 'yielded' much longer and behaved more stiff. This indicates that it is the low properties perpendicular-to-grain and in shear that led to early nonlinear behaviour. The load carrying capacity also changed considerably. When only the fracture energies in tension perpendicular-to-grain and longitudinal shear were increased (model 'G90.v'), the global behaviour did not change a lot except that after the first artificial softening, a larger ductility was reached. If the transverse tension strength and the longitudinal shear strength were increased together with the fracture energies (model '90.v'), nearly twice the displacement could be reached. This behaviour was similar for the last case with modified material parameters where additionally, the rolling shear strength and fracture energy were increased (model '90.v.roll').

The 'iso' model was repeated for the beech joint with one vhss dowel. The load carrying capacity was higher than for the model with the default material properties and more ductile.

The shown influence of material parameters on the calculation results enhances again the need of further study into how the necessary mechanical properties are derived.

**Table 5-4: Material properties for beech joints**

Parameter	Units	default	'iso'	'G90.v'	'90.v'	'90.v.roll'
$E_{11}$		13000	13000	13000	13000	13000
$E_{22} = E_{33}$		860	860	860	860	860
$G_{12} = G_{13}$		810	810	810	810	810
$G_{23}$		59	59	59	59	59
$f_{t,0}$	MPa	41	41	41	41	41
$f_{c,0}$		45	45	45	45	45
$f_{t,90}$		1.0	<b>41</b>	1.0	<b>10</b>	<b>10</b>
$f_{c,90}$		14.2	<b>45</b>	14.2	14.2	14.2
$f_v$		6.9	<b>40</b>	6.9	<b>10</b>	<b>10</b>
$f_{roll}$		0.5	<b>40</b>	0.5	0.5	<b>10</b>
$G_{f,0}$		100	100	100	100	100
$G_{f,90}$	N/mm	0.71	<b>100</b>	<b>50</b>	<b>50</b>	<b>50</b>
$G_{f,v}$		1.2	<b>100</b>	<b>50</b>	<b>50</b>	<b>50</b>
$G_{f,roll}$		0.6	<b>100</b>	0.6	0.6	<b>10</b>
$\eta$	-	0.0001	0.0001	0.0001	0.0001	0.0001

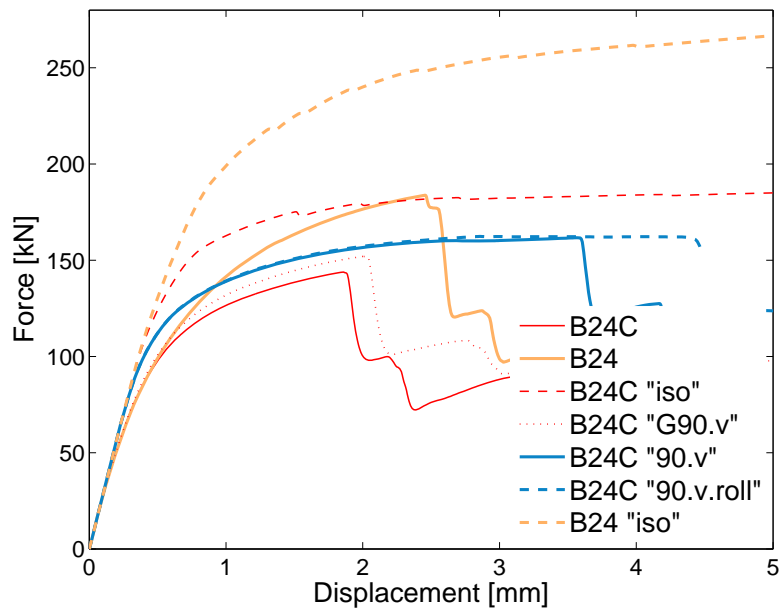


Figure 5-55: Load-slip graphs for beech model with 24 mm hss dowel and different material properties

#### 5.4.2 Joints with three dowels

The models with three dowels in a row were more brittle as can be seen in Figure 5-56. The saw-tooth like behaviour reflected the progressive failure around the dowels. The first dowel with local failure in the row of elements directly underneath the dowel was the one close to the joint end. The simulations of the joints with azobé stopped in the elastic range of the steel dowels when no difference between hss and vhs dowels can be observed. However, damage in the timber members did already take place. This can be seen also in the load-slip curve where a small yield drop can be identified and the curve is not linear. The reason for the premature calculation exit due to convergence problems should be due to the different material properties for azobé. Nothing else in the model was changed. If considering Table 5-2, it can be observed that the ratios between the different material properties change considerably. For instance, the tension strength perpendicular-to-grain and the shear strength do not increase as much as the other strength values. This could lead to convergence problems for azobé, but less for spruce and beech.

Figure 5-57a shows the damage variable  $d_{c,0}$  indicating damage in compression parallel-to-grain for the beech model with three hss dowels. The crushing of fibres underneath the dowels can be nicely seen. In Figure 5-57b, the onset of splitting due to  $\sigma_{22}$  can be observed. The interaction between the dowels led to earlier splitting. The crack initiation also between the dowels is a realistic prediction. If looking at the load carrying capacity of a beech joint with one hss dowel (= 144 kN) in comparison with the load carrying capacity of the same joint with three hss dowels (= 314 kN), a strong decrease in capacity

can be observed. The strength of a joint with three dowels is only 2.2 times the strength of a joint with one dowel.

The same discussion as for the joints with one dowel is valid. Higher ductility can be reached by changing the material parameters where especially the fracture energy is a significant calibration value. Certainly the azobé joint could yield better results when the mechanical properties are adjusted in order to reach higher displacements and thus also higher load carrying capacities.

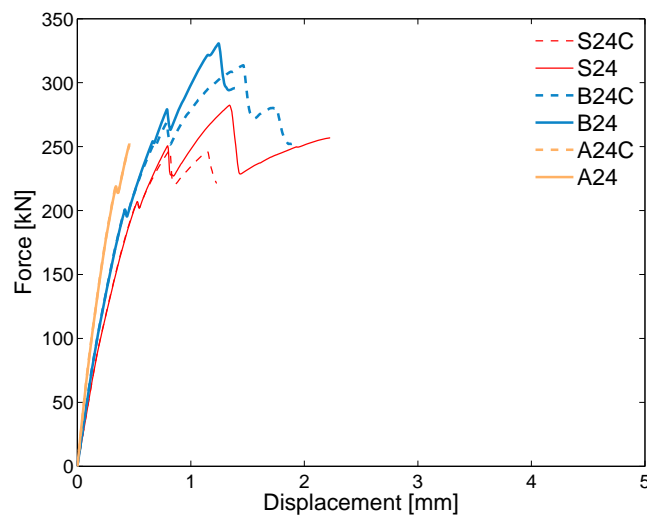


Figure 5-56: Load-slip graphs for all models with three 24 mm dowels

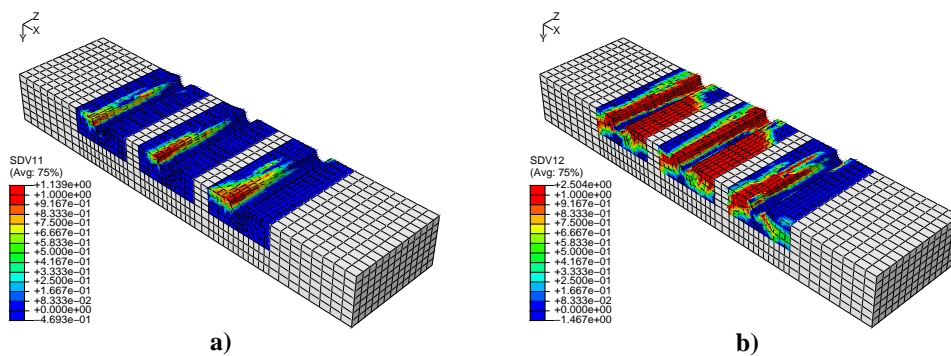


Figure 5-57: Beech joint with three 24 mm hss dowels at last increment;  
a) damage variable  $d_{c,0}$ , b) damage variable  $d_{t,90}$

### 5.4.3 Joints with five dowels

The results for the joints with five dowels are even more brittle. The maximum load carrying capacity cannot be reached at all as can be seen in Figure 5-58. Convergence problems led to an early exit. No dowel bending could be observed yet. However, failure started which led to a nonlinear load-slip behaviour as can be seen in Figure 5-58 where the initiation of cracks can be observed in the slightly saw-tooth shaped curves. Figure 5-59a shows the stress component  $\sigma_{11}$  that indicates the compression stresses directly underneath the dowels. Figure 5-59b shows the initiation of failure in compression parallel-to-grain.

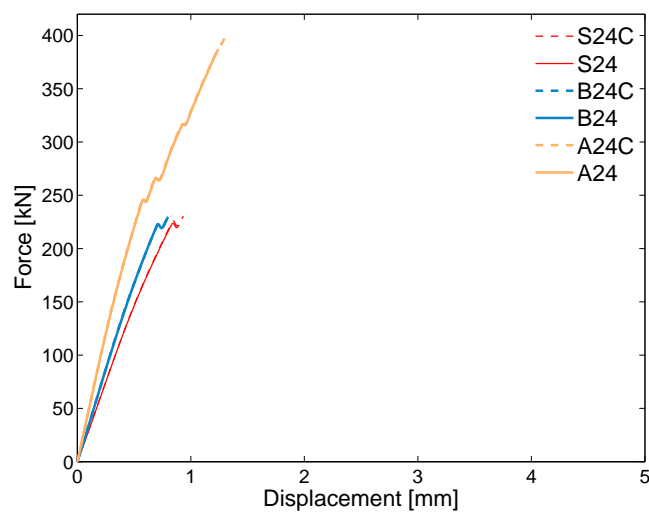


Figure 5-58: Load-slip graphs for all models with five 24 mm dowels

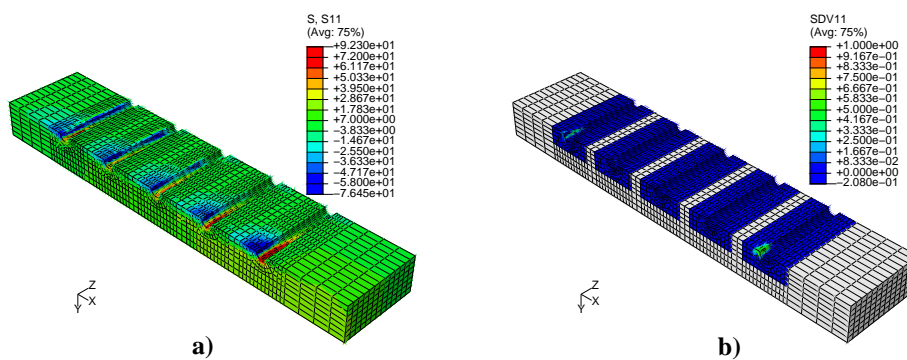


Figure 5-59: Azobé joint with five 24 mm vhs dowels at last increment;  
 a) stress component  $\sigma_{11}$ , b) damage variable  $d_{c,0}$

## 5.5 CONCLUSIONS

A major advantage of the developed material model is the possibility to visualise damage due to different failure mechanisms. For instance, the crushing of fibres underneath the dowel is caused by compression parallel-to-grain and can be identified with the damage variable  $d_{c,0}$ . The other major advantage is the possibility to reproduce ductile behaviour under compression stresses and brittle behaviour under tension and shear not only for uniaxial states of stress, but also for complex 3D structures. These innovative features of the developed mathematical model can be used to thoroughly analyse damage mechanisms that occur during experiments.

The developed material model needs a limited number of material parameters when compared to other approaches (e.g. Grosse, 2005, Fleischmann, 2005) to provide insight in the mechanical behaviour of wood. Furthermore, the used parameters are well-defined mechanical properties that can be derived from experimental results. The material model works in combination with contact algorithms (i.e. friction) and other material models.

The transition from the linear elastic to the nonlinear elastic regime with distinct ductile behaviour due to compression stresses parallel-to-grain is seen in the model predictions. However, the observed load drop at small deformations is not expected to reflect the failure of the timber in splitting or shearing which is expected at higher deformations. This early load drop seen in the model is caused by complete failure of the row of elements directly underneath the dowels and the subsequent lack of load transfer and stress redistribution to the still intact next row of elements. The collapsed elements show spurious energy modes and eventually lead to calculation exit.

As the spurious energy modes are strongly connected to the 3D strength and damage onset of the material model, the modification of the material parameters towards more 'isotropic' material with less strength differences in the different material directions lead to a more robust calculation reaching higher model deformations.

Further research should deal with improvements with regards to the spurious energy modes and the load transfer and stress redistribution between elements. Better element formulations or progressive element deletion could be possible solutions in order to reach higher ductility of the models.



# 6

## COMPONENT TESTS

*The two material parameters that are needed for the design of timber joints are embedment strength of the timber members and bending capacity of the steel fastener. In this chapter, the necessary component tests to establish the two needed input values are presented. Tension tests on the two dowel steel grades used for joint tests are undertaken. Furthermore, dowel embedment tests parallel-to-grain with spruce, beech, azobé, cumaru and purpleheart are carried out. Three of these species are also used for the joint tests.*

*Embedment tests enhance understanding of the mechanical behaviour of the system timber-dowel.*

### 6.1 INTRODUCTION

In order to design timber joints with semi-rigid fasteners, two material parameters are needed. Firstly, the bending capacity of the steel fasteners is needed. The first part of this chapter will discuss tension tests on the same steel dowels that are later used for joint tests. Two steel grades were used, high strength steel dowels and very high strength steel dowels with a mean tension strength of about 1200 MPa.

The second part deals with embedment tests. Just like the tension tests on steel dowels, the embedment tests were carried out as pretests for joint tests. Embedment tests are less complex tests than joint tests and it is thus simpler to understand the contribution of certain aspects such as wood species, steel grade or dowel diameter to the global mechanical behaviour. This also explains the importance of embedment tests for modelling. The model control and calibration is straightforward. The validity and reliability of models are verified more easily.

The equations given in the European timber design code EC5 (CEN, 2004b) for different dowel-type fasteners such as nails, bolts and dowels are valid for all timber species and depend on the fastener diameter and the material (characteristic) density.

In previous research (Whale and Smith, 1986b, Whale and Smith, 1986c, Ehlbeck and Werner, 1992b, Hübner et al., 2008, Vreeswijk, 2003), tests were carried out on softwood, European and tropical hardwoods. Own test results on the wood species spruce, beech, azobé, cumaru and purpleheart were added to this already existing database. The extended database was analysed with regards to equations for joint design. Differences between wood species and steel grades are discussed more thoroughly as this may be relevant also for joint analyses. A thorough discussion of the embedment test results can be found in Sandhaas et al. (2010).

## 6.2 TENSION TESTS ON STEEL DOWELS

The ordered 12 mm dowels were of steel grade 12.9 (vhss) and galvanised S235 (mild steel). The 24mm vhss dowels were obtained through a thermal treatment from 42CrMoS4 alloy steel (CEN, 2006) whereas the 24 mm galvanised mild steel dowels were made from 11SMnPb30 (CEN, 2008), a free-cutting steel grade. Standard tensile tests have been carried out and the results can be seen in Table 6-1. All results, graphs and steel certificates are given in Appendix A.

**Table 6-1: Results of tension tests on steel dowels**

Steel grade	diameter	number of specimens	MoE [MPa]		$R_{p0.2}$ [MPa]		$R_m$ [MPa]		strain at failure [%] (number of specimens)
			mean	COV	mean	COV	mean	COV	
vhss	12	5	219242	3.8%	1324	9.4%	1399	9.5%	7.29 (2)
	24	7	210883	2.2%	1297	1.6%	1379	1.0%	11.54 (2)
hss	12	6	199851	9.9%	609	19.4%	638	16.3%	9.96 (2)
	24	3	215367	10.0%	517	16.2%	541	14.9%	12.72 (2)

For the vhss dowels, a mean proof strength at 0.2% extension of  $R_{p0.2} = 1311$  MPa and an ultimate strength of  $R_m = 1389$  MPa was found. The ordered mild steel did not correspond to mild steel grades, but to hss grades with mean values of  $R_{p0.2} = 563$  MPa and  $R_m = 590$  MPa. Obviously, their mechanical properties are considerably higher than the values for S235 which was the ordered steel grade.

For a lesser quantity of specimens, extensometers were used to record the strain at failure. As can be seen in Table 6-1, around 10% strain at failure could be reached for vhss. However, the strength values found for 12 mm and 24 mm dowels were quite different. For the hss dowels, the steel grade was simply different for the two diameters (even within the diameters – see Table A-1 results for 12 mm hss dowels). As for the vhss dowels, the 24 mm dowels were produced by thermal treatment from steel 42CrMoS4. Standard bolts M12 12.9 were used as 12 mm dowels instead. This explains the differences in results. The two dowel diameters were of different origin.

Especially the results for the ‘mild steel’ dowels did not meet the expectations. S235 was ordered for the 12 mm dowels, but the actual strength values are much higher and are corresponding to hss. Furthermore, no hardening could be observed at all (for this, please refer to Figures A-1 to A-5 where the stress-strain curves of the tension tests are given). The difference between  $R_{p0,2}$  and  $R_m$  was much less than expected which is an important finding. It seems that the dowels had undergone a mechanical and/or thermal treatment which completely changed their mechanical properties.

A closer look was given to the surface roughness. Since the surface roughness is an important parameter influencing the embedment strength as shown by Rodd (1973), the roughness of the used dowels was measured at eight points per dowel. Table 6-2 gives the results. However, no significant difference could be measured between hss galvanised and black vhss steel dowels. Quite the contrary, the hss dowels had a slightly rougher surface than the vhss dowels. Therefore, also Vickers hardness tests were carried out. The vhss steel dowels were more than twice as hard as the hss dowels.

**Table 6-2: Surface roughness measurements on dowels**

	hss dowels (galvanised), n = 56	vhss dowels (black), n = 64
Mean diameter	23.94 / 11.96 mm	23.97 / 11.78 mm
mean surface roughness Ra	0.88 $\mu\text{m}$	0.80 $\mu\text{m}$
COV of Ra	34.8%	30.1%
Mean Vickers hardness	221 HV	492 HV

As stated in the beginning, the plastic bending capacity of the steel dowel is needed in order to design timber joints. Therefore, this issue is discussed more thoroughly in the following.

Two equations are available for the calculation of the bending capacity of a dowel. The yield moment of the dowels can be calculated with Equation (6-1) from mechanics for the full plastic capacity or with the empirical regression equation (6-2) from EC5 (CEN, 2004b).

$$M_y = f_{y,k} \frac{d^3}{6} \quad (6-1)$$

$$M_y = 0.3 f_{u,k} d^{2.6} \quad (6-2)$$

where  $M_y$  = plastic moment in [kNm],  $d$  = dowel diameter in [mm],  $f_{u,k}$  = characteristic ultimate strength in [MPa],  $f_{y,k}$  = characteristic yield strength in [MPa].

The background of Equation (6-2) is explained in Blaß et al. (2000). It is assumed that dowels reach their full plastic capacity at bending angles of 45°. However, observed

bending angles of dowels in joints are much less than  $45^\circ$  (Jorissen, 1998). This means that only the outer areas are under plastic strain and that subsequently not the full plastic capacity is used. The activated bending moment of the dowel will lie between the elastic and the fully plastic capacity.

EN 26891 (CEN, 1991) states that joints should be tested up to ultimate load or up to a deformation of 15 mm. A slip of 15 mm however means that thin dowels approach a full plastic hinge whereas thick dowels will not as they will have to deform much less to reach a global joint deformation of 15 mm. Equation (6-2) was derived based on the above considerations as it was argued that the theoretical Equation (6-1) is not safe enough as the calculated theoretical bending capacity of the dowels is too high.

Furthermore, Equation (6-2) uses the ultimate strength  $f_u$  of the dowels by arguing that the ratio of  $f_y/f_u$ , the strain hardening, has a certain value. The yield strength  $f_y$  is substituted as a percentage of the ultimate strength  $f_u$ . Blaß et al. (2000) stated explicitly that such a derivation of the effective bending capacity is conservative for a high tension strength of the fasteners and a low density of the wood.

However, nowadays high performance vhss dowels are available that show considerable yielding without brittle behaviour. The ratio of  $f_y$  over  $f_u$  is significantly changing for vhss in comparison to mild steel. There is a smaller difference between ultimate and yield strength for vhss. Basically the yielding plateau is not existent and as can be seen in Table 6-1, the ratio of  $f_y$  over  $f_u$  is around 0.94 whereas it is around 0.65-0.70 for mild steel of grades S235 and 355. Equation (6-2) was derived for mild steel dowels and is punishing for vhss dowels (Figure 6-1). Furthermore, as shown in Figure 6-1, the influence of the fastener diameter is getting more significant for bigger diameters.

The difference of ordered steel grades and actually delivered steel grades points out an important issue for timber design. Maybe not only minimum, but also maximum properties of the steel fasteners should be given. Failure modes of joints could completely change if much higher steel grades with higher bending capacities are used.

In this research, also the most unfavourable combination ‘vhss and 24 mm dowels’ was used. The argumentation above motivates the choice of Equation (6-1) in order to predict the load carrying capacity of the timber joints. Generally, the prediction using Equation (6-2) from EC5 should be better for the thinner 12 mm dowels and for mild steel. Equation (6-1) instead should deliver better predictions for the thicker 24 mm dowels and vhss – provided that the deformation of the joint at failure is big enough.

Figure 6-2 illustrates another reason why the theoretical Equation (6-1) should be chosen. It can be seen that the plastified region is fastly increasing with increasing deformation angles of a 12 mm dowel (definition of increase of plastification  $x$  is given in Figure 6-3). This means that apparently even with small deformation angles a large section of the dowel is already plastified.

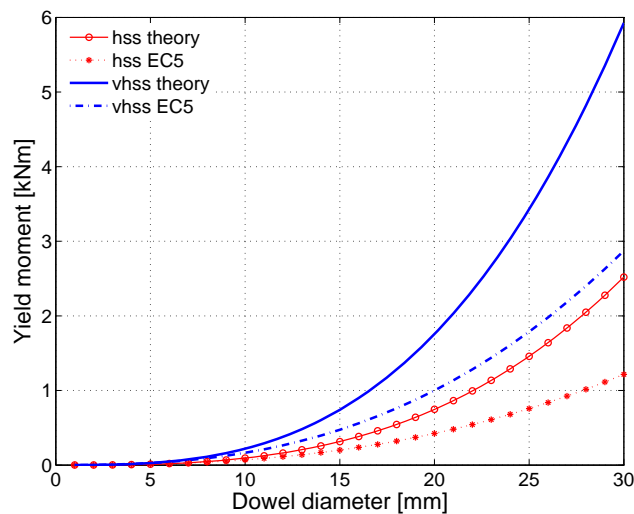


**Figure 6-1: Relationship between steel grades, diameter and yield moment of the dowel (values for  $f_y$  and  $f_u$  given in Table 6-1)**

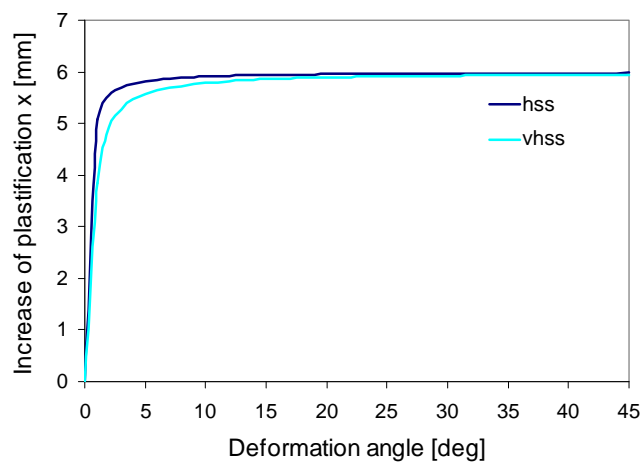


**Figure 6-2: Increase of plastification for a 12 mm dowel with increasing deformation angle**

An important remark is on the influence zone as defined in Figure 6-3. This influence zone is needed to derive the outer strains depending on the bending angle. Here, an influence zone of half the diameter was chosen. However, this is a simplified assumption. Per steel grade for instance, the influence zone will change.

Figure 6-4 finally shows the development of the ‘true’ moment of a 12 mm dowel of mild steel and vhss with increasing bending angles and thus increasing plastification. The value of the moment at  $x = 0$  is the elastic moment  $M_{el}$  and at  $x = r = 6$  mm it is the fully plastic moment  $M_{pl}$  (Equation (6-1)).

The development of the ‘true’ moment is gradual. The full plastic moment is only reached at about 85% of the radius. But as seen, a plastification of about 85% of the radius is reached already at small bending angles.

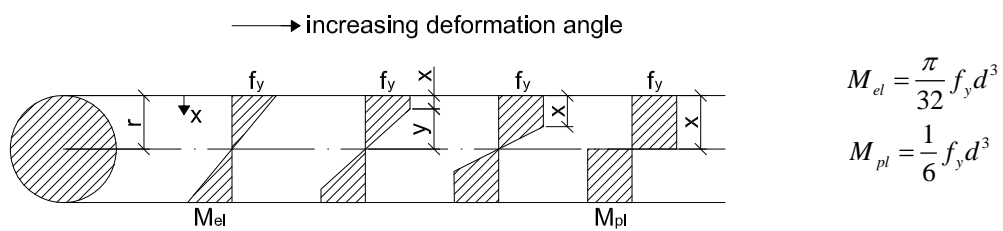
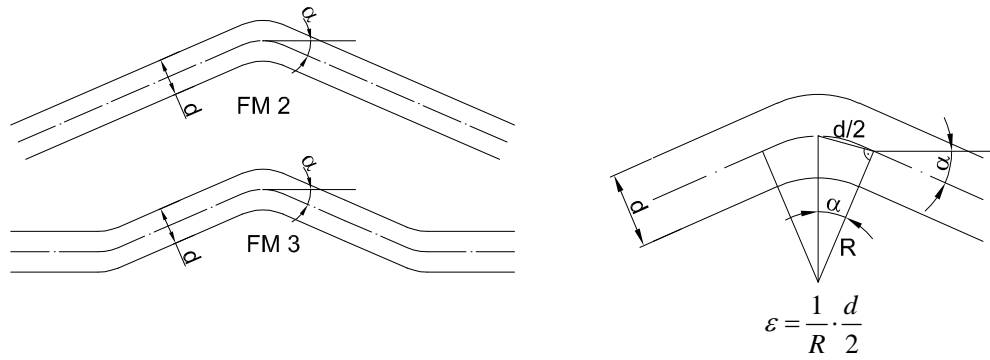


Figure 6-3: Geometrical definitions

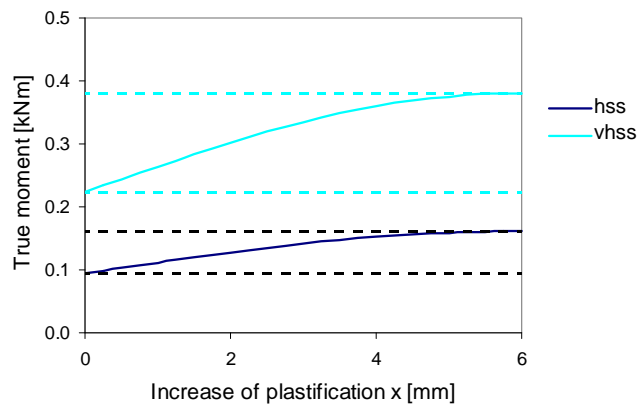


Figure 6-4: Development of true moment with increasing plastification, 12 mm dowel

## 6.3 EMBEDMENT TESTS

### 6.3.1 Literature review

The European method to determine embedding strength described in EN 383 (CEN, 2007) was developed by Whale and Smith (1989). The existing design rules used in EC5 (CEN, 2004b) are based on their research results (Whale and Smith, 1986a) and those of Ehlbeck and Werner (1992a). The test range (Whale and Smith, 1986b, Whale and Smith, 1986c, Ehlbeck and Werner, 1992b) was from softwood over European hardwood to tropical hardwood. Recent experimental research was performed by Sawata and Yasumura (2002) on Japanese pine and Hübner et al. (2008) on clear specimens of European hardwood. Both studies resulted in especially large databases with 1000 and 2187 specimens, respectively. In Hübner et al. it is stated explicitly that 30 specimens should be tested per series in order to create statistically reliable databases. Furthermore, Hübner et al. investigated the embedment behaviour of specimens with different moisture content. Vreeswijk (2003) carried out embedment tests focussing however on tropical hardwood.

A remark is given at this stage on the testing method as defined in EN 383. The European test is a full-hole test whereas for instance the relevant American standard ASTM D5764-97a (ASTM, 2007) also provides a scheme for a half-hole test. There are ongoing discussions about these two testing setups. Some researchers prefer the half-hole tests in order to surely avoid fastener bending. However, it is the author's opinion that half-hole tests are not correctly representing embedment as the influence of the wood on the side and above the fastener is not taken into account. If looking at numerical modelling of embedment tests for instance, all wood material around the fastener is stressed and can therefore not be neglected (Figure 4-50 in Schoenmakers (2010) gives a good example for a test perpendicular to the grain). Furthermore, by choosing a thin enough specimen, fastener bending is not considered as being of relevance. Unfortunately, no comparative studies seem to be available where tests applying both protocols were done.

The sampling of the specimens was similar for Whale and Smith (1986b), (1986c) and Ehlbeck and Werner (1992b) who sampled based on density considerations. Ehlbeck and Werner for instance sampled respecting the following two conditions. Firstly, the mean density of all specimens of one wood species had to lie between 1.05 and 1.25 times the 5%-fractile of the density (calculated assuming a Gaussian normal distribution). Secondly, the density of every single specimen should not be less than 90% or more than 110% of the mean density of the test series. In Hübner et al. (2008) tests were performed on clear wood whereas in Vreeswijk (2003), the sampling was random.

All above-mentioned research was carried out according to EN 383 and the results may therefore be compared. For the assembling of the database however, only embedment properties parallel-to-grain were considered. The test results of Sawata and Yasumura (2002) and Hübner et al. (2008) were not considered. Whale and Smith (1986b), (1986c) and Ehlbeck and Werner (1992b) used tension and compression test specimens, the tests

in Vreeswijk (2003) were carried out only in compression. In Ehlbeck and Werner, it was concluded that compression tests usually led to lower embedment strength values. In the database of Whale and Smith, the same trend could be observed with a maximum difference between tension and compression results of 9% for the tests with 20 mm dowels on Sitka spruce, where the compression test results themselves already had a coefficient of variation (COV) of 18.6%. Therefore, no distinction was made between tension and compression tests.

A difference laid in different specimen geometries as shown in Figure 6-5. The low width of the specimens of Whale and Smith with 3d is remarkable.

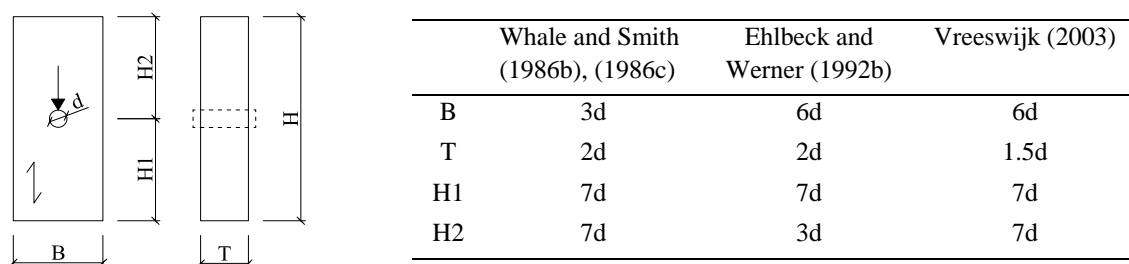


Figure 6-5: Embedment test specimens and geometry

The tests were carried out up to different maximum deformations by the different authors. Whale and Smith stopped the tests at a maximum displacement of 2.1 mm, but not all specimens reached this deformation limit. In Ehlbeck and Werner, tests were carried out up to 5 mm displacement. Also here not all specimens reached the limit before splitting. Vreeswijk instead continued testing up to final splitting. All authors used wood from a 20/65 climate chamber. Whale and Smith and Vreeswijk measured the moisture content at testing. Further conclusions were given in Ehlbeck and Werner. They concluded that the dowel diameter did not influence embedment strength of azobé (*Lophira alata*). They also observed quite different deformation behaviour of beech (*Fagus sylvatica*) in comparison to other European hardwoods. In general, wood with higher densities (most tropical hardwoods) was more susceptible to splitting than European hardwood with lower density values.

The final remark on past research concerns the equations with whom the embedding strength is determined and which are different in different standards.

In EC5, the characteristic embedding strength of dowelled or bolted joints is determined according to Equation (6-3):

$$f_{h,0,k} = 0.082(1 - 0.01d)\rho_k \quad (6-3)$$

where  $f_{h,0,k}$  = characteristic embedding strength parallel-to-grain in [MPa],  $d$  = dowel diameter in [mm] and  $\rho_k$  = characteristic density in [ $\text{kg}/\text{m}^3$ ].

As already stated, Equation (6-3) was derived from research by Whale and Smith (1986a) and Ehlbeck and Werner (1992a) depending on diameter and density. Steel type and moisture content were not varied. The step from mean values to characteristic values was done by replacing mean density by characteristic density. The regression coefficients were not changed.

### 6.3.2 Test setup and specimens

The tests were carried out at Karlsruhe University according to EN 383 (CEN, 2007), the European standard for embedment tests. The test setup shown in Figure 6-6 basically corresponded to the embedment tests of Ehlbeck and Werner (1992b). Two transducers were measuring the displacement of the wooden specimen with respect to the test rig. In order to do so, a pin was inserted in a small hole 37 mm above the loaded zone (see Figure 6-6b). By inserting the pin through the wood, asymmetry could be avoided. An even more precise method is described in Vreeswijk (2003), where tests were carried out by actually measuring the displacement of the bolt with respect to the wooden specimen leading to a more complex test setup, but also to more precise results because then, all external influence was avoided and the real behaviour of the steel-timber system was measured.

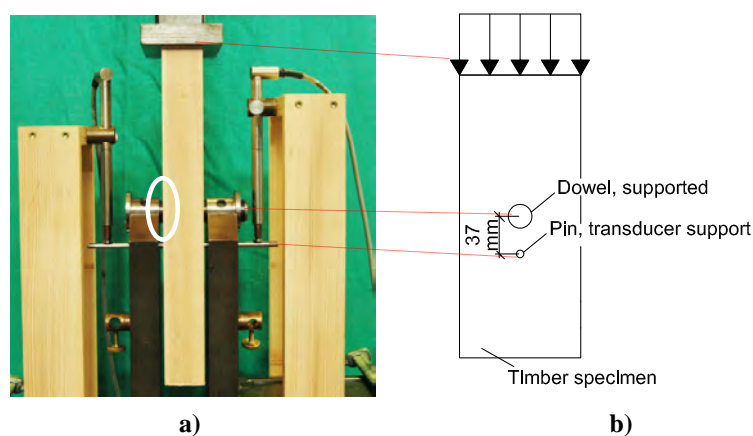


Figure 6-6: Setup embedment test, a) specimen in rig with transducers, b) drawing

All embedment tests were carried out parallel to the grain with dowel diameters of 12 mm and 24 mm of two different steel grades. The same dowels were used in the joint tests later on. The dimensions of the test specimens were the same as in Vreeswijk (2003) (see Figure 6-5) except for the thicknesses which were rounded: 20 mm for the tests with 12 mm dowels and 40 mm for the tests with 24 mm dowels. The distance between the test rig and the specimen (indicated with an ellipse in Figure 6-6) was varied due to different embedment behaviour of the species with a maximum distance of 5 mm on each side. However, the dowels remained straight ensuring thus an approximately uniform stress distribution. Another variation of the tests was an insertion of a Teflon strip between

load-transferring steel plate and timber specimen. No statistically relevant difference, not even in the length of the ductile branch, could be observed with and without Teflon.

In Table 6-3, all test specimens are listed together with their densities and moisture contents. The number of specimens is given and the varied parameters during the test such as steel grade of the dowels.

The spruce and beech test specimens were stored in a climate chamber at normal climate 20/65. The tropical hardwood instead was stored in a 20/85 climate chamber except for 11 azobé specimens which were stored in a fog chamber. The tropical hardwood specimens were sawn from beams which had undergone four-point bending tests. The static MoE and MoR is thus known.

**Table 6-3: Embedment test specimens**

Wood species	Density [kg/m <sup>3</sup> ]		Moisture content [%]		Dowel diameter			
	mean	COV	mean	COV	12 mm		24 mm	
					hss	vhss	hss	vhss
Spruce ( <i>Picea abies</i> )	465	7.9%	12.7	8.5%	7	6	5	5
Beech ( <i>Fagus sylvatica</i> )	683	7.3%	11.9	4.8%	5	5	5	5
Purpleheart ( <i>Peltogyne</i> sp)	881	14.6%	14.8	5.2%	5	7	5	5
Cumaru Peru ( <i>Dipteryx odorata</i> )	918	4.8%	14.6	5.1%	7	7	5	5
Cumaru Brasil ( <i>Dipteryx odorata</i> )	1166	2.3%	13.0	5.3%	3	8	-	-
Azobé ( <i>Lophira alata</i> )	1067	4.6%	20.5	11.1%	7	11	5	5
Azobé wet ( <i>Lophira alata</i> )	1226	2.8%	43.3	7.2%	-	6	-	5

The grain direction and position of the annual rings of the test specimens was observed. For beech, the position of the annual rings may, at least partially, explain the behaviour of the specimens as will be discussed in section 6.3.4. The spruce specimens were of low density with annual ring widths of up to 7 mm. Azobé had interlocked grain. The maximum observed slope of grain was about 8° of one azobé specimen which constitutes a low value. The main grain direction of the rest of the specimens was parallel to the force direction.

Not all the test specimens reached 5 mm displacement before splitting. In order to be sure that embedment tests were carried out and no splitting tests, a reinforcement as shown in Figure 6-7 was glued onto some specimens, at a distance of 1.5d from the hole to exclude stress field interferences. The maximum force did not change. The displacement

capability was increased by the reinforcement as could be expected (see Figure 6-8). The specimens were thus not separated in further analysis.

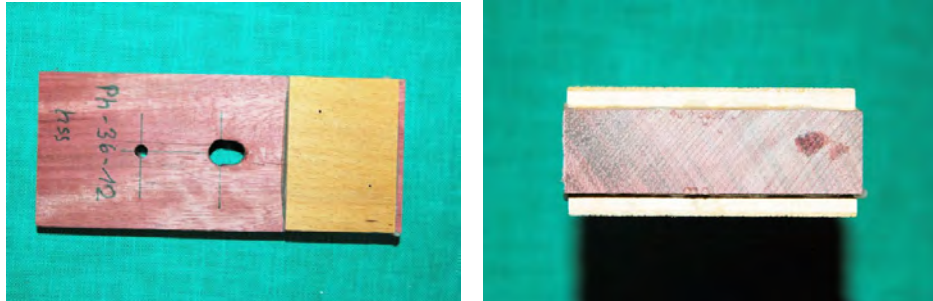


Figure 6-7: Purpleheart specimen with reinforcement, 12 mm vhss dowel

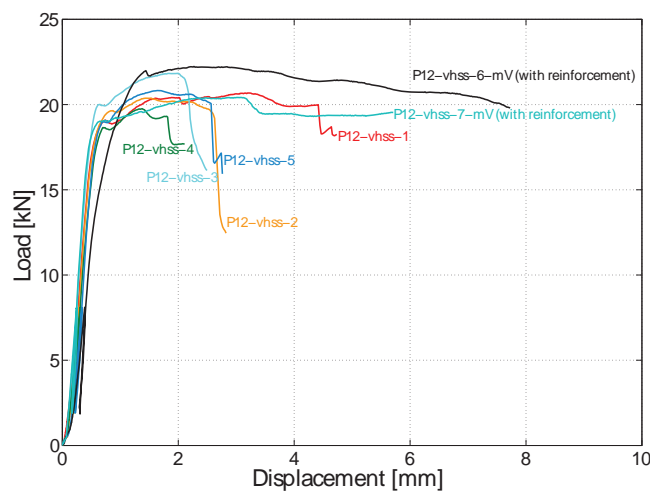


Figure 6-8: Purpleheart, 12 mm vhss dowel

### 6.3.3 Test results

In total 139 tests were carried out with at least five specimens per series. Table 6-4 lists the test results and the theoretical embedding strength calculated with Equation (6-3) where the measured density of the test specimens was used instead of the characteristic density. The results are listed separately for the two steel grades. A trend can be observed: the tests with vhss dowels reached higher load carrying capacities than the tests with hss dowels. As the dowels remained elastic and Young's modulus is the same for both steel grades, an explanation from literature is the influence of different surface roughnesses (Rodd, 1973). However, no different surface roughness was measurable as shown in Table 6-2 and therefore, it cannot be the reason for the different behaviour. The only measurable difference between hss and vhss steel dowels was a different hardness. It

is astonishing how clearly the trend of different embedment strengths for different steel grades can be seen, even considering the scatter of the test results.

In literature, the moisture content of the specimens was not varied, except for Hübner et al. (2008), where embedment tests on ash specimens were carried out with mean moisture contents of 4.4%, 16.3% and 18.9%. A decrease of the embedment strength parallel-to-grain between 4% and 21% with increasing moisture content could be observed. This trend is confirmed with the test results for azobé. The specimens stored at 20/85 with a mean m.c. of 21% reached a mean embedding strength of 75 MPa. The specimens coming from the fog chamber had a mean m.c. of 43% and a mean embedding strength of 63.5 MPa which results in a strength decrease of about 2% for 1% moisture content increase if linearly interpolated up to fibre saturation point.

The following graphs show mean load-deformation data per series. The graphs were averaged until the first specimen of one series failed. The ultimate deformation may thus be different for the single test results (see Appendix). Figure 6-9 shows mean load-deformation curves for the azobé series. The difference between vhss and hss and also between dowel diameters can be seen.

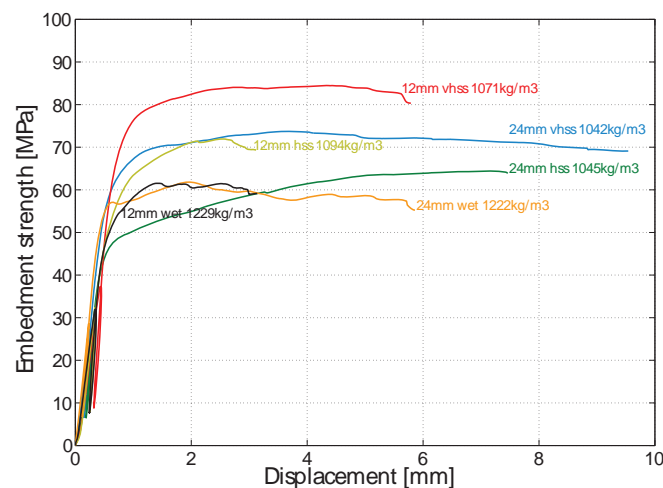


**Figure 6-9: Mean stress-deformation curves per series, azobé**

Figure 6-10 shows mean load-displacement graphs for all specimens with 12 mm dowels of vhss steel. Interesting is the difference of the cumaru wood from two different sources as can be also seen in Table 6-4. The differences in ductility between species with similar densities such as azobé and purpleheart are pronounced. Figure 6-11 shows two typical specimens after testing.

**Table 6-4: Test results embedment tests**

Wood species	Dowel diameter	Steel grade	n	Moisture content [%]		f <sub>emb</sub> (test) [MPa]		Density [kg/m <sup>3</sup> ]		f <sub>emb</sub> (vhss) / f <sub>emb</sub> (hss)	f <sub>emb, EC5</sub> [MPa]	f <sub>emb</sub> (test) / f <sub>emb</sub> (EC5)
				mean	COV	mean	COV [%]	mean	COV [%]			
Spruce	12	hss	7	13.3	10.4	24.6	14.8	482	6.6	1.28	34.8	0.71
		vhss	6	12.7	10.9	31.4	13.9	444	12.4		32.0	0.98
	24	hss	5	12.3	3.1	28.2	8.3	469	5.9	1.35	29.3	0.96
		vhss	5	12.4	2.5	38.0	8.4	463	3.0		28.9	1.32
Beech	12	hss	5	11.8	0.9	46.5	17.0	644	1.5	1.12	46.5	1.00
		vhss	5	11.8	0.8	52.2	6.7	633	3.0		45.9	1.14
	24	hss	5	12.1	6.1	49.8	2.7	725	4.2	1.18	45.2	1.10
		vhss	5	12.0	7.8	58.6	2.3	730	2.4		45.5	1.29
Purple-heart	12	hss	5	14.0	3.8	70.0	17.1	955	2.3	1.24	68.9	1.02
		vhss	7	14.6	4.3	87.0	4.2	949	2.8		68.4	1.27
	24	hss	5	15.5	2.3	52.4	27.5	792	19.3	1.24	49.3	1.06
		vhss	5	15.4	2.9	65.1	25.7	801	21.2		49.9	1.31
Cumar u Peru	12	hss	7	14.2	4.3	66.9	16.1	919	6.5	1.11	66.3	1.01
		vhss	7	14.3	5.7	74.4	8.5	893	4.6		64.4	1.15
	24	hss	5	15.0	2.9	63.6	9.1	938	3.3	1.17	58.4	1.09
		vhss	5	15.1	4.2	74.5	4.0	933	2.1		58.1	1.28
Cumar u Brasil	12	hss	3	12.4	1.4	91.1	8.8	1192	0.6	1.18	86.0	1.06
		vhss	8	13.3	5.0	107.7	3.6	1156	2.1		83.4	1.29
	12	hss	7	19.7	8.9	73.1	7.0	1094	3.6	1.19	78.9	0.93
		vhss	11	19.2	9.1	86.8	8.3	1071	4.1		77.3	1.12
Azobé	12	hss	5	23.3	1.8	65.7	9.7	1045	5.1	1.13	65.1	1.01
	24	vhss	5	21.6	11.2	74.1	5.2	1042	5.7		64.9	1.14
Azobé wet	12	vhss	6	43.6	7.0	64.0	9.4	1229	2.8	-	88.7	0.72
	24	vhss	5	43.0	8.2	62.8	7.7	1222	3.1		76.2	0.82

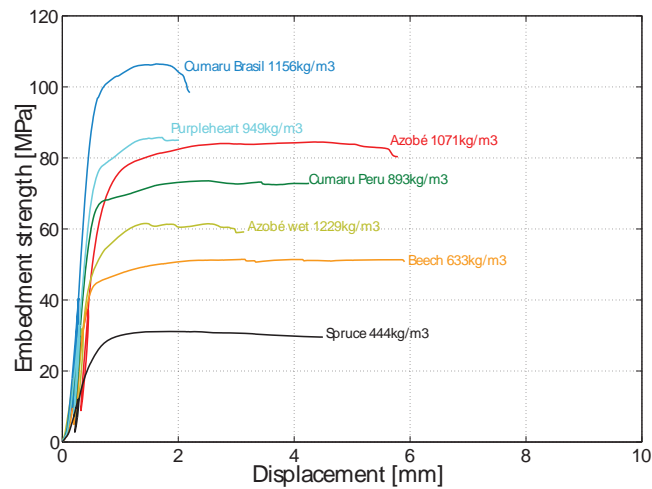


Figure 6-10: Mean stress-deformation curves per series, 12 mm vhss dowel

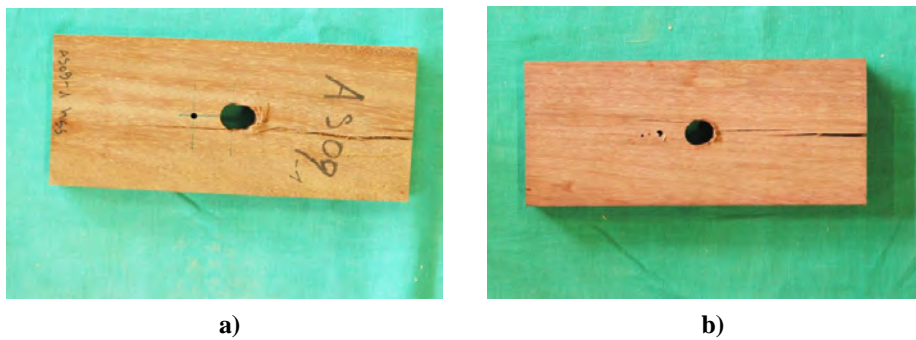


Figure 6-11: a) Azobé, b) Purpleheart, 24 mm vhss dowel

The graph of density versus embedment strength at time of test is shown in Figure 6-12, no adjustments to 12% moisture content were made. The regression line is nearly identical with Equation (6-3) from EC5 (CEN, 2004b) for 12 mm dowels. The group changing the regression much is the series with wet azobé. If a multiple linear regression is performed with the variables density, dowel diameter and m.c., then  $R^2$  is improving considerably as can be seen in Figure 6-13. Of course, this is just an indication for further research because only few wet specimens were tested. But it shows that for tropical hardwood, the influence of moisture content should be better assessed because these species are generally used under wet climate and in waterworks. It must be kept in mind however that in such a climate a lower  $k_{mod}$  is applied in design calculations.

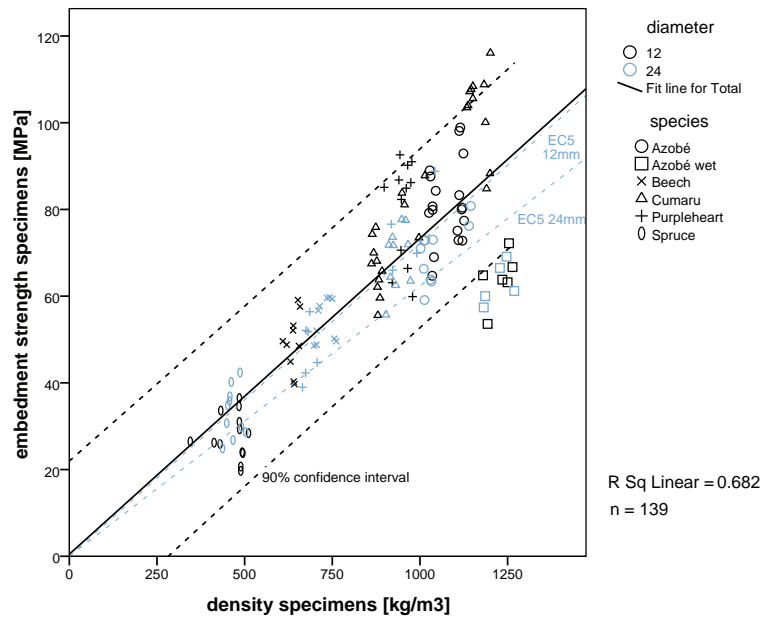


Figure 6-12: Density versus embedment strength

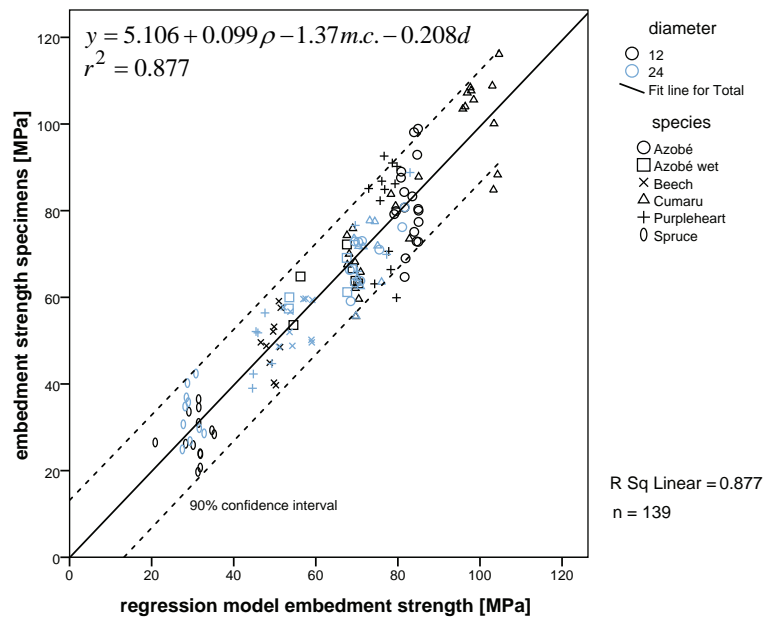


Figure 6-13: Linear regression model versus test results

Figure 6-14 shows a boxplot of ratio  $f_{h,0}$  over diameter  $d$  for all species. A mean equation similar to Equation (6-3) from EC5 (CEN, 2004b) was derived from the 139 test results. It can be seen from the equation indicatively shown in Figure 6-14 that the dowel diameter has less influence (a factor of 0.0082 instead of 0.01). This was already stated in

Ehlbeck and Werner (1992b). However here, merely trends are shown as too few test data were available in order to perform a significant statistical analysis.

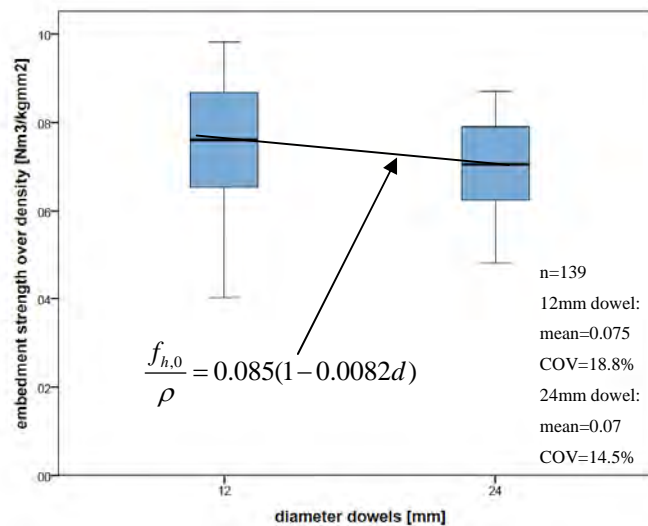


Figure 6-14: Boxplot of all data, wet azobé included

### 6.3.4 Ductility of beech

Special attention is given to the embedment tests with beech due to the observed high ductility. In Figure 6-15, the results for the series beech with 24 mm vhs steel dowels are shown. In the load-displacement graphs, a slight yield drop can be seen at the beginning of the plastic part. This behaviour could not be observed for instance for the azobé specimens. In Figure 6-16, a photo of a beech specimen with a 12 mm hss dowel is shown. The specimen sustained a displacement of 15 mm without splitting. Beech has many rays which reinforce the wood in radial direction ( $MoE_{radial}$  significantly bigger than  $MoE_{tangential}$ ). As a direct result, splitting of beech in radial direction within the many rays may be easier than splitting in tangential direction. This fact may explain the results observed in the embedment tests as shown in Figure 6-16 and Figure 6-17. In Figure 6-16, the annual rings are oriented at about  $45^\circ$ . The reinforcement of the rays may have helped to avoid splitting whereas in Figure 6-17, the annual rings are oriented perpendicular to the dowel axis. The rays could therefore not reinforce the timber for tension stresses perpendicular to the grain that develop during the embedment tests.

This is an interesting finding also for joints as an (theoretical) optimal orientation of the annual rings could also improve ductility of a joint.

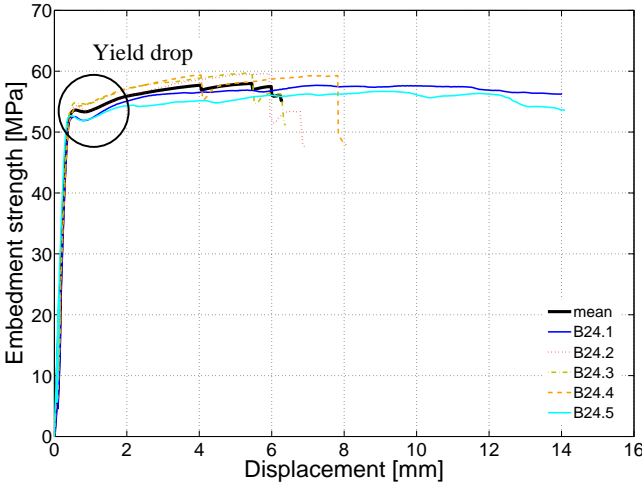


Figure 6-15: Results for beech, 24 mm vhs dowel

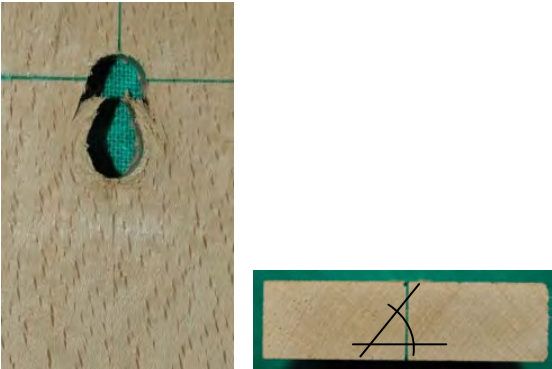


Figure 6-16: Beech, 12 mm hss dowel, 45° annual rings

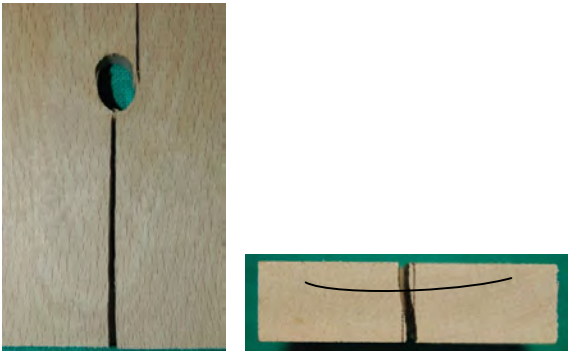


Figure 6-17: Beech, 12 mm hss dowel, 0° annual rings

## 6.4 COMPARISON WITH DATABASE

To complete the chapter on the embedment tests, the test results were included in a database taken from literature (Whale and Smith, 1986b, Whale and Smith, 1986c, Ehlbeck and Werner, 1992b, Vreeswijk, 2003). Hübner and Schickhofer (2007) published only mean values for ash (*Fraxinus excelsior*, clear wood) which were included. Figure 6-18 shows a density histogram of all the specimens of the available test results on solid wood parallel-to-grain.

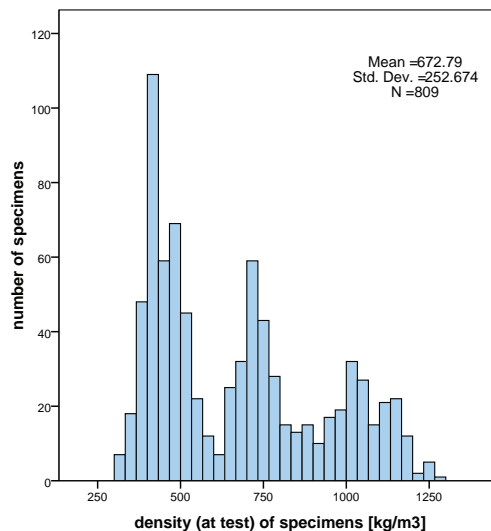


Figure 6-18: Density histogram of database

In order to compare test results from different sources, the densities as reported in Table 6-4 and related to the moisture content at time of test are adjusted to a relative moisture content of 12%. This is not defined in EN 383 (CEN, 2007) and also an adjustment of the strength properties is not mentioned. However, it was chosen to also adjust the embedment strengths according to EN 384 (CEN, 2004a), where the compression strength parallel to grain should be reduced by 3% for every percentage point difference in moisture content. As stated earlier, the results for wet azobé gave a reduction in strength of about 2% for every percentage point difference in moisture content which confirms the above-mentioned approach. Uncertainties are connected with the results in Ehlbeck and Werner (1992b) as they did not measure the moisture content during the test. For their results, a moisture content of 12% is assumed.

Figure 6-19 shows a classical density versus embedment strength graph of all 809 results. The density values are adjusted to 12% moisture content and also the embedment strength values are adjusted as explained in EN 384 (CEN, 2004a). It can be seen that for a general applicability of design equations such as Equation (6-3), the density range of the timber must be large enough. The new testing series is a valuable completion of the database. Due to the adjustments, the wet azobé comes into line with the test results. The

regression lines for the softwood and tropical hardwood are similar and have a  $R^2$ -value of 0.533 for softwood and 0.652 for tropical hardwood. For European hardwood, however, the  $R^2$ -value is lower with 0.319.

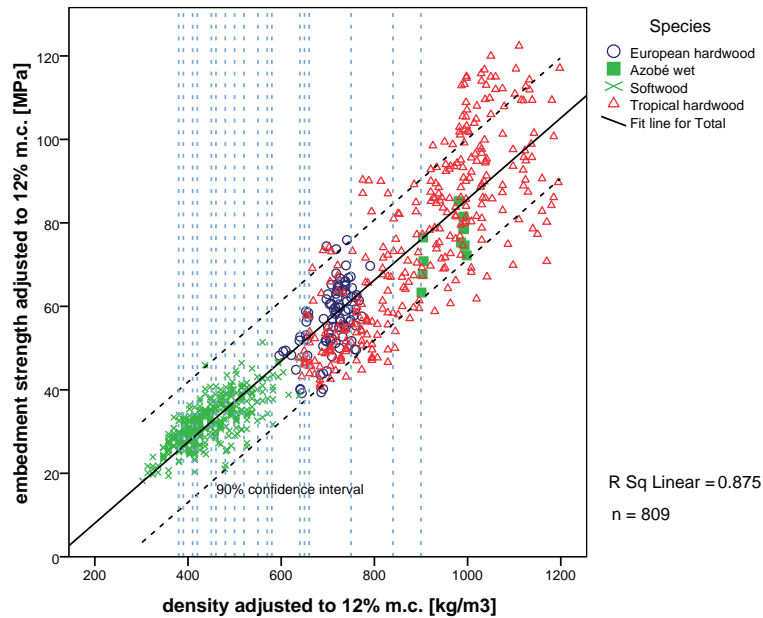


Figure 6-19: Density versus embedment strength, all adjusted

The dotted vertical lines in Figure 6-19 show the characteristic density values for different strength grades from C18 to D70 (CEN, 2009). In EN 338 (CEN, 2009), the strength classes are divided into rather small density increments as can be seen by the small distance between the vertical lines, each representing a different strength class. These small increments seem to be rather artificial in comparison to the scatter and the benefit resulting from small increments. Embedment strength is much more dependent on local properties of timber than strength grading procedures that assess full boards. Furthermore, Van de Kuilen (1999) has already shown that there is no correlation between density and load carrying capacity of timber joints. Design however is carried out using the strength properties given in EN 338 (CEN, 2009).

If now plotting the test results versus Equation (6-3) from EC5 (CEN, 2004b) with a density adjusted to 12% m.c. as done in Figure 6-20, one can see that the predictions are good for softwood, but less so for wood with higher densities as also stated in Ehlbeck and Werner (1992a) where a regression equation for hardwood is given with a higher regression coefficient than Equation (6-3):

$$f_{h,0} = 0.102(1 - 0.01d)\rho \quad (\text{Ehlbeck and Werner, 1992a}) \quad (6-4)$$

where  $f_{h,0}$  = embedding strength parallel-to-grain in [MPa],  $d$  = dowel diameter in [mm] and  $\rho$  = density [kg/m<sup>3</sup>].

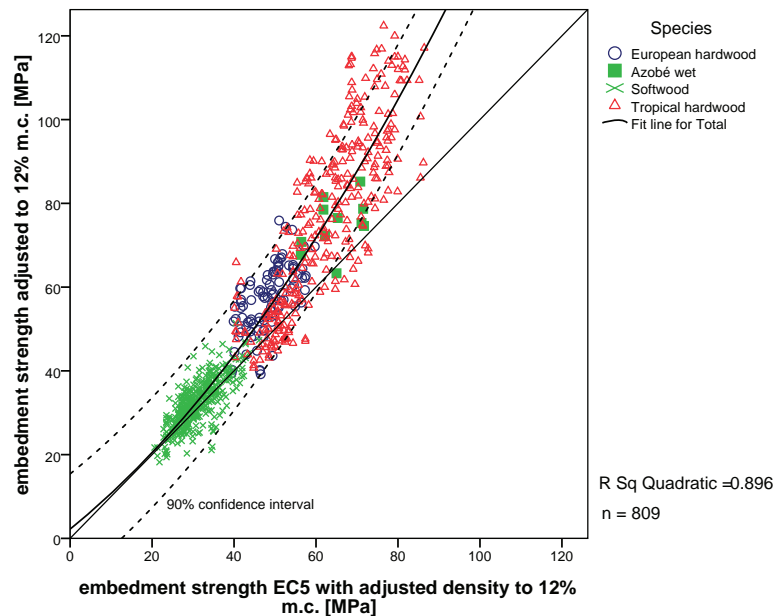


Figure 6-20: EC5 Equation (6-3) versus adjusted test results

If a linear multiple regression analysis with density and diameter as independent parameters is carried out, an equation similar to Equations (6-3) and (6-4) can be derived:

$$f_{h,0} = 0.095(1 - 0.0089d)\rho \quad (6-5)$$

where  $f_{h,0}$  = embedding stress parallel-to-grain in [MPa],  $d$  = dowel diameter in [mm] and  $\rho$  = density in [ $\text{kg}/\text{m}^3$ ].

The corresponding graph of the model versus the adjusted test results is shown in Figure 6-21. Equation (6-5) is confirming the findings from Ehlbeck and Werner (1992b) and own observations as discussed earlier. The dependence on the dowel diameter is less pronounced (0.0085 instead of 0.01) and the regression value of 0.082 is increased to 0.095.

At this stage it is remembered that in EC5 (CEN, 2004b) the transfer of the regression equation was done by simply applying the characteristic density instead of the mean density. However, Whale and Smith (1986a) and Ehlbeck and Werner (1992a) chose the embedment test species under certain density criteria whereas here, the assembling was purely random.

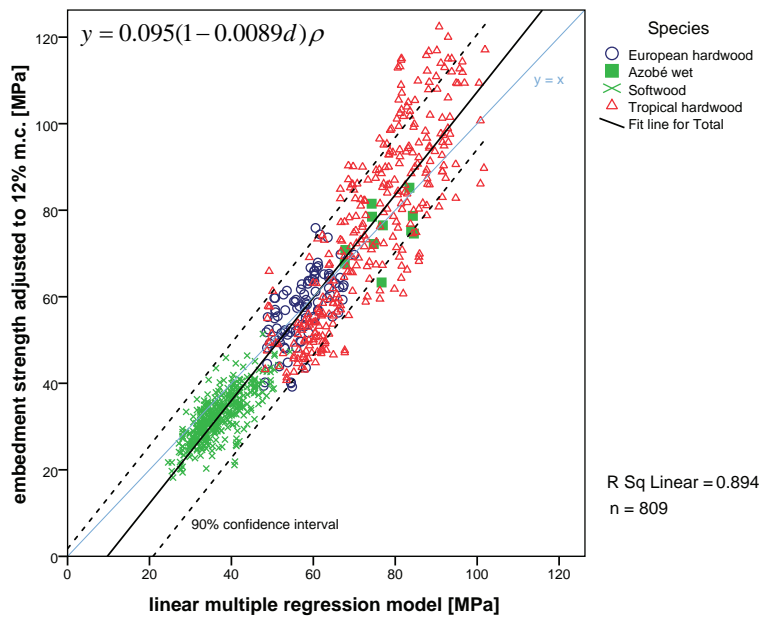


Figure 6-21: Linear regression model versus adjusted test results

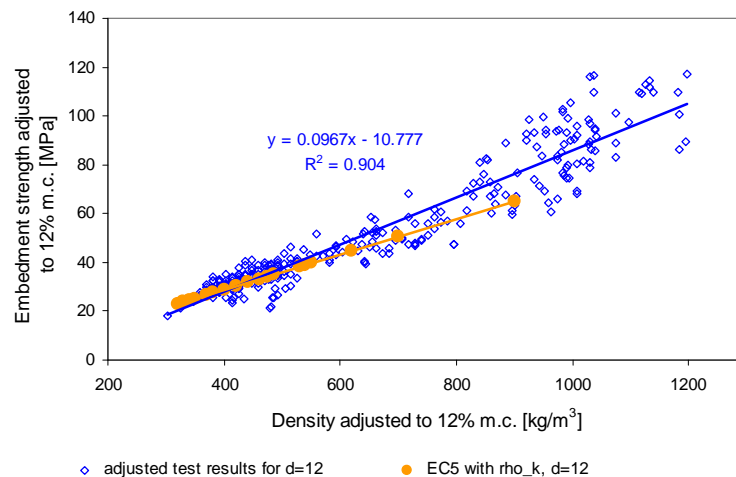


Figure 6-22: Adjusted test results and results for Equation (6-3) for softwood and hardwood, versus density at 12% m.c.,  $d = 12$  mm

Figure 6-22 shows another interesting finding. It shows embedment test results for a dowel diameter of  $d = 12$  mm over the density, both values adjusted to 12% m.c. Additionally, the results of Equation (6-3) were inserted with  $d = 12$  mm and the characteristic density of all softwood and hardwood strength classes (CEN, 2009).

It would be expected that the results for Equation (6-3) are lying underneath the regression line. This is not the case for softwood, especially not for the lower strength classes. An explanation may be that the lower strength classes have inherent not visible local defects (that is why they are assigned to lower classes) that govern during

embedment tests. This again would confirm the dependency of embedment strength on local timber properties.

## 6.5 CONCLUSIONS

### Steel

The same dowels and steel grades were used for the embedment and the joint tests. As expected, the strength of the vhs dowels corresponded to the steel grade vhs. However, the 'mild steel' dowels had significantly higher mechanical properties than ordered and corresponded to hss instead. Furthermore, no hardening at all could be observed. Therefore, the plastic bending capacity of the dowels needed to calculate the load carrying capacity of the joints (Chapter 7) was derived using the theoretical equation from mechanics.

### Embedment tests

Considerable differences in embedment strength using the two different steel grades could be observed. This could not be motivated by different surface roughness of the dowels. However, no friction tests were carried out to investigate the friction coefficient for the two dowel types on wood.

The used wood species showed different ductility which at least for beech could be satisfactorily explained with different anatomical features.

The current EC5 equation to determine the embedment strength is overly conservative for high density wood species. Furthermore, the observed influence of the dowel diameter on the embedment strength seems to be lower than assumed in EC 5.

# 7

## JOINT TESTS

*Tests on double-shear timber joints with timber members loaded parallel-to-grain and slotted-in steel plates have been carried out. One, three and five dowels in a row have been used with diameters of 12 mm and 24 mm and two different steel grades. Three different wood species were chosen, spruce, beech and azobé. Apart from proving that very high strength steels can be used as dowels in timber joints, these tests are needed to verify the validity and reliability of the developed material model. Furthermore, the test results give new insights in the influence of different wood species and steel grades, in the effective number of fasteners and joint stiffness.*

### 7.1 INTRODUCTION

Tests have been carried out on double-shear timber joints with slotted-in steel plates with very high strength steel dowels using species with densities between 350 and 1100 kg/m<sup>3</sup>. Comparative tests were done on the same joints, but with hss dowels. The number of dowels varied between one, three and five in a row. The dowel diameters were 12 and 24 mm. Different aspects can be checked and motivate these experiments:

- Validity of developed material model;
- Potential of using very high strength steel dowels;
- Influence of different wood species;
- Effective number of fasteners;
- Stiffness of joints.

In timber joints with dowel-type fasteners, the preferred failure mode is combined failure of the fastener (one or two plastic hinges per shear plane) and the timber (embedment). Apart from the geometry, the load carrying capacity is therefore defined by the embedment strength of the timber and the yield moment of the dowel type fastener.

The utilisation of very high strength steels vhss with subsequent higher bending capacities is promising in order to optimise joints and obtain high performance joints. Thinner dowels and thinner member sections should lead to the same load carrying capacity as thicker hss dowels with bigger member cross sections – as long as failure mode 2 or 3 is reached. Another option is that with the same dimensions, fewer dowels could be used to obtain the same strength performance. As for the deformation capacity of the joints, very high strength steels available nowadays are able to ensure a good overall ductile behaviour without brittle failure modes.

This is especially valid and even more advantageous for high density timber. The embedment strength of species with high densities is higher. Therefore, less member thickness would be needed when using vhss dowels in comparison to softwood in order to reach a ductile failure mode. In the Netherlands, tropical hardwood with high densities is used for bridges and waterworks such as lock gates or mooring posts. The practical applicability is hence guaranteed.

## 7.2 LITERATURE REVIEW

Many test results on timber joints with timber members loaded parallel-to-grain and dowel-type fasteners, both dowels and bolts, are available. Generally, it is difficult to build-up a database where the single results can be compared. The test setup was different, timber-to-timber or steel-to-timber joints with different geometries and materials were tested. Often, not all testing parameters were known or not everything (for instance measuring positions) was given. It can be stated however that most of the research was focussed on softwood and only some research was done with hardwood (Werner, 1993, Gehri and Fontana, 1983).

Within the scope of this thesis, this short literature review is limited to research carried out using vhss dowels as the substitution of mild steel dowels is promising for practice. In previous research, vhss dowels were mainly used to ensure brittle failure modes in joints (Schmid, 2002) with few exceptions (Gehri and Fontana, 1983). Especially Gehri and Fontana's tests (1983) are interesting as they carried out large-scale joint tests with different wood species and steel grades. In 2006, first tests were undertaken at TU Delft to investigate the applicability of hss dowels in double-shear timber-to-timber joints with one dowel (Hieralal, 2006). Azobé and spruce joints were assembled with steel dowels of grade S690 and diameters of  $d = 8, 16, 24, 30$  mm. Failure mode 3 with 2 plastic hinges per shear plane was expected to occur in all specimens, but did not occur in the spruce specimens. The ductility of all joints was high with deformations at maximum load of at least  $v_{\max} = 15$  mm in most cases with a distinctive plastic branch. The ratio of  $v_{\max}$  over dowel diameter was decreasing with increasing diameter.

Further tests using vhss dowels were carried out on double-shear timber joints with slotted-in steel plates, e.g. Groesen and Kranenburg, 2007, Langedijk, 2007, Van de Kuilen and De Vries, 2008, Islamaj, 2009), Van de Kuilen, (2009). Tests were carried out

with spruce and 8 mm vhss dowels of grade 12.9 with one, three and five dowels in a row. Two series of joint tests with three dowels were designed. A first series was undertaken with three dowels exactly in a row. In the second series, the middle dowel was shifted by  $1d$  leading to a staggered dowel pattern. The authors stated that plastic hinges could develop and that all joints showed a ductile failure. The deformation at maximum load decreased with increasing number of dowels. No difference could be observed in the two series with three dowels in a row.

Islamaj (2009) carried out tests on double-shear timber joints with slotted-in steel plates with tropical hardwoods and very high strength and high strength steel dowels. The dowel diameter was again 8 mm. One, three and five dowels in a row were used. As for the effective number of dowels  $n_{ef}$ , a higher effective number was observed for the joints with hss dowels. In other words, the influence of more dowels in a row is reducing the capacity of joints with vhss more than the capacity of joints with hss dowels which could nearly reach a full load carrying capacity ( $n_{ef} = n$ ). Islamaj's tests were the same tests as the tests carried out within the scope of this thesis. Therefore, for the analysis of the experiments his results can be compared with the own results.

## 7.3 EXPERIMENTAL PROGRAMME

### 7.3.1 Type of joints

Double-shear timber joints with timber members loaded parallel-to-grain and slotted-in steel plates were tested at Stevinlab II of University of Technology Delft. Three different wood species were used: spruce glulam as a (reference) softwood species, beech glulam as a European hardwood and azobé as a tropical hardwood. All three species are used for structural purposes with beech glulam being a rather new product (Frese, 2006) where nearly no joint tests were carried out yet. Azobé is frequently used especially for waterworks and bridges where large sections are needed.

The steel dowels had a diameter of 12 mm and 24 mm. The choice of the diameter was based on the following considerations. 12 mm dowels were used widely in literature (Jorissen, 1998) and are also often applied in practice. 24 mm dowels seem to be big, but they are used for high-strength members with large sections as typical for azobé structures. Half of the tests were carried out with vhss dowels. Comparative tests were done on the same joints, but with hss dowels. The number of dowels in a row was one, three and five. This is because one dowel is needed at least and in practice, five dowels are usually the maximum number of dowels in a row. To interpolate, three dowels in a row were chosen. No variation was done on the number of rows.

The end and edge distances listed in Table 7-1 were the same for all specimens and correspond to the minimum distances specified in EC5. It should be noted that the fastener spacing  $a_1$  was smaller than the end distance  $a_{3,t}$ . The spacing  $a_1$  is different in

many tests from literature and hence care should be taken when comparing the ductility of joints of different research projects.

**Table 7-1: Spacing, edge and end distance**

Loaded end $a_{3,t}$	$7d$
Spacing $a_1$	$5d$
Edge distance $a_4$	$3d$

Figure 7-1 shows a drawing of the three different specimens. Of both joints shown in Figure 7-1, one joint was tested. The other joint only served to append the specimen and was designed to be much stronger than the joint to be tested. An exception to this are the test series A24-1, A24-3 and B24-1 (nomination see next page) with identical upper and lower joints. Therefore, during the test, both joints were tested and measured. The maximum force of the joint that failed first was considered.

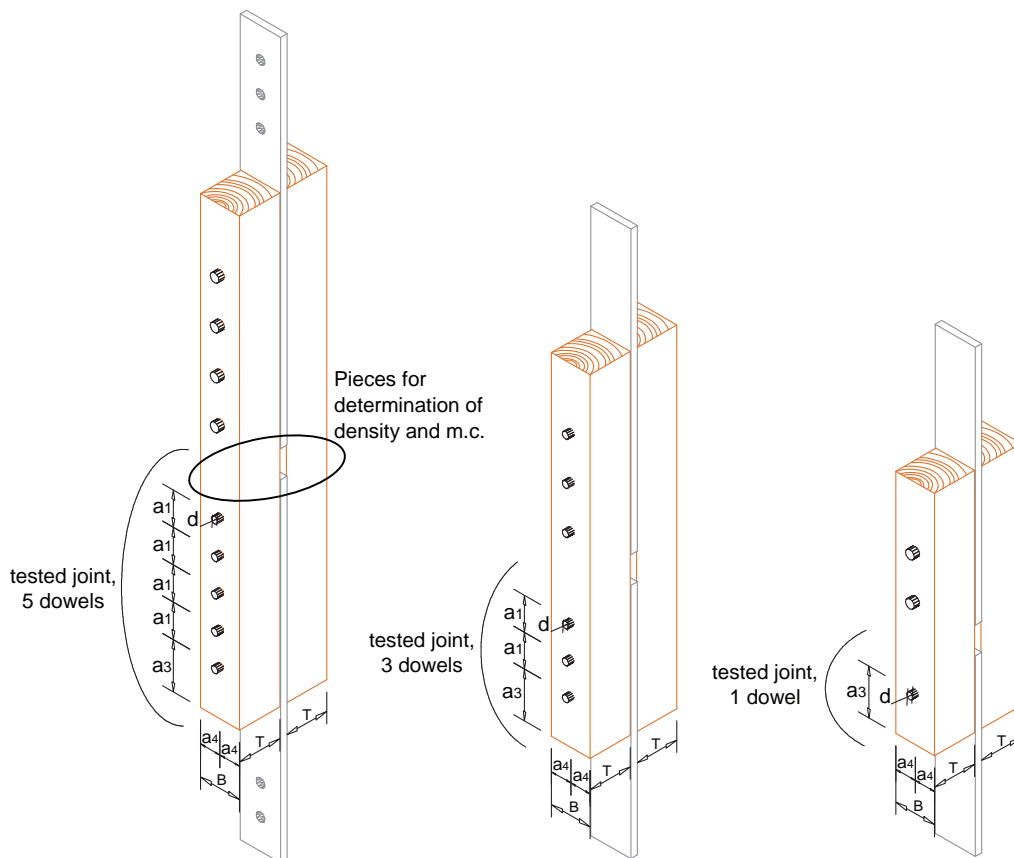


**Figure 7-1: Drawings of test specimens**

Figure 7-2 shows a flowchart of the tests. Per series, five specimens were tested which led to a total of 180 tests.

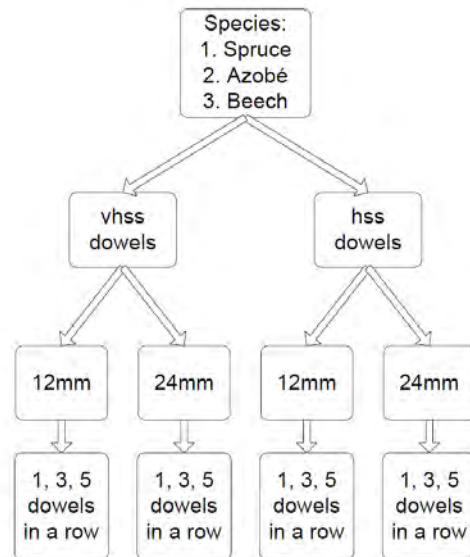
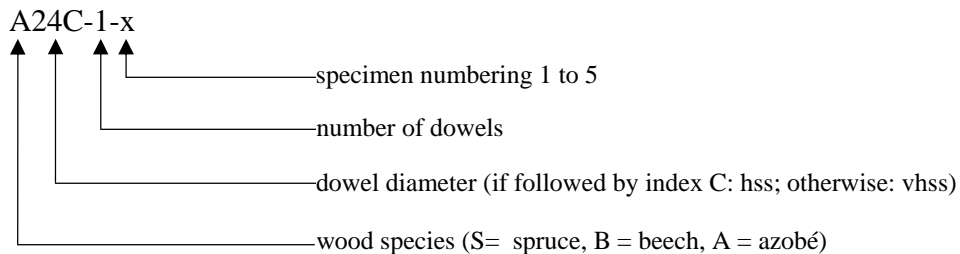


Figure 7-2: Flowchart of joint tests, five specimens per series

The nomination of the specimens was as follows:



### 7.3.2 Used materials

#### Wood

The ordered **spruce glulam** (*Picea abies*) was of quality GL28h according to EN 1194 (CEN, 1999) and was from Northern German origin. GL28h means that the quality of the lamellae should be C30 with a mean density of 460 kg/m<sup>3</sup> according to EN 338 (CEN, 2009). All specimens were produced and assembled at TU Delft. The wood was stored in a 20/65 standard climate. Grain angle and annual ring width were not measured also because the ring width is not correlated to the load carrying capacity according to Jorissen (1998).

**Beech glulam** (*Fagus sylvatica*) was sawn and assembled at TU Delft with a rather big hole clearance. The glulam was produced at the University of Technology Munich by using planks that were intended for furniture producers. Therefore, the quality of the planks was not assessed by strength grading methods known for structural timber, but by other visual assessment rules. Virtually no knots were present. The quality was high. The specimens were not stored in a climate chamber, but have always been stored inside. Grain angle and annual ring width were not measured.

**Azobé** (*Lophira alata*) is an African wood species and was from certified origin (FSC). The smaller specimens with 12 mm dowels were produced and assembled at TU Delft. These specimens were stored in a 20/85 climate. The specimens with the 24 mm dowels inclusive the assembling was done by a specialised company. They were not stored in a climate chamber but simply inside and visual grading was carried out (NEN, 2009). The grain angle was not measured. Azobé can suffer from interlocked grain, but this parameter was not evaluated.

### Steel

The dowels were of steel grade 12.9 (vhss) and galvanised high strength steel instead of S235 as ordered. Standard tensile tests have been carried out and were presented and discussed in chapter 6. For the vhss dowels, a mean proof strength at 0.2% extension of  $R_{p0,2} = 1311$  MPa and an ultimate strength of  $R_m = 1389$  MPa was found. The galvanised hss dowels instead had values of  $R_{p0,2} = 563$  MPa and  $R_m = 590$  MPa.

The steel plates were of S690 and were 12 mm thick.

### 7.3.3 Design of test specimens

As in previous research, the joints were designed with the Johansen equations (EYM), without considering the factors deriving from the partial safety approach in EC5 (CEN, 2004b).

The **geometry** was chosen according to the minimum distances required by EC5 which were given in Table 7-1. The timber member thickness was chosen such that the failure mode of the joints with vhss was lying on the boundary between failure mode 2 and 3 with one or two plastic hinges per shear plane respectively.

The **bending capacity** of the dowels was calculated with the theoretical Equation (6-1) as was motivated in section 6.2 – Equation (6-1) is repeated here:

$$M_y = f_{y,k} \frac{d^3}{6} \quad (7-1)$$

The **embedment strength** was calculated according to Ehlbeck and Werner (Ehlbeck and Werner, 1992a) as the embedment strength equation in EC5 was considered to yield too conservative results. The mean densities were used to calculate the embedment strength

(spruce 445 kg/m<sup>3</sup>, beech 715 kg/m<sup>3</sup>, azobé 1120 kg/m<sup>3</sup>). Equation (7-2) resulted from a regression analysis of embedment test results on hardwoods:

$$f_{h,0} = 0.102(1 - 0.01d)\rho_{mean} \quad (7-2)$$

where  $f_{h,0}$  = embedment strength parallel to grain in [MPa],  $d$  = dowel diameter in [mm],  $\rho_{mean}$  = mean density in [kg/m<sup>3</sup>].

The **fabrication process** of the specimens was not controlled with regard to the drilling of the holes. During the tests, varying conditions could be observed. Some of the specimens were hard to assemble, others easy which indicated differences in bolt holes. As for the azobé specimens, the 12 mm specimens were assembled at TU Delft whereas the 24 mm specimens were assembled by a company. Therefore, the assembling of the 24 mm specimens was carried out more precisely than the one of the 12 mm specimens. The preciseness of assembling is another issue to remember as the fabrication tolerances may influence the strength (Jorissen, 1998) and it certainly influences the stiffness  $K_{ser}$ . The layout of the wooden members with regard to density, orientation of annual rings, knots etc was random except for the spruce specimens where the two wood members of one joint had comparable densities.

### 7.3.4 Testing protocol and setup

The tests were carried out according to EN 26819 (CEN, 1991). The test protocol is shown in Figure 7-3. The estimated load carrying capacity cannot be established unambiguously. Usually, a first test is needed to give an estimate. In this research, usually a lower value than 40% of  $F_{est}$  was chosen for the big specimens as any damage in the first loop that serves to settle the specimens should be avoided.

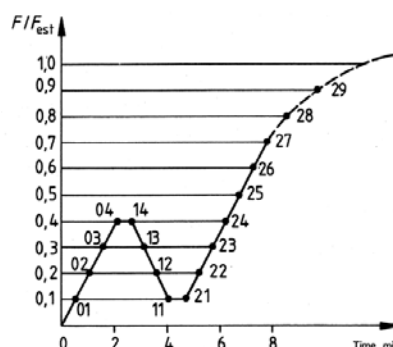


Figure 7-3: Test protocol according to EN 26819 (CEN, 1991)

Due to the big range of expected load carrying capacities (15 kN to 1400 kN), two different testing rigs have been used. For the smaller tests, a Dowty Rotel with 250 kN capacity was used. The loading scheme was force-controlled up to 70% of the estimated

maximum force and afterwards displacement-controlled up to failure. The velocity of the tests was hence calculated by the machine. The transition point between force-controlled and displacement-controlled (70% of maximum force) had to be reached at 500 s. The tests with an estimated load carrying capacity above 250 kN were carried out with a specially assembled testing rig equipped with a 2500 kN hydraulic jack. This Meccano machine was controlled manually in displacement control. The testing velocity was also chosen manually and varied between 0.03 mm/s and 0.04 mm/s, depending on the test pieces. All joints failed between 5 to 15 min with few exceptions of joints where high deformations were reached.

An overview of the test rigs is shown in Figure 7-4.

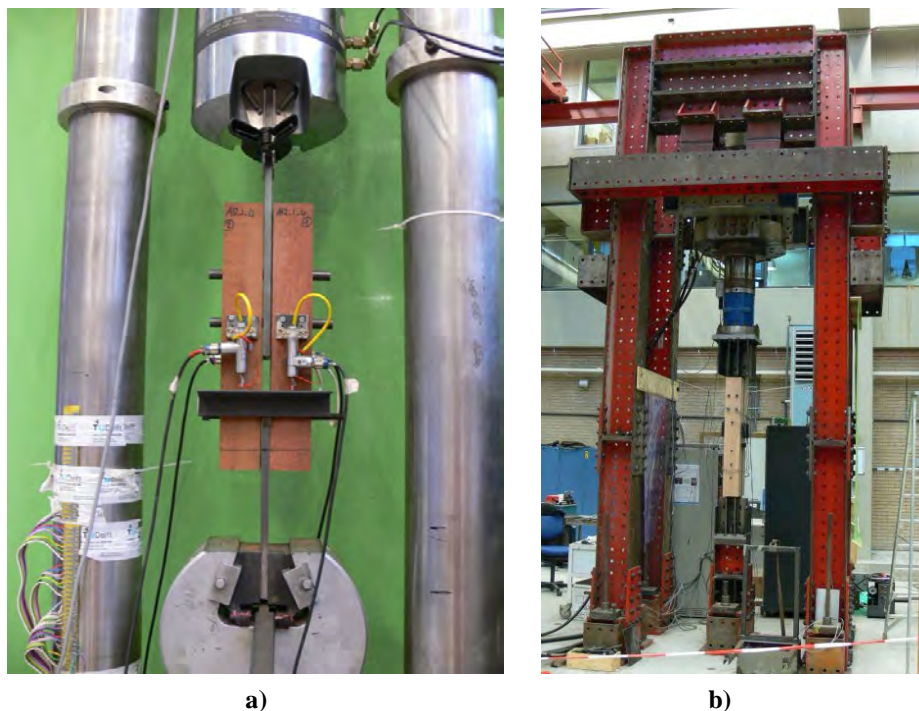


Figure 7-4: The two test rigs, a) 250 kN Dowty Rotel, b) 2500 kN Meccano

Figure 7-5 shows a technical drawing of a specimen with one dowel with the position of the transducers. The deformation measurements were taken with four LVDTs (one LVDT on front and rear of both timber members). They were measuring the displacement of the timber members relative to the steel plate. The distance  $D_{LVDT}$  between the fixing of the transducers (on the wood members) and the steel angles serving as transducer support (on the steel plates) was recorded and was changing between tests with 12 mm and 24 mm dowels. This distance  $D_{LVDT}$  is given in Appendix B. The measuring distance was rather short and did not cover the complete joint. The elastic elongation of the steel plate was

hence neglected. Except for local embedment around the hole due to stress peaks, no plastic deformation was observed<sup>23</sup>.

Finally, the technical specifications of the test setup are given in Table 7-2.

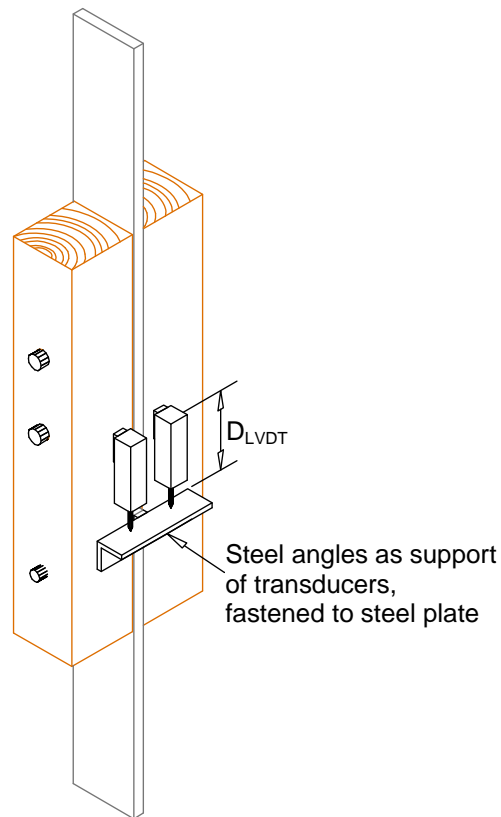


Figure 7-5: Position of transducers, same on rear side

Table 7-2: Specifications of testing equipment

<b>Control programme</b>					
frequency control input:	5 ms				
frequency readout:	1 s				
<b>Meccano machine</b>			<b>Dowty Rotel</b>		
instrument	range	resolution	instrument	range	resolution
load cell	2500 kN	1.22 kN	load cell	300 kN	0.15 kN
LVDT's no.1-6	50 mm	0.013 mm	LVDT's no.1-8	40 mm	0.019 mm
LVDT's no 7-8	200 mm	0.051 mm			

<sup>23</sup> Numerical models proved that the elastic elongation is small; the local plastic embedment deformations of the steel plates were measured with the test setup.

## 7.4 TEST RESULTS

### 7.4.1 General results

A total of 179 tests were carried out. First of all, pure test results in terms of load-slip curves and load carrying capacities are presented. The subsequent interpretation part of the results discusses special aspects as influence of density, wood species and steel grade, ductility, effective number  $n_{ef}$  or joint stiffness  $K_{ser}$ . All results and descriptive statistics can be found in Appendix B.

Both density and moisture content of the specimens was measured directly after the tests. The moisture content of the specimens was measured with the oven-dry method. The pieces taken from the timber members to carry out these measurements were situated directly above the failed joint (location indicated in Figure 7-1).

Figure 7-6 to Figure 7-7 show the mean load-displacement graphs of the tests – please note that the curves are averaged per series until the first failure within one series occurred. (For instance, a spruce specimen with one 12 mm hss dowel failed early due to a large knot cluster directly at the dowel having thus much less ductility than the other results of the series, see Figure B-28). The plastic branches per test specimen may be of different length as can be seen in Table 7-3 where the mean results of the displacements and their COVs are given.

The graphs show clearly the trend of less ductile behaviour of joints with multiple dowels. Also the increase in load carrying capacity when using more dowels is visible.

The higher load carrying capacity of joints with vhss dowels can also be seen except for the tests of spruce with three 24 mm dowels (Figure 7-7a). When looking at the graphs, it can be seen that the nonlinear regime of the joints with hss dowels started earlier.

Another interesting finding is the similar load carrying capacity between beech and azobé although the respective densities at test are quite different with  $\rho_{\text{mean}}(\text{azobé}) = 1120 \text{ kg/m}^3$  and  $\rho_{\text{mean}}(\text{beech}) = 715 \text{ kg/m}^3$ . It must be recalled though that the m.c. was quite different for beech (mean m.c. = 9%) and azobé (mean m.c. = 21%). Azobé was wet and had thus lower mechanical properties than beech that was dry. Especially the compression strength is significantly depending on the moisture content. If both wood species would have had the same m.c., the test results would be different. A bigger difference in terms of load carrying capacity between beech and azobé would be expected.

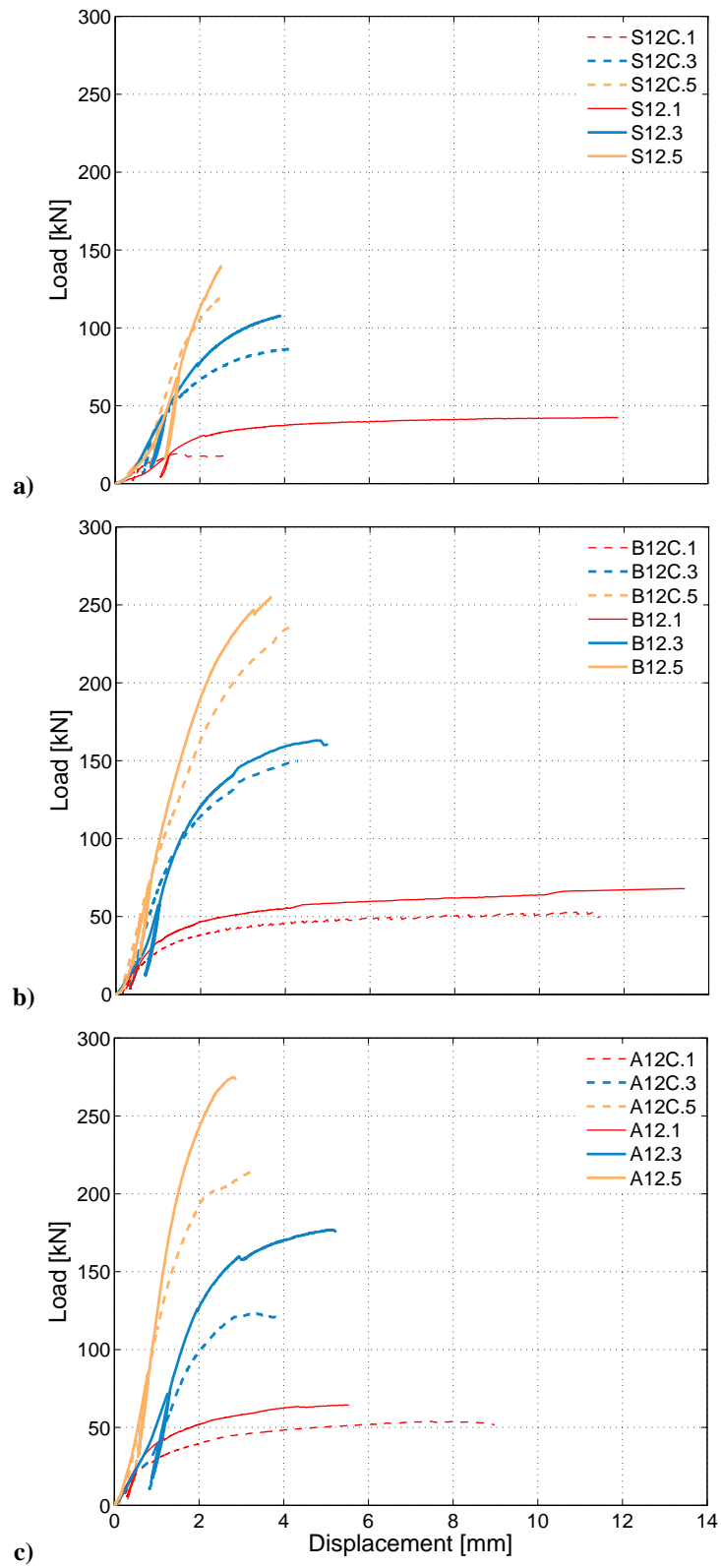


Figure 7-6: Means of series 12 mm dowels, a) spruce, b) beech, c) azobé

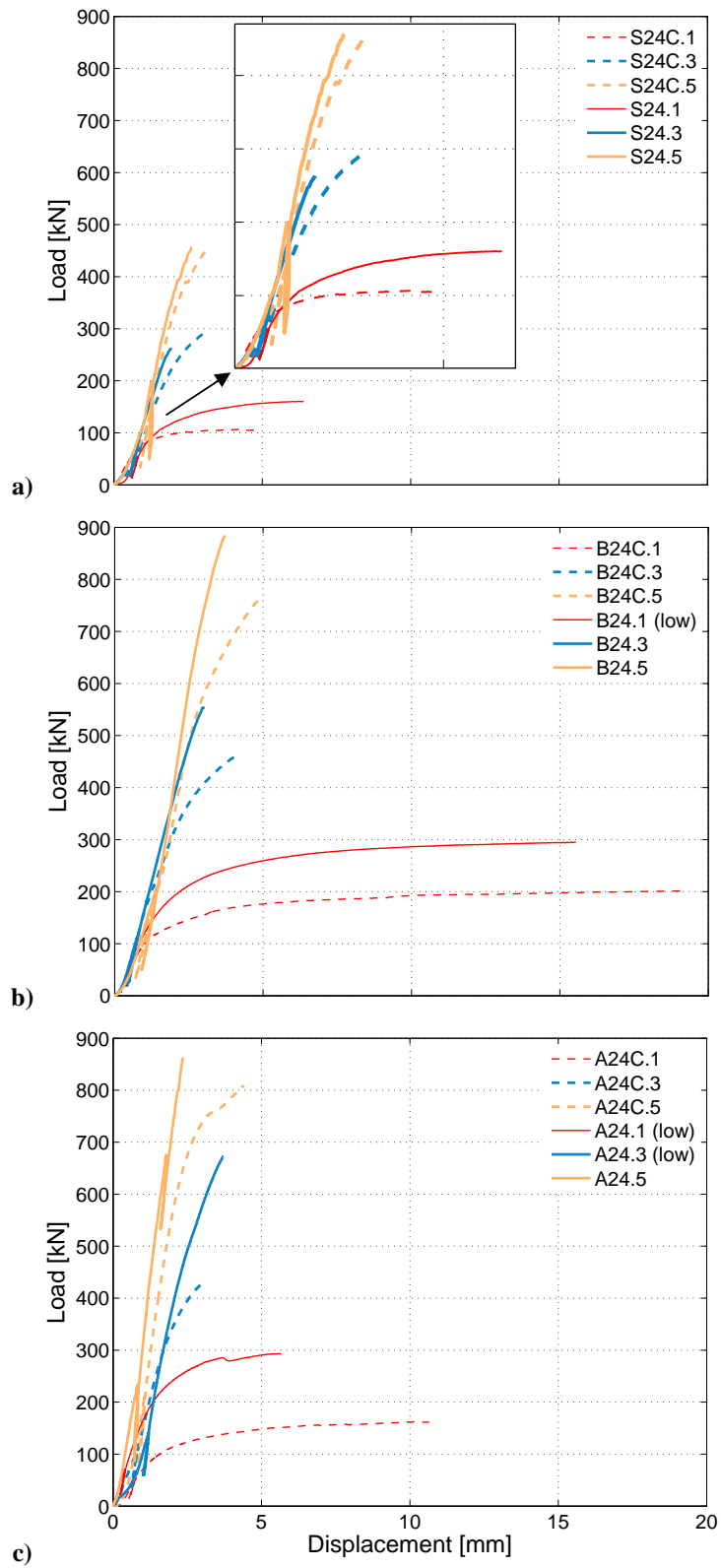


Figure 7-7: Means of series 24 mm dowels, a) spruce, b) beech, c) azobé

In Table 7-3, all results are given. Per parameter, the main points are identified:

- **Density:**  
The mean values are  $445 \text{ kg/m}^3$  for spruce,  $715 \text{ kg/m}^3$  for beech and  $1120 \text{ kg/m}^3$  for azobé. Generally, the COV is low. The single high value of the COV for spruce with one 24 mm hss dowel derives from one single specimen and is probably a measuring error. Please consider that these are the densities during the test. The values may need an adjustment to 12% m.c. for further evaluations.
- **m. c.:**  
The mean m. c. is 12% for spruce, 21% for azobé and 9% for beech.
- **Density at 12% m.c.:**  
The measured density (at measured m.c.) is adjusted to a moisture content of 12%.
- **$F_{max}$ :**  
Generally, the COV is unexpectedly low. The specimens with vhss reach higher load carrying capacities except for the spruce specimens with three 24 mm vhss dowels. The increase of the vhss specimens in comparison to the hss specimens is between 10% and 69%. Please consider that the m.c. was varying.
- **Failure modes:**  
The expected failure modes did not always occur. The joints with vhss dowels were designed to lay on the boundary between FM 2 and 3 which means for the joints with hss dowels that they should clearly lie in FM 3. However, not all joints with hss dowels failed in FM 3 (see Table B-7).
- **$v(F_{max})$  and  $v_{max}$ :**  
The COV is high (expectedly) and the displacement measured at  $F_{max}$  is in most cases only slightly bigger than the maximum displacement, even for the tests with one dowel. This indicates that the load-slip curve was still increasing when the specimens failed. The specimens with one dowel are more ductile than the specimens with multiple dowels. The ratio between displacements at maximum load over the dowel diameters  $v(F_{max})/d$  decreases considerably with bigger diameters as was also observed by Hiralal (2006).
- **$K_{ser}$ :**  
The COV is high. The expectation of a higher  $K_{ser}$  when more dowels in a row are used is not observable.  $K_{ser}$  for three and five dowels is often similar and sometimes even no increase between one and more dowels could be observed. This is probably a strong indication on how manufacturing influences the value of  $K_{ser}$  (definition of  $K_{ser}$  see Figure 7-25).

Table 7-3: Test results joint tests

number of dowels	grade	n	density [kg/m <sup>3</sup> ]		m. c. [%]		density at 12% m.c.		$F_{max}$ [kN]		FM	$v(F_{max})$ [mm]		$v(F_{max})/d$		$V_{max}$ [mm]		$K_{ser}$ [kN/mm]	
			mean	COV [%]	mean	COV [%]	mean	COV [%]	mean	COV [%]		mean	COV [%]	mean	COV [%]	mean	COV [%]	mean	COV [%]
1	vhss	5	457	5.8	12.1	1.6	457	3.4	44	15.1	20.7	2	3.4	3.7	15.7	20.6	20	32.6	
		5	456	3.6	11.9	2.4	456	32	8.4	2/3	48.0	2.7	12.7	34.1	21	34.5			
	vhss	5	485	2.7	12.4	2.4	483	115	6.3	1/2	29.3	9.6	5.9	28.3	51	8.4			
		5	462	7.0	12.7	1.6	460	90	9.4	2/3	5.0	5.6	7.5	5.6	51	20.9			
	5	vhss	5	478	1.9	12.6	1.5	475	169	15.7	1/2	25.2	14.1	3.7	25.6	68	6.5		
5			460	5.6	12.5	1.9	458	136	9.3	2	3.3	17.1	11.3	4.9	43.8	52	12.3		
vhss		5	722	2.5	8.7	3.1	744	70	6.0	2	15.9	14.6	5.8	16.3	49	44.2			
		5	720	1.6	8.6	3.4	742	59	3.6	3	15.5	7.2	5.0	15.8	36	40.6			
3		vhss	5	732	4.8	8.7	1.4	754	173	4.9	2	6.5	34.9	14.5	7.6	23.5	67	8.4	
	5		730	2.2	8.5	0.7	754	157	4.6	3	5.9	23.2	13.1	7.1	26.6	61	28.8		
	vhss	5	703	2.3	8.5	1.0	726	294	2.5	2	5.3	17.4	24.5	5.7	19.8	129	13.3		
		5	718	3.1	8.8	12.6	739	240	2.5	2/3	4.5	8.8	20.0	5.1	29.7	110	4.2		
	1	vhss	5	1115	2.3	22.0	1.4	1024	72	2.7	2	7.9	17.1	6.0	9.4	18.0	53	12.4	
5			1115	2.3	21.4	1.4	1029	57	6.5	3	11.1	41.1	4.8	13.9	31.9	45	29.5		
vhss		5	1131	4.0	22.9	3.1	1031	183	7.9	2	4.8	23.4	15.2	7.4	20.5	64	11.2		
		5	1117	1.4	21.8	0.9	1027	128	7.6	2/3	3.7	35.7	10.6	5.2	16.0	39	6.7		
5		vhss	5	1130	3.9	17.2	2.4	1080	281	13.2	1/2	2.9	15.3	23.4	3.2	8.7	158	22.1	
	5		1115	1.6	21.7	0.8	1027	233	14.1	2/3	4.0	56.1	19.4	5.6	44.8	132	6.0		
	vhss	5	413	4.2	12.0	1.8	413	165	4.2	2	11.2	54.9	0.5	13.5	45.0	118	13.8		
		5	424	10.8	12.2	1.9	423	110	12.2	2	5.2	22.0	0.2	7.8	28.3	126	27.5		
	3	vhss	5	410	3.5	11.8	1.7	410	297	18.0	1	2.6	36.2	0.1	3.5	51.9	122	6.6	
5			418	3.7	11.9	1.1	419	324	5.1	2	3.9	23.1	0.2	4.1	23.1	127	22.3		
vhss		4	439	4.7	12.5	2.3	437	570	9.4	1	3.6	24.1	0.2	3.6	24.1	247	44.0		
		5	436	4.4	12.4	1.7	435	482	9.3	2	3.6	7.6	0.1	3.7	7.3	137	6.1		
1		vhss	5	710	1.0	8.5	2.0	733	300	2.4	2	20.0	21.8	0.8	21.3	18.0	157	7.7	
	5		718	2.2	8.7	8.0	741	208	3.6	3	23.8	16.2	1.0	24.1	16.6	114	20.4		
	vhss	5	724	0.9	8.3	1.3	749	659	5.1	2	4.2	12.4	0.2	4.4	11.7	205	2.9		
		5	711	1.7	8.4	0.8	734	510	5.0	2/3	6.0	29.4	0.2	7.1	26.3	202	17.2		
	5	vhss	5	695	2.3	9.4	4.5	712	927	3.5	1/2	4.1	13.5	0.2	5.6	46.6	192	6.3	
5			701	1.0	9.8	2.9	715	823	5.3	2/3	6.5	24.0	0.3	6.9	27.4	171	7.2		
vhss		5	1154	1.9	21.5	3.1	1064	306	6.4	2	5.3	28.2	0.2	7.2	23.7	201	17.5		
		5	1122	3.1	21.5	5.9	1035	181	10.6	3	15.2	36.8	0.6	18.9	12.2	103	15.1		
3		vhss	5	1116	1.9	21.3	6.6	1030	706	5.5	1/2	4.2	14.7	0.2	4.5	19.4	246	13.8	
	5		1104	2.3	22.6	10.7	1008	539	7.2	2/3	5.0	24.7	0.2	5.0	24.9	186	33.3		
	vhss	5	1101	1.3	15.9	15.7	1064	1128	16.0	1/2	3.5	36.9	0.1	3.7	38.7	374	40.9		
		5	1118	2.4	22.5	6.9	1022	867	11.0	2/3	4.9	26.3	0.2	6.7	31.5	321	16.8		

Notes: density established with Archimedes's principle; m.c. established with oven-dry method;  $v(F_{max})$  = displacement at  $F_{max}$ ;  $V_{max}$  = ultimate displacement;

$K_{ser}$  established according to Figure 7-25

When dealing with timber joints, the load carrying capacity is not only determined by the geometry, the bending capacity of the fasteners and the embedment strength, but is also influenced by other factors. Otherwise the results cannot be explained satisfyingly. This is especially valid for joints with multiple dowels. If joints split early, the load carrying capacity will be often lower than for joints that deformed more (an exception to this is a joint with knots in the dowelled region – see Figure B-28). A reason for this could be that the load may not have been distributed evenly over all dowels. Therefore, the effective number  $n_{ef}$  will also be influenced by the failure modes, i.e. whether a joint splits early or fails at large deformations where load redistributions have taken place. If two extreme cases are considered, this becomes obvious: in a joint that fails only in embedment, redistribution will have taken place, high deformations and thus high load carrying capacities will be reached,  $n_{ef}$  will be approximately equal to  $n$ . On the other hand, when a joint splits immediately, no redistribution of the loads will have taken place with a subsequent low  $n_{ef}$  and low deformation and load carrying capacity. Whether a joint splits early or not may depend on the wood species, the dowel diameter and the steel grade among others. Of course minimum end and edge distances and spacings must be maintained as they have significant influence on the failure modes. In chapter 6 and Sandhaas et al. (2010) it could be seen that indeed different ductility could be reached with different wood species. Further research into the influence of wood species and how to measure this influence (e.g. with MoE, density, hardness, anatomical features as parameters) would maybe help to improve the available criteria. Good numerical models should also be able to support this type of research.

#### 7.4.2 Density versus load carrying capacity

A correlation between load carrying capacity and density could not be found as can be seen in Figure 7-8. No trend of increasing strength with increasing density analogously to embedment strength can be seen. This confirms earlier research by Van de Kuilen (1999). As only few test results were available, also the tests with multiple dowels were considered by assuming that the maximum load is distributed evenly over individual dowels.

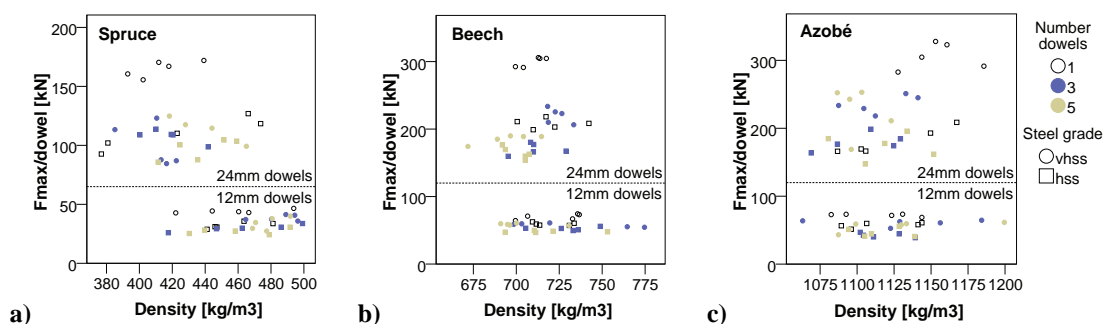


Figure 7-8: Density versus load per dowel, a) spruce, b) beech, c) azobé

### 7.4.3 Influence of wood species – ductility and splitting

Firstly, the tests using spruce glulam and the series with 24 mm dowels must be particularly addressed. The joints with three or five vhss dowels of 24 mm failed in failure mode 1 without developing plastic hinges as predicted with Johansen. The same joints with three and five hss dowels of 24 mm failed in failure mode 2 with a bending angle of only 0.5 to 1 degrees, virtually nothing. The reason for this is probably the poor quality of the ordered GL28h spruce glulam. Annual rings with widths of up to 11 mm were measured and big knots and knot clusters were present. Ringshake failure occurred frequently. The low quality of the spruce wood was also noted during the embedment tests. The joint tests, except the ones with one 24 mm dowel seemed to be splitting tests rather than joint tests and not all failed within the joint that was to be tested. Therefore, the series with three vhss dowels was reinforced laterally at the supports to avoid premature splitting outside the joint itself. The results, however, were brittle failures with even lower results for the joint strength than the same joints with hss dowels. This effect was mentioned in section 7.4.1 and can be seen in Table 7-3 and Figure 7-7a. The results for the spruce specimens with three 24 mm vhss dowels must subsequently be handled with care. Even more, considering the poor quality of the spruce glulam, also all other experiments with spruce must be treated carefully. On the other hand one could say that the tests represented a realistic image of glulam used in practice. For analysing and comparing purposes however, this fact complicates matters.

Before discussing the test results for the different wood species, it should be recalled that important mechanical properties for splitting are the tension strength perpendicular-to-grain and the shear strength. These two values are higher for hardwoods, and among hardwood species, they are higher for tropical hardwoods with higher densities. A more ductile behaviour can thus be expected from joints with hardwood due to the higher resistance in splitting. As will be shown however, this is not all – azobé has higher transverse tension and shear strength than beech, but it still shows less ductility. Also Ehlbeck and Werner (1992b) stated that tropical species were more susceptible to splitting than European hardwoods with lower densities.

Table 7-4 shows the load carrying capacities for the three wood species. The azobé specimens can take between 42% and 137% higher loads than the same spruce specimens. At the same time, the displacements at  $F_{max}$  are similar. During the tests, the observed failures of the spruce specimens were more sudden than the failures of the azobé specimens. The spruce specimens split completely and fell apart whereas the azobé specimens did not split due to the interlocked grain.

**Table 7-4: Load carrying capacities for different species (all mean values)**

	number of dowels	grade	$F_{max}$ [kN]			$F_{azobé}/$	$F_{beech}/$	$F_{azobé}/$	$v(F_{max})$ [mm]		
			spruce	beech	azobé	$F_{spruce}$	$F_{spruce}$	$F_{beech}$	spruce	beech	azobé
12mm dowel	1	vhss	44	70	72	1.63	1.59	1.03	15.1	15.9	7.9
		hss	32	59	57	1.79	1.86	0.97	9.8	15.5	11.1
	3	vhss	115	173	183	1.58	1.50	1.05	5.6	6.5	4.8
		hss	90	157	128	1.42	1.75	0.81	5.0	5.9	3.7
	5	vhss	169	294	281	1.66	1.74	0.96	3.6	5.3	2.9
		hss	136	240	233	1.72	1.77	0.97	3.3	4.5	4.0
24mm dowel	1	vhss	165	300	306	1.85	1.82	1.02	11.2	20.0	5.3
		hss	110	208	181	1.64	1.89	0.87	5.2	23.8	15.2
	3	vhss	297	659	706	2.37	2.22	1.07	2.6	4.2	4.2
		hss	324	510	539	1.66	1.58	1.06	3.9	6.0	5.0
	5	vhss	570	927	1128	1.98	1.63	1.22	3.6	4.1	3.5
		hss	482	823	867	1.80	1.71	1.05	3.6	6.5	4.9

The load carrying capacities of the spruce and beech specimens showed the same ratios than spruce and azobé, but the deformation capacities of the beech specimens were higher. The beech specimens failed at similar or even higher loads than the azobé specimens. This is an unexpected finding considering the different densities of the two wood species ( $\rho_{\text{mean}}(\text{azobé}) = 1120\text{kg/m}^3$  and  $\rho_{\text{mean}}(\text{beech}) = 715\text{kg/m}^3$  with a mean m.c. of 21.0% and 8.7% respectively)<sup>24</sup>. This is due to the higher deformation capacity of the beech specimens. At this stage, it is interesting to recall the results of the embedment tests where beech showed a high ductility. When looking at the embedment test results given in Table 6-4, the results for the embedment strength for beech were between 21% and 40% lower than for azobé at similar m.c.. The ductility instead was higher for beech with 25.5 in comparison to azobé with 15.6 as given in Sandhaas et al. (2010) which can be explained with the high number of radial rays in beech that reinforce the wood structure. Neglecting differences in m.c., azobé has a higher density and higher embedment strength and still the joint strength is similar to beech. In comparison to beech, the ductility was less for azobé also for the joint tests.

Table 7-5 shows the results from Islamaj (2009). His results were similar for both wood species. The load carrying capacity for azobé and cumaru was not different with a maximum of 9% for the tests with one dowel. For the tests with one dowel however, the COV for the tests with cumaru was much higher than for all other tests.

<sup>24</sup> In section 7.4.6, the measured load carrying capacities are adjusted to a m.c. of 12%. The adjusted values for  $F_{\text{max}}$  are given in Table B-8.

**Table 7-5: Results from Islamaj (2009) (all dowels 8 mm, mean values)**

number of dowels	grade	$F_{max}$ [kN]				$F_{Azobé}/$ $F_{Cumaru}$	Cumaru F(vhss)/ F(hss)	Azobé F(vhss)/ F(hss)
		Cumaru	COV [%]	Azobé	COV [%]			
1	vhss	41	14.6	45	6.5	1.09	1.71	1.72
	hss	24	22.6	26	7.8	1.09		
3	vhss	92	6.7	93	5.3	1.01	1.33	1.32
	hss	69	2.2	70	5.7	1.02		
5	vhss	138	6.4	145	6.5	1.05	1.34	1.37
	hss	103	7.2	106	5.7	1.03		

Figure 7-9 shows an example of a beech joint with one vhss dowel 24 mm. The crushing of the fibres with the zigzagging of the rays can be clearly seen. The high ductility of beech probably also influences the effective number of fasteners  $n_{ef}$  as will be discussed in section 7.4.5.

In Table B-7, the bending angles and failure modes in terms of Johansen are listed.

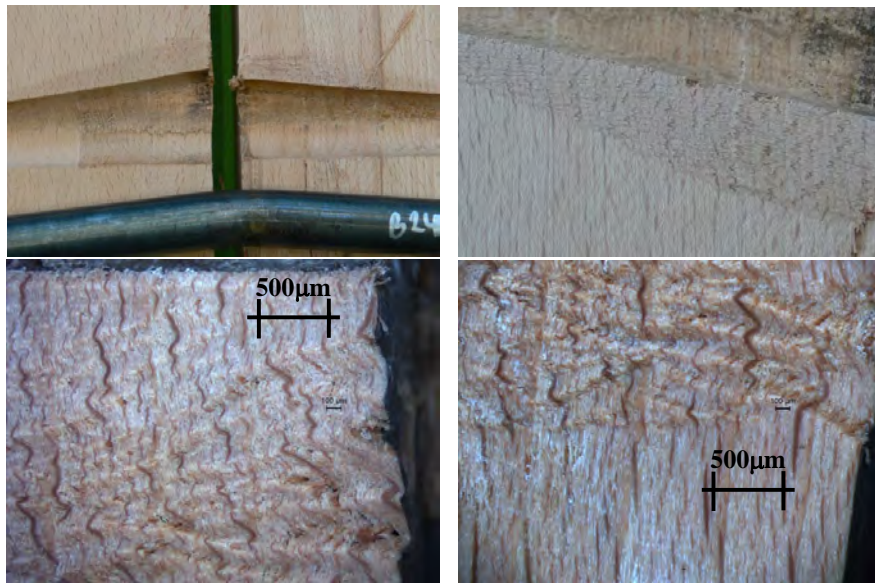


**Figure 7-9: Beech with 24 mm vhss dowel and 6.3x magnification, specimen B24-1-5**

Figure 7-10 to Figure 7-13 show again mean load-slip curves, but this time the test series are shown not per wood species but per dowel type. All above mentioned points can be found back in the figures.

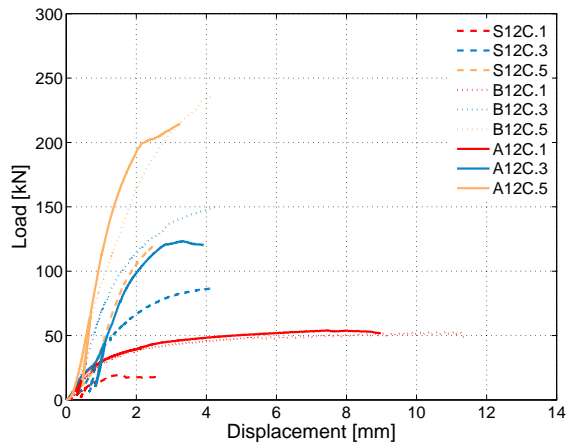


Figure 7-10: Test series with 12 mm hss dowels

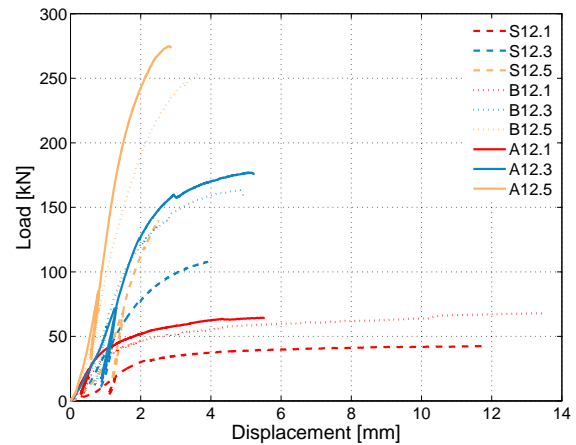


Figure 7-11: Test series with 12 mm vhss dowels

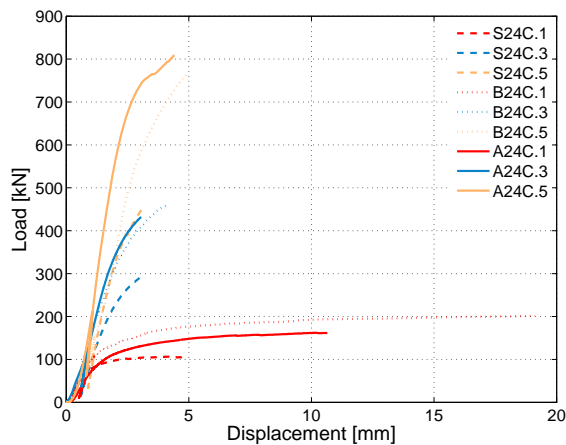


Figure 7-12: Test series with 24 mm hss dowels

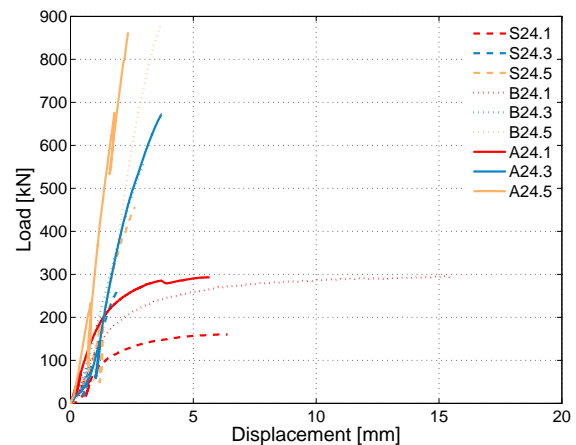


Figure 7-13: Test series with 24 mm vhss dowels

#### 7.4.4 Influence of steel grade

Except for the already discussed series with three 24 mm vhss dowels in spruce, all specimens with vhss dowels reached a higher load carrying capacity in comparison with hss dowels. Not only the load carrying capacity was higher with vhss dowels, but also using vhss dowels, ductile failure modes could be reached (see Table 7-3) which is an important finding for practice. But also for the series with three 24 mm dowels in spruce, the higher theoretical load carrying capacity is evident when looking at the detail in Figure 7-7a: the load-slip curve for the series with hss dowels had an earlier transition from linear to nonlinear regime. The joints with hss dowels bend earlier than the joints with vhss dowels.

The increase in capacity between hss and vhss dowels ranges from 13% to a maximum of 69% as can be seen in Table 7-6. The only surprising values are the ratios for the beech specimens with 12 mm dowels. They seem to be lower than expected. In order to

consider all possible issues including the dowels, more tension tests were carried out on 12 mm dowels. The hss dowels used in spruce, beech and azobé were tested to establish the load carrying capacity. Indeed, as can be seen in Table A-1, differences could be observed. The dowels used for the beech specimens had higher mechanical properties. This explains why the trend of about 30% higher load carrying capacity with vhss dowels cannot be found for the 12 mm beech specimens.

**Table 7-6: Ratios  $F_{\max}(\text{vhss})$  over  $F_{\max}(\text{hss})$**

	number of dowels	F(vhss)/ F(hss)	
		12 mm dowel	24 mm dowel
spruce	1	1.38	1.50
	3	1.29	0.92
	5	1.25	1.18
beech	1	1.18	1.44
	3	1.10	1.29
	5	1.22	1.13
azobé	1	1.26	1.69
	3	1.43	1.31
	5	1.21	1.30

Islamaj's (2009) results show the same trends. He found an increase in capacity between 32% and 72% with similar results for the species cumaru and azobé.

As already stated, the bending capacity of different steel grades is expected to be different due to the considerably higher strength of vhss. Therefore, joints with vhss dowels should deform less and are supposed to fail in failure modes with less plastic hinges than joints with hss dowels, always assumed that the dowel diameters remain the same. These assumptions could be confirmed in the tests. The deformation angles were measured (for failure mode 3 only central bending angle as indicated in Figure 6-3) and are indeed lower for vhss (Table B-7). As also stated in Jorissen (1998), bending angles of  $45^\circ$  were never reached. Two typical results are shown in Figure 7-14 and Figure 7-15 (please note that in the test series beech with one 24 mm vhss dowel both joints were tested – double tests with identical upper and lower joint).



**Figure 7-14: 24 mm hss dowel, test B24C-1-3**



**Figure 7-15: 24 mm vhss dowel, test B24-1-2**

Also for the embedment tests, different strengths were found for hss and vhss dowels (Table 6-4). As stated, this increase of embedment strength for vhss dowels could not be explained with different surface roughness of the dowels. Therefore, apart from a different bending capacity of the dowels, there must be also another effect that leads to an increase in load carrying capacity.

#### 7.4.5 Effective number $n_{ef}$ of fasteners

A lot of research effort has been put into the development of correct prediction equations for the load carrying capacity of dowelled joints. The mechanics-based models are in most cases based on the Johansen equations (European Yield Model EYM, 1949) which were developed per shear plane per dowel for ductile failures due to embedment or a combination of embedment and dowel bending. Three failure modes (FM) are possible according to Johansen: pure embedment failure (FM1), one plastic hinge in the dowel per shear plane (FM2), two plastic hinges in the dowel per shear plane (FM3). However, also other failure modes can occur as identified in Quenneville and Mohammad (2000). These other failure modes such as row shear-out, group tear-out or splitting are brittle failure modes that occur often in joints with multiple dowels or in joints with dowels that have a low slenderness ratio. An effect of these brittle failure modes is that the load carrying capacity of a joint with multiple dowels is less than the sum of the load carrying capacity of the single dowels.

EC5 (CEN, 2004b) deals with this fact by introducing an effective number  $n_{ef}$  of fasteners:

$$F_{joint} = n_{ef} \cdot n_{SP} \cdot F_{per\_SP} \quad (7-3)$$

where  $F_{joint}$  = strength of joint with  $n$  dowels;  $n_{ef}$  = effective number of fasteners;  $n_{SP}$  = number of shear planes;  $F_{per\_SP}$  = strength of joint per shear plane according to Johansen.

The current equation in EC5 to estimate the effective number  $n_{ef}$  is given in Equation (7-4). As can be seen, this equation is solely based on geometrical considerations and its main message is that only when the distance  $a_1$  between fasteners is at least  $17d$ , then  $n_{ef} \approx n$ . No other influences such as material properties or slenderness ratios are considered.

$$n_{ef} = \min \left\{ \begin{array}{l} n \\ n^{0.9} \sqrt[4]{\frac{a_1}{13d}} \end{array} \right. \quad (7-4)$$

Another approach was chosen by Quenneville (2008). Instead of basing predictions on the Johansen equations and then reducing the obtained load carrying capacities with  $n_{ef}$  to account for brittle failures, Quenneville developed equations for each possible failure mode. The strength of a joint is then calculated by taking the minimum of each single

joint resistance as shown in Equation (7-5) (assuming thus that the brittle failure modes are uncoupled).

$$R_d = \min \begin{cases} R_{embedment} \\ R_{row\_shear} \\ R_{tear-out} \\ R_{net\_tension} \\ R_{splitting} \end{cases} \quad (\text{Quenneville, 2008}) \quad (7-5)$$

Quenneville's equations for the single failure modes are derived from test results and are based on geometric considerations together with mechanical properties of wood (embedment, tension and shear strength) and steel (plastic bending capacity). Compared to Equation (7-4) from EC5, Quenneville's equations consider not only the spacing  $a_l$  and the dowel diameter, but a laborious combination of all end distances, spacings, number of rows and number of dowels per row. The derivation of the empirical equations for the single failure modes is based on a huge database of tests where many parameters were varied: among others dowel diameters, slenderness ratios, edge and end distances, spacings, member thicknesses or single- and double-shear timber-to-timber and steel-to-timber joints. Implicitly, Quenneville included also the slenderness ratio of the dowels into his empirical equations.

Equation (7-4) from EC5 was determined by Jorissen (1998) through a regression analysis of about 1000 test results. Equation (7-4) results in characteristic values. Jorissen's tests were double shear timber-to-timber joints with timber members loaded parallel-to-grain. The wood species was spruce and exclusively 12 mm dowels were used. The thickness of the middle and side members was varied in order to change the slenderness ratio keeping however the dowel diameter constant. Jorissen stated that other dowel diameters should be taken into account to better describe joint behaviour. He concluded that of all influence parameters, the slenderness ratio was the least determining. This is the reason why the slenderness ratio was not considered in the simplified design rules for EC5 shown in Equation (7-4).

One aspect plays a role when looking into a possible additional influence of the dowel diameter and the subsequent different slenderness ratio. The slenderness ratio cannot be taken into account by simply changing the thickness of the member. The dowel diameter itself will have an influence as it has on the embedment strength. An additional parameter to adjust Equation (7-4) could be a slenderness parameter that is established investigating dowel diameter effects or the incorporation of more geometrical data analogously to Quenneville (2008).

Another potential additional parameter could aim at taking a possible influence of the steel grades into account. One approach could be to introduce the ratio of the yield strength  $f_y$  and ultimate strength  $f_u$  which is different for the different steel grades or maybe the different hardness has an influence.

Before further analysing the test results shown in Figure 7-16 and Figure 7-17, it must be underlined that not enough test results are available to reliably propose changes in Equation (7-4). Mere ideas can be given based on the here presented tests with different wood species, steel grades and dowel diameters. As the test series carried out by Islamaj (2009) is comparable to the own test series, his results are also considered. The effective number  $n_{ef}$  was established as the ratio of the mean maximum load  $F_{max}$  of the joint series with multiple dowels over the mean  $F_{max}$  of the respective joint series with one dowel.

Figure 7-16 shows the effective number calculated from the test results for all test series with three dowels including the results from Islamaj (2009). The black line indicates the effective number  $n_{ef} = 2.12$  as calculated according to Equation (7-4). The first observation is that  $n_{ef}$  as defined by EC5 is on the safe side except for the already discussed tests on spruce specimens with 24 mm vhss dowels and for Islamaj's azobé series with 8 mm vhss dowels. Furthermore, there seems to be a trend that joints with vhss have a lower  $n_{ef}$  than joints with hss. This is especially valid for the tests with 8 mm and 24 mm dowels. This difference seems to be lower for the beech series. An influence of the dowel diameter on the other hand cannot be observed.

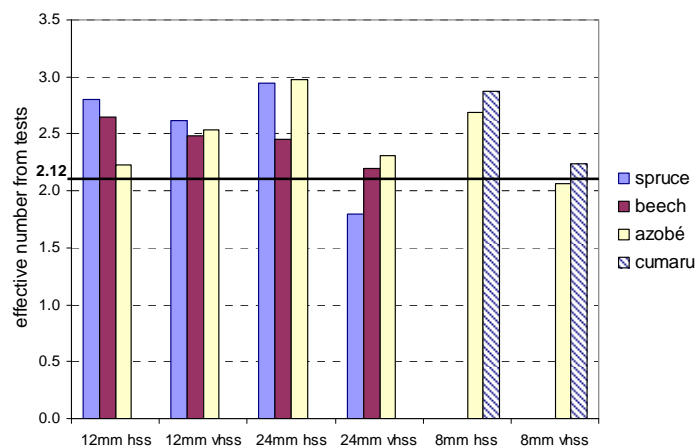


**Figure 7-16: Effective number of fasteners, joint series with 3 dowels (results 8 mm dowels from Islamaj, 2009),  $n_{ef,EC5} = 2.12$**

Figure 7-17 shows the effective number for the test series with five dowels with  $n_{ef} = 3.35$  according to EC5. Again,  $n_{ef}$  is on the safe side except for the beech series with 24 mm vhss dowels and for Islamaj's azobé series with 8 mm vhss dowels.

A possible explanation for the beech series is the high deformation state and subsequent high load carrying capacities reached in the joints with one dowel. The trend of less difference between joints with vhss and hss dowels can be observed for all beech series, 12 mm and 24 mm dowels, three and five dowels in a row. Here, it is interesting to remember that the displacement at  $F_{max}$   $v(F_{max})$  was often close to the ultimate displacement  $v_{max}$  which indicates that the joints could have still taken higher loads if

they would not have failed in splitting before. The ductility however decreases considerably when multiple dowels are used. Therefore, a high deformation capacity of joints with one dowel leads to a low  $n_{ef}$ .

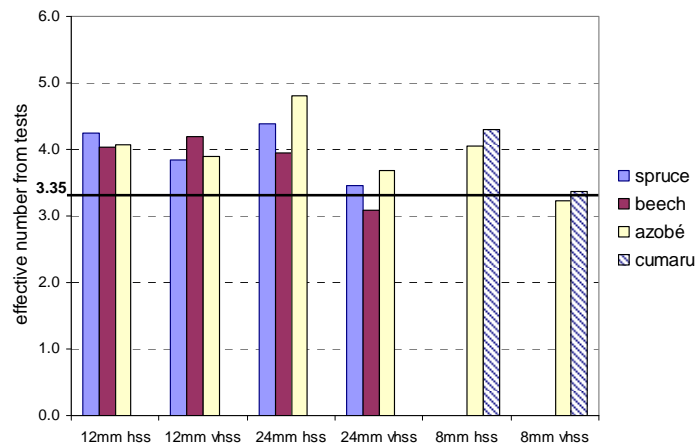


**Figure 7-17: Effective number of fasteners, joint series with 5 dowels (results 8 mm dowels from Islamaj, 2009),  $n_{ef,EC5} = 3.35$**

The trend observed in Figure 7-16 can be confirmed in Figure 7-17. The effective number  $n_{ef}$  tends to be lower for joints with vhss dowels, especially for 8 mm and 24 mm dowels. A tendency of a lower  $n_{ef}$  for vhss can be expected based on the following consideration: hss has a lower strength and starts yielding at an earlier stage than vhss. This means that hss dowels start deforming at lower loads which helps to avoid splitting at low deformations. Vhss dowels are more rigid and they bend later in comparison to hss dowels. The stress redistribution will therefore be better for joints using hss dowels.

In the same line of discussion, a difference should be seen between the different wood species as their strength differs a lot. The ratio of the strength of the dowel and of the strength of the wood will therefore have an influence on  $n_{ef}$ . A closer look into the combination of a ‘performance class’ of the timber and the steel grade would be interesting. Spruce (low performance class) combined with vhss or azobé (high performance class) combined with hss should act differently on  $n_{ef}$ .

Moreover, there seems to be an influence of the wood species. As discussed above, beech for instance shows high ductility when testing joints with one dowel. The subsequent reduction of deformation capacity for multiple-bolted joints leads to lower  $n_{ef}$  for ductile wood species. The effective number is always referred to the load carrying capacity of a joint with one fastener what makes it a dependent parameter,  $n_{ef}(F_{one\ dowel})$ . Joints with high density and less ductile wood species on the other hand split already at an early stage even with only one dowel which led to different  $n_{ef}$ . Often, for these wood species, a joint deformation of 15 mm or a deformation of 5 mm of embedment tests cannot be reached. This effect leads to a low load carrying capacity of the joints with one dowel and

subsequently to high values for  $n_{ef}$ . The observed results in terms of load carrying capacity for azobé and beech confirm this. Although azobé has a higher density, the beech specimens had a similar load carrying capacity (m.c. of azobé was higher). Obviously, redistribution effects also depend on the failure modes of the joints. If no embedment took place, the effective number will be low as no load redistribution occurred.

The observed bending angles (Table B-7) confirm the discussed issues on influence of steel grade and ductility of the joints with one dowel. For the joints with one dowel, the observed bending angles are big (mean 10°) with the biggest angles for the beech joints (mean 15°). The bending angles of the 12 mm dowels are comparable for both steel grades whereas a bigger difference can be observed between 24 mm hss and vhss dowels. The bending angles are decreasing considerably when testing joints with three or five dowels (between 1° and 5°). For these multiple dowelled joints, the bending angles of the hss dowels are consistently bigger than the angles for vhss dowels.

Considering the above discussion, Equation (7-4) from EC5, which is based on purely geometrical considerations, should also depend on material properties such as steel grade and wood species together with a dependence on a slenderness ratio evaluated with different dowel diameters.

#### 7.4.6 Predictions - Johansen equations

After having carried out all tests, the predictions as described in section 7.3.3 can be repeated, but using now the measured properties of the test specimens, i.e. measured geometrical data such as thickness and dowel diameter and measured material properties such as density and yield strength. As the moisture content was measured, both predictions and test results were adjusted to a moisture content of 12%. This was done analogously to the embedment test results. The measured densities were calculated for a m.c. of 12% and the load carrying capacities were reduced by 3% for every percentage point difference in moisture content. The empirical Equation (6-5) to calculate the embedment strength was used instead of Equation (7-2) from Ehlbeck and Werner (1992a). Equation (6-5) is shown again below:

$$f_{h,0} = 0.095(1 - 0.0089d_{measured})\rho_{12\%} \quad (7-6)$$

where  $f_{h,0}$  = embedment strength parallel to grain in [MPa],  $d_{measured}$  = measured dowel diameter in [mm],  $\rho_{12\%}$  = measured density in [kg/m<sup>3</sup>] at 12% m.c..

The effective bending capacity of the dowels was established with theoretical Equation (7-1). The values for the yield strength of the dowels were taken from Table 6-1. For the

12 mm hss dowels, a difference per wood species was observed. Therefore, the proper yield strength per test series was applied<sup>25</sup>. The measured dowel diameters were used.

As for the bending capacity of the dowels, a more precise discussion can be carried out as the deformation angles were measured. With this information, the outer strain can be calculated and the true bending moment of the dowels can be determined which will lie between the fully elastic and the fully plastic moment (see section 6.2).

Figure 7-18 shows the calculated ‘true’ moments of the dowels (deformation angles see Table B-7) together with the elastic moment (equation given in Figure 6-3), the plastic moment according to Equation (6-1) and the bending moment according to Equation (6-2) from EC5. First of all, it can be seen that the prediction from EC5 is even lower than the elastic moment for 24 mm dowels. As expected, the true moments lie between the elastic and the plastic value. However, it can be seen that the measured values are much closer to the values for the plastic moment. This confirms the findings from section 6.2 and the decision of establishing the bending moment with Equation (6-1).

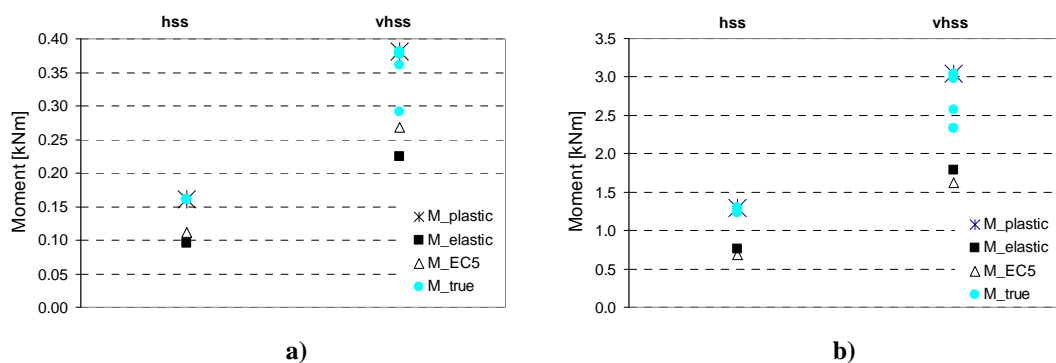


Figure 7-18: Bending moments of steel dowels, a) 12 mm dowels, b) 24 mm dowels

The two graphs in Figure 7-19 show the measured maximum load carrying capacities versus the predicted results (both adjusted to a m.c. of 12%). No effective number was applied to predict the load carrying capacity, the load carrying capacity per dowel per shear plane was simply multiplied with number of shear planes and dowels. The agreement between measurements and predictions is surprisingly good with a less good agreement for the 12 mm dowel series. For comparative reasons, Figure 7-20 shows the measured versus the predicted results where the measured input values were used, no adjustment to a m.c. of 12% was done. No significant difference can be seen. The  $R^2$ -value is not improving. However, the regression line is closer to the diagonal  $y = x$  when using the adjusted values which still indicates a better prediction.

<sup>25</sup> 24mm dowels:  $f_{y,vhss} = 1324\text{MPa}$ ,  $f_{y,hss} = 517\text{MPa}$ ; 12mm dowels:  $f_{y,vhss} = 517\text{MPa}$ ,  
Table A-1: 12mm hss dowels in azobé  $f_y = 490\text{MPa}$ , in beech  $f_y = 760\text{MPa}$ , in spruce  $f_y = 560\text{MPa}$ .

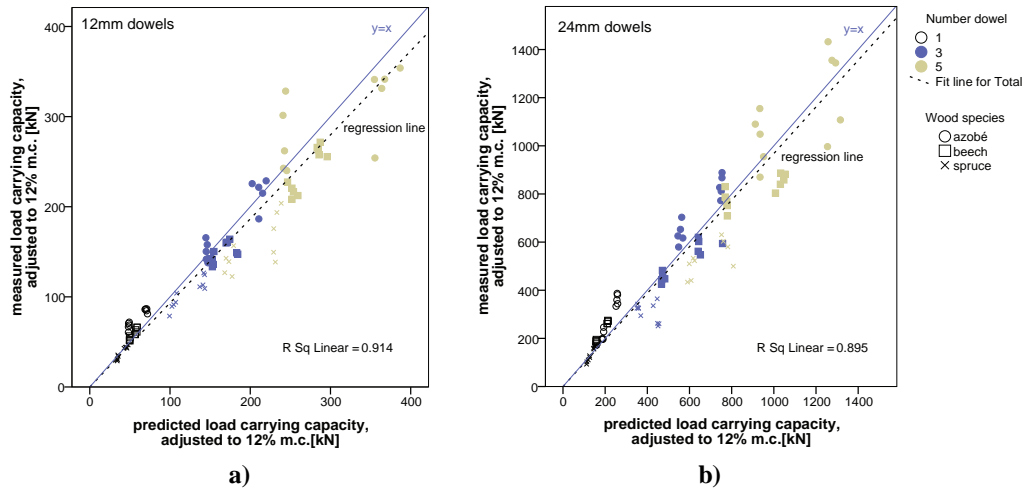


Figure 7-19: Measured versus predicted load carrying capacities – all adjusted to 12% m.c.,  
a) 12 mm dowels, b) 24 mm dowels

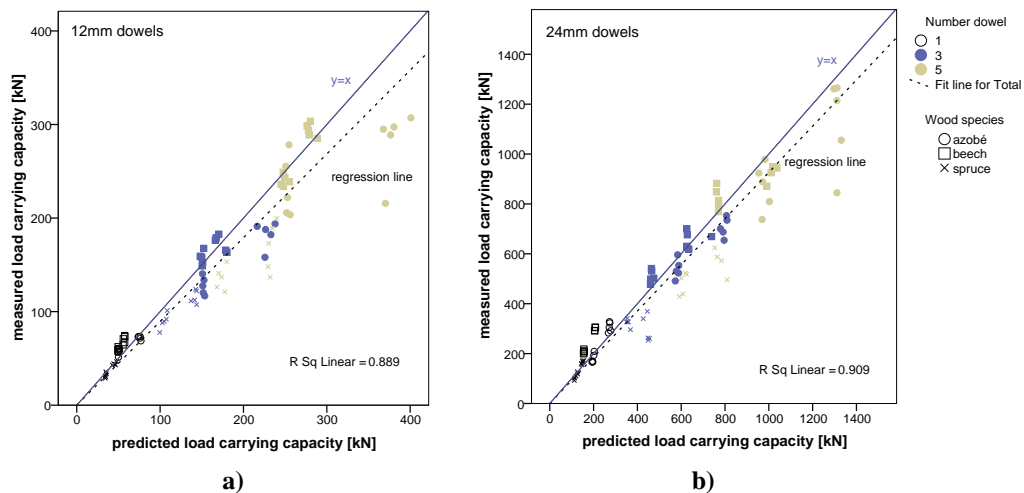


Figure 7-20: Measured versus predicted load carrying capacities – no adjustments to 12% m.c.,  
a) 12 mm dowels, b) 24 mm dowels

If now the adjusted predicted results are corrected with an effective number  $n_{ef}$ , the results are shifting towards a safer direction with lower values for measurements compared to predicted load carrying capacities. Figure 7-21 and Figure 7-22 show the graphs where the predictions were corrected with  $n_{ef}$  from EC5 (Equation (7-4)). Figure 7-23 and Figure 7-24 instead show the results with  $n_{ef}$  calculated from the test results (see Figure 7-16, Figure 7-17 and Tables B-5 and B-6). Speaking in terms of mean values and not of characteristic values, the predictions applying  $n_{ef}$  from EC5 yield conservative results. Nearly all test results have higher load carrying capacities. The predictions applying the measured  $n_{ef}$  give better results. This is certainly valid for 12 mm dowels where the diagonal  $y = x$  is close to the regression line. No difference in prediction quality can be observed for the different steel grades or wood species.

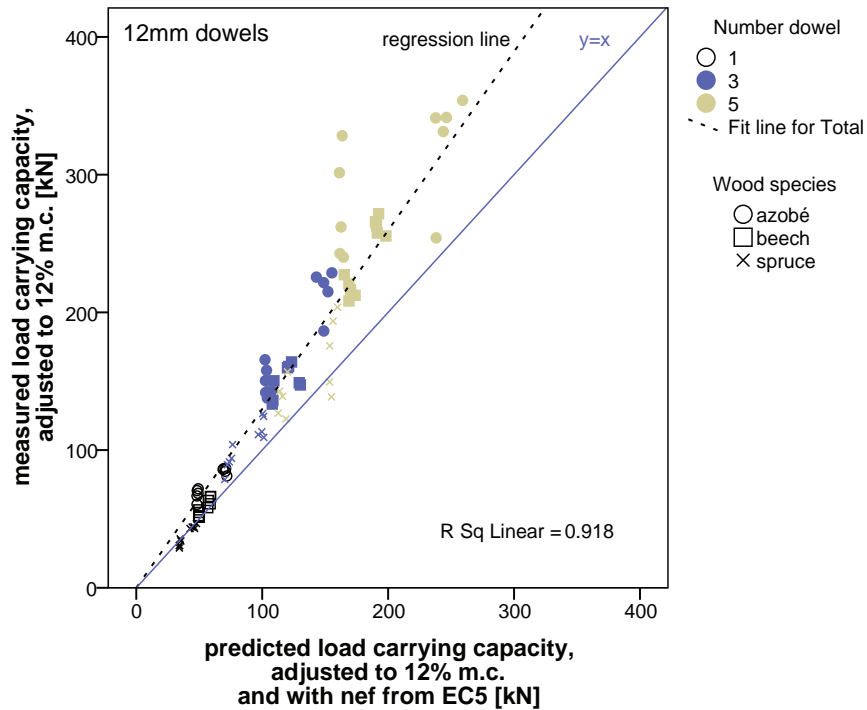


Figure 7-21: Measured versus predicted load carrying capacities reduced with  $n_{ef}$  from EC5 all adjusted to 12% m.c., 12 mm dowels

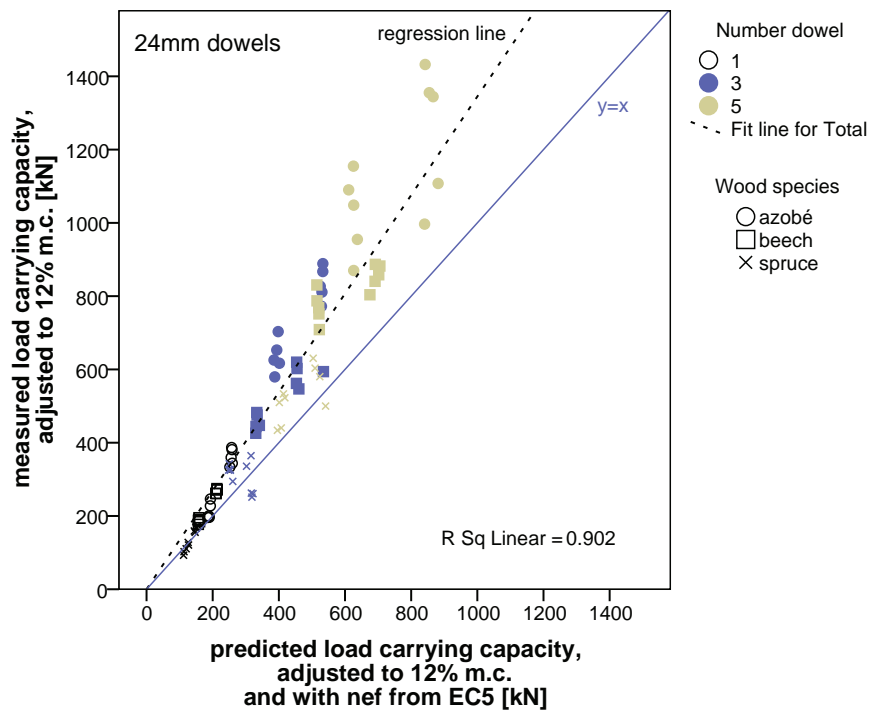


Figure 7-22: Measured versus predicted load carrying capacities reduced with  $n_{ef}$  from EC5 all adjusted to 12% m.c., 24 mm dowels

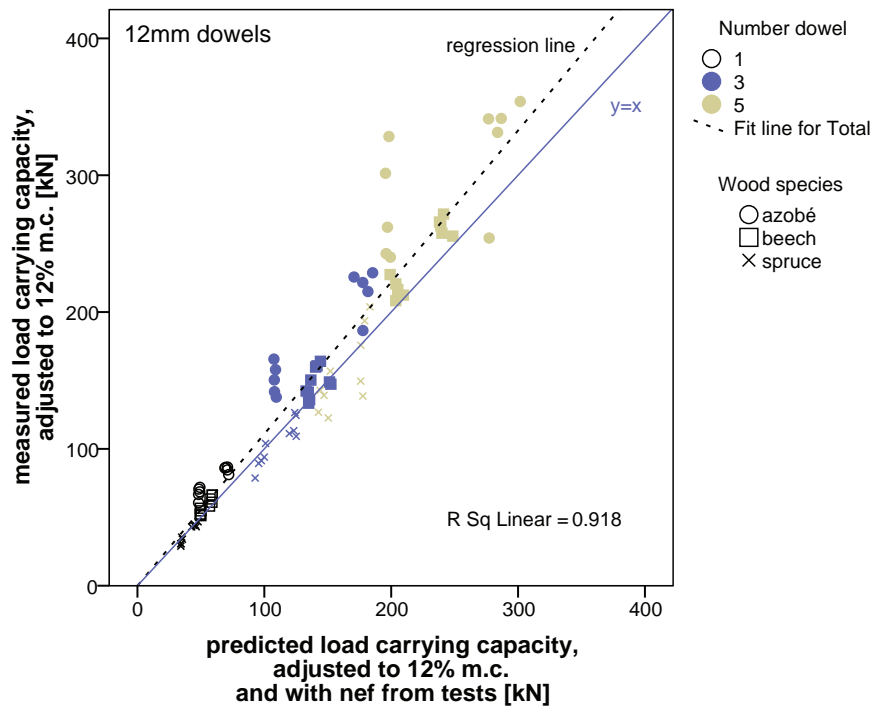


Figure 7-23: Measured versus predicted load carrying capacities reduced with  $n_{ef}$  from tests all adjusted to 12% m.c., 12 mm dowels

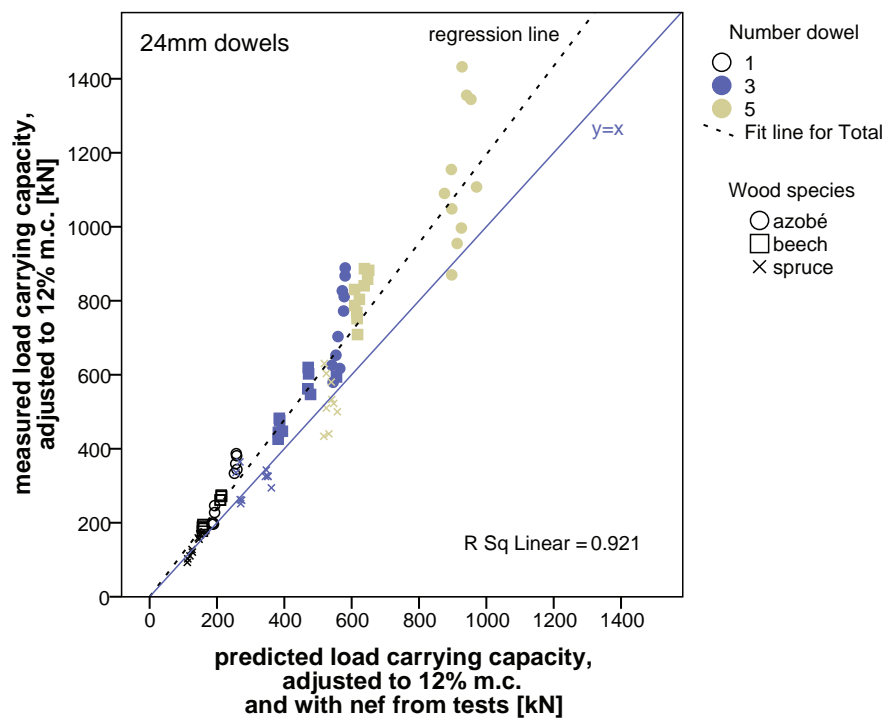


Figure 7-24: Measured versus predicted load carrying capacities reduced with  $n_{ef}$  from tests all adjusted to 12% m.c., 24 mm dowels

### 7.4.7 Stiffness $K_{ser}$

Figure 7-25 shows the used testing protocol from EN 26891 (CEN, 1991) in terms of load-slip. Important measuring points of the resulting load-slip curve are defined. By means of these measuring points, the stiffness  $K_{ser}$  per joint can be calculated. According to EN 26891, the slips at points 01 and 04 must be taken as then the actual stiffness of the joints is determined. The purpose of the initial loop (points 01 to 11) is to settle the test specimen before carrying out the experiment up to failure.

Among others,  $K_{ser}$  is susceptible to manufacturing processes and a rather large scatter can be expected. An example that illustrates a cause of scatter due to fabrication tolerances is shown in Figure 7-26 where different drilling qualities are shown.

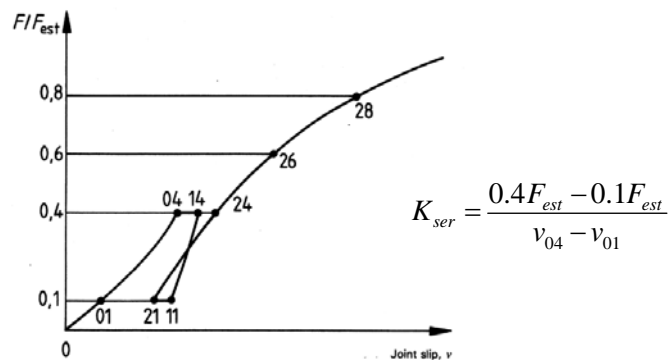


Figure 7-25: Test protocol according to EN 26819 (CEN, 1991) with determination of  $K_{ser}$

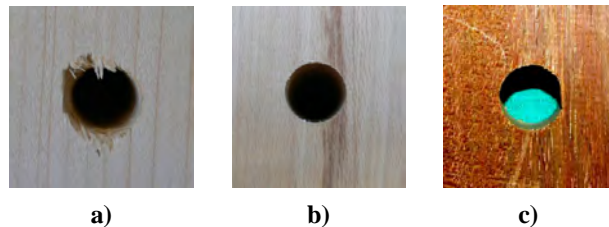


Figure 7-26: Examples of drilling differences: a) spruce – b) beech – c) azobé

For each specimen, the stiffness  $K_{ser}$  as defined in Figure 7-25 was determined. Apart from an expected variation due to the natural scatter of wood or fabrication issues, the determination of stiffness values is also heavily influenced by the test execution, mainly by two issues:

- Estimated load carrying capacity  $F_{est}$ :  
Only after a first test, the chosen value for  $F_{est}$  can be verified. Therefore,  $F_{est}$  may change during a test series or may not correspond to the actual reached load carrying capacity. Furthermore, in order to not damage the specimens, a lower value for  $F_{est}$  may be chosen. This is certainly necessary for big specimens that

reach a high load carrying capacity as then, 40% of  $F_{est}$  may damage the joint locally.

- Measuring locations:

In the standards that define testing protocols such as EN 26891, no provisions are given as to where the testing data should be measured. For instance, whether the measuring instruments should be fastened in the barycentre lines of the joints or whether they should cover the whole joint by measuring outside the joint.

In EC5, an empirical regression equation is given to determine a value for  $K_{ser}$  per shear plane per fastener based on mean density and dowel diameter. Equation (7-7) is based on test results on timber-to-timber joints (just like  $n_{ef}$ ) that failed in failure mode 3 with two plastic hinges per shear plane. It is defined that the obtained value should be multiplied by two for steel-to-timber joints.

$$K_{ser} = \rho_{mean}^{1.5} \frac{d}{23} \quad (7-7)$$

where  $K_{ser}$  = stiffness in [N/mm],  $d$  = dowel diameter in [mm],  $\rho_{mean}$  = mean density in [kg/m<sup>3</sup>].

Equation (7-7) was used to predict  $K_{ser}$  where the measured dowel diameters and densities were employed. Analogously to the other analyses of experimental results,  $K_{ser}$  was predicted two times, firstly with the measured densities and secondly with the densities that were adjusted to a m.c. of 12%<sup>26</sup>. Moreover, the prediction of  $K_{ser}$  according to Equation (7-7) will show a large scatter. All measured and predicted stiffness values are given in Appendix B.

The following graphs show measured values of  $K_{ser}$  and  $F_{max}$  per dowel where it is assumed that stiffness and strength is distributed evenly (which may not be the case for specimens that split early without significant deformations as discussed previously). Consequently, the values per dowel are obtained by simply dividing through the number of dowels. The values shown are thus per two shear planes of a steel-to-timber joint.

Figure 7-27 shows the measured values for  $K_{ser}$  per dowel over the measured density at test. It should be expected that the values of  $K_{ser}$  increase with increasing density as Equation (7-7) proposes this. This trend is very low in Figure 7-27 (if all three wood species are combined, the regression equation is slightly inclined with a  $R^2$ -value of 0.04). The dependence from the dowel diameter which is linear in Equation (7-7) and thus should lead to a factor 2 between 12 mm and 24 mm dowels is clearer, at least for the joints with one dowel. For joints with more dowels this effect vanishes. No difference could be found for different steel grades.

---

<sup>26</sup> If not otherwise indicated, the graphs show the predicted stiffness  $K_{ser,pred}$  determined with the measured density that was not adjusted to 12% m.c. The results between adjusted predictions and the predictions using the measured densities without adjustment do not differ significantly.

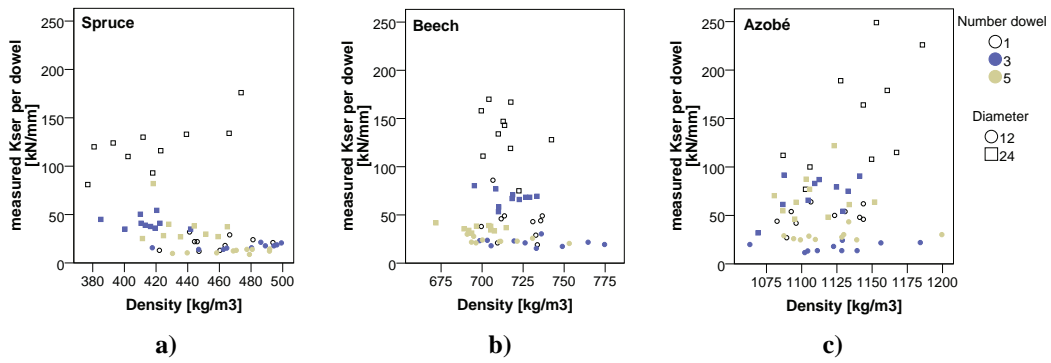


Figure 7-27:  $K_{ser}$  per dowel (with two shearplanes) versus density, a) spruce, b) beech, c) azobé

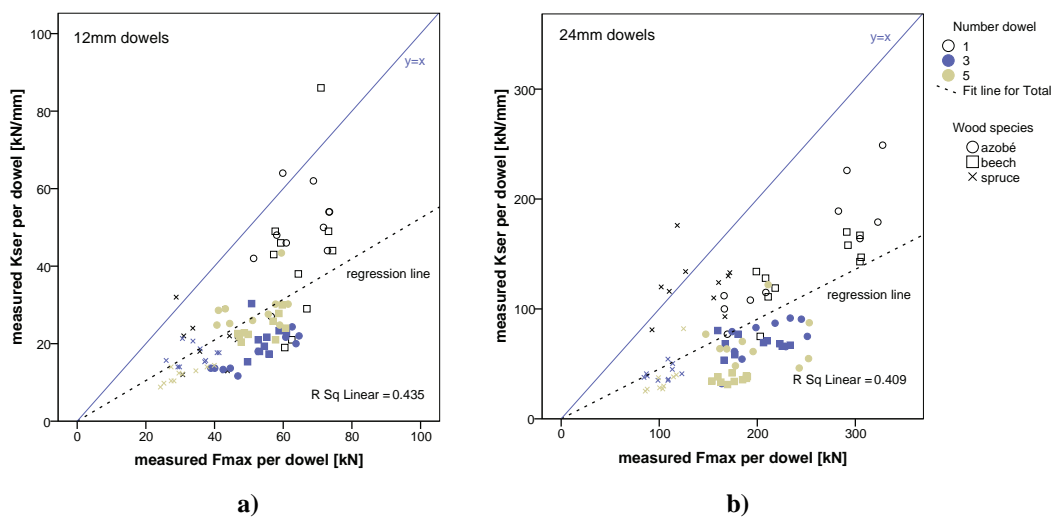


Figure 7-28:  $K_{ser}$  per dowel versus  $F_{max}$  per dowel, a) 12 mm dowels, b) 24 mm dowels

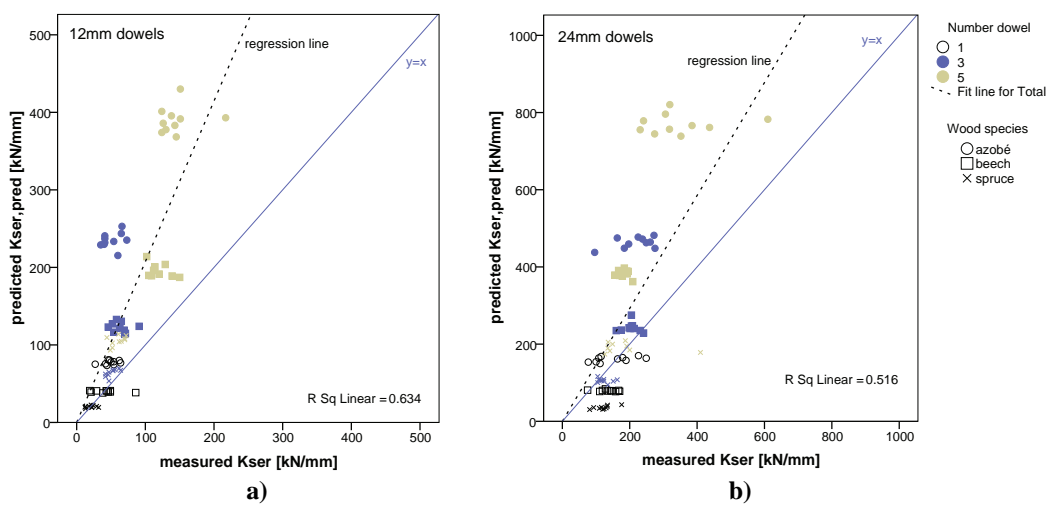


Figure 7-29: Measured value of  $K_{ser}$  versus prediction with measured values for all steel grades, a) 12 mm dowels, b) 24 mm dowels

Figure 7-28 shows the measured values of  $K_{ser}$  and  $F_{max}$  per dowel. When looking at the  $R^2$ -value from the linear regression, it is obvious that the correlation is low for both dowel diameters. Again no difference could be found for vhss and hss.

Figure 7-29 shows the comparison between predicted values according to Equation (7-7) and measured values per joint, thus per two shear planes and one, three or five dowels. It is clear that the prediction quality for multiple dowel joints is rather bad. The measured values are consequently lower than the predicted values. If looking at joints with one dowel, the prediction quality for 12 mm dowels in spruce and beech is better than for azobé. With 24 mm dowels instead, the stiffness is underestimated for spruce and also for beech whereas for azobé with a large scatter in the measured values, the prediction is better.

It seems that an effective number  $n_{ef}$  could be also applied to  $K_{ser}$ . The observation of such a  $n_{ef}$  seems logical.  $K_{ser}$  is sensitive to initial slip which is mainly caused by fabrication tolerances. If more than one dowel is used, the probability of fabrication inaccuracies is increasing.

## 7.5 CONCLUSIONS

A comprehensive joint test series including the wood species spruce, beech and azobé has been carried out using two different steel grades, vhss and hss. The experimental results have been discussed in this chapter and are summarised below:

- In timber joints, hss dowels can be replaced by vhss dowels. Joints with vhss reached higher loads than the same joints with hss dowels.
- Joints with spruce have a lower load carrying capacity than joints with beech and azobé. No large difference in load carrying capacity could be observed between joints with beech and azobé. However, the used azobé had a higher moisture content than the beech wood. Therefore, a higher difference in load carrying capacity is expected when both wood species are used at the same moisture content.
- No strong correlation could be found between density of the wood and load carrying capacity of the joints using one wood species.
- The failure modes can be predicted with the Johansen equations. This is valid also for different steel grades and wood species.
- Ductile failure modes with one or two plastic hinges per shear plane were possible also when using vhss dowels as modern vhss steel grades possess enough deformation capacity.
- Compared to hss dowels, the failure modes of the joints with vhss dowels were shifted towards failure modes with less plastic hinges. Furthermore, the bigger the dowel diameters, the more a shift towards modes with no plastic hinges or one plastic hinge per shear plane could be observed.

- The observed effective number  $n_{ef}$  for more dowels in a row showed a trend to be lower for the joints with vhss dowels. The difference between  $n_{ef}$  for hss and vhss dowels was smaller for beech. This may be due to the higher deformation capability of beech and hence higher ultimate loads in the joints with one dowel.
- On wood species level, the stiffness  $K_{ser}$  is not strongly related to the density of the used wood species and only weakly to the dowel diameter. An effective number  $n_{ef}$  could be used for  $K_{ser}$ .

# 8

## COMPARISON TESTS - MODELS

*This chapter compares the modelling results obtained in chapter 5 with test results given in chapters 6 and 7. The global load-slip curves are discussed and the observed failure modes are compared with the predicted failure modes. The prediction quality, especially regarding global load-slip curves and failure modes, is evaluated. Conclusions as to how numerical models could be improved are given.*

### 8.1 INTRODUCTION

Simulation results (chapter 5) based on the developed material model (chapter 4) are compared with experimental results. Two basic groups of models and tests are covered:

- Embedment models – experimental results are given in chapter 6;
- Joint models – experimental results are given in chapter 7.

The comparisons between pure material models and experimental results taken from literature were already shown in chapter 5. The models and the test specimens are not presented in this chapter. All necessary information on geometry, boundary conditions etc. were already given in the relevant chapters 5, 6 and 7.

However, more simulations will be carried out varying the material properties if the comparison between model and experiment is not satisfying. This means that a calibration is carried out after knowing the experimental outcomes and the models lose their predictive character. Properties such as elastic stiffness, strength values or fracture energies can be easily changed without the need to introduce artificial or non-realistic values. Recalling section 4.5 where the difficulties related to the determination of the mechanical material parameters were exhaustively discussed, modifications of material input values are admissible. The used initial properties are defective and no absolute values so that they can be changed within the large range of experimental results.

## 8.2 EMBEDMENT SPECIMENS

The comparisons between models and tests were carried out for three wood species. Although more wood species were used in the experimental part, only the three wood species spruce, beech and azobé were modelled as these three species were later used for the joint tests and models. The default material parameters as used in chapter 5 are given in Table 8-1. Moreover, a parameter study for azobé was undertaken where the MoE parallel-to-grain and the strength properties and fracture energies for tension perpendicular-to-grain and shear were increased. The modified material parameters for azobé are given in the last two columns of Table 8-1.

**Table 8-1: Default material properties and modified values, all wood species**

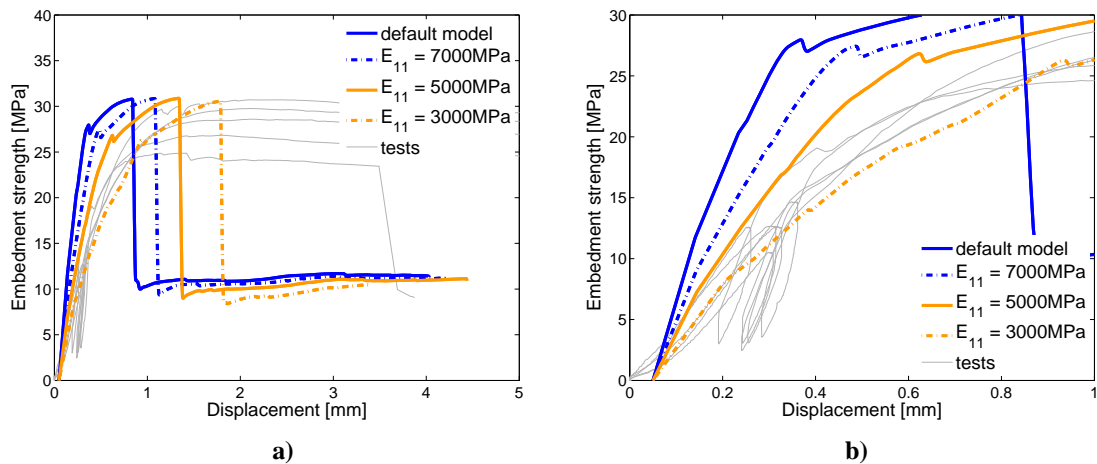
Parameter	Units	spruce default	beech default	azobé default	azobé '90.v.roll'	azobé 'all.E <sub>11</sub> '
$E_{11}$		11000	13000	20000	20000	<b>15000</b>
$E_{22}=E_{33}$		370	860	1330	1330	1330
$G_{12}=G_{13}$		690	810	1250	1250	1250
$G_{23}$		50	59	91	91	91
$f_{t,0}$	MPa	24	41	72	72	72
$f_{c,0}$		36	45	58	58	58
$f_{t,90}$		0.7	1.0	1.0	<b>2.0</b>	<b>2.0</b>
$f_{c,90}$		4.3	14.2	23.2	23.2	23.2
$f_v$		6.9	6.9	8.6	<b>12</b>	<b>12</b>
$f_{roll}$		0.5	0.5	0.6	<b>1.0</b>	<b>1.0</b>
$G_{f,0}$		60	100	180	180	180
$G_{f,90}$	N/mm	0.5	0.71	0.71	<b>5</b>	<b>5</b>
$G_{f,v}$		1.2	1.2	1.5	<b>7</b>	<b>7</b>
$G_{f,roll}$		0.6	0.6	0.7	<b>1</b>	<b>1</b>
$\eta$	-	0.0001	0.0001	0.0001	0.0001	0.0001

Figure 8-1 to Figure 8-3 show the overlap between test results and model predictions for the spruce, beech and azobé specimens with 24 mm dowels.

The prediction for the spruce specimen, shown in Figure 8-1 with default material parameters is good in terms of embedment strength. However, the stiffness is too high. It is already known from literature that the stiffness is often too high when modelling (Dias et al., 2010). Therefore, the elastic stiffness parallel-to-grain  $E_{11}$  was reduced as indicated in Figure 8-1. In Figure 8-1b, a detail of the stiffness is shown. The modelling results were offset by 0.05 mm in order to account for the slip in the experimental results. The model with  $E_{11} = 5000$  MPa forms the upper bound and the one with  $E_{11} = 3000$  MPa the lower bound of the test results. The two stiffness values are much smaller than the default stiffness of  $E_{11} = 11000$  MPa. Furthermore, the early entrance in the nonlinear regime can be seen in Figure 8-1b where the load-slip curves have a slight bend between 0.1 and

0.2 mm deformation. The reason for this bend could be the onset of damage in tension perpendicular-to-grain.

The brittle strength drop, the artificial softening, of the models was already discussed in chapter 5 and is due to spurious energy modes and does not reflect the actual splitting of the timber member.



**Figure 8-1: Embedment specimens spruce with 24 mm dowel; a) test results and models with default parameters and reduced longitudinal MoE,  $E_{II}$ ; b) detail of stiffness**

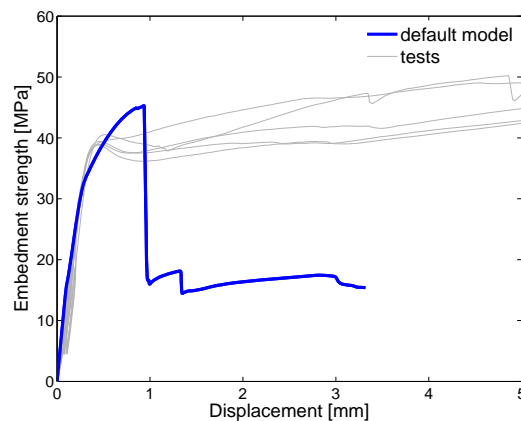


**Figure 8-2: Embedment specimens beech with 24 mm dowel, test results and default model**

The predicted stiffness for the beech specimen, Figure 8-2, with default material properties is much better than for spruce and the load carrying capacity is also satisfying whereas the observed yield drop in the tests could not be reproduced. A possible, future improvement of the material model in order to avoid artificial softening would be very valuable for such a ductile wood species as beech. The prediction of the displacements is not valuable yet.

The predictions for the azobé specimen, Figure 8-3, with default properties are the best predictions in terms of embedment strength-deformation behaviour. Again, the obtained displacements of more than 5 mm during tests could not be predicted with the models. The default model has a higher elastic stiffness than the test results, the obtained embedment strength is satisfying, but the artificial softening leads to failure already at about 0.8 mm. As a consequence, the MoE parallel-to-grain was decreased and the strength values and fracture energies of the brittle failures transverse tension and shear were increased, see Table 8-1. The modifications can be also justified by experimental outcomes. For instance, Van de Kuilen and Blaß (2005) found a mean shear strength for azobé (*Lophira alata*) of 17.7 MPa which is higher than the chosen value of 8.6 MPa.

The last modification of increasing the perpendicular ‘brittle properties’ should help to avoid spurious energy modes at an early stage at small deformations. If the perpendicular properties are increasing, an element that has already failed parallel-to-grain can withstand higher deformations than with lower perpendicular properties. The first modification of a lower MoE parallel-to-grain should decrease the initial stiffness of the model. However, the stiffness does not only depend on the MoE parallel-to-grain, but also on the stiffness values in the other material directions.

A better choice of the used material properties should help to improve the prediction quality considerably as it is the mechanical properties which define element failure. This statement can be verified when looking at Figure 8-3. The decrease of the MoE parallel-to-grain has nearly no effect on the model outcomes. This may be due to a too small reduction from 20000 MPa to 15000 MPa as for instance, the MoE parallel-to-grain of the spruce model was reduced by more than factor 2 (Figure 8-1). Another cause could be the contribution of the other stiffness components perpendicular-to-grain and in shear which were not reduced.

The increase of strength and fracture energy values for tension perpendicular-to-grain, longitudinal and rolling shear (model ‘90.v.roll’) instead showed an immediate effect as can be seen in Figure 8-3. The model ‘90.v.roll’ is a good fit to the upper bound experimental curve and indeed reaches a higher ductility with a deformation of about 2 mm before artificial softening occurs.

Figure 8-4 shows exemplarily the experimental and the model results for spruce in terms of damage in compression parallel-to-grain ( $d_{c,0}$ , Figure 8-4a) and tension perpendicular-to-grain ( $d_{t,90}$  which is coupled to  $d_v$  and  $d_{roll}$ , Figure 8-4b). The increase of damage due to compression parallel-to-grain reflects the crushing of wood fibres underneath the dowel during an embedment test. The coupled damage in tension perpendicular-to-grain and shear as shown in Figure 8-4b reflects the transverse tension and shear cracking.

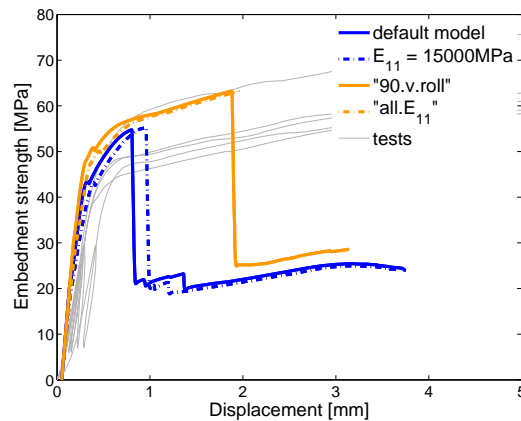


Figure 8-3: Embedment specimens azobé with 24 mm dowel, test results and models

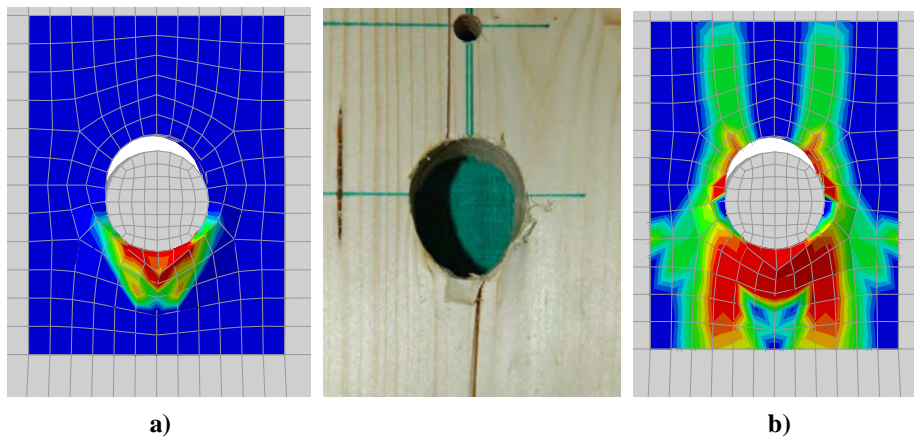


Figure 8-4: Embedment specimen spruce with 24 mm dowel, test result and model in terms of a)  $d_{c,0}$  ; and b)  $d_{t,90}$  (see Figure 5-37)

## 8.3 JOINTS

### 8.3.1 Spruce joints

Figure 8-5 shows the comparison between the test results and the model for a spruce joint with one 24 mm vhs dowel. The numerical results are offset by 0.5 mm to exclude the initial slip observed in tests. The model prediction is good in terms of load carrying capacity, stiffness and ductility. However, the calculations stopped too early due to the extensively discussed spurious energy modes and the reached ductility is hence less than the one observed in tests. Especially the stiffness prediction is surprisingly good after the observations made for the embedment tests.

In Figure 8-6, the comparison for the joints with three 24 mm vhs dowels are shown. The model predicts the tests outcomes satisfyingly well, both in terms of load carrying

capacity and shape of the load-slip curve with the saw-tooth shape indicating damage in the perpendicular and shear directions. The predicted stiffness is too high. If a longitudinal stiffness value of  $E_{11} = 4000$  MPa is taken, which was the best fit for the embedment models, the stiffness prediction quality improves. However, the prediction of the load carrying capacity decreases.

Figure 8-7 finally shows the numerical and test results for the spruce joints with five 24 mm vhss dowels in a row. The FE model stopped at an early stage due to convergence problems and could not predict load carrying capacity at all. However, the predicted stiffness is good.

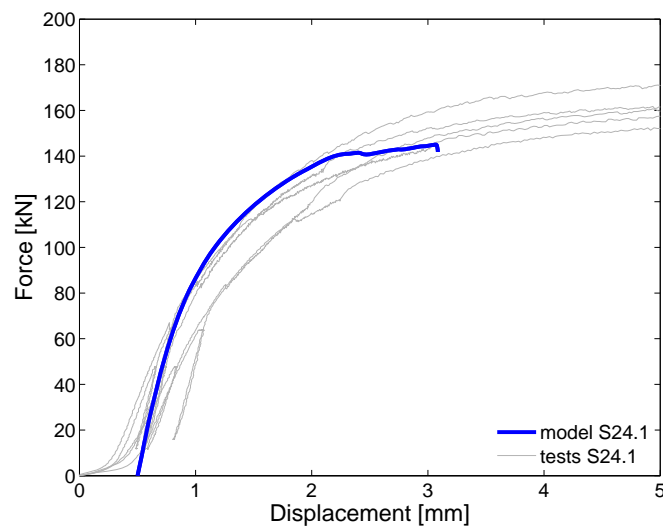


Figure 8-5: Spruce joints with one 24 mm vhss dowel, test results and model

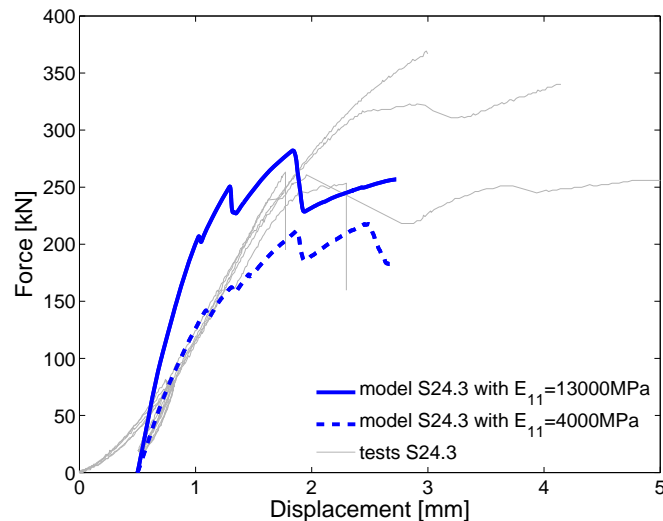
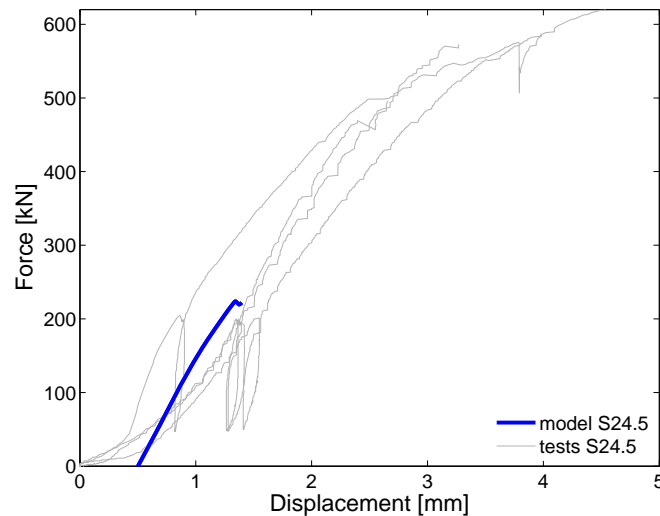


Figure 8-6: Spruce joints with three 24 mm vhss dowels, test results and model



**Figure 8-7: Spruce joints with five 24 mm vhs dowels, test results and model**

Figure 8-8 shows the model results of a spruce joint with one 24 mm vhs dowel in terms of damage due to compression parallel-to-grain together with a photo of a tested specimen. The damage is indicated correctly. However, it seems as if shear and perpendicular damage starts at too small deformations as can be seen in Figure 8-9. The test series S24-1 reached an average maximum displacement of  $v_{max} = 13.5$  mm which is much higher than the deformations of the model with  $v_{max} = 2.6$  mm before calculation exit due to convergence problems. This means that the shown shear and perpendicular damage is too high for a deformation of only 2.6 mm. On the other hand, wood enters the plastic regime at low deformations already which can be also seen when analysing the models (Dias et al., 2010). As discussed in section 5.4.3 for joints with five dowels and shown in Figure 8-1b for embedment models, early damage that is expressing itself in a slight saw-tooth shape of the load-slip curve is a realistic prediction and leads to nonlinear behaviour already at low deformations.

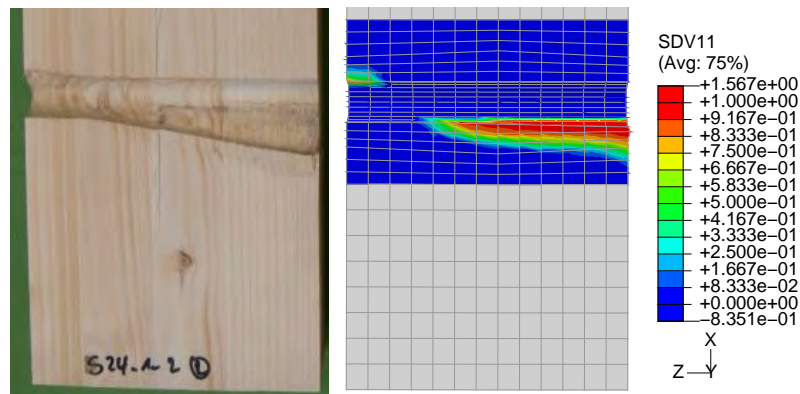


Figure 8-8: Spruce joint, one 24 mm vhs dowel, test with  $v_{max} = 18$  mm and model result in terms of  $d_{c,0}$  and with  $v_{max} = 2.6$  mm

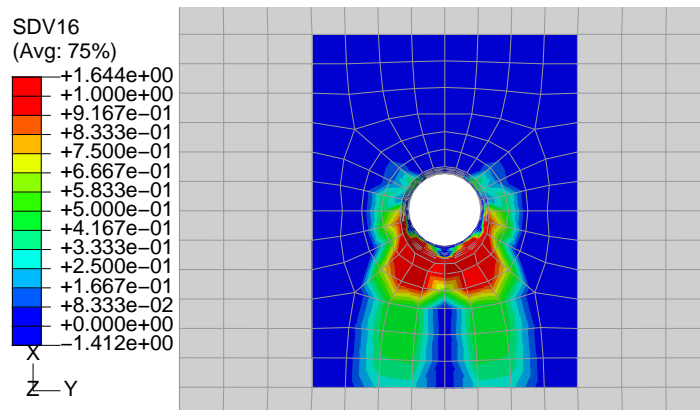


Figure 8-9: Spruce joint, one 24 mm vhs dowel, model result in terms of  $d$ , and with  $v_{max} = 2.6$  mm, inner side (steel plate side) of model

### 8.3.2 Beech joints

The numerical and experimental results for the beech joints with 24 mm hss dowels in terms of load-displacement are shown analogously to the spruce results. Firstly, Figure 8-10 shows the overlapping curves for the joints with one dowel, then the comparison for the joints with three dowels is shown in Figure 8-11 and lastly, the joints with five dowels are presented in Figure 8-12. For the joints with one dowel, the prediction is acceptable apart from the fact that the model is not ductile enough. The artificial softening led to an abortion of the numerical calculations before the physical failure of the joint is reached, both numerically and phenomenologically. Beech is a ductile wood species reaching high deformations. The poor quality of the model with five dowels can be seen immediately. It did not even reach the load level of the model with three dowels. This is in line with the results for spruce. However, the models with three dowels in a beech joint are worse than the one for a spruce joint. Not only the slip is underestimated, but also the reached

maximum load is far too low. The softening starts at approximately half the experimental load carrying capacity. The reached load carrying capacity of the model is similar to the capacity reached by the spruce models (Figure 8-6). This is a reasonable result considering that the tension strength perpendicular-to-grain and the shear strength do not differ a lot between spruce and beech (Table 5-2).

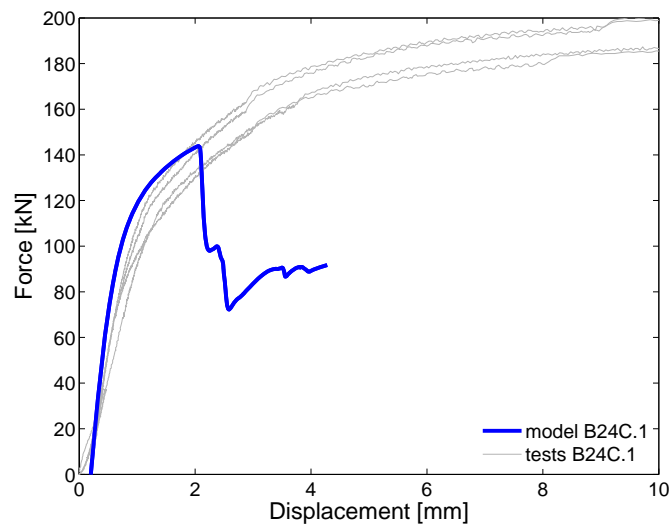


Figure 8-10: Beech joints with one 24 mm hss dowel, test results and model

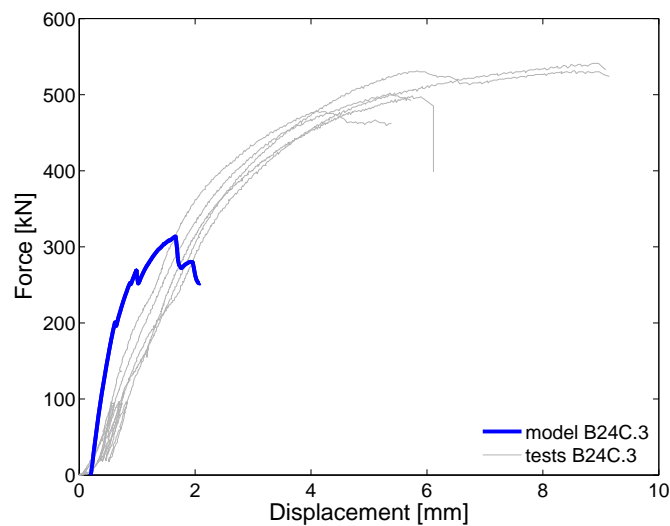
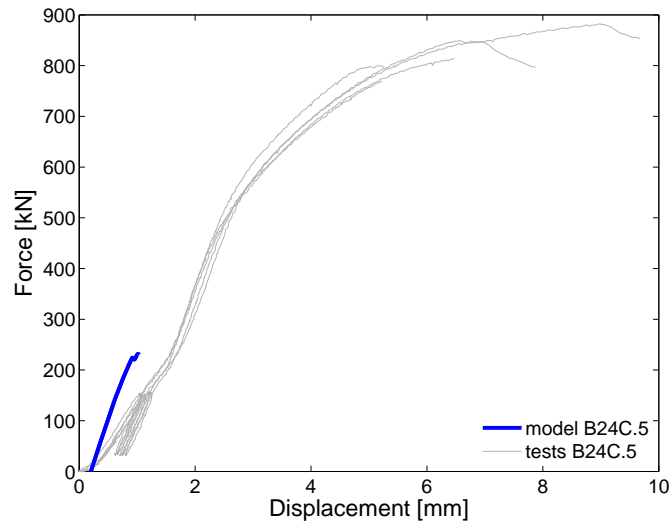


Figure 8-11: Beech joints with three 24 mm hss dowels, test results and model



**Figure 8-12: Beech joints with five 24 mm hss dowels, test results and model**

The model with three dowels was re-run with different material properties with the aim to increase the ductility and the load carrying capacity of the model. The results in terms of load-displacement are shown in Figure 8-13. Figure 8-14 shows a different scale of Figure 8-13 in order to clarify the initial behaviour. Table 8-2 gives the used default and modified material properties of beech. This investigation is done analogously to section 5.4.1 where similar modifications were carried out to influence the load-slip behaviour of a beech joint with one dowel. When using nearly isotropic properties as given in Table 8-2 (variation 'A', variation 'iso' in Table 5-4), the behaviour is indeed more ductile. The joint reached a displacement of 6 mm before calculation exit due to convergence problems. However, the prediction quality of the stiffness decreased considerably. Model variation 'A' has the same elastic stiffness than the default model, but the load-displacement graphs of the two models separate at around 0.45 mm deformation (see Figure 8-14). The brittle mechanisms in transverse tension and shear of the default model led to an earlier entry in the nonlinear range in comparison to the nearly isotropic model 'A'. In order to further improve the model in terms of higher load carrying capacity and more ductile behaviour without losing the effect of early damage in transverse tension and shear, the default properties were again modified in order to understand the influence of different material properties on the global load-displacement behaviour. First of all, the properties of the nearly isotropic case 'A' were reduced in model variation 'B'. However, the global load-slip curve remained qualitatively the same, but a lower load carrying capacity was reached as the lower transverse and shear properties led to an earlier transition into the nonlinear range. An increase in tension strength perpendicular-to-grain and longitudinal shear without changing the fracture energies did not change the load-slip curve. An increase of the strength in rolling shear together with an increase of the fracture energies in transverse tension, longitudinal and rolling shear (model variation 'C') instead led to a different behaviour. The load carrying capacity increased in comparison to the

default model while damage still decreased the stiffness of the joint at higher deformations. However, also here, the calculation stopped earlier due to convergence problems. Variations 'D', 'E' and 'F' further improved the default model results in terms of load carrying capacity and ductility (not variation 'F'). In all model variations, the fracture energies and strength values for transverse tension and shear were increased, but less strong than in variation 'A', the nearly isotropic case. Variation 'F' combined increased strength properties and fracture energies with a decrease in longitudinal elastic stiffness  $E_{11}$ . With this modification, it was tried to obtain a lower stiffness closer to the experimental results. However, the resulting load-slip graph of variant 'F' is not satisfying. The lower longitudinal stiffness can be seen only in the detail, Figure 8-14, and not in the global load-displacement curve. An additional decrease of the longitudinal elastic stiffness  $E_{11}$  did not lead to better predictions.

All discussed material modifications led to a better prediction quality of load carrying capacity and ductility in comparison to the default model, but the stiffness prediction quality decreased due to less influence of brittle failures in transverse tension and shear. Another option to reach higher load carrying capacities without losing the effect of perpendicular damage should be to increase the compression strength parallel-to-grain. This was done in model variation 'G'. Variation 'G' reached indeed a higher load carrying capacity, but the ductility and stiffness prediction did not improve. If lastly, the rolling shear properties were increased as done in variation 'H', the global load-slip curve approached again the variations 'A' and 'B'.

**Table 8-2: Default material properties and variation 'A' to 'H' for beech joints with three dowels**

Parameter	Units	default	'A'	'B'	'C'	'D'	'E'	'F'	'G'	'H'
$E_{11}$		13000	13000	13000	13000	13000	13000	<b>10000</b>	13000	13000
$f_{t,0}$		41	41	41	41	41	41	41	41	41
$f_{c,0}$		45	45	45	45	45	45	45	<b>70</b>	45
$f_{t,90}$	MPa	1.0	<b>41</b>	<b>20</b>	1.0	<b>4</b>	<b>10</b>	<b>10</b>	<b>10</b>	<b>10</b>
$f_{c,90}$		14.2	<b>45</b>	14.2	14.2	14.2	14.2	14.2	14.2	14.2
$f_v$		6.9	<b>40</b>	<b>20</b>	6.9	<b>9</b>	<b>12</b>	<b>12</b>	<b>12</b>	<b>12</b>
$f_{roll}$		0.5	<b>40</b>	<b>20</b>	<b>10</b>	<b>1.0</b>	<b>1.0</b>	<b>1.0</b>	<b>1.0</b>	<b>20</b>
$G_{f,0}$		100	100	<b>50</b>	100	100	100	100	100	100
$G_{f,90}$	N/	0.71	<b>100</b>	<b>50</b>	<b>100</b>	<b>10</b>	<b>10</b>	<b>10</b>	<b>10</b>	<b>10</b>
$G_{f,v}$	mm	1.2	<b>100</b>	<b>12</b>	<b>100</b>	<b>12</b>	<b>12</b>	<b>12</b>	<b>12</b>	<b>12</b>
$G_{f,roll}$		0.6	<b>100</b>	<b>12</b>	<b>100</b>	<b>1</b>	<b>1</b>	<b>1</b>	<b>1</b>	<b>12</b>

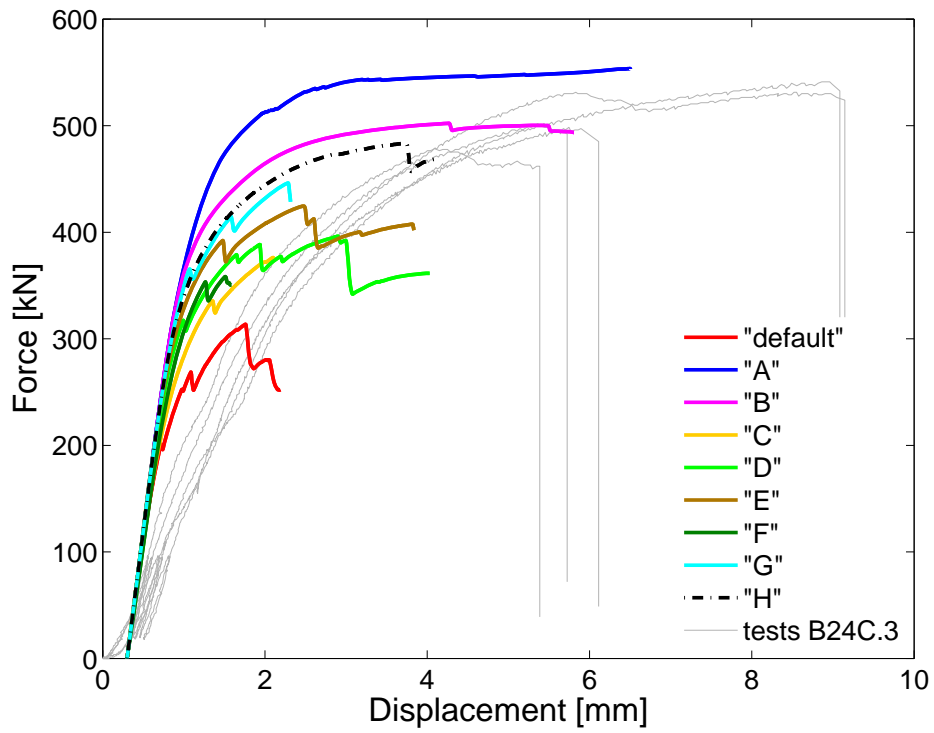


Figure 8-13: Beech joints with three 24 mm hss dowels, different model input values

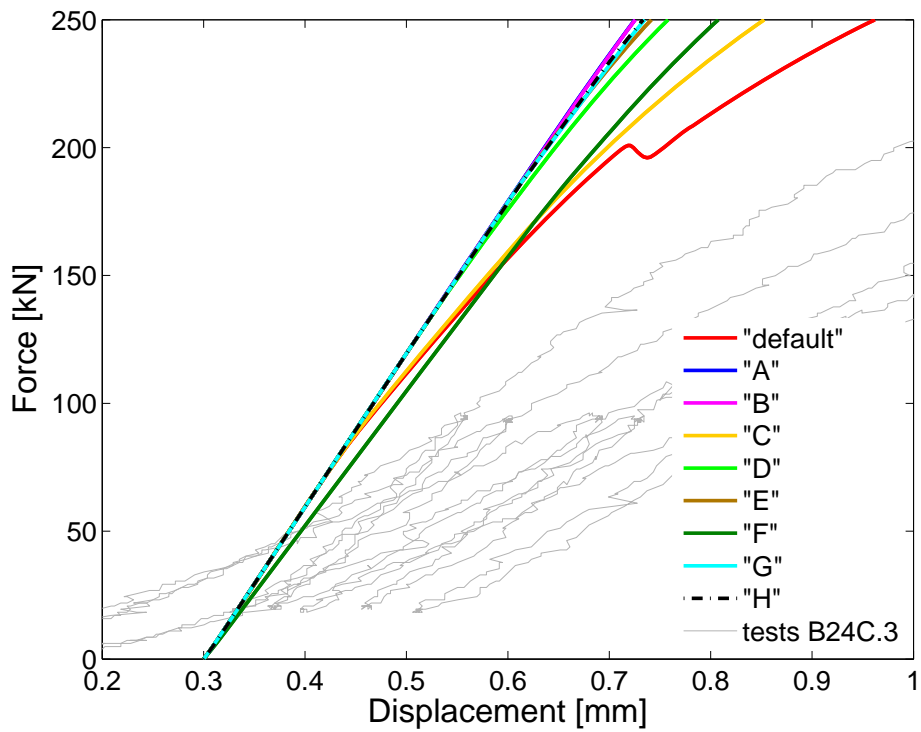


Figure 8-14: Detail of Figure 8-13

### 8.3.3 Azobé joints

The joint models with azobé were run with the default material properties and with the calibrated properties from the embedment models (Table 8-1, model variation = 'all.E<sub>11</sub>'). In Figure 8-15 showing the overlap for the joint with one 24 mm vhss dowel, it can be seen that the prediction quality improved when using the model variation 'all.E<sub>11</sub>'. A considerably higher ductility was reached for the joint with one dowel. The joint with three 24 mm vhss dowels could reach a higher load carrying capacity when using model variation 'all.E<sub>11</sub>' as can be seen in Figure 8-16. However, the predictions of the joint with five dowels as given in Figure 8-17 are unuseable. As with spruce and beech, the calculations stopped at low deformations due to convergence problems. However, similar to the models of the joints with five dowels using spruce and beech (Figure 8-7 and Figure 8-12 respectively), the stiffness is predicted satisfyingly well. The joint with azobé given in Figure 8-17 started to fail at a displacement of around 0.8 mm where the first saw-tooth in the load-displacement graph can be seen.

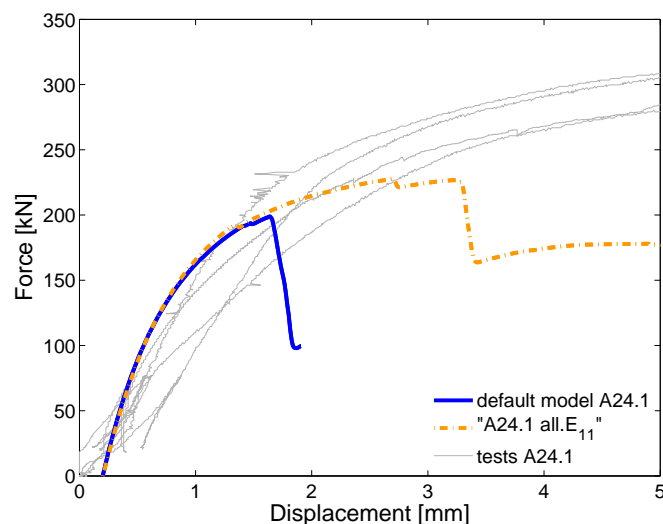


Figure 8-15: Azobé joints with one 24 mm vhss dowel, test results and model

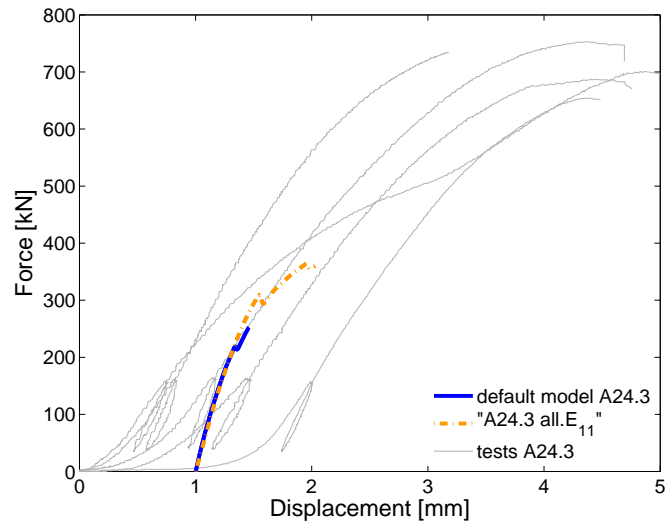


Figure 8-16: Azobé joints with three 24 mm vhs dowels, test results and model

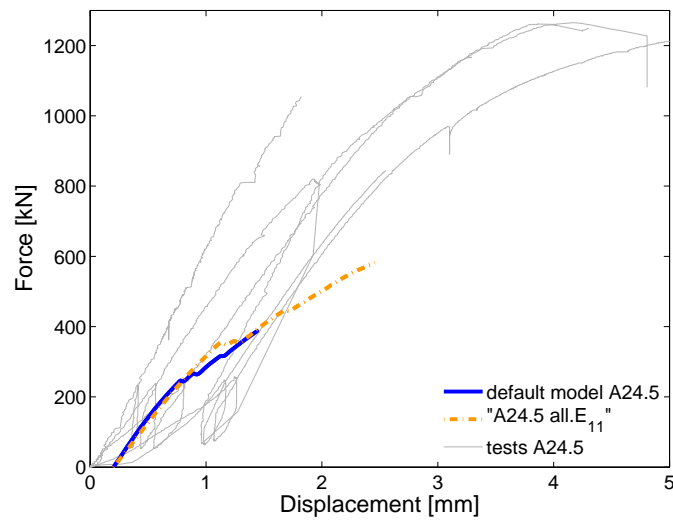


Figure 8-17: Azobé joints with five 24 mm vhs dowels, test results and model

## 8.4 CONCLUSIONS

The comparison of the load-displacement curves of numerical and experimental results has shown the capability of the developed material model to simulate the early onset of damage already at low deformations as observed also during embedment and joint tests. The models were able to model nonlinear behaviour caused by two effects, elastic perfectly plastic behaviour in compression parallel-to-grain and brittle damage due to transverse and shear stresses. The latter manifested in saw-tooth shapes of the load-displacement curves.

The predictions of the load carrying capacity of joints with one dowel using the developed material model are satisfying until the spurious energy modes of the elements directly underneath the dowels are reached. When joints with three or five dowels are simulated, the prediction quality is rather poor except for spruce joints with three dowels. The poor prediction quality is due to early calculation exit caused by convergence problems in the large models with three and five dowels. The stiffness of the joints is overestimated when compared to experimental results.

Generally, it can be said that the results for embedment models were better than for joint models. Also, the calibration (changing the used mechanical material properties) of the embedment models to the experimental curves was better than for the joint models. This could be due to the minor complexity of the embedment specimens that have rigid dowels. The parameter study modifying the material properties has shown the sensitivity of the model to changes of these properties. It seems that the performance of the model improves if the ratio between the parallel and perpendicular strength and shear values is decreasing. This could also be an explanation why the spruce joints with three dowels gave better results as the chosen material properties showed less difference between tension strength parallel and perpendicular to the grain for instance in comparison to beech and spruce.

The difficulties with deriving material properties for wood have been already discussed. For instance, the tension strength values perpendicular-to-grain for beech and azobé are rather lower bound values, an increase would thus be admissible without leading to unrealistic values. Therefore, a persisting problem is the determination of material properties.

All numerical calculations were aborted due to observed spurious energy modes in the completely collapsed elements directly underneath the dowels. This abortion took place before the numerical models failed 'physically'. In other words, the models failed due to local numerical problems in the elements underneath the dowels without which the calculations would have carried on providing a continuation of the load-displacement curve up to global model failure. The models were not able to transfer the loading from the failed elements to the neighbouring elements. These numerical problems must be addressed in future research in order to improve the quality of the load-displacement behaviour in comparison to test results.



# 9

## CLOSURE

*The two main tasks of the thesis are addressed in this closure. One task was to develop reliable analysis techniques and models to predict the mechanical behaviour of timber joints with a specific focus on wood species with large density differences and vhs dowels. The other task was to develop high-performance joints to improve the versatility and competitiveness of timber. Here, it is discussed to which extent these two main tasks have been achieved. Recommendations for further research are given.*

### 9.1 CONCLUSIONS

This study covered the development of a material model, its application within finite element simulations and an extensive testing series to which the modelling outcomes have been compared. Therefore, conclusions can be drawn with regards to modelling and experimental results.

#### Modelling

In order to be able to predict the load carrying capacity, numerical models for embedment testing and steel-to-timber joints have been developed. For this, a thorough literature survey has been conducted. Shortcomings in existing models have been discussed such as the fact that generally, models are able to simulate either ductile or brittle behaviour. The lack of a valid constitutive material model for the proper modeling of failure has been identified as being a major drawback of existing approaches. Therefore, a more comprehensive 3D material model has been developed, based on the principles of continuum damage mechanics (CDM).

It was shown that ductile and brittle failures could be combined in one single approach. Different failure modes could be identified and damage caused by different stress components was correctly simulated with the developed material model. The large differences in strength parallel and perpendicular to the grain, typical for wood, could be captured without creating unadmissible stress interactions. The material model was able to

properly simulate initial nonlinear ductile behaviour in joints which is caused by crushing of the wood fibres directly underneath the dowel. Also, a stable softening curve could be found when simulating a brittle model response. What has become clear is the difference between Young's modulus parallel-to-grain  $E_{11}$  and the actual stiffness of a joint whose timber members are loaded parallel-to-grain. In all models where  $E_{11}$  has been taken on the basis of the expected value for the wood species, a lower stiffness was found in the tests, confirming results from literature (Dias, 2005). However, the material model was able to indicate a correct stiffness reduction caused by damage in the (weak) perpendicular directions and shear while still showing an increasing load-slip curve.

The mechanical material parameters needed for the constitutive relationship are clearly defined and represent physically significant values such as elastic properties, load carrying capacities and fracture energies. It has been shown that physically possible 'new' values, e.g. higher tension strength perpendicular-to-grain, can be chosen for calibration purposes. A lack of knowledge on material parameters exists for tension strength perpendicular to the grain, shear strength as well as fracture energy values. Values obtained from standardized tests cannot be used one-to-one when modelling material properties around fasteners. In addition, only values for spruce are available whereas beech and azobé are different species with different cell wall structures.

However, the implemented material model is based on a smeared approach that, depending on the selected mesh size, cannot always predict the mechanical behaviour of heterogeneous materials, when the microstructure has a dominant effect on the failure mode. Also, an increased shear strength under transverse compression has not been implemented. In order to solve mesh dependency, it was shown that regularised results can be obtained by using the crack band method if models show localised solutions.

The predictions of the load carrying capacity of joints with one dowel using the developed material model were satisfactory until spurious energy modes (i.e. excessive 3D distortion) of the elements directly underneath the dowels were observed. When joints with three or five dowels are simulated, the prediction quality is rather poor and an early calculation exit could be observed. All numerical calculations were aborted due to observed spurious energy modes in the completely collapsed elements directly underneath the dowels. This abortion took place before the numerical models failed 'physically'. In other words, the models failed due to local numerical instabilities in the elements underneath the dowels without which the calculations may have continued resulting in a continuation of the load-displacement curve up to global failure. No stress redistribution took place and the still intact elements did not take over the load.

### Experiments

In this research, a comparison has been made between timber joints with slotted-in steel plates using high strength steel (hss,  $f_u = 400 - 600$  MPa) and very high strength steel (vhss,  $f_u = 700 - 1100$  MPa) dowels. The comparison has shown that the load carrying capacity can be increased by a percentage between 10% and 69% when using vhss dowels, depending on the geometry, fastener diameter and wood species. Beech seems to

be particularly favourable where brittleness is concerned as beech proved to be a highly ductile wood species. On wood species level, no correlation between density and load carrying capacity of the joints could be found which confirmed earlier findings from literature (Van de Kuilen, 1999). Similar observations were found for the correlation between density and stiffness  $K_{ser}$ .

A comparison between the test results and current Eurocode 5 design rules has shown a difference between actual and predicted resistance in terms of mean values. This is caused by two important factors. Firstly, the yield moment of the fasteners as currently given in EC5 is conservative for vhss dowels with diameters of 12 mm and more. The yielding and plastic deformation capacity of vhss is such, that also with relatively thick dowels (12-24 mm) full plastic hinges can develop at the steel-wood shear plane. The second important parameter is the embedment strength. On the basis of a number of tests and literature data, a better prediction model for the embedment strength has been derived. This prediction model together with the equation for the bending capacity of a circular dowel with a fully developed plastic section modulus improved the prediction of the load carrying capacity applying the Johansen equations.

Based on the embedment tests, it could also be concluded that the used steel grade had a strong influence because higher embedment strengths between 11% and 35% were obtained when vhss dowels were used. According to literature (Rodd, 1973), this difference is caused by different friction coefficients. Even though friction tests have not been carried out, measurements of the surface roughness showed no difference between the two steel grades. In addition, even though the absolute value of the embedment strength is dependent on the wood density, wood yielding below the fastener and final splitting is also greatly dependent on the species.

Finally, the influence of the number of fasteners in a row has been studied, both for load carrying capacity and stiffness of timber joints. As current code rules take only the number of fasteners into account and not the steel grade, this effect has been studied for the three species and the used steel grades. Here, no clear influence of the steel grade, the wood species or the diameter could be found, but effective numbers seem to be higher by around 17% for joints using hss in comparison to joints using vhss. The effective number of fasteners established by the tests is higher by 3% to 43% in comparison to code prescriptions. Also, the joint stiffness seems to be dependent of the number of fasteners in a row.

## 9.2 RECOMMENDATIONS

### Modelling

The first and foremost problem that should be solved is the spurious energy modes of the completely collapsed elements under compression directly underneath the dowel. The excessive mesh distortion must be controlled in order to avoid artificial softening effects and to obtain numerical stability beyond local failure of the first row of elements below

the fastener. Furthermore, stress redistribution between neighbouring elements must be enabled. Once the most stressed elements have completely failed, the neighbouring elements should take over. Possibilities to deal with spurious energy modes could be the development of new element formulations that allow for total failure without excessive distortions. Another option is to allow for deletion of the collapsed elements with a subsequent reset of the model and calculation restart. Furthermore, additional remeshing within the framework of large deformations (arbitrary Lagrangian-Eulerian (ALE) approaches) could be a possible tool to solve the lack of load transfer and to control excessive mesh distortion (e.g. Rodríguez-Ferran et al., 2002).

Finally, the uncertainty connected with the derivation of valuable material parameters for timber must be addressed. In this thesis it was found in compliance with literature (Dias, 2010) that a proper derivation of mechanical properties needed for timber joint modelling based on data from literature is difficult. Also, the Poisson effect and consequential stress and damage interactions in different material directions should be investigated further. Better defined material properties could remove one source of uncertainty of the modelling.

Once satisfying solutions for the numerical issues, i.e. the spurious energy modes, are implemented, the developed material model is a valid alternative for timber engineers. In order to obtain an even more general material model useable also for other models than joints, the subroutine could be extended with viscosity formulations to account for the influence of moisture content and load duration. Random assignment of stochastic material properties similar to Frese (2006) could further broaden the model applicability. Finally, the subroutine could be inserted in more innovative FE environments where state-of-the-art FE tools such as dissipation-based arclength methods (Van der Meer, 2010) are available in order to improve computational robustness and convergency.

### Experiments

The test series should be completed using mild steel dowels which was one of the starting ideas of this research. The observed difference in embedment strength using hss and vhss dowels should be investigated further as a deeper understanding of this effect should also help to better understand joint behaviour where the same effect is expected.

The analysis of possible influences of wood species, steel grades or slenderness ratios on timber joint behaviour should be deepened. A special focus of further research should be the verification if the effective number of fasteners is indeed higher for joints using lower steel grades.

Another important evaluation of the testing data is the static ductility ratio which has not been established here. Also, a cyclic testing series on joints with vhss dowels should be redone in order to gain important insights about the feasibility of these joints in seismic regions for instance. A minor point for further research is the corrosion sensitivity of vhss in relation to different species.

## REFERENCES

- Allix, O., Feissel, P. and Thévenet, P. (2003) A delay damage mesomodel of laminates under dynamic loading: basic aspects and identification issues. *Computers and Structures*, 81, 1177-1191.
- Ashkenazi, E.K., Lavrov, A.V., Myl'nikova, O.S. and Popov, V.D. (1973) Experimental investigation of the strength of anisotropic materials in biaxial and triaxial compression. *Mekhanika Polimerov*, 6, 991-996.
- Ballerini, M. and Rizzi, M. (2005) A numerical investigation on the splitting strength of beams loaded perpendicular-to-grain by multiple dowel-type connections. *CIB-W18 Meeting 38*. Karlsruhe, Germany, Paper 38-7-1.
- Bathe, K.J. (2002) *Finite-Elemente-Methoden*. Berlin, Springer.
- Bažant, Z.P. and Oh, B.H. (1983) Crack band theory for fracture of concrete. *Matériaux et Constructions*, 16, 155-177.
- Bickerdicke, M. and Quenneville, P. (2006) Predicting the row shear failure mode in parallel-to-grain bolted connections. *9th World Conference of Timber Engineering WCTE*. Portland, Oregon.
- Bigorgne, L., Brunet, M. and Maigre, H. (2010) Wood transverse fracture analysis at the mesoscopic scale. *ICEM 14 - 14th International Conference on Experimental Mechanics*. Poitiers, France.
- Blaß, H.J. and Bejtka, I. (2008) Numerische Berechnung der Tragfähigkeit und der Steifigkeit von querzugverstärkten Verbindungen mit stiftförmigen Verbindungsmitteln. *Karlsruher Berichte zum Ingenieurholzbau Band 10*, Universitätsverlag Karlsruhe.
- Blaß, H.J., Bienhaus, A. and Krämer, V. (2000) Effective bending capacity of dowel-type fasteners. *CIB-W18 Meeting 33*. Delft, The Netherlands, Paper 33-7-5.

- Blaß, H.J. and Schmid, M. (2001) Querkzugfestigkeit von Vollholz und Brettschichtholz. *Holz als Roh- und Werkstoff*, 58, 456-466.
- Bocquet, J.F. (1997) Modélisation des déformations locales du bois dans les assemblages brochés et boulonnés. *PhD thesis*, University Blaise Pascal Clermont-Ferrand.
- Boström, L. (1994) The stress-displacement relation of wood perpendicular to the grain Part 2. Application of the fictitious crack model to the compact tension specimen. *Wood Science and Technology*, 28, 319-327.
- Bouchair, A. and Vergne, A. (1995) An application of the Tsai criterion as a plastic-flow law for timber bolted joint modeling. *Wood Science and Technology*, 30, 3-19.
- Campilho, R.D.S.G., De Moura, M.F.S.F., Barreto, A.M.J.P., Morais, J.J.L. and Domingues, J.J.M.S. (2009) Fracture behaviour of damaged wood beams repaired with an adhesively-bonded composite patch. *Composites: Part A*, 40, 852-859.
- Clouston, P.L. and Lam, F. (2001) Computational modeling of strand-based wood composites. *Journal of Engineering Mechanics*, 127, 844-851.
- Cofer, W.F., Du, Y. and Hermanson, J.C. (1999) The development of a simple three dimensional constitutive model for the analysis of wood. *AMD Applied Mechanics Division; Mechanics of Cellulosic Materials*, 85, 107-124.
- Denzler, J.K. and Glos, P. (2007) Determination of shear strength values according to EN 408. *Materials and Structures*, 40, 79-86.
- Dias, A.M.P.G. (2005) Mechanical behaviour of timber-concrete joints. *PhD thesis*, University of Technology Delft.
- Dias, A.M.P.G., Van de Kuilen, J.W.G., Cruz, H.M.P. and Lopes, S.M.R. (2010) Numerical modelling of the load-deformation behavior of doweled softwood and hardwood joints. *Wood and Fiber Science*, 42, 480-489.
- Dinwoodie, J.M. (1968) Failure in Timber. Part 1. Microscopic Changes in Cell-Wall Structure Associated with Compression Failure. *Journal of the Institute of Wood Science*, 21, 37-53.
- Eberhardsteiner, J. (2002) *Mechanisches Verhalten von Fichtenholz; experimentelle Bestimmung der biaxialen Festigkeitseigenschaften*. Wien, Springer.
- Edlund, B. (1982) Bruchhypothesen für orthotropes Material. IN EHLBECK, J. & STECK, G. (Eds.) *Ingenieurholzbau in Forschung und Praxis*. Karlsruhe, Bruderverlag.
- Ehlbeck, J. and Werner, H. (1992a) Softwood and hardwood embedding strength for dowel-type fasteners. *CIB-W18 Meeting 25*. Ahus, Sweden, Paper 25-7-2.
- Ehlbeck, J. and Werner, H. (1992b) Tragfähigkeit von Laubholzverbindungen mit stabförmigen Verbindungsmitteln. *Forschungsbericht Versuchsanstalt für Stahl, Holz und Steine*, Abt. Ingenieurholzbau, Universität Karlsruhe.
- Federal Highway Administration (2005) Evaluation of LS-Dyna wood material model 143. *Publication No. FHWA-HRT-04-096*, U.S. Department of Transportation.

- Federal Highway Administration (2007) Manual for LS-Dyna wood material model 143. *Publication No. FHWA-HRT-04-097*, U.S. Department of Transportation.
- Feih, S. and Shercliff, H.R. (2005a) Composite failure prediction of single-L joint structures under bending. *Composites: Part A*, 36, 381-395.
- Feih, S. and Shercliff, H.R. (2005b) Quality assessment of curved composite components in peel joint structures. *Composites: Part A*, 36, 397-408.
- Fleischmann, M. (2005) Numerische Berechnung von Holzkonstruktionen unter Verwendung eines realitätsnahen orthotropen elasto-plastischen Werkstoffmodells. *PhD thesis*, Technische Universität Wien.
- Foschi, R.O. (1974) Load-slip characteristics of nails. *Wood Science*, 7, 69-76.
- François, P. and Morlier, P. (1993) Plasticité du bois en compression simple. *Matériaux et techniques*, 81, 5-14.
- Franke, S. (2008) Zur Beschreibung des Tragverhaltens von Holz unter Verwendung eines photogrammetrischen Messsystems. *PhD thesis*, Bauhaus-Universität Weimar.
- Frese, M. (2006) Die Biegefestigkeit von Brettschichtholz aus Buche. Experimentelle und numerische Untersuchungen zum Laminierungseffekt., *PhD thesis*, Technische Universität Karlsruhe.
- Garab, J., Keunecke, D., Hering, S., Szalai, J. and Niemz, P. (2010) Measurement of standard and off-axis elastic moduli and Poisson's ratios of spruce and yew wood in the transverse plane. *Wood Science and Technology*, 44, 451-464.
- Gehri, E. and Fontana, M. (1983) Betrachtungen zum Tragverhalten von Passbolzen in Holz-Holz-Verbindungen. *Int. Bericht 83-1*, Baustatik und Stahlbau, ETH Zürich.
- Gibson, L.J. and Ashby, M.F. (1997) *Cellular solids. Structures and properties - Second edition*. Cambridge University Press.
- Gross, D. and Seelig, T. (2011) *Bruchmechanik. Mit einer Einführung in die Mikromechanik*. Berlin, Springer.
- Grosse, M. (2005) Zur numerischen Simulation des physikalisch nichtlinearen Kurzzeittragverhaltens von Nadelholz am Beispiel von Holz-Beton-Verbundkonstruktionen. *PhD thesis*, Bauhaus-Universität Weimar.
- Hankinson, R.L. (1921) Investigation of crushing strength of spruce at varying angles of grain. *U. S. Air Service Information Circular Vol. 3 No. 259*.
- Hashin, Z. (1980) Failure criteria for unidirectional fiber composites. *Journal of Applied Mechanics*, 47, 329-334.
- Hemmer, K. (1985) Versagensarten des Holzes der Weißtanne (*Abies alba*) unter mehrachsiger Beanspruchung. *PhD thesis*, Technische Universität Karlsruhe.

- Hieralal, R. (2006) Application of high strength steel in steel pin connections and double-shear timber joints. *Master thesis*, Faculty of Civil Engineering, University of Technology Delft.
- Hill, R. (1948) A theory of the yielding and plastic flow of anisotropic metals. *Proceedings Royal Society (London), Series A*, 193, 281-297.
- Hoffman, O. (1967) The brittle strength of orthotropic materials. *Journal of Composite Materials*, 1, 200-206.
- Hofstetter, K., Hellmich, C. and Eberhardsteiner, J. (2005) Development and experimental validation of a continuum micromechanics model for the elasticity of wood. *European Journal of Mechanics A/Solids*, 24, 1030-1053.
- Hübner, U., Bogensperger, T. and Schickhofer, G. (2008) Embedding strength of European hardwoods. *CIB-W18 Meeting 41*. St. Andrews by-the-Sea, Canada, Paper 41-7-5.
- Hübner, U. and Schickhofer, G. (2007) Forschung an der TU Graz - Die Festigkeitskenngröße "Lochleibung" für die Laubholzart Esche. *6. Grazer Holzbau-Fachtagung*. Graz, Austria, Paper C.
- Islamaj, L. (2009) Application of high strength steel dowels in steel-to-timber double-shear joints with slotted-in steel plate. *Master thesis*, Faculty of Civil Engineering, University of Technology Delft.
- Johansen, K.W. (1949) Theory of timber connections. *International Association of Bridge and Structural Engineering (IABSE), Publication 9*, Basel, Switzerland.
- Jorissen, A. (1998) Double-shear timber connections with dowel-type fasteners. *PhD thesis*, University of Technology Delft.
- Juhasz, T.J. (2003) Ein neues physikalisch basiertes Versagenskriterium für schwach 3D-verstärkte Faserverbundlamine. *PhD thesis*, Technische Universität Braunschweig.
- Kasal, B. and Leichti, R.J. (2005) State of the art in multiaxial phenomenological failure criteria for wood members. *Progress in Structural Engineering and Materials*, 7, 3-13.
- Keenan, F.J. (1973) Shear strength of glued-laminated timber beams. *PhD thesis*, University of Toronto.
- Kollmann, F.F.P. and Côté, W.A. (1984) *Principles of wood science and technology. Vol. 1 Solid wood*. Berlin, Springer.
- Landis, E.N., Vasic, S., Davids, W.G. and Parrod, P. (2002) Coupled experiments and simulations of microstructural damage in wood. *Experimental Mechanics*, 42, 389-394.
- Langedijk, A. (2007) Houtverbindingen met hoge sterkte staal. *Bachelor thesis*, Faculty of Civil Engineering, University of Technology Delft.

- Larsen, H.J. and Gustafsson, P.J. (1989) Design of end-notched beams. *CIB-W18 Meeting 22*. Berlin, German Democratic Republic, Paper 22-10-1.
- Lopes, C.S. (2009) Damage and failure of non-conventional composite laminates. *PhD thesis*, University of Technology Delft.
- Mackenzie-Helnwein, P., Eberhardsteiner, J. and Mang, H.A. (2003) A multi-surface plasticity model for clear wood and its application to the finite element analysis of structural details. *Computational Mechanics*, 31, 204-218.
- Mackenzie-Helnwein, P., Müllner, H.W., Eberhardsteiner, J. and Mang, H.A. (2005) Analysis of layered wooden shells using an orthotropic elasto-plastic model for multi-axial loading of clear spruce wood. *Computer Methods in Applied Mechanics and Engineering*, 194, 2661-2685.
- Maimí, P. (2006) Modelización constitutiva y computacional del daño y la fractura de materiales compuestos. *PhD thesis*, Universitat de Girona.
- Maimí, P., Camanho, P.P., Mayugo, J.A. and Dávila, C.G. (2007) A continuum damage model for composite laminates: Part I - constitutive model. *Mechanics of Materials*, 39, 897-908.
- Mandery, W.L. (1969) Relationship between perpendicular compressive stress and shear strength of wood. *Wood Science*, 1, 177-182.
- Matzenmiller, A., Lubliner, J. and Taylor, R.L. (1995) A Constitutive Model for Anisotropic Damage in Fiber-Composites. *Mechanics of Materials*, 20, 125-152.
- Moses, D.M. and Prion, H.G.L. (2003) A three-dimensional model for bolted connections in wood. *Canadian Journal of Civil Engineering*, 30, 555-567.
- Moses, D.M. and Prion, H.G.L. (2004) Stress and failure analysis of wood composites: a new model. *Composites Part B-Engineering*, 35, 251-261.
- Nahas, M.N. (1986) Survey of failure and post-failure theories of laminated fiber-reinforced composites. *Journal of Composites Technology and Research*, 8, 138-153.
- Nardi-Berti, R. (1993) La struttura anatomica del legno ed il riconoscimento dei legnami italiani di più corrente impiego. *Contributi scientifico-pratici per una migliore conoscenza ed utilizzazione del legno Vol. XXIV*, Istituto del Legno, Consiglio Nazionale delle Ricerche, Firenze, Italy.
- Needleman, A. (1988) Material Rate Dependence and Mesh Sensitivity in Localisation Problems. *Computer Methods in Applied Mechanics and Engineering*, 67, 69-85.
- Neuhaus, H. (1983) Über das elastische Verhalten von Fichtenholz in Abhängigkeit von der Holzfeuchtigkeit. *Holz Als Roh-Und Werkstoff*, 41, 21-25.
- Neuhaus, H. (1994) *Lehrbuch des Ingenieurholzbaus*. Stuttgart, Teubner.
- Patton-Mallory, M. (1997) Modeling bolted connections in wood: review. *Journal of Structural Engineering*, 123, 1054-1062.

- Patton-Mallory, M., Cramer, S.M., Smith, F.W. and Pellicane, P.J. (1997) Nonlinear material models for analysis of bolted wood connections. *Journal of Structural Engineering*, 123, 1063-1070.
- Persson, K. (2000) Micromechanical modelling of wood and fibre properties. *PhD thesis*, Lund University.
- Pinho, S.T., Dávila, C.G., Camanho, P.P., Iannucci, L. and Robinson, P. (2005) Failure modes and criteria for FRP under in-plane or three-dimensional stress states including shear non-linearity. *Technical Report NASA/TM-2005-213530*, NASA Langley Research Center, Hampton, VA.
- Poulsen, J.S. (1998) Compression in clear wood. *PhD thesis*, Technical University of Denmark.
- Puck, A. (1992) Faser-Kunststoff-Verbunde mit Dehnungs- oder Spannungskriterien auslegen? *Kunststoffe*, 82, 431-434.
- Puck, A. (1996) *Festigkeitsanalyse von Faser-Matrix-Laminaten*. München, Carl Hanser Verlag.
- Quenneville, J.H.P. (2008) Design of bolted connections: A comparison of a proposal and various existing standards. *10th World Conference of Timber Engineering WCTE*. Miyazaki, Japan.
- Quenneville, J.H.P. and Mohammad, M. (2000) On the failure modes and strength of steel-wood-steel bolted timber connections loaded parallel-to-grain. *Canadian Journal of Civil Engineering*, 27, 761-773.
- Racher, P. and Bocquet, J.F. (2005) Non-linear analysis of dowelled timber connections: a new approach for embedding modelling. *Electronic Journal of Structural Engineering*, 5, 1-9.
- Rahman, M.U., Chiang, Y.J. and Rowlands, R.E. (1991) Stress and failure analysis of double-bolted joints in Douglas-fir and Sitka spruce. *Wood and Fiber Science*, 23, 567-589.
- Reichert, T. (2009) Development of 3D lattice models for predicting nonlinear timber joint behaviour. *PhD thesis*, Napier University Edinburgh.
- Reiterer, A. and Stanzl-Tschegg, S.E. (2001) Compressive behaviour of softwood under uniaxial loading at different orientations to the grain. *Mechanics of Materials*, 33, 705-715.
- Riyanto, D.S. and Gupta, R. (1996) Effect of ring angle on shear strength parallel to the grain of wood. *Forest Products Journal*, 46, 87-92.
- Rodd, P.D. (1973) The analysis of timber joints made with circular dowel connectors. *PhD thesis*, University of Sussex.
- Rodríguez-Ferran, A., Pérez-Foguet, A. and Huerta, A. (2002) Arbitrary Lagrangian-Eulerian (ALE) formulation for hyperelastoplasticity. *International Journal for Numerical Methods in Engineering*, 53, 1831-1851.

- Rots, J.G., Belletti, B. and Invernizzi, S. (2008) Robust modeling of RC structures with an "event-by-event" strategy. *Engineering Fracture Mechanics*, 75, 590-614.
- Rots, J.G. and Invernizzi, S. (2004) Regularized sequentially linear saw-tooth softening model. *International Journal for Numerical and Analytical Methods in Geomechanics*, 28, 821-856.
- Rowlands, R.E., Rahman, M.U., Wilkinson, T.L. and Chiang, Y.I. (1982) Single-bolted and multiple-bolted joints in orthotropic materials. *Composites*, 13, 273-279.
- Sandhaas, C. (2011) 3D Material Model for Wood, Based on Continuum Damage Mechanics. *Stevinrapport 6-11-4*, Stevin II Laboratory, University of Technology Delft.
- Sandhaas, C. and Van de Kuilen, J.W.G. (2008) Approaches for numerical modelling of timber joints. *Doktorandenkolloquium*. Stuttgart, Germany.
- Sandhaas, C., Van de Kuilen, J.W.G., Blaß, H.J. and Ravenshorst, G. (2010) Embedment tests parallel-to-grain and ductility in tropical hardwood species. *11th World Conference of Timber Engineering WCTE*. Riva del Garda, Italy.
- Sawata, K. and Yasumura, M. (2002) Determination of embedding strength of wood for dowel-type fasteners. *Journal of Wood Science*, 48, 138-146.
- Sawata, K. and Yasumura, M. (2003) Estimation of yield and ultimate strengths of bolted timber joints by nonlinear analysis and yield theory. *Journal of Wood Science*, 49, 383-391.
- Schlangen, E. and Garboczi, E.J. (1997) Fracture simulations of concrete using lattice models: Computational aspects. *Engineering Fracture Mechanics*, 57, 319-332.
- Schmid, M. (2002) Anwendung der Bruchmechanik auf Verbindungen mit Holz. *PhD thesis*, Technische Universität Karlsruhe.
- Schmidt, J. and Kaliske, M. (2006) Zur dreidimensionalen Materialmodellierung von Fichtenholz mittels eines Mehrflächen-Plastizitätsmodells. *Holz als Roh- und Werkstoff*, 64, 393-402.
- Schoenmakers, J.C.M. (2010) Fracture and failure mechanisms in timber loaded perpendicular to the grain by mechanical connections. *PhD thesis*, University of Technology Delft.
- Shih, C.F. and Lee, D. (1978) Further developments in anisotropic plasticity. *Journal of Engineering Materials and Technology*, 100, 294-302.
- Sjödin, J., Serrano, E. and Enquist, B. (2008) An experimental and numerical study of the effect of friction in single dowel joints. *Holz als Roh- und Werkstoff*, 66, 363-372.
- Sluys, L.J. (1992) Wave Propagation, Localisation and Dispersion in Softening Solids. *PhD thesis*, Technische Universiteit Delft.
- Smith, I., Landis, E. and Gong, M. (2003) *Fracture and fatigue in wood*. Chichester, Wiley.

- Snow, M., Asiz, A. and Smith, I. (2006) Modelling fracture in bolted engineered wood products. *9th World Conference of Timber Engineering WCTE*. Portland, Oregon.
- Spengler, R. (1982) Festigkeitsverhalten von Brettschichtholz unter zweiachsiger Beanspruchung; Teil 1: Ermittlung des Festigkeitsverhaltens von Brettelelementen aus Fichte durch Versuche. *SFB96, Heft 62, Berichte zur Zuverlässigkeitstheorie der Bauwerke*, Technische Universität München.
- Stupnicki, J. (1968) Analysis of the behaviour of wood under external load based on a study of the cell structure. *Acta Polytechnica Scandinavica*, Civil Engineering and Building Construction Series No 53, Trondheim.
- Toussaint, P. (2009) Application et modélisation du principe de la précontrainte sur des assemblages de structure bois. *PhD thesis*, Université Henri Poincaré - ENSTIB, Nancy.
- Tsai, S.W. and Wu, E.M. (1971) A general theory of strength for anisotropic materials. *Journal of Composite Materials*, 5, 58-80.
- Van de Kuilen, J.W.G. (1999) The residual load carrying capacity of timber joints. *Heron*, 44, 187-214.
- Van de Kuilen, J.W.G. (2009) Verbindungsmittel aus hochfesten Stählen - Stabdübelverbindungen. *Tagungsband Ingenieurholzbau - Karlsruher Tage: Forschung für die Praxis*. Karlsruhe, Germany.
- Van de Kuilen, J.W.G. and Blaß, H.J. (2005) Mechanical properties of azobé (*Lophira alata*). *Holz als Roh- und Werkstoff*, 63, 1-10.
- Van de Kuilen, J.W.G. and De Vries, P.A. (2008) Timber joints with high strength steel dowels. *10th World Conference of Timber Engineering WCTE*. Miyazaki, Japan.
- Van de Kuilen, J.W.G. and Leijten, A.J.M. (2002) Schuifsterkte bepaling van zeven houtsoorten voor de toepassing in verkeersbruggen. *Report 2001-4/HE43*, Sectie Staal- & Houtconstructies, Technische Universiteit Delft.
- Van der Linden, M.R.L., Van de Kuilen, J.W.G. and Blaß, H.J. (1994) Application of the Hoffman yield criterion for load sharing in timber sheet pile walls. *Pacific Timber Engineering Conference*. Gold Coast, Australia, 412-417.
- Van der Meer, F.P. (2010) Computational Modeling of Failure in Composite Laminates. *PhD thesis*, University of Technology Delft.
- Van der Put, T.A.C.M. (1993) Discussion and proposal of a general failure criterion for wood. *CIB-W18 Meeting 26*. Athens, USA, Paper 26-6-1.
- Van Groesen, J. and Kranenburg, M. (2007) Houtverbindingen met hoge sterkte staal. *Bachelor thesis*, Faculty of Civil Engineering, University of Technology Delft.
- Vasic, S., Smith, I. and Landis, E. (2005) Finite element techniques and models for wood fracture mechanics. *Wood Science and Technology*, 39, 3-17.
- Vreeswijk, B. (2003) Verbindingen in hardhout. *Master thesis*, Faculty of Civil Engineering, University of Technology Delft.

- Wagenführ, R. (2007) *Holzatlas*. Fachbuchverlag Leipzig.
- Werner, H. (1993) Untersuchungen von Holz-Verbindungen mit stiftförmigen Verbindungsmitteln unter Berücksichtigung streuender Einflußgrößen. *PhD thesis*, Universität Karlsruhe.
- Whale, L.R.J. and Smith, I. (1986a) The derivation of design clauses for nailed and bolted joints in Eurocode 5. *CIB-W18 Meeting 19*. Florence, Italy, Paper 19-7-6.
- Whale, L.R.J. and Smith, I. (1986b) Mechanical joints in structural timber - Information for probabilistic design. *Report 17/86*, TRADA, High Wycombe.
- Whale, L.R.J. and Smith, I. (1986c) Mechanical timber joints. *Report 18/86*, TRADA, High Wycombe.
- Whale, L.R.J. and Smith, I. (1989) A method for measuring the embedding characteristics of wood and wood-based materials. *Materials and Structures*, 22, 403-410.
- Wittel, F.K., Dill-Langer, G. and Kröplin, B.H. (2005) Modeling of damage evolution in soft-wood perpendicular to grain by means of a discrete element approach. *Computational Materials Science*, 32, 594-603.
- Wood Handbook (1999) *Wood as an engineering material*. Madison, Forest Products Society.
- Wu, E.M. (1967) Application of fracture mechanics to anisotropic plates. *Journal of Applied Mechanics*, 34, 967-974.
- Wu, E.M. (1972) Optimal experimental measurements of anisotropic failure tensors. *Journal of Composite Materials*, 6, 472-489.

## STANDARDS

- ASTM D5764-97a - Standard test method for evaluating dowel-bearing strength of wood and wood-based products. USA, ASTM, 2007.
- EN 26891:1991 (NEN ISO 6819:1991). Timber structures - Joints made with mechanical fasteners - General principles for the determination of strength and deformation characteristics. Brussels, CEN, 1991.
- NEN-EN 1194:1999. Timber structures - Glued laminated timber - Strength classes and determination of characteristic values. Brussels, CEN, 1999.
- NEN-EN 408:2003. Timber structures - Structural timber and glued laminated timber - Determination of some physical and mechanical properties. Brussels, CEN, 2003.
- NEN-EN 384:2004. Structural timber - Determination of characteristic values of mechanical properties and density. Brussels, CEN, 2004.
- NEN-EN 1995 1-1:2004, Eurocode 5. Design of timber structures - Part 1-1: General - Common rules and rules for buildings. Brussels, CEN, 2004.

NEN-EN 10083-3:2006. Steels for quenching and tempering - Part 3: Technical delivery conditions for alloy steels. Brussels, CEN, 2006.

NEN-EN 383:2007. Timber structures - Test methods - Determination of embedment strength and foundation values for dowel-type fasteners. Brussels, CEN, 2007.

NEN-EN 10277-3:2008. Bright steel products - Technical delivery conditions - Part 3: Free-cutting steels. Brussels, CEN, 2008.

NEN-EN 338:2009. Structural timber - Strength classes. Brussels, CEN, 2009.

NEN 5493:2010. Quality requirements for hardwoods in civil engineering works and other structural applications. Delft, NEN, 2010.

**Finite Element Software package:**

ABAQUS<sup>®</sup> Version 6.8, Dassault Systèmes Simulia Corp., Providence, RI, USA, 2008.

# CURRICULUM VITAE

<b>Name</b>	Carmen Sandhaas
<b>Born</b>	8 <sup>th</sup> of October 1975 in Bühl (Baden), Germany
<b>Education</b>	
October 1997 – April 2004	Civil Engineering, Universität Karlsruhe (TH) Intermediate thesis at UTS Sydney: ' <i>Determination of global flexural stiffness of timber bridges, using dynamic methods</i> ' Master thesis at CNR-IVALSA Florence: ' <i>Seismic behaviour of historical timber-frame buildings</i> '
February 2007 – September 2011	Doctoral Candidate, University of Technology Delft
<b>Working experience</b>	
July 2004 – August 2005	Junior Façade Engineer, Schmidlin AG Fassadentechnologie, Aesch (BL), Switzerland
September 2005 – January 2007	Researcher, CNR-IVALSA Trees and Timber Institute, San Michele all'Adige (TN), Italy
Since October 2011	Wissenschaftliche Mitarbeiterin, Lehrstuhl für Holzbau und Baukonstruktionen, Karlsruhe Institute of Technology, Germany



# Appendices



# A

## COMPONENT TESTS

### A.1 TENSION TESTS ON STEEL DOWELS

**Table A-1: Results of tension tests on steel dowels**

			Young's modulus [MPa]	R <sub>p0.2</sub> [MPa]	R <sub>m</sub> [MPa]	strain at failure		
tests with strain gauges								
20.05.2009	vhss	12mm	227414	1460	1551	-		
			228952	1450	1529	-		
		24mm	212669	1270	1365	-		
			212824	1280	1363	-		
tests with extensometer								
01.10.2010	vhss	12mm	210785	1280	1349	7.39%		
			213211	1190	1258	7.19%		
		24mm	210587	1290	1366	11.57%		
			209355	1300	1382	11.51%		
	hss	12mm	201567	1320	1382	-		
			213385	1330	1399	-		
		24mm	197064	750	761	8.37%		
			198500	510	544	11.54%		
tests with strain gauges								
31.03.2011	vhss	12mm	215846	1240	1310	-		
		24mm	215791	1290	1393	-		
	hss	12mm	206919	585	625	-		
		24mm	210404	570	589	-		
tests with strain gauges								
19.05.2011	hss	12mm	163234	490	536	-	length	used in
			217822	760	771	-	150mm	azobé
			215566	560	593	-	180mm	beech
						200mm	spruce	

It was not possible to trace the batches except for the 12 mm 12.9 steel bolts where the batches were indicated. No certificates were available for the 12 mm dowels. No satisfying explanations connected to the test setup or test procedure were found to explain the differences in the test results.

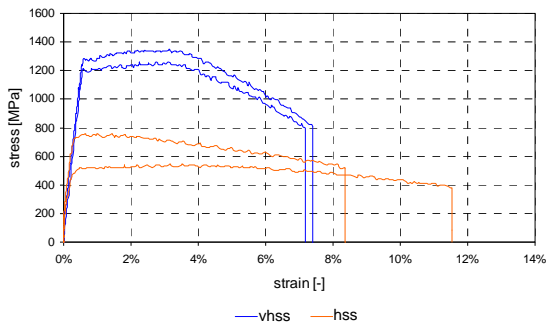


**Figure A-1: Tests with extensometers, 12 mm dowels**

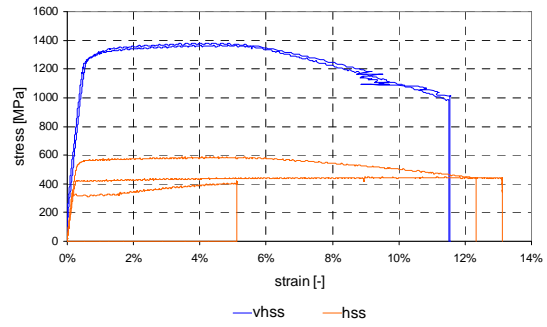


**Figure A-2: Tests with extensometers, 24 mm dowels**

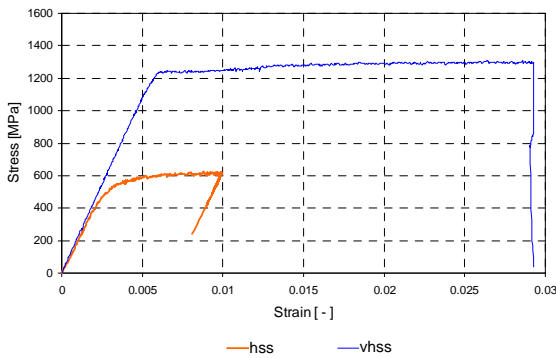


**Figure A-3: Tests with strain gauges 31.03.2011, 12 mm dowels**

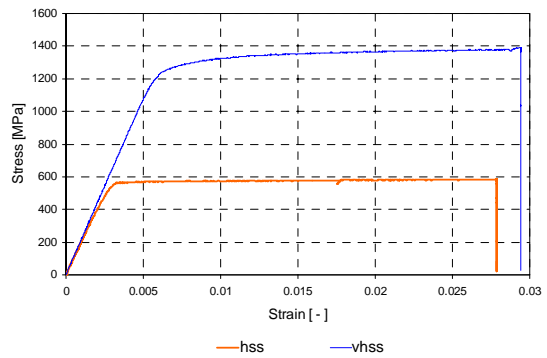


**Figure A-4: Tests with strain gauges 31.03.2011, 24 mm dowels**

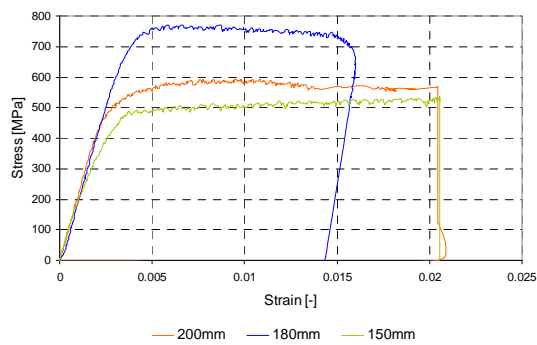


**Figure A-5: Tests with strain gauges 19.05.2011, 12 mm hss dowels**

## A.2 STEEL CERTIFICATES

### Certificate for 24 mm hss dowels

<b>Auszug aus Werkzeugeignis nach EN 10204/2.2</b>							
<b>Werkstoff : 11SMNPB30+C</b>				<b>15.04.2009</b>			
<b>Abmessung : rd 24</b>							
<b>Menge : 10200 kg</b>							
<b>Bestellung :</b>							
<b>Charge : 65941</b>							
<b>Chemische Werte :</b>							
<b>C</b> <i>min: 0.00</i> <i>max: 0.14</i>	<b>Mn</b> <i>min: 0.90</i> <i>max: 1.30</i>	<b>Si</b> <i>min: 0.00</i> <i>max: 0.05</i>	<b>P</b> <i>min: 0.00</i> <i>max: 0.11</i>	<b>S</b> <i>min: 0.27</i> <i>max: 0.33</i>	<b>Cr</b> <i>min:</i> <i>max:</i>	<b>Al</b> <i>min:</i> <i>max:</i>	<b>Pb</b> <i>min: 0.20</i> <i>max: 0.35</i>
<b>0.07</b>	<b>1.065</b>	<b>0.0090</b>	<b>0.063</b>	<b>0.288</b>			<b>0.284</b>
<b>Ni</b> <i>min:</i> <i>max:</i>	<b>Mo</b> <i>min:</i> <i>max:</i>	<b>Cu</b> <i>min:</i> <i>max:</i>	<b>Sn</b> <i>min:</i> <i>max:</i>	<b>Ti</b> <i>min:</i> <i>max:</i>	<b>Te</b> <i>min:</i> <i>max:</i>	<b>N</b> <i>min:</i> <i>max:</i>	<b>Nb</b> <i>min:</i> <i>max:</i>
<i>*kv=keine Vorschrift</i>							
<b>Mechanische Werte :</b>							
<b>Zugfestigkeit N/mm<sup>2</sup> : 564</b>							
<i>min: max:</i>							
<b>Streckgrenze N/mm<sup>2</sup> : 561</b>							
<i>min: max:</i>							
<b>Dehnung % : 12,3</b>							
<i>min: max:</i>							
<b>HB160</b>							
<b>rissgeprüft</b>							

Certificates for original 24 mm steel dowels, vhss dowels

These steel bars were treated thermally in order to obtain a higher strength equivalent to bolt grade 12.9

Blankstahl 42 CrMoS 4 V+SH 24,0 mm rd.Tol. DIN 671 h 9 Länge: 6-6,5 mtr.										
Charge: 40149										
Werkstoffnorm: DIN EN 10083										
Chemische Zusammensetzung in %										
C	Si	Mn	P	S	Cr	V	Mo	Ni	Al	Cu
0.400	0.310	0.850	0.011	0.027	1.030		0.160			
Mechanische Eigenschaften										
Zugfestigkeit			: 1102 N/mm <sup>2</sup>			Dehnung			: 15.1 %	
Streckgrenze			: 1021 N/mm <sup>2</sup>			Einschnürung			: 56.6 %	
Kerbschlagarbeit (ISO-V)			: 72 J							

Product / Specifications	Dimensions	Quality / Finished condition	Prod. batch No.
Peeled bar, rd EN-10083 EN-10277;EN-10278	rd 24,00 h9 6000+200	42CrMoS4+QT+SH	w/ 4706/3

**I. CHEMICAL COMPOSITION**

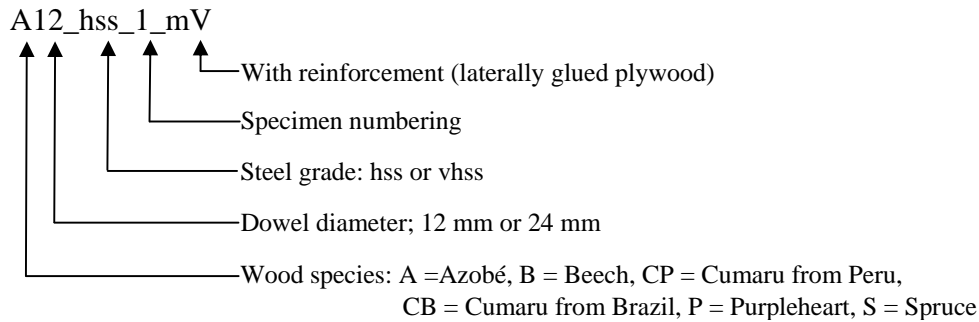
Charge No.	C	Mn	Si	P	S	Cr	Ni	Cu	Mo	Al	Pb	N <sub>2</sub>
X06686	0.41	0.79	0.22	0.009	0.026	1.02	0.07	0.13	0.16	.022		

**II. MECHANICAL TESTS**

Charge No.	R <sub>0.2</sub> /R <sub>0.01</sub> * [Mpa]	R <sub>m</sub> [Mpa]	A5* [%]	Hardness [HB]	Other tests*
X06686	1055	1115	14.0		

\* test is carried out under the agreement made when placing the order

### A.3 NAMING EMBEDMENT TESTS



### A.4 DESCRIPTIVE STATISTICS EMBEDMENT TESTS

Table A-2: Descriptive statistics for moisture content

	m.c. [%]	n	mean	stdev	COV [%]	max	min	5%	95%
12mm dowel	Azobé	vhss 11	19.2	1.75	9.1	21.3	17.2	16.1	22.4
		hss 7	19.7	1.76	8.9	21.2	17.1	16.4	23.1
	Azobé wet	vhss 6	43.6	3.07	7.0	48.3	40.3	37.6	49.6
	Beech	vhss 5	11.8	0.10	0.8	11.9	11.7	11.6	12.0
		hss 5	11.8	0.11	0.9	11.9	11.6	11.6	12.0
	Cumaru Brazil	vhss 8	13.3	0.67	5.0	13.9	12.2	12.0	14.5
		hss 3	12.4	0.17	1.4	12.5	12.2	12.0	12.8
	Cumaru Peru	vhss 7	14.3	0.82	5.7	15.0	13.0	12.8	15.9
		hss 7	14.2	0.61	4.3	14.6	13.1	13.0	15.3
	Purpleheart	vhss 7	14.6	0.63	4.3	15.3	13.6	13.4	15.7
		hss 5	14.0	0.54	3.8	14.5	13.4	12.9	15.1
	Spruce	vhss 6	12.7	1.38	10.9	14.0	11.0	10.0	15.4
		hss 7	13.3	1.38	10.4	14.4	11.1	10.7	15.9
	24mm dowel	Azobé	vhss 5	21.6	2.42	11.2	23.2	17.4	16.7
		hss 5	23.3	0.43	1.8	24.0	22.8	22.5	24.2
Azobé wet		vhss 5	43.0	3.54	8.2	46.7	38.6	35.9	50.1
Beech		vhss 5	12.0	0.94	7.8	13.6	11.1	10.1	13.9
		hss 5	12.1	0.73	6.1	13.3	11.4	10.6	13.5
Cumaru Peru		vhss 5	15.1	0.64	4.2	16.1	14.5	13.8	16.4
		hss 5	15.0	0.43	2.9	15.6	14.4	14.1	15.9
Purpleheart		vhss 5	15.4	0.44	2.9	15.8	14.9	14.5	16.3
		hss 5	15.5	0.35	2.3	16.1	15.2	14.8	16.2
Spruce		vhss 5	12.4	0.30	2.5	12.8	12.0	11.8	13.0
		hss 5	12.3	0.38	3.1	12.5	11.6	11.5	13.0

**Table A-3: Descriptive statistics for density**

	density [kg/m <sup>3</sup> ]	n	mean	stdev	COV [%]	max	min	5%	95%
12mm dowel	Azobé	vhss 11	1071	43.92	4.1	1124	1026	992.5	1150.2
		hss 7	1094	39.16	3.6	1126	1035	1019.8	1168.2
	Azobé wet	vhss 6	1229	34.71	2.8	1264	1180	1161.9	1296.8
		Beech	vhss 5	633	18.91	3.0	658	609	594.7
	hss 5		644	9.67	1.5	655	631	624.5	663.5
	Cumaru Brazil	vhss 8	1156	23.74	2.1	1201	1134	1111.5	1199.8
		hss 3	1192	6.81	0.6	1200	1187	1176.3	1208.4
	Cumaru Peru	vhss 7	893	41.13	4.6	956	862	814.9	970.8
		hss 7	919	59.64	6.5	1014	879	805.7	1031.7
	Purpleheart	vhss 7	949	26.69	2.8	977	898	898.0	999.1
		hss 5	955	22.43	2.3	979	921	910.0	1000.4
	Spruce	vhss 6	444	54.96	12.4	485	345	336.7	550.3
hss 7		482	31.64	6.6	511	413	422.3	542.2	
24mm dowel	Azobé	vhss 5	1042	59.00	5.7	1145	1002	923.1	1160.9
		hss 5	1045	53.79	5.1	1140	1011	937.0	1153.8
	Azobé wet	vhss 5	1222	37.96	3.1	1269	1182	1145.9	1298.9
		Beech	vhss 5	730	17.67	2.4	750	710	694.8
	hss 5		725	30.77	4.2	761	698	663.0	787.0
	Cumaru Peru	vhss 5	933	19.92	2.1	959	911	892.7	972.9
		hss 5	938	30.69	3.3	973	903	876.0	999.6
	Purpleheart	vhss 5	801	170.11	21.2	1043	675	457.8	1143.4
		hss 5	792	153.12	19.3	991	665	483.3	1100.3
	Spruce	vhss 5	463	13.77	3.0	487	452	435.4	491.0
		hss 5	469	27.69	5.9	503	437	413.6	525.2

**Table A-4: Descriptive statistics for embedment strength**

	embedment strength [MPa]	n	mean	stdev	COV [%]	max	min	5%	95%
12mm dowel	Azobé	vhss 11	86.8	7.21	8.3	98.9	79.2	73.8	99.7
		hss 7	73.1	5.14	7.0	80.0	64.7	63.4	82.9
	Azobé wet	vhss 6	64.0	6.04	9.4	72.2	53.6	52.3	75.8
		Beech	vhss 5	52.2	3.49	6.7	57.6	48.8	45.2
	hss 5		46.5	7.92	17.0	59.1	39.7	30.5	62.5
	Cumaru Brazil	vhss 8	107.7	3.93	3.6	116.1	103.5	100.4	115.0
		hss 3	91.1	8.00	8.8	100.1	84.8	72.3	109.9
	Cumaru Peru	vhss 7	74.4	6.35	8.5	83.8	67.5	62.3	86.4
		hss 7	66.9	10.77	16.1	87.8	55.6	46.5	87.3
	Purpleheart	vhss 7	87.0	3.61	4.2	92.6	82.3	80.1	93.8
		hss 5	70.0	11.94	17.1	90.2	59.9	46.0	94.1
	Spruce	vhss 6	31.4	4.36	13.9	36.5	25.9	22.9	39.8
hss 7		24.6	3.65	14.8	29.3	19.7	17.7	31.5	
24mm dowel	Azobé	vhss 5	74.1	3.83	5.2	80.8	71.0	66.4	81.8
		hss 5	65.7	6.39	9.7	76.2	59.1	52.9	78.6
	Azobé wet	vhss 5	62.8	4.83	7.7	69.1	57.4	53.1	72.6
		Beech	vhss 5	58.6	1.35	2.3	59.7	56.7	55.9
	hss 5		49.8	1.33	2.7	52.0	48.6	47.2	52.5
	Cumaru Peru	vhss 5	74.5	2.96	4.0	77.7	71.7	68.5	80.4
		hss 5	63.6	5.78	9.1	71.9	55.7	51.9	75.2
	Purpleheart	vhss 5	65.1	16.71	25.7	88.8	51.8	31.5	98.8
		hss 5	52.4	14.43	27.5	69.9	39.0	23.3	81.4
	Spruce	vhss 5	38.0	3.20	8.4	42.4	34.8	31.6	44.5
		hss 5	28.2	2.35	8.3	30.7	24.9	23.4	32.9

Note: 5% and 95% fractiles calculated with Student's t-distribution as only few specimens were available.

## A.5 LOAD-SLIP GRAPHS OF EMBEDMENT TESTS

### AZOBE

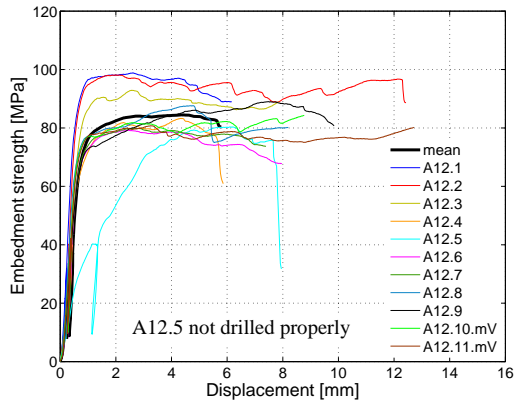


Figure A-6: Azobé, 12 mm v-hss dowel

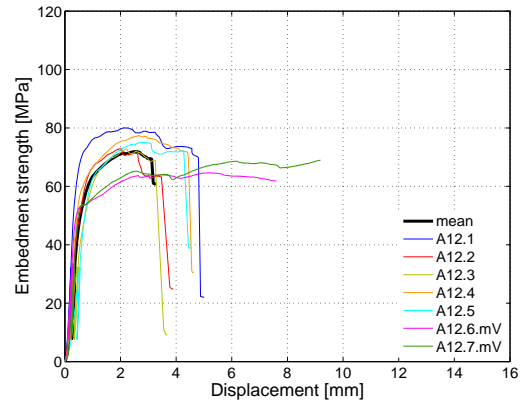


Figure A-9: Azobé, 12 mm hss dowel

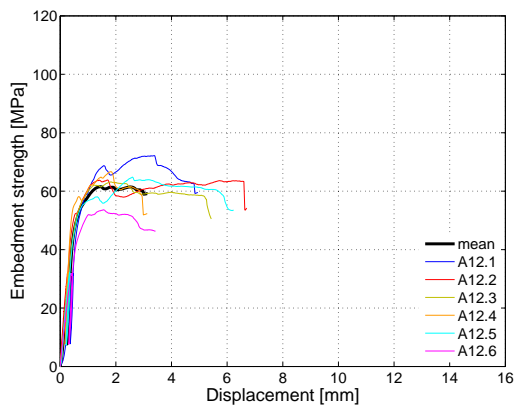


Figure A-7: wet Azobé, 12 mm v-hss dowel

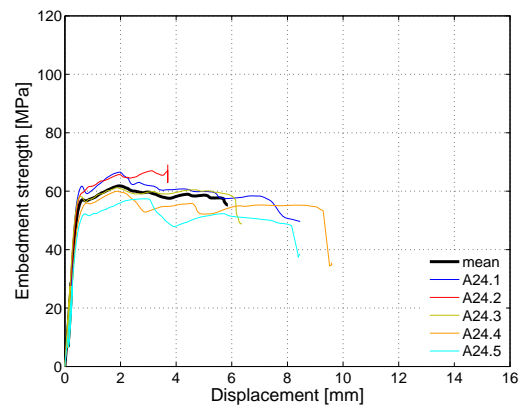


Figure A-10: wet Azobé, 24 mm v-hss dowel

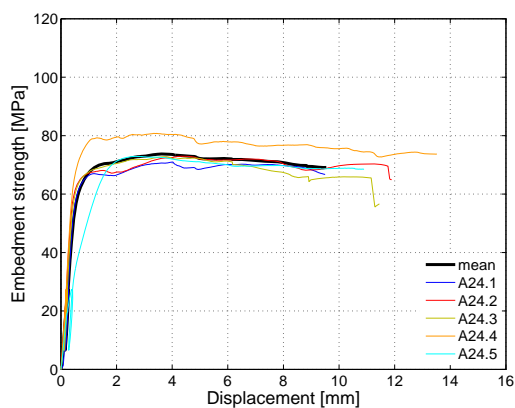


Figure A-8: Azobé, 24 mm v-hss dowel

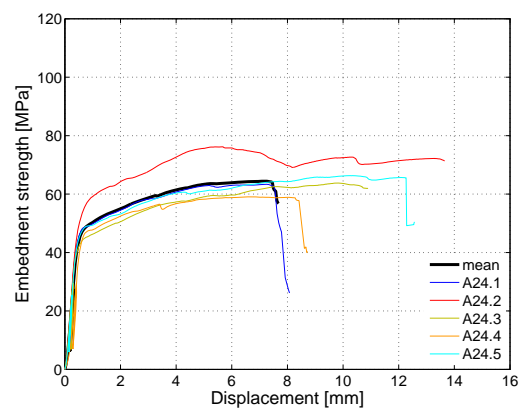
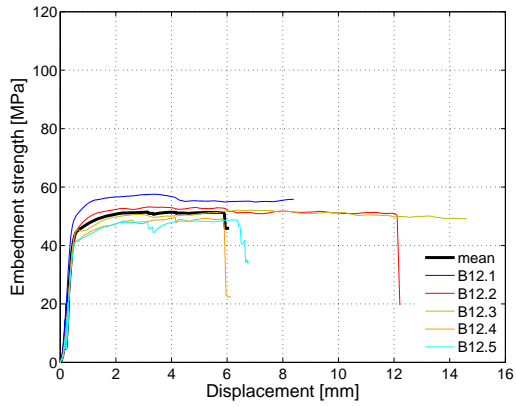
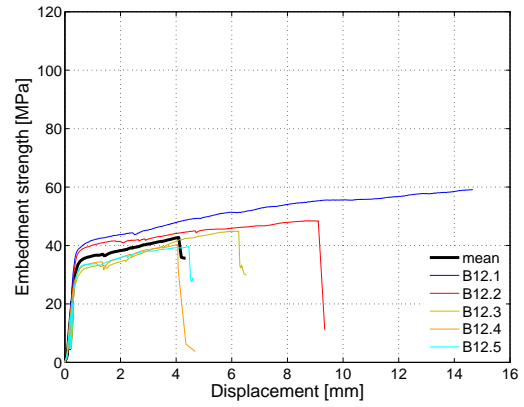


Figure A-11: Azobé, 24 mm hss dowel

**BEECH**



**Figure A-12: Beech, 12 mm vhss dowel**



**Figure A-14: Beech, 12 mm hss dowel**

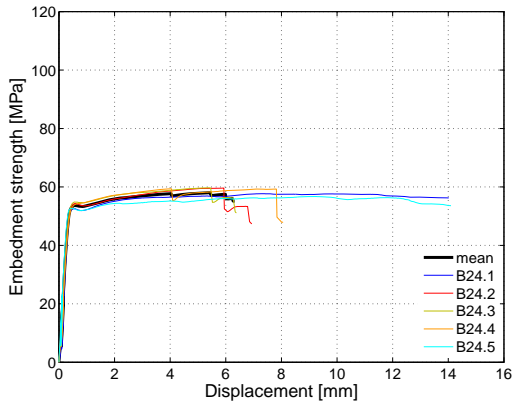


**Figure A-13: Beech, 24 mm vhss dowel**

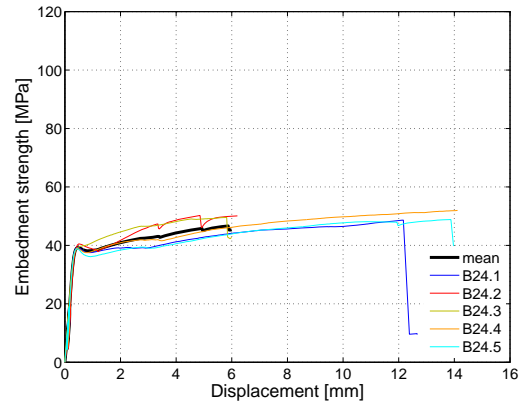


**Figure A-15: Beech, 24 mm hss dowel**

**CUMARU**

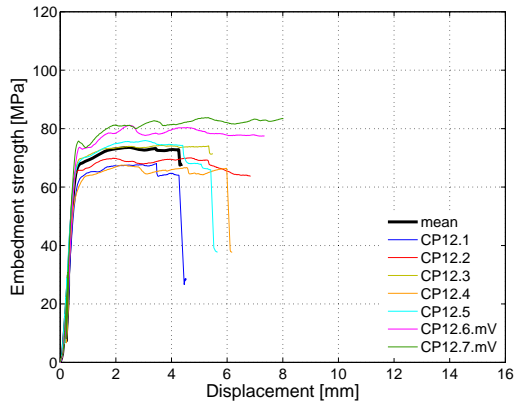


Figure A-16: Cumaru Peru, 12 mm vhss dowel

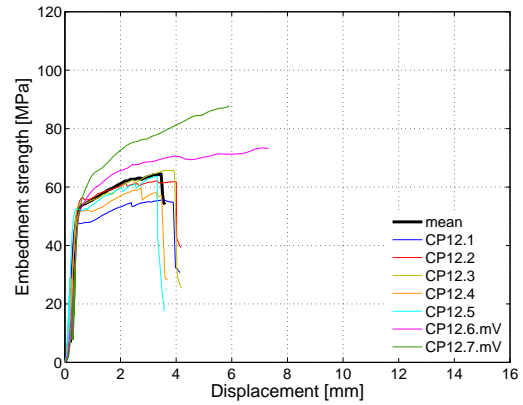


Figure A-19: Cumaru Peru, 12 mm hss dowel

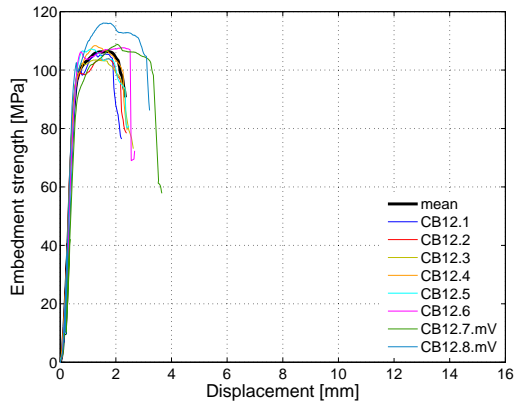


Figure A-17: Cumaru Brazil, 12 mm vhss dowel

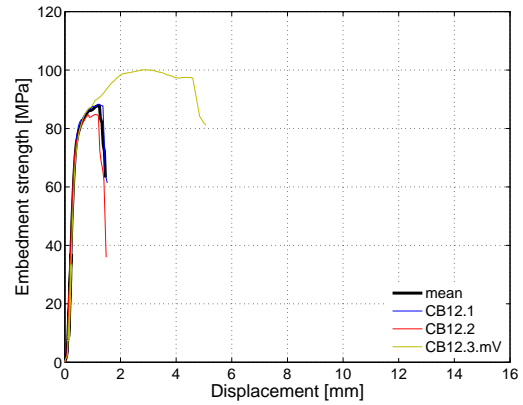


Figure A-20: Cumaru Brazil, 12 mm hss dowel

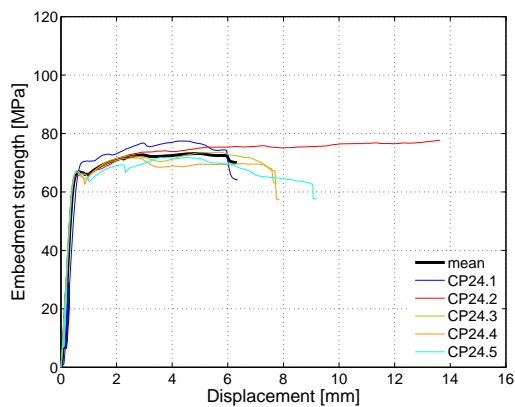


Figure A-18: Cumaru Peru, 24 mm vhss dowel

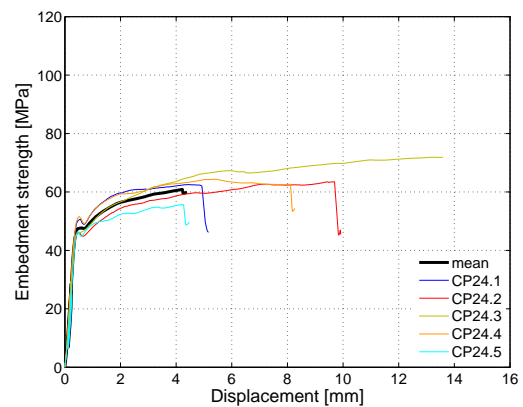
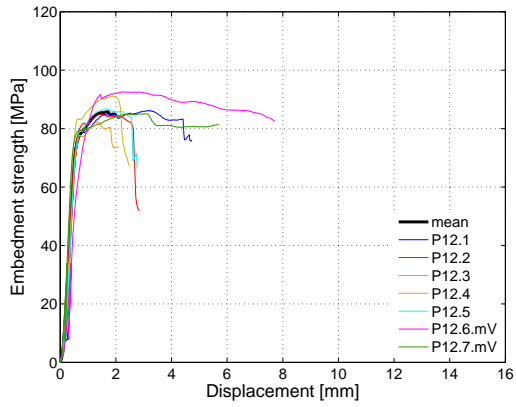
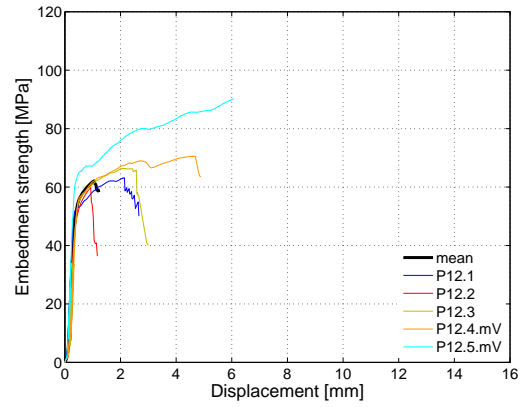


Figure A-21: Cumaru Peru, 24 mm hss dowel

**PURPLEHEART**



**Figure A-22: Purpleheart, 12 mm vhss dowel**



**Figure A-24: Purpleheart, 12 mm hss dowel**

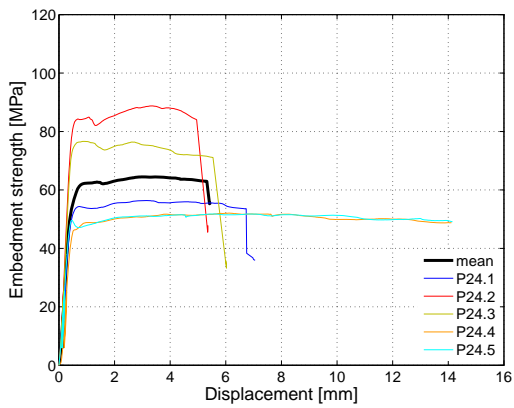


**Figure A-23: Purpleheart, 24 mm vhss dowel**

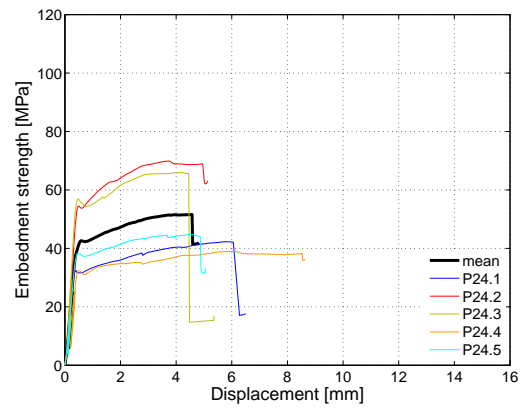


**Figure A-25: Purpleheart, 24 mm hss dowel**

**SPRUCE**

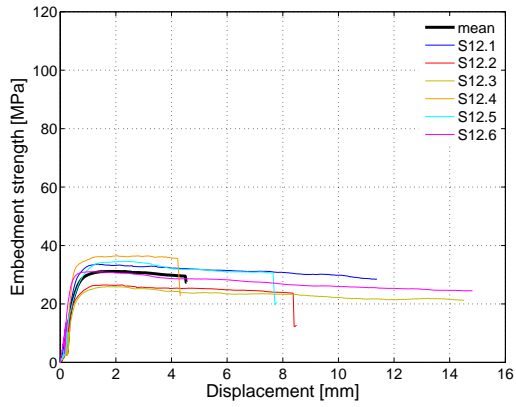


**Figure A-26: Spruce, 12 mm vhss dowel**

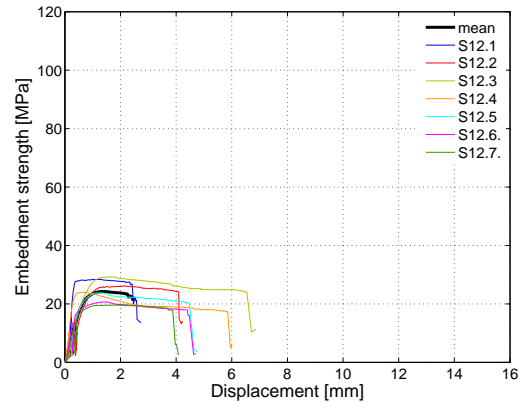


**Figure A-28: Spruce, 12 mm hss dowel**

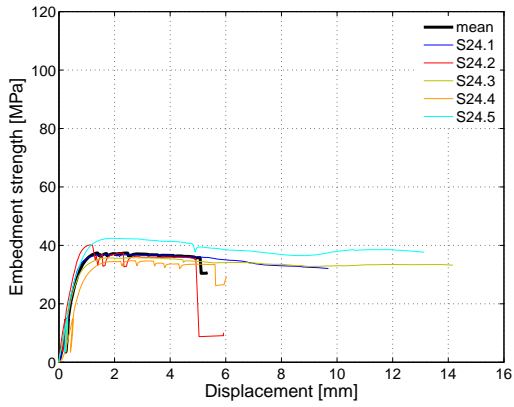


**Figure A-27: Spruce, 24 mm vhss dowel**

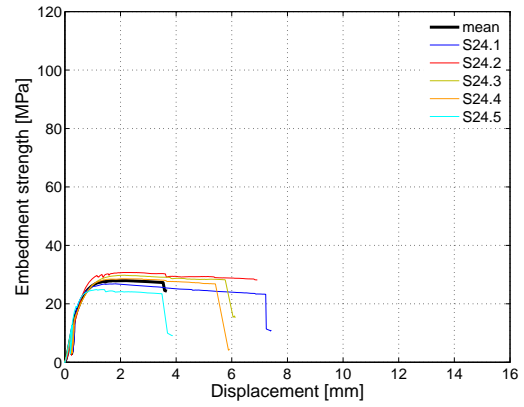


**Figure A-29: Spruce, 24 mm hss dowel**

## A.6 SINGLE EMBEDMENT TESTS

### Legend:

- mc\_test = moisture content at test
  - rho\_test = density at test
  - rho\_12% = density at 12% moisture content
  - F\_max = maximum force
  - EC5\_test = embedment strength according to EC5 with rho\_test
  - F\_emb = embedment strength of test
  - F\_emb\_12% = embedment strength adjusted to 12% moisture content
  - WA1, WA2 = ultimate displacement measured by transducers
  - v\_max = ultimate displacement
  - v(F\_max) = displacement at F\_max
  - Teflon = teflon strip between rig and specimen used or not
  - Distance between rig and specimen = distance between dowel support and timber (see ellipse in Figure 6-6)
- Only tropical hardwood:
- Reinforcement (laterally glued plywood) used or not
  - Original beam = number of the strength-graded beams (only tropical hardwood) from which the test specimens were sawn  
(properties see Table A-10)

### Only spruce and beech:

- Width rings = mean width of annual rings
- Angle rings = mean angle of rings (0° = rings parallel to width = perpendicular to dowel axis)

**Table A-5: Azobé, single test results (continues following page)**

test number	species	test specimen	new name	diameter [mm]	steel grade	mc_test [%]	rho_test [kg/m <sup>3</sup> ]	rho_12% [kg/m <sup>3</sup> ]	F_max [kN]	EC5_test [MPa]	F_emb [MPa]	F_emb_12% [MPa]	WA1 [mm]	WA2 [mm]	v_max [mm]	v(F_max) [mm]	Teflon	Reinforcement	distance between rig and specimen [mm]	original beam
12	Azobé	as23_1	A12_vhss_01	12	vhss	20.5	1115	1036	23.7	80.5	98.9	116.7	6.3	6.1	6.2	2.6	no		23	
13	Azobé	as23_2	A12_vhss_02	12	vhss	21.0	1112	1029	23.6	80.2	96.1	115.8	12.3	12.5	12.4	2.0	no		23	
14	Azobé	as23_3	A12_vhss_03	12	vhss	21.3	1124	1038	22.3	81.1	92.9	109.6	8.3	7.4	7.8	2.6	yes		23	
15	Azobé	as23_4	A12_vhss_04	12	vhss	21.3	1112	1027	20.0	80.2	83.3	98.3	6.0	5.7	5.9	4.3	yes		23	
16	Azobé	as23_5	A12_vhss_05	12	vhss	20.9	1121	1038	19.3	80.9	80.4	94.8	7.1	9.0	8.0	6.2	yes		23	
88	Azobé	AS09-17	A12_vhss_06	12	vhss	18.3	1026	971	19.0	74.0	79.2	93.5	7.6	8.3	8.0	2.4	yes	5.0	9	
89	Azobé	AS09-18	A12_vhss_07	12	vhss	18.7	1036	978	19.2	74.8	79.9	94.3	7.5	7.3	7.4	2.5	yes	5.0	9	
86	Azobé	AS09-15	A12_vhss_08	12	vhss	17.4	1030	983	21.0	74.3	87.6	101.8	8.5	7.9	8.2	4.7	yes	1.0	9	
87	Azobé	AS09-16	A12_vhss_09	12	vhss	17.2	1028	982	21.4	74.2	89.0	102.9	10.3	9.4	9.8	7.5	yes	1.0	9	
69	Azobé	AS09-11	A12_vhss_10_mV	12	vhss	17.9	1045	993	20.2	75.4	84.3	99.2	9.2	8.3	8.8	8.8	yes	5.05	9	
70	Azobé	AS09-12	A12_vhss_11_mV	12	vhss	17.2	1036	990	19.4	74.8	80.7	93.3	12.2	13.2	12.7	3.2	yes	5.05	9	
17	Azobé	as23_6	A12_hss_1	12	hss	20.7	1119	1038	19.2	80.7	80.0	94.4	4.6	5.4	5.0	2.2	yes		23	
18	Azobé	as23_10	A12_hss_2	12	hss	20.4	1110	1033	17.5	80.1	72.9	86.0	4.9	2.9	3.9	2.0	yes		23	
19	Azobé	as23_9	A12_hss_3	12	hss	20.9	1121	1038	17.5	80.9	72.8	85.9	2.9	4.4	3.7	2.2	yes		23	
20	Azobé	as23_7	A12_hss_4	12	hss	21.2	1126	1041	18.6	81.3	77.4	91.3	4.0	5.5	4.6	2.7	yes		23	
21	Azobé	as23_8	A12_hss_5	12	hss	20.6	1107	1028	18.0	79.9	75.1	88.6	4.5	4.6	4.5	2.7	yes		23	
71	Azobé	AS09-13	A12_hss_6_mV	12	hss	17.1	1035	990	15.5	74.7	64.7	74.6	7.8	7.4	7.6	5.1	yes	5.05	9	
75	Azobé	AS09-14	A12_hss_7_mV	12	hss	17.3	1040	993	16.5	75.0	69.0	79.9	9.6	8.8	9.2	9.2	yes	5.05	9	
6	Azobé wet	as31_1	A12_wet_1	12	vhss	43.2	1254	981	17.3	90.5	72.2	85.2	4.4	5.5	4.9	3.4	no		31	
7	Azobé wet	as31_2	A12_wet_2	12	vhss	40.3	1235	986	15.3	89.1	63.8	75.3	6.7	6.7	6.7	1.7	no		31	
8	Azobé wet	as31_3	A12_wet_3	12	vhss	40.9	1250	994	15.2	90.2	63.2	74.6	6.3	4.6	5.4	1.8	no		31	
9	Azobé wet	as31_4	A12_wet_4	12	vhss	42.9	1264	991	16.0	91.2	66.7	78.7	3.2	3.1	3.1	1.8	no		31	
10	Azobé wet	as44_1	A12_wet_5	12	vhss	46.1	1180	905	15.6	85.1	64.8	76.5	6.4	6.0	6.2	2.6	no		44	
11	Azobé wet	as44_2	A12_wet_6	12	vhss	48.3	1193	901	12.9	86.1	53.6	63.3	4.2	2.7	3.4	1.6	no		44	

test number	species	test specimen	new name	diameter [mm]	steel grade	mc_test [%]	rho_test [kg/m <sup>3</sup> ]	rho_12% [kg/m <sup>3</sup> ]	F_max [kN]	EC5_test [MPa]	F_emb [MPa]	F_emb_12% [MPa]	WA1 [mm]	WA2 [mm]	v_max [mm]	v(F_max) [mm]	Tellon	Reinforcement	distance between rig and specimen [mm]	original beam
90	Azobé	AS41-2	A24_vhss_1	24	vhss	17.4	1002	956	68.1	62.4	71.0	82.5	9.7	9.3	9.5	4.0	yes		5.0	41
100	Azobé	AS09-1	A24_vhss_2	24	vhss	23.0	1037	944	70.0	64.6	73.0	86.1	11.8	12.0	11.9	4.3	no		5.0	9
101	Azobé	AS20-1	A24_vhss_3	24	vhss	21.8	1011	930	69.9	63.0	72.8	85.9	11.9	11.0	11.5	3.8	no		5.0	20
102	Azobé	AS22-1	A24_vhss_4	24	vhss	23.2	1145	1041	77.5	71.4	80.8	95.3	13.7	13.4	13.5	3.3	no		5.0	22
103	Azobé	AS44-1	A24_vhss_5	24	vhss	22.7	1015	926	70.0	63.3	72.9	86.0	11.1	10.7	10.9	2.7	no		5.0	44
95	Azobé	AS41-1	A24_hss_1	24	hss	24.0	1033	933	60.8	64.4	63.4	74.8	7.9	8.3	8.1	7.2	yes		5.0	41
104	Azobé	AS22-2	A24_hss_2	24	hss	23.3	1140	1036	73.1	71.0	76.2	89.9	13.6	13.7	13.7	5.7	no		5.0	22
105	Azobé	AS44-3	A24_hss_3	24	hss	22.8	1030	939	61.2	64.2	63.8	75.3	10.8	11.0	10.9	9.8	no		5.0	44
106	Azobé	AS20-2	A24_hss_4	24	hss	23.3	1013	920	56.7	63.1	59.1	69.7	8.8	8.7	8.7	6.7	no		5.0	20
107	Azobé	AS44-2	A24_hss_5	24	hss	23.3	1011	918	63.7	63.0	66.3	78.3	12.8	12.4	12.6	10.2	no		5.0	44
1	Azobé wet	as31_1	A24_wet_1	24	vhss	38.6	1228	992	63.9	76.5	66.5	78.5	8.6	8.3	8.5	2.0	no			31
2	Azobé wet	as31_2	A24_wet_2	24	vhss	40.9	1247	991	66.3	77.7	69.1	81.5	3.3	4.1	3.7	3.7	no			31
3	Azobé wet	as31_3	A24_wet_3	24	vhss	42.4	1269	998	58.8	79.1	61.2	72.2	6.0	6.8	6.4	1.9	no			31
4	Azobé wet	as44_1	A24_wet_4	24	vhss	46.7	1186	905	57.6	73.9	60.0	70.8	9.3	9.9	9.6	1.9	no			44
5	Azobé wet	as44_2	A24_wet_5	24	vhss	46.5	1182	904	55.1	73.7	57.4	67.7	8.2	8.7	8.5	2.9	no			44

**Table A-6: Beech, single test results**

test number	species	test specimen	new name	diameter [mm]	steel grade	mc_test [%]	rho_test [kg/m <sup>3</sup> ]	rho_12% [kg/m <sup>3</sup> ]	F_max [kN]	ECS_test [MPa]	F_emb [MPa]	F_emb_12% [MPa]	WA1 [mm]	WA2 [mm]	v_max [mm]	v(F_max) [mm]	Telfon	distance between ring and specimen [mm]	width rings [mm]	angle rings [°]
51	Beech	1-1	B12_vhss_1	12	vhss	11.9	668	659	13.8	47.5	57.6	57.4	8.8	8.0	8.4	3.4	no	2.5	2.0	48
53	Beech	1-4	B12_vhss_2	12	vhss	11.7	639	641	12.8	46.1	53.2	52.7	12.2	12.2	12.2	3.2	yes	5.05	2.0	54
55	Beech	1-5	B12_vhss_3	12	vhss	11.8	638	639	12.5	46.0	52.1	51.8	15.0	14.2	14.6	6.8	yes	5.05	2.0	51
56	Beech	2-1	B12_vhss_4	12	vhss	11.9	609	610	11.9	43.9	49.6	49.4	5.9	6.4	6.1	4.1	yes	5.05	1.5	0
57	Beech	2-2	B12_vhss_5	12	vhss	11.7	620	622	11.7	44.7	48.8	48.3	6.9	6.6	6.8	6.3	no	5.05	1.5	0
52	Beech	1-2	B12_hss_1	12	hss	11.8	662	663	14.2	47.0	59.1	58.8	14.8	14.6	14.7	14.7	no	2.5	2.0	36
54	Beech	1-3	B12_hss_2	12	hss	11.8	665	666	11.6	47.3	48.5	48.2	8.9	9.7	9.3	8.8	yes	5.05	2.0	49
58	Beech	2-3	B12_hss_3	12	hss	11.9	631	632	10.8	45.5	44.9	44.8	7.0	6.0	6.5	6.2	no	5.05	1.5	0
59	Beech	2-4	B12_hss_4	12	hss	11.8	640	641	9.7	46.2	40.3	40.0	4.3	5.1	4.7	4.0	yes	5.05	1.5	0
60	Beech	2-5	B12_hss_5	12	hss	11.6	642	644	9.5	46.3	39.7	39.2	4.5	4.8	4.6	4.5	no	5.05	1.5	0
93	Beech	BU-1-1	B24_vhss_1	24	vhss	13.6	714	704	55.4	44.5	57.7	60.5	14.3	13.7	14.0	7.3	yes	5.0	2.5	33
124	Beech	BU-3-1	B24_vhss_2	24	vhss	11.6	735	738	57.2	45.8	59.6	58.9	6.7	7.1	6.9	5.9	no	5.0	3.0	24
125	Beech	BU3-2	B24_vhss_3	24	vhss	11.8	743	744	57.3	46.3	59.7	59.3	6.1	6.7	6.4	5.4	no	5.0	3.0	20
128	Beech	BU-2-1	B24_vhss_4	24	vhss	11.1	750	756	57.0	46.7	59.4	57.8	8.1	8.0	8.1	4.0	no	5.0	2.5	12
129	Beech	BU-4-1	B24_vhss_5	24	vhss	12.1	710	709	54.4	44.2	56.7	56.9	14.2	14.0	14.1	9.0	no	5.0	2.5	48
98	Beech	BU-1-2	B24_hss_1	24	hss	13.3	698	690	46.7	43.5	48.6	50.5	13.0	12.4	12.7	12.2	yes	5.0	2.5	33
126	Beech	BU-2-2	B24_hss_2	24	hss	11.7	756	758	48.2	47.1	50.2	49.7	5.8	6.6	6.2	4.9	no	5.0	2.5	10
127	Beech	BU-3-3	B24_hss_3	24	hss	12.0	761	761	47.6	47.4	49.6	49.6	6.2	5.7	6.0	5.8	no	5.0	3.0	16
130	Beech	BU-4-2	B24_hss_4	24	hss	11.9	705	706	49.9	43.9	52.0	51.8	14.2	14.0	14.1	14.1	no	5.0	2.0	54
131	Beech	BU-4-3	B24_hss_5	24	hss	11.4	705	709	46.9	43.9	48.8	48.0	14.4	13.8	14.1	13.8	no	5.0	2.0	54

**Table A-7: Cumaru, single test results (continues following page)**

test number	species	test specimen	new name	diameter [mm]	steel grade	mc_test [%]	rho_test [kg/m <sup>3</sup> ]	rho_12% [kg/m <sup>3</sup> ]	F_max [kN]	EC5_test [MPa]	F_emb [MPa]	F_emb_12% [MPa]	WA1 [mm]	WA2 [mm]	v_max [mm]	(F_max) [mm]	Teflon	Reinforcement	distance between rig and specimen [mm]	original beam
32	Cumaru Brazil	c52_1	CB_vhss_1	12	vhss	13.2	1151	1139	25.3	83.1	105.6	109.4	2.4	2.0	2.2	1.3	yes			52
33	Cumaru Brazil	c52_2	CB_vhss_2	12	vhss	13.7	1137	1120	25.0	82.0	104.0	109.3	2.6	2.2	2.4	1.7	yes			52
34	Cumaru Brazil	c52_3	CB_vhss_3	12	vhss	13.9	1134	1115	24.8	81.8	103.5	109.4	2.9	2.3	2.6	1.3	yes			52
35	Cumaru Brazil	c52_4	CB_vhss_4	12	vhss	13.8	1151	1133	26.0	83.1	108.4	114.3	2.3	2.5	2.4	1.3	yes			52
36	Cumaru Brazil	c52_5	CB_vhss_5	12	vhss	13.7	1142	1125	25.7	82.4	107.2	112.7	2.6	2.3	2.5	1.1	no			52
37	Cumaru Brazil	c52_6	CB_vhss_6	12	vhss	13.3	1146	1133	25.8	82.7	107.7	111.9	2.7	2.7	2.7	2.2	no			52
77	Cumaru Brazil	C94-3	CB_vhss_7_mv	12	vhss	12.2	1183	1181	26.1	85.4	108.8	109.4	4.2	3.1	3.7	2.1	yes	yes	5.05	94
78	Cumaru Brazil	C94-5	CB_vhss_8_mv	12	vhss	12.3	1201	1198	27.9	86.7	116.1	117.1	3.2	3.3	3.2	1.6	yes	yes	1.0	94
38	Cumaru Brazil	c94_1	CB12_hss_1	12	hss	12.5	1200	1195	21.2	86.6	88.3	89.7	1.6	1.5	1.5	1.2	yes		2.5	94
39	Cumaru Brazil	c94_2	CB12_hss_2	12	hss	12.5	1190	1185	20.4	85.9	84.8	86.1	1.6	1.4	1.5	1.1	yes		2.5	94
40	Cumaru Brazil	c94_4	CB12_hss_3_mv	12	hss	12.2	1187	1185	24.0	85.7	100.1	100.7	5.4	4.7	5.1	2.9	no	yes	2.5	94
22	Cumaru Peru	cp46_1	CP12_vhss_1	12	vhss	14.5	877	858	16.3	63.3	68.1	73.2	4.6	4.5	4.5	3.5	yes			46
23	Cumaru Peru	cp46_2	CP12_vhss_2	12	vhss	14.9	868	846	16.8	62.6	70.0	76.1	6.7	7.0	6.8	4.6	yes			46
24	Cumaru Peru	cp46_3	CP12_vhss_3	12	vhss	15.0	864	841	17.8	62.3	74.3	81.0	5.3	5.7	5.5	3.7	yes			46
25	Cumaru Peru	cp46_4	CP12_vhss_4	12	vhss	14.8	862	841	16.2	62.2	67.5	73.2	6.6	5.8	6.2	2.2	yes			46
26	Cumaru Peru	cp46_5	CP12_vhss_5	12	vhss	14.7	874	853	18.2	63.1	75.9	82.1	5.7	5.6	5.7	3.0	yes	yes	5.05	46
74	Cumaru Peru	CUM-11	CP12_vhss_6_mv	12	vhss	13.0	956	948	19.5	69.0	81.1	83.6	7.6	7.1	7.3	2.5	yes	yes		
84	Cumaru Peru	CUM-12	CP12_vhss_7_mv	12	vhss	13.3	949	938	20.1	68.5	83.8	87.0	8.4	7.7	8.0	5.3	yes	yes	1.0	
27	Cumaru Peru	cp46_6	CP12_hss_1	12	hss	14.6	880	860	13.3	63.5	55.6	60.0	4.4	3.9	4.1	3.5	yes			46
28	Cumaru Peru	cp46_7	CP12_hss_2	12	hss	14.6	879	859	14.9	63.4	62.1	67.0	4.5	3.9	4.2	3.3	yes			46
29	Cumaru Peru	cp46_8	CP12_hss_3	12	hss	14.6	892	872	15.8	64.4	65.8	70.9	3.7	4.7	4.2	3.9	yes			46
30	Cumaru Peru	cp46_9	CP12_hss_4	12	hss	14.5	886	867	14.3	63.9	59.6	64.1	3.8	3.5	3.7	2.7	yes			46
31	Cumaru Peru	cp46_10	CP12_hss_5	12	hss	14.2	883	866	15.3	63.7	63.8	68.0	3.9	3.3	3.6	3.3	yes			46
76	Cumaru Peru	CUM-13	CP12_hss_6_mv	12	hss	13.5	997	984	17.6	71.9	73.5	76.8	7.4	7.2	7.3	7.1	yes	yes	5.05	
85	Cumaru Peru	CUM-14	CP12_hss_7_mv	12	hss	13.1	1014	1004	21.1	73.2	87.8	90.7	5.9	5.9	5.9	5.9	yes	yes	1.0	

test number	species	test specimen	new name	diameter [mm]	steel grade	mc_test [%]	rho_test [kg/m <sup>3</sup> ]	rho_12% [kg/m <sup>3</sup> ]	F_max [kN]	EC5_test [MPa]	F_emb [MPa]	F_emb_12% [MPa]	WA1 [mm]	WA2 [mm]	v_max [mm]	v(F_max) [mm]	Teflon	Reinforcement	distance between rig and specimen [mm]	original beam
91	Cuamru Peru	CP32-1	CP24_vhss_1	24	vhss	15.1	959	933	74.4	59.8	77.5	84.7	6.9	5.8	6.4	4.3	yes		5.0	32
108	Cuamaru Peru	CP02-1	CP24_vhss_2	24	vhss	15.2	948	922	74.6	59.1	77.7	85.2	13.5	13.7	13.6	13.6	no		5.0	2
109	Cuamaru Peru	CP32-3	CP24_vhss_3	24	vhss	16.1	922	889	70.7	57.5	73.6	82.7	8.0	7.5	7.7	5.7	no		5.0	32
110	Cuamaru Peru	CP39-1	CP24_vhss_4	24	vhss	14.6	924	903	68.8	57.6	71.7	77.3	8.1	7.6	7.9	2.5	no		5.0	39
111	Cuamaru Peru	CP39-2	CP24_vhss_5	24	vhss	14.5	911	891	69.0	56.8	71.8	77.2	9.2	9.2	9.2	4.5	no		5.0	39
96	Cuamaru Peru	CP32-2	CP24_hss_1	24	hss	15.6	931	902	60.0	58.0	62.5	69.3	5.3	5.0	5.2	4.5	yes		5.0	32
112	Cuamaru Peru	CP02-2	CP24_hss_2	24	hss	14.9	973	948	60.9	60.6	63.5	69.0	9.7	10.1	9.9	9.7	no		5.0	2
113	Cuamaru Peru	CP02-3	CP24_hss_3	24	hss	15.1	966	940	69.0	60.2	71.9	78.6	13.2	14.0	13.6	13.3	no		5.0	2
114	Cuamaru Peru	CP23-1	CP24_hss_4	24	hss	15.1	916	891	61.8	57.1	64.4	70.4	8.4	8.1	8.3	5.4	no		5.0	23
115	Cuamaru Peru	CP39-3	CP24_hss_5	24	hss	14.4	903	884	53.4	56.3	55.7	59.7	4.7	4.2	4.5	4.3	no		5.0	39

**Table A-8: Purpleheart, single test results**

test number	species	test specimen	new name	diameter [mm]	steel grade	mc_test [%]	rho_test [kg/m <sup>3</sup> ]	rho_12% [kg/m <sup>3</sup> ]	F_max [kN]	EC5_test [MPa]	F_emb [MPa]	F_emb_12% [MPa]	WA1 [mm]	WA2 [mm]	v_max [mm]	v(F_max) [mm]	Teflon	Reinforcement	distance between rig and specimen [mm]	original beam
41	Purpleheart	ph28_1	P12_vhss_1	12	vhss	14.4	974	954	20.7	70.3	86.2	92.4	5.0	4.5	4.7	3.2	no		2.5	28
42	Purpleheart	ph28_2	P12_vhss_2	12	vhss	15.3	961	933	20.4	69.3	84.9	93.3	3.1	2.6	2.8	1.5	yes		2.5	28
43	Purpleheart	ph28_3	P12_vhss_3	12	vhss	15.1	977	951	21.8	70.5	91.0	99.4	2.7	2.3	2.5	2.0	yes		2.5	28
44	Purpleheart	ph28_4	P12_vhss_4	12	vhss	15.1	947	921	19.8	68.3	82.3	90.0	1.8	2.4	2.1	1.4	yes		2.5	28
45	Purpleheart	ph28_5	P12_vhss_5	12	vhss	14.3	940	921	20.8	67.8	86.8	92.8	3.0	2.5	2.8	1.7	no		2.5	28
72	Purpleheart	PH36-11	P12_vhss_6_mv	12	vhss	14.1	943	926	22.2	68.0	92.6	98.5	8.9	6.5	7.7	2.3	yes	yes	5.05	36
82	Purpleheart	PH36-12	P12_vhss_7_mv	12	vhss	13.6	898	885	20.4	64.8	85.1	89.2	5.7	5.7	5.7	3.0	yes	yes	1.0	36
46	Purpleheart	ph28_6	P12_hss_1	12	hss	14.2	921	903	15.2	66.5	63.1	67.3	2.7	2.6	2.7	2.1	no		2.5	28
47	Purpleheart	ph28_7	P12_hss_2	12	hss	14.5	979	958	14.4	70.6	59.9	64.3	0.9	1.5	1.2	0.9	yes		2.5	28
48	Purpleheart	ph28_8	P12_hss_3	12	hss	14.5	965	944	15.9	69.6	66.4	71.4	3.0	3.1	3.0	2.1	no		2.5	28
73	Purpleheart	PH28-9	P12_hss_4_mv	12	hss	13.5	946	933	16.9	68.3	70.6	73.8	5.1	4.7	4.9	4.7	yes	yes	5.05	28
83	Purpleheart	PH28-10	P12_hss_5_mv	12	hss	13.4	965	953	21.6	69.6	90.2	94.0	6.3	5.8	6.1	6.1	yes	yes	1.0	28
92	Purpleheart	PH32-1	P24_vhss_1	24	vhss	14.9	686	689	54.1	42.8	56.4	61.3	7.4	6.7	7.1	3.1	yes		5.0	32
116	Purpleheart	PH12-1	P24_vhss_2	24	vhss	14.9	1043	1017	85.2	65.0	88.8	96.5	5.6	5.1	5.4	3.3	no		5.0	12
117	Purpleheart	PH33-1	P24_vhss_3	24	vhss	15.6	918	889	73.6	57.2	76.6	84.9	6.3	5.8	6.0	1.0	no		5.0	33
118	Purpleheart	PH41-1	P24_vhss_4	24	vhss	15.7	675	653	50.0	42.1	52.1	57.8	13.9	14.3	14.1	6.1	no		5.0	41
119	Purpleheart	PH41-2	P24_vhss_5	24	vhss	15.8	681	659	49.7	42.4	51.8	57.7	14.6	13.7	14.2	5.6	no		5.0	41
97	Purpleheart	PH32-2	P24_hss_1	24	hss	16.1	674	650	40.6	42.0	42.3	47.5	6.7	6.3	6.5	5.8	yes		5.0	32
120	Purpleheart	PH12-2	P24_hss_2	24	hss	15.3	991	963	67.1	61.8	69.9	76.8	5.3	5.0	5.1	3.7	no		5.0	12
121	Purpleheart	PH33-2	P24_hss_3	24	hss	15.5	922	894	63.3	57.5	66.0	72.9	5.9	4.8	5.4	4.2	no		5.0	33
122	Purpleheart	PH32-3	P24_hss_4	24	hss	15.6	665	644	37.4	41.4	39.0	43.2	8.6	8.7	8.6	6.0	no		5.0	32
123	Purpleheart	PH41-3	P24_hss_5	24	hss	15.2	707	687	42.9	44.1	44.7	49.0	5.5	4.6	5.0	4.6	no		5.0	41

**Table A-9: Spruce, single test results**

test number	species	test specimen	new name	diameter [mm]	steel grade	mc_test [%]	rho_test [kg/m <sup>3</sup> ]	rho_12% [kg/m <sup>3</sup> ]	F_max [kN]	ECS_test [MPa]	F_emb [MPa]	F_emb_12% [MPa]	W/A1 [mm]	W/A2 [mm]	v_max [mm]	v(F_max) [mm]	Teflon	distance between rings and specimen [mm]	width rings [mm]	angle rings [°]
49	Spruce	1	S12_vhss_1	12	vhss	11.9	432	432	8.1	31.2	33.6	33.5	12.1	10.7	11.4	1.4	no	2.5	4.0	62
61	Spruce	5	S12_vhss_2	12	vhss	11.6	345	346	6.4	24.9	26.5	26.2	8.3	8.7	8.5	1.6	yes	5.05	6.0	0
62	Spruce	7	S12_vhss_3	12	vhss	11.0	430	434	6.2	31.0	25.9	25.1	14.0	15.0	14.5	1.7	yes	5.05	7.0	0
63	Spruce	8	S12_vhss_4	12	vhss	14.0	485	476	8.8	35.0	36.5	36.7	4.5	4.1	4.3	2.0	yes	5.05	2.5	0
66	Spruce	6	S12_vhss_5	12	vhss	13.9	484	476	8.3	34.9	34.6	36.6	7.7	7.8	7.8	2.3	yes	5.05	1.5	58
79	Spruce	FI-11	S12_vhss_6	12	vhss	14.0	485	476	7.5	35.0	31.0	32.9	15.2	14.4	14.8	1.0	yes	1.0	2.0	52
50	Spruce	4	S12_hss_1	12	hss	13.1	511	506	6.8	36.9	28.4	29.4	2.6	2.9	2.7	1.2	no	2.5	4.0	71
64	Spruce	9	S12_hss_2	12	hss	11.1	413	416	6.3	29.8	26.2	25.5	4.7	3.8	4.2	2.1	yes	5.05	6.0	0
65	Spruce	10	S12_hss_3	12	hss	11.7	486	487	7.0	35.1	29.3	29.0	6.3	7.4	6.9	1.6	no	5.05	3.0	61
67	Spruce	2	S12_hss_4	12	hss	14.3	493	483	5.8	35.6	24.0	25.7	6.4	5.6	6.0	0.7	no	5.05	1.5	56
68	Spruce	3	S12_hss_5	12	hss	14.4	495	485	5.7	35.7	23.8	25.5	4.8	4.7	4.8	1.2	yes	5.05	1.5	55
80	Spruce	FI-12	S12_hss_6	12	hss	14.0	489	480	5.0	35.3	20.7	21.9	4.6	4.9	4.7	1.4	yes	1.0	2.0	51
81	Spruce	FI-13	S12_hss_7	12	hss	14.4	489	479	4.7	35.3	19.7	21.1	4.1	4.1	4.1	1.8	yes	1.0	2.0	48
94	Spruce	FI-1	S24_vhss_1	24	vhss	12.4	458	456	35.5	28.5	36.9	37.4	9.7	9.6	9.7	1.9	yes	5.0	3.0	pitch
132	Spruce	FI-3	S24_vhss_2	24	vhss	12.5	462	460	38.6	28.8	40.2	40.8	6.6	5.4	5.9	1.1	no	5.0	3.0	pitch
133	Spruce	FI-4	S24_vhss_3	24	vhss	12.0	457	457	34.3	28.5	35.8	35.8	14.2	14.2	14.2	2.7	no	5.0	1.5/5	0
134	Spruce	FI-5	S24_vhss_4	24	vhss	12.2	452	451	33.4	28.2	34.8	35.0	6.5	5.6	6.0	2.7	no	5.0	2/3	0
135	Spruce	FI-7	S24_vhss_5	24	vhss	12.8	487	484	40.7	30.3	42.4	43.5	13.4	12.9	13.1	1.9	no	5.0	2/2	0
99	Spruce	FI-2	S24_hss_1	24	hss	12.4	467	465	25.8	29.1	26.8	27.2	7.4	7.5	7.4	1.8	yes	5.0	3.0	pitch
136	Spruce	FI-6	S24_hss_2	24	hss	12.3	449	448	29.5	28.0	30.7	31.0	6.8	7.0	6.9	2.1	no	5.0	2/3	0
137	Spruce	FI-8	S24_hss_3	24	hss	12.5	491	489	28.6	30.6	29.8	30.2	6.3	6.0	6.1	2.1	no	5.0	2/2	0
138	Spruce	FI-9	S24_hss_4	24	hss	12.5	503	501	27.5	31.3	28.6	29.0	5.9	5.9	5.9	2.1	yes	5.0	2/2	0
139	Spruce	FI-10	S24_hss_5	24	hss	11.6	437	439	23.9	27.2	24.9	24.6	3.7	4.0	3.9	1.4	no	5.0	5.0	0

**Table A-10: Four-point bending tests of original beams**

species	original beam	rho_beam [kg/m <sup>3</sup> ]	mc_beam	Edyn_wet	MoE_static global [MPa]	MoE_static local [MPa]	MoR [MPa]
A_wet	31	1289	42.5	21213.6	17416.1	23649.6	103.7
	44	1138	42.1	15262.2	11316.9	12870.1	64.5
	44	1138	42.1	15262.2	11316.9	12870.1	64.5
Cumaru_B	52	1165	14.7	22380.4	21188.9	27117.5	134.4
	94	1175	17.4	21954.4	19686.7	22601.5	138.1
Cumaru_P	2	1011	14.5	18335.7	15266.6	17116.7	64.2
	23	924	15.6	18937.5	13510.6		92.0
	32	962	16.1	20738.2	15209.6	13194.4	103.9
	39	975	15.8	18134.0	13804.1	18832.1	97.1
	46	968	14.7	18782.5	13234.2	15463.8	75.6
Azobé	9	1233	52.4	16816.2	11967.6	17778.9	59.6
	20	691	36.8	-	13783.0	15704.2	81.4
	22	1201	34.2	20078.8	15634.2	19903.6	96.3
	23	1226	35.8	21452.4	17044.3	18890.4	75.3
	41	1114	39.8	15635.9	12366.2	16029.2	80.0
Purpleheart	44	1138	42.1	15262.2	11316.9	12870.1	64.5
	12	976	16.1	21678.3	17243.4	22874.4	88.3
	28	951	17.1	21112.8	15809.5	19530.9	89.0
	32	683	17.1	16651.8	12144.2	14888.4	79.1
	33	954	17.4	20070.7	14575.5	17843.5	55.5
	36	853	17.9	20667.6	16296.4	19850.3	48.4
	41	687	17.4	17964.9	13301.1	16186.3	84.9

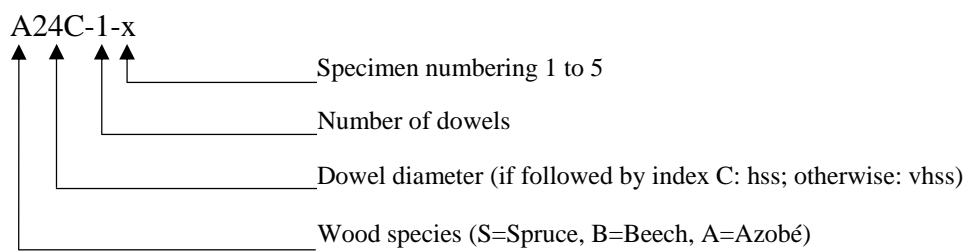
Legend:

- rho\_beam = density at test
- mc\_beam = moisture content at test
- Edyn\_wet = dynamic MoE at test
- MoEstatic\_global = global MoE of four-point-bending test
- MoEstatic\_local = local MoE of four-point-bending test
- MoR = MoR of test

# B

## JOINT TESTS

### B.1 NAMING



## B.2 DESCRIPTIVE STATISTICS AND MEASURED PARAMETERS

**Table B-1: Descriptive statistics for moisture content**

m.c. [%]		n	mean	stdev	COV [%]	max	min	5%	95%		
12mm dowel	spruce	1	vhss	5	12.1	0.2	1.6	12.3	11.8	11.7	12.5
			hss	5	11.9	0.3	2.4	12.4	11.7	11.4	12.5
		3	vhss	5	12.4	0.3	2.4	12.7	12.0	11.8	13.0
			hss	5	12.7	0.2	1.6	12.9	12.4	12.3	13.1
		5	vhss	5	12.6	0.2	1.5	12.8	12.3	12.2	13.0
			hss	5	12.5	0.2	1.9	12.8	12.1	12.0	12.9
	beech	1	vhss	5	8.7	0.3	3.1	8.4	9.1	8.1	9.2
			hss	5	8.6	0.3	3.4	8.2	8.9	8.0	9.2
		3	vhss	5	8.7	0.1	1.4	8.9	8.6	8.4	8.9
			hss	5	8.5	0.1	0.7	8.6	8.4	8.4	8.6
		5	vhss	5	8.5	0.1	1.0	8.5	8.3	8.3	8.6
			hss	5	8.8	1.1	12.6	10.8	8.2	6.6	11.0
Azobé	1	vhss	5	22.0	0.3	1.4	22.5	21.6	21.3	22.6	
		hss	5	21.4	0.3	1.4	21.8	21.1	20.8	22.0	
	3	vhss	5	22.9	0.7	3.1	23.6	22.1	21.4	24.3	
		hss	5	21.8	0.2	0.9	22.1	21.6	21.4	22.2	
	5	vhss	5	17.2	0.4	2.4	17.9	16.9	16.4	18.1	
		hss	5	21.7	0.2	0.8	21.8	21.5	21.3	22.0	
24mm dowel	spruce	1	vhss	5	12.0	0.2	1.8	12.2	11.7	11.5	12.4
			hss	5	12.2	0.2	1.9	12.7	12.1	11.8	12.7
		3	vhss	5	11.8	0.2	1.7	12.0	11.6	11.4	12.2
			hss	5	11.9	0.1	1.1	12.1	11.8	11.6	12.1
		5	vhss	4	12.5	0.3	2.3	12.9	12.3	11.9	13.1
			hss	5	12.4	0.2	1.7	12.7	21.1	12.0	12.8
	beech	1	vhss	5	8.5	0.2	2.0	8.7	8.2	8.1	8.8
			hss	5	8.7	0.7	8.0	10.0	8.1	7.3	10.1
		3	vhss	5	8.3	0.1	1.3	8.4	8.1	8.0	8.5
			hss	5	8.4	0.1	0.8	8.5	8.3	8.3	8.5
		5	vhss	5	9.4	0.4	4.5	9.8	9.0	8.5	10.2
			hss	5	9.8	0.3	2.9	10.1	9.4	9.3	10.4
Azobé	1	vhss	5	21.5	0.7	3.1	22.7	20.9	20.1	22.8	
		hss	5	21.5	1.3	5.9	23.6	19.8	18.9	24.0	
	3	vhss	5	21.3	1.4	6.6	23.0	19.3	18.5	24.1	
		hss	5	22.6	2.4	10.7	25.7	19.7	17.8	27.5	
	5	vhss	5	15.9	2.5	15.7	18.8	13.6	10.9	20.9	
		hss	5	22.5	1.5	6.9	24.4	20.5	19.4	25.6	

Table B-2: Descriptive statistics for density (at test)

		density [kg/m <sup>3</sup> ]	n	mean	stdev	COV [%]	max	min	5%	95%	
12mm dowel	spruce	1	vhss	5	457.4	26.6	5.8	494	422	403.8	511.1
			hss	5	455.8	16.5	3.6	481	441	422.5	489.1
		3	vhss	5	485.0	12.9	2.7	496	465	458.9	511.0
			hss	5	462.5	32.3	7.0	499	418	397.5	527.5
		5	vhss	5	477.9	9.2	1.9	492	469	459.4	496.3
			hss	5	459.8	25.8	5.6	492	430	407.9	511.7
	beech	1	vhss	5	722.2	17.8	2.5	737	700	686.5	758.0
			hss	5	719.9	11.5	1.6	734	709	696.7	743.0
		3	vhss	5	732.1	35.3	4.8	775	699	660.9	803.2
			hss	5	729.9	16.0	2.2	749	705	697.8	762.1
		5	vhss	5	702.6	16.1	2.3	731	691	670.2	735.0
			hss	5	718.0	22.0	3.1	753	694	673.5	762.4
azobé	1	vhss	5	1114.6	26.0	2.3	1144	1083	1062.2	1167.0	
		hss	5	1115.4	25.5	2.3	1144	1089	1063.9	1166.8	
	3	vhss	5	1131.0	45.1	4.0	1184	1063	1040.1	1221.9	
		hss	5	1117.1	16.2	1.4	1139	1102	1084.5	1149.7	
	5	vhss	5	1129.8	43.6	3.9	1200	1087	1041.9	1217.8	
		hss	5	1115.3	18.1	1.6	1139	1094	1078.8	1151.9	
24mm dowel	spruce	1	vhss	5	412.8	17.5	4.2	439	393	377.5	448.1
			hss	5	424.1	45.6	10.8	474	377	332.2	516.1
		3	vhss	5	409.6	14.4	3.5	422	385	380.6	438.5
			hss	5	418.4	15.4	3.7	442	400	387.3	449.5
		5	vhss	4	438.8	20.5	4.7	465	418	395.2	482.5
			hss	5	436.4	19.4	4.4	459	411	397.3	475.5
	beech	1	vhss	5	709.5	7.4	1.0	718	699	694.5	724.5
			hss	5	718.5	15.6	2.2	742	701	686.9	750.0
		3	vhss	5	723.9	6.3	0.9	733	718	711.2	736.6
			hss	5	710.5	12.0	1.7	729	695	686.3	734.8
		5	vhss	5	695.2	16.2	2.3	714	672	662.7	727.8
			hss	5	700.7	7.3	1.0	707	692	685.9	715.5
	azobé	1	vhss	5	1154.2	21.5	1.9	1186	1128	1110.9	1197.5
			hss	5	1122.5	34.3	3.1	1167	1087	1053.5	1191.5
		3	vhss	5	1115.7	21.7	1.9	1141	1088	1072.1	1159.4
			hss	5	1103.8	25.6	2.3	1129	1069	1052.2	1155.4
		5	vhss	5	1100.8	13.8	1.3	1123	1087	1073.1	1128.5
			hss	5	1118.1	27.1	2.4	1152	1081	1063.4	1172.7

**Table B-3: Descriptive statistics for load carrying capacity**

Fmax,test [kN]		n	mean	stdev	COV [%]	max	min	5%	95%	
12mm dowel	spruce	1	vhss 5	44.1	1.5	3.4	46.6	42.7	41.0	47.1
			hss 5	32.0	2.7	8.4	35.7	28.8	26.6	37.4
		3	vhss 5	115.5	7.2	6.3	124.0	107.4	100.9	130.0
			hss 5	89.6	8.4	9.4	101.1	77.7	72.7	106.6
		5	vhss 5	169.3	26.6	15.7	199.7	136.7	115.6	223.0
			hss 5	135.7	12.6	9.3	153.3	121.2	110.3	161.1
	beech	1	vhss 5	70.0	4.2	6.0	74.4	64.4	61.5	78.5
			hss 5	59.4	2.1	3.6	62.5	57.2	55.1	63.8
		3	vhss 5	173.4	8.4	4.9	182.8	163.5	156.4	190.5
			hss 5	157.3	7.2	4.6	167.6	148.9	142.8	171.7
		5	vhss 5	294.0	7.3	2.5	303.5	285.2	279.2	308.7
			hss 5	240.2	6.1	2.5	249.0	233.8	228.0	252.5
azobé	1	vhss 5	72.0	1.9	2.7	73.5	68.8	68.1	76.0	
		hss 5	57.3	3.7	6.5	60.9	51.4	49.8	64.9	
	3	vhss 5	182.6	14.4	7.9	193.8	158.1	153.6	211.6	
		hss 5	127.7	9.7	7.6	140.4	116.8	108.3	147.2	
	5	vhss 5	280.8	37.0	13.2	307.1	215.7	206.3	355.3	
		hss 5	233.0	32.8	14.1	278.3	203.5	167.0	299.0	
24mm dowel	spruce	1	vhss 5	165.1	6.9	4.2	172.0	155.6	151.2	179.0
			hss 5	110.0	13.4	12.2	126.9	92.7	83.0	137.1
		3	vhss 5	297.4	53.4	18.0	369.3	253.5	189.7	405.0
			hss 5	323.7	16.6	5.1	341.2	296.2	290.3	357.1
		5	vhss 4	570.1	53.8	9.4	624.0	496.0	455.3	684.9
			hss 5	482.1	44.8	9.3	522.8	429.0	391.8	572.5
	beech	1	vhss 5	299.8	7.3	2.4	305.9	291.3	285.2	314.4
			hss 5	208.0	7.4	3.6	218.2	199.1	193.0	222.9
		3	vhss 5	659.1	33.8	5.1	700.8	619.1	590.9	727.2
			hss 5	510.4	25.4	5.0	541.1	479.0	459.2	561.6
		5	vhss 5	927.0	32.4	3.5	949.4	871.4	861.6	992.3
			hss 5	822.6	43.9	5.3	882.4	769.0	734.2	911.1
	azobé	1	vhss 5	305.9	19.5	6.4	327.8	291.4	266.7	345.2
			hss 5	180.7	19.2	10.6	208.7	166.1	142.0	219.4
		3	vhss 5	706.1	39.0	5.5	753.2	654.5	627.5	784.8
			hss 5	538.7	39.0	7.2	596.0	491.1	460.1	617.2
		5	vhss 5	1128.0	180.0	16.0	1265.0	844.6	765.4	1490.7
			hss 5	867.5	95.3	11.0	978.6	737.3	675.5	1059.4

Table B-4: Descriptive statistics for stiffness Kser

Kser,test [kN/mm]		n	mean	stdev	COV [%]	max	min	5%	95%		
12mm dowel	spruce	1	vhss	5	20	6.4	32.6	29	13	7	32
			hss	5	21	7.4	34.5	32	12	7	36
		3	vhss	5	51	4.3	8.4	56	46	42	60
			hss	5	51	10.7	20.9	64	42	30	73
		5	vhss	5	68	4.4	6.5	72	62	59	77
			hss	5	52	6.3	12.3	61	44	39	64
	beech	1	vhss	5	49	22.8	44.2	86	29	3	95
			hss	5	36	14.2	40.6	49	19	7	64
		3	vhss	5	67	5.3	8.4	71	58	57	79
			hss	5	61	17.3	28.8	91	46	27	97
		5	vhss	5	129	13.7	13.3	150	105	99	154
			hss	5	110	4.7	4.2	114	102	101	119
azobé	1	vhss	5	53	6.4	12.4	62	44	40	66	
		hss	5	45	13.6	29.5	64	27	18	73	
	3	vhss	5	64	6.0	11.2	73	54	52	76	
		hss	5	39	2.8	6.7	41	35	36	47	
	5	vhss	5	158	10.9	22.1	217	124	119	163	
		hss	5	132	7.2	6.0	143	124	117	145	
24mm dowel	spruce	1	vhss	5	118	16.3	13.8	133	93	85	151
			hss	5	126	34.6	27.5	176	81	56	195
		3	vhss	5	122	8.1	6.6	135	113	106	138
			hss	5	127	28.3	22.3	163	105	70	184
		5	vhss	4	247	108.7	44.0	410	187	15	479
			hss	5	137	8.4	6.1	149	126	121	154
	beech	1	vhss	5	157	8.5	7.7	170	143	141	176
			hss	5	114	24.7	20.4	134	75	67	166
		3	vhss	5	205	7.2	2.9	213	198	189	218
			hss	5	202	35.4	17.2	241	160	126	268
		5	vhss	5	192	12.1	6.3	209	178	169	218
			hss	5	171	12.5	7.2	191	156	145	195
azobé	1	vhss	5	201	31.7	17.5	249	164	135	263	
		hss	5	103	15.4	15.1	115	77	71	133	
	3	vhss	5	246	33.5	13.8	275	197	180	314	
		hss	5	186	62.2	33.3	249	96	61	311	
	5	vhss	5	374	152.8	40.9	610	231	67	682	
		hss	5	321	53.7	16.8	385	241	209	425	

Note: 5% and 95% fractiles calculated with Student's t-distribution as only few specimens were available.

**Table B-5: Effective numbers for specimens with 12 mm dowels ( $a_1 = 60$  mm)**

species	grade	number of dowels	$F_{max}$ [kN]	$n_{ef}$ tests	$n_{ef}$ EC5	$n_{ef}(\text{tests})/ n_{ef}(\text{EC5})$	$n_{ef}(\text{hss})/ n_{ef}(\text{vhss})$
spruce	hss	1	32	-	-	-	
		3	90	2.80	2.12	1.32	
		5	136	4.24	3.35	1.27	
	vhss	1	44	-	-	-	
		3	115	2.62	2.12	1.24	1.07
		5	169	3.84	3.35	1.15	1.10
beech	hss	1	59	-	-	-	
		3	157	2.65	2.12	1.25	
		5	240	4.04	3.35	1.21	
	vhss	1	70	-	-	-	
		3	173	2.48	2.12	1.17	1.07
		5	294	4.20	3.35	1.25	0.96
azobé	hss	1	57	-	-	-	
		3	128	2.23	2.12	1.05	
		5	233	4.06	3.35	1.21	
	vhss	1	72	-	-	-	
		3	183	2.53	2.12	1.20	0.88
		5	281	3.90	3.35	1.16	1.04

**Table B-6: Effective numbers for specimens with 24 mm dowels ( $a_1 = 120$  mm)**

species	grade	number of dowels	$F_{max}$ [kN]	$n_{ef}$ tests	$n_{ef}$ EC5	$n_{ef}(\text{tests})/ n_{ef}(\text{EC5})$	$n_{ef}(\text{hss})/ n_{ef}(\text{vhss})$
spruce	hss	1	110	-	-	-	
		3	324	2.94	2.12	1.39	
		5	482	4.38	3.35	1.31	
	vhss	1	165	-	-	-	
		3	297	1.80	2.12	0.85	1.63
		5	570	3.45	3.35	1.03	1.27
beech	hss	1	208	-	-	-	
		3	510	2.45	2.12	1.16	
		5	823	3.96	3.35	1.18	
	vhss	1	300	-	-	-	
		3	659	2.20	2.12	1.04	1.12
		5	927	3.09	3.35	0.92	1.28
azobé	hss	1	181	-	-	-	
		3	539	2.98	2.12	1.41	
		5	867	4.80	3.35	1.43	
	vhss	1	306	-	-	-	
		3	706	2.31	2.12	1.09	1.29
		5	1128	3.69	3.35	1.10	1.30

**Table B-7: Predicted failure modes using test properties (density adjusted to 12% m.c.) and from tests, deformation angles**

	number of dowels	grade	FM <sub>test</sub>	FM <sub>pred</sub>	mean deformation angles	remarks on test results	
12mm dowel	spruce	1	vhss	2	2	11	FM2
			hss	2/3	3	9	FM2 with FM3 on one side
		3	vhss	1/2	2	3	test 5 in FM1
			hss	2/3	3	4	test 4 in FM3
		5	vhss	1/2	2	1	test 1+3 in FM1
	hss		2	3	3	FM2	
	beech	1	vhss	2	2	16	FM2
			hss	3	3	17	all in FM3
		3	vhss	2	2	5	FM2
			hss	3	3	4	all in FM3
		5	vhss	2	2	3	FM2
	hss		2/3	3	2	all slightly in FM3	
	azobé	1	vhss	2	2	8	FM2
			hss	3	3	12	all in FM3
		3	vhss	2	2	5	FM2
hss			2/3	3	5	test 1 in FM3, rest FM2	
5		vhss	1/2	2	1	test 1 in FM1, rest FM2	
	hss	2/3	3	5	test 2+5 in FM2, rest FM3		
24mm dowel	spruce	1	vhss	1/2	2	4	test 5 in FM1, rest in FM2
			hss	2	2/3	4	FM2
		3	vhss	1	2	-	FM1
			hss	2	2/3	1	FM2
		5	vhss	1	2	-	FM1
	hss		2	2/3	1	FM2	
	beech	1	vhss	2	2	9	FM2
			hss	3	3	19	FM3
		3	vhss	2	2	1	FM2
			hss	2/3	2	4	test 2+3 in FM3, rest in FM2
		5	vhss	1/2	2	1	test 2+4 in FM2, rest in FM1
	hss		2/3	2	4	test 1+2 slightly in FM3, rest in FM2	
	azobé	1	vhss	2	2	2	FM2
			hss	3	3	16	all in FM3
		3	vhss	1/2	2	1	test 1 in FM1
hss			2/3	3	3	test 1+2 in FM2, rest FM3	
5		vhss	1/2	2	1	test 2+5 in FM2, rest FM1	
	hss	2/3	3	3	test 1+5 in FM3, rest FM2		

**Table B-8: Measured and predicted values load carrying capacities, all adjusted to 12% m.c. and prediction with measured  $n_{ef}$  (see Tables B-5 and B-6)**

	n° of dowels	grade	density at 12% m.c.		$F_{test,12\%}$ [kN]		$F_{pred,12\%}$ (no $n_{ef}$ )	$F_{pred,12\%}$ (with $n_{ef}$ from tests)	$F_{pred}(\text{with } n_{ef})$ / $F_{test}$	pred. FM
			mean	COV [%]	mean					
12mm dowels	spruce	1	vhss	457	5.8	44	45	45	1.03	2
			hss	456	3.5	32	35	35	1.08	2/3
		3	vhss	483	2.4	117	141	123	1.05	1/2
			hss	460	6.8	91	104	97	1.07	2/3
		5	vhss	475	1.8	172	232	178	1.04	1/2
			hss	458	5.4	138	174	147	1.07	2
	beech	1	vhss	744	2.4	63	58	58	0.92	2
			hss	742	1.6	53	50	50	0.93	3
		3	vhss	754	4.8	156	177	146	0.93	2
			hss	754	2.2	141	153	135	0.96	3
		5	vhss	726	2.2	263	287	241	0.92	2
			hss	739	3.8	217	253	204	0.94	2/3
	azobé	1	vhss	1024	2.2	85	70	70	0.83	2
			hss	1029	2.1	68	49	49	0.72	3
		3	vhss	1031	3.5	215	212	179	0.83	2
hss			1027	1.5	151	146	108	0.72	2/3	
5		vhss	1080	4.1	324	366	285	0.88	1/2	
		hss	1027	1.6	275	243	197	0.72	2/3	
24mm dowels	spruce	1	vhss	413	4.1	165	149	149	0.91	1/2
			hss	423	10.6	111	119	119	1.08	2
		3	vhss	410	3.4	295	446	268	0.91	1
			hss	419	3.7	323	358	351	1.09	2
		5	vhss	437	4.8	579	776	536	0.93	1
			hss	435	4.4	488	608	533	1.09	2
	beech	1	vhss	733	1.1	183	212	212	1.16	2
			hss	741	2.3	119	158	158	1.33	3
		3	vhss	749	0.9	562	667	489	0.87	2
			hss	734	1.7	550	473	387	0.70	2/3
		5	vhss	712	2.3	904	1034	640	0.71	1/2
			hss	715	1.1	909	774	613	0.67	2/3
	azobé	1	vhss	1064	1.6	234	256	256	1.10	2
			hss	1035	2.4	150	190	190	1.27	3
		3	vhss	1030	0.7	690	750	577	0.84	1/2
hss			1008	3.5	444	557	553	1.25	2/3	
5		vhss	1064	2.9	1142	1279	943	0.83	1/2	
		hss	1022	2.0	745	933	896	1.20	2/3	
								mean	0.96	
								COV	17.7	

**Table B-9:  $K_{ser,test}$  and  $K_{pred}$  prediction adjusted to 12% m.c.**

	n° dowels	grade	$K_{pred,12\%}$	$K_{ser}$ [kN/mm]		$K_{ser}/$ dowel	$K_{pred}/$ $K_{ser}$	density at 12% m.c. [kg/m <sup>3</sup> ]	m.c. [%]	$F_{test}$ [kN]	$F_{test}/$ dowel	
				COV								
12mm dowels	spruce	1	20	20	32.6	20	1.02	457	12.1	44	44	
		hss	20	21	34.5	21	0.95	456	11.9	32	32	
		3	vhss	65	51	8.4	17	1.28	483	12.4	115	38
			hss	62	51	20.9	17	1.20	460	12.7	90	30
		5	vhss	106	68	6.5	14	1.57	475	12.6	169	34
			hss	102	52	12.3	10	1.98	458	12.5	136	27
	beech	1	vhss	42	49	44.2	49	0.85	744	8.7	70	70
		hss	42	36	40.6	36	1.18	742	8.6	59	59	
		3	vhss	128	67	8.4	22	1.92	754	8.7	173	58
			hss	128	61	28.8	20	2.10	754	8.5	157	52
		5	vhss	202	129	13.3	26	1.57	726	8.5	294	59
			hss	208	110	4.2	22	1.89	739	8.8	240	48
	azobé	1	vhss	68	53	12.4	53	1.28	1024	22.0	72	72
		hss	69	45	29.5	45	1.52	1029	21.4	57	57	
		3	vhss	205	64	11.2	21	3.23	1031	22.9	183	61
			hss	206	39	6.7	13	5.22	1027	21.8	128	43
		5	vhss	366	158	22.1	32	2.32	1080	17.2	281	56
			hss	343	132	6.0	26	2.60	1027	21.7	233	47
24mm dowels	spruce	1	vhss	35	118	13.8	118	0.30	413	12.0	165	165
		hss	36	126	27.5	126	0.29	423	12.2	110	110	
		3	vhss	104	122	6.6	41	0.85	410	11.8	297	99
			hss	107	127	22.3	42	0.85	419	11.9	324	108
		5	vhss	191	247	44.0	49	0.77	437	12.5	570	114
			hss	189	137	6.1	27	1.38	435	12.4	482	96
	beech	1	vhss	83	157	7.7	157	0.53	733	8.5	300	300
		hss	84	114	20.4	114	0.74	741	8.7	208	208	
		3	vhss	262	205	2.9	68	1.28	749	8.3	659	220
			hss	248	202	17.2	67	1.23	734	8.4	510	170
		5	vhss	395	192	6.3	38	2.06	712	9.4	927	185
			hss	397	171	7.2	34	2.32	715	9.8	823	165
	azobé	1	vhss	145	201	17.5	201	0.72	1064	21.5	306	306
		hss	140	103	15.1	103	1.36	1035	21.5	181	181	
		3	vhss	414	246	13.8	82	1.68	1030	21.3	706	235
			hss	401	186	33.3	62	2.16	1008	22.6	539	180
		5	vhss	723	374	40.9	75	1.93	1064	15.9	1128	226
			hss	682	321	16.8	64	2.12	1022	22.5	867	173

### B.3 LOAD-SLIP GRAPHS

#### AZOBE

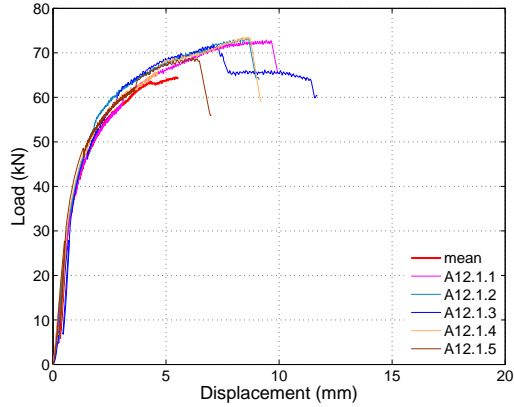


Figure B-1: Azobé, one 12 mm vhss dowel

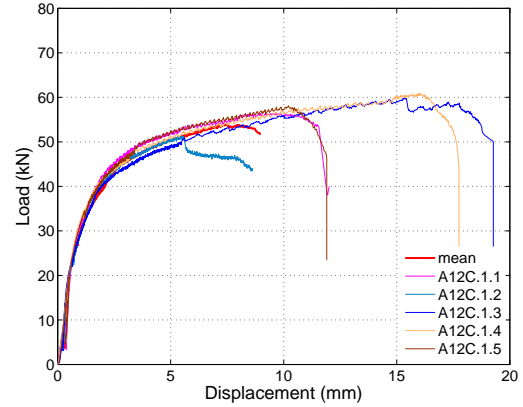


Figure B-4: Azobé, one 12 mm hss dowel

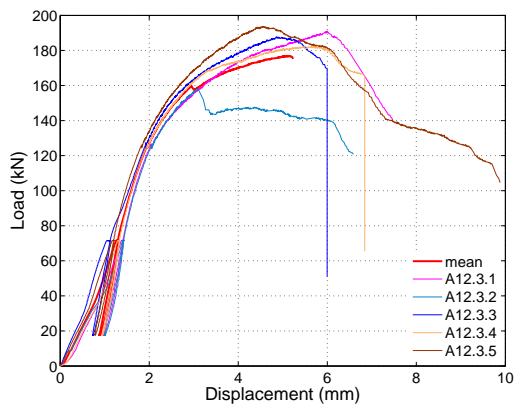


Figure B-2: Azobé, three 12 mm vhss dowels

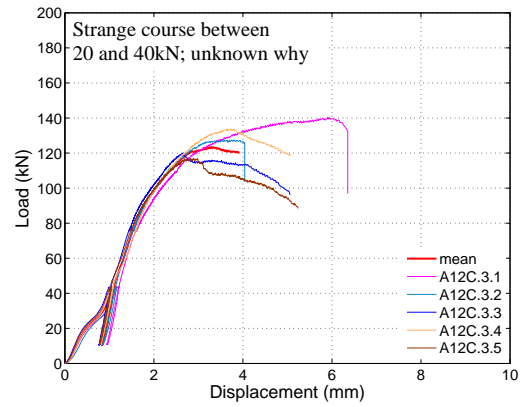


Figure B-5: Azobé, three 12 mm hss dowels

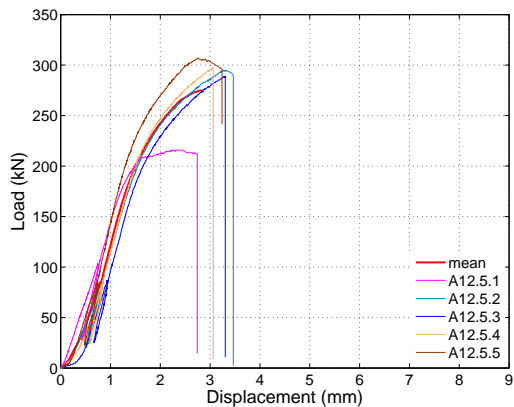


Figure B-3: Azobé, five 12 mm vhss dowels

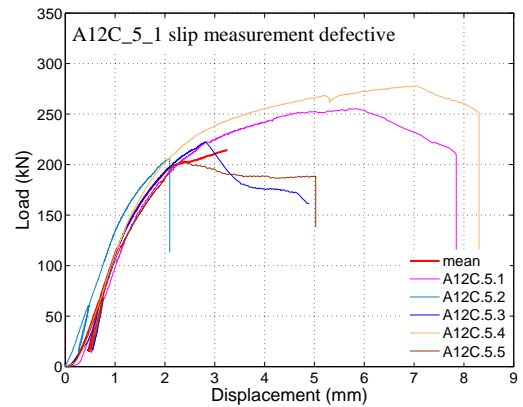


Figure B-6: Azobé, five 12 mm hss dowels

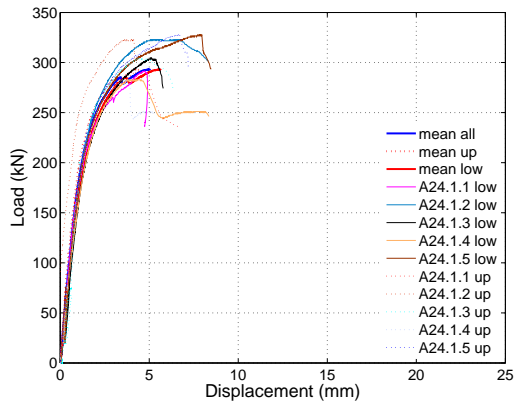


Figure B-7: Azobé, one 24 mm vhss dowel

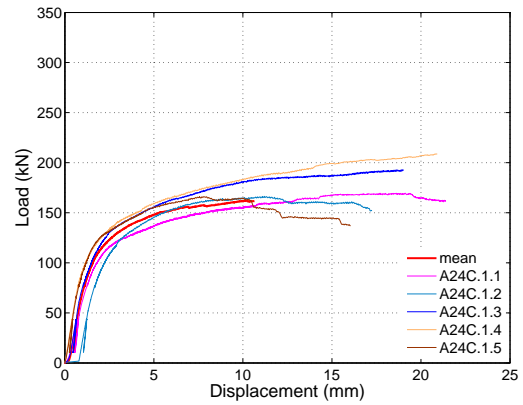


Figure B-10: Azobé, one 24 mm hss dowel

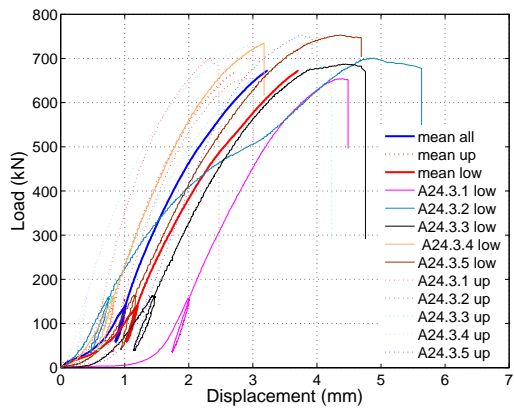


Figure B-8: Azobé, three 24 mm vhss dowels

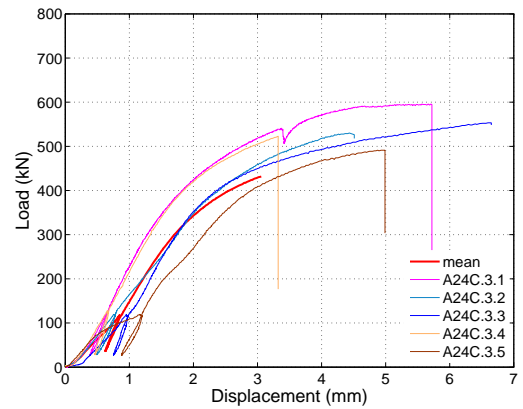


Figure B-11: Azobé, three 24 mm hss dowels

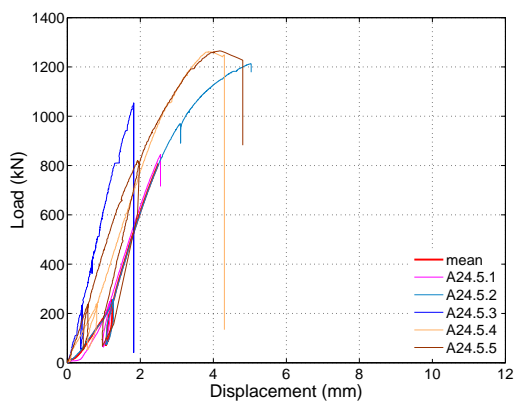


Figure B-9: Azobé, five 24 mm vhss dowels

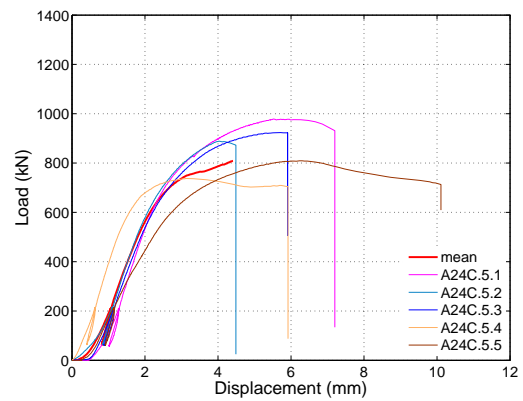
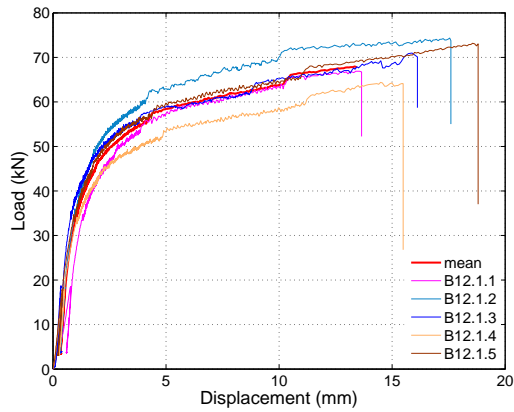
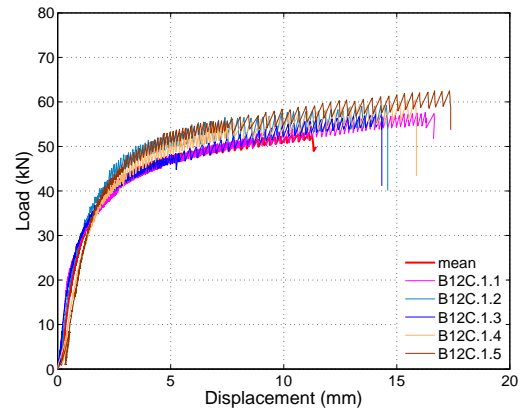


Figure B-12: Azobé, five 24 mm hss dowels

**BEECH**



**Figure B-13: Beech, one 12 mm vhss dowel**



**Figure B-16: Beech, one 12 mm hss dowel**

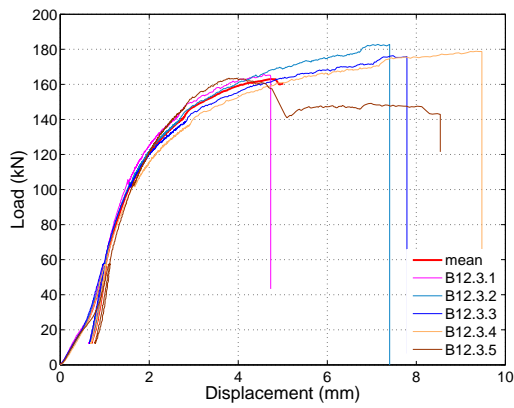


**Figure B-14: Beech, three 12 mm vhss dowels**

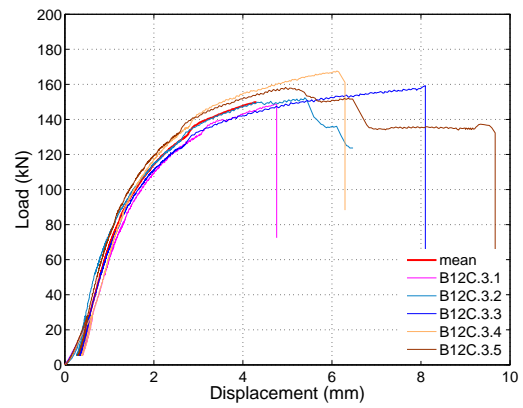


**Figure B-17: Beech, three 12 mm hss dowels**

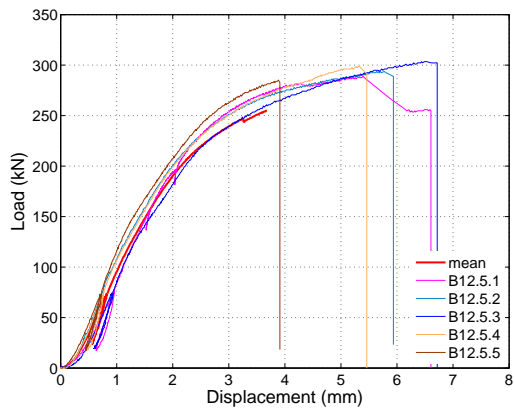


**Figure B-15: Beech, five 12 mm vhss dowels**

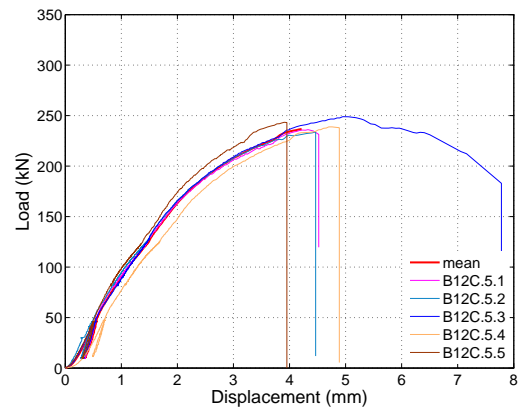


**Figure B-18: Beech, five 12 mm hss dowels**

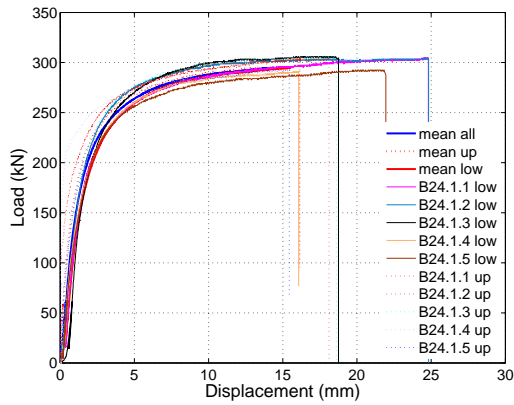


Figure B-19: Beech, one 24 mm vhs dowel

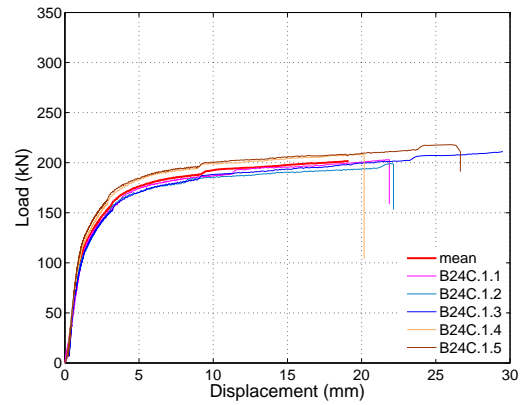


Figure B-22: Beech, one 24 mm hss dowel

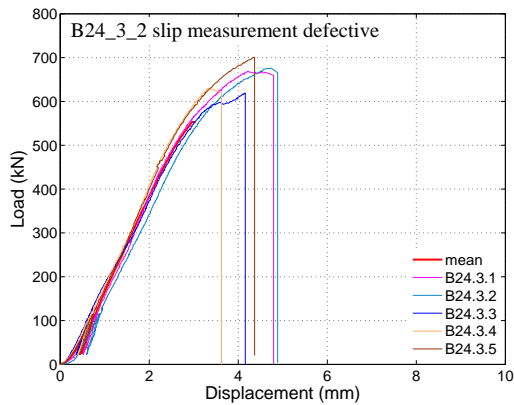


Figure B-20: Beech, three 24 mm vhs dowels

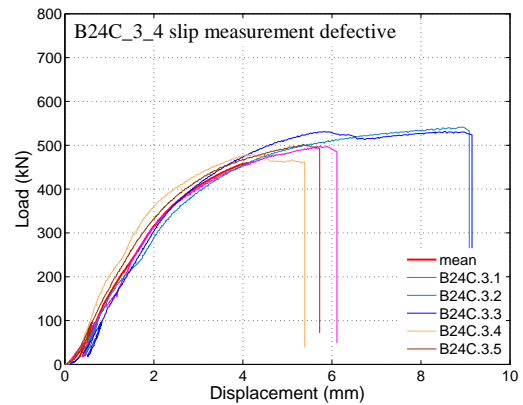


Figure B-23: Beech, three 24 mm hss dowels

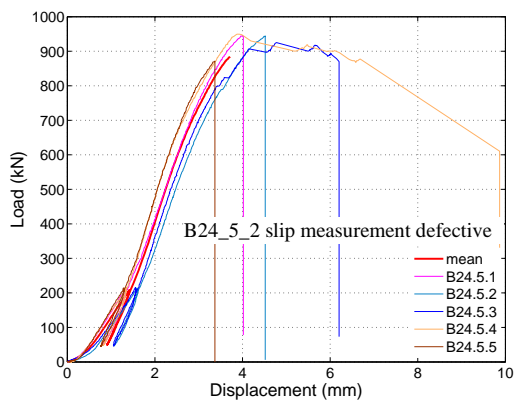


Figure B-21: Beech, five 24 mm vhs dowels

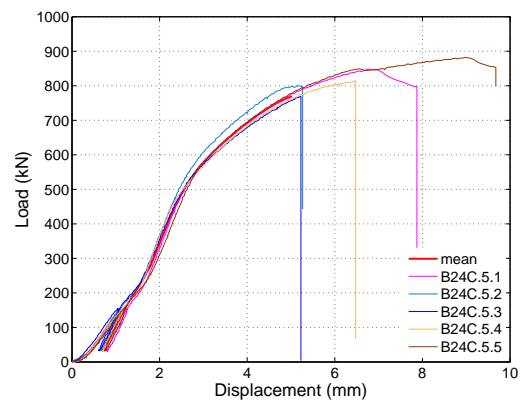
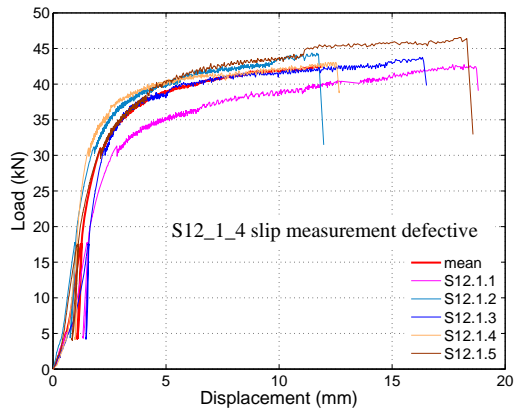
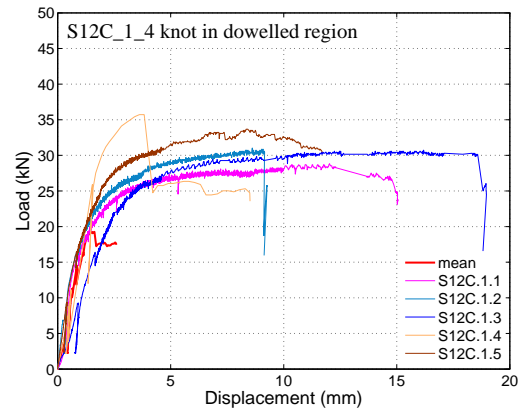


Figure B-24: Beech, five 24 mm hss dowels

**SPRUCE**



**Figure B-25: Spruce, one 12 mm vhs dowel**



**Figure B-28: Spruce, one 12 mm hss dowel**

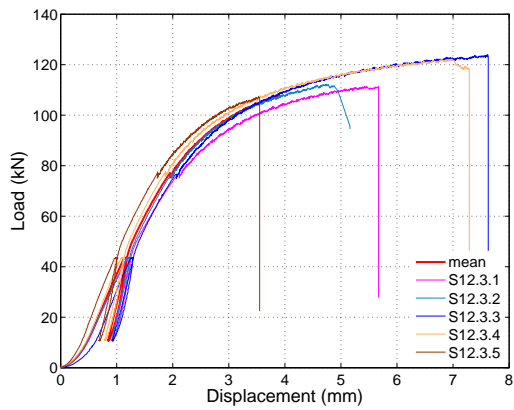


**Figure B-26: Spruce, three 12 mm vhs dowels**

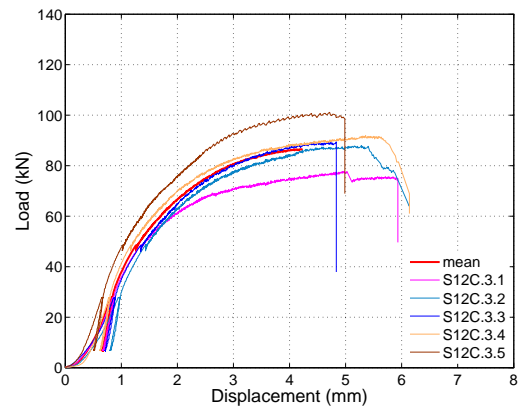


**Figure B-29: Spruce, three 12 mm hss dowels**

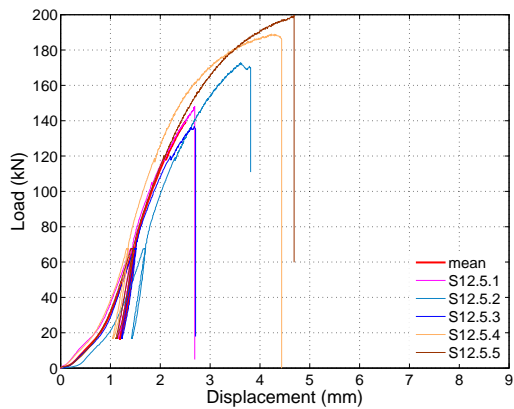


**Figure B-27: Spruce, five 12 mm vhs dowels**

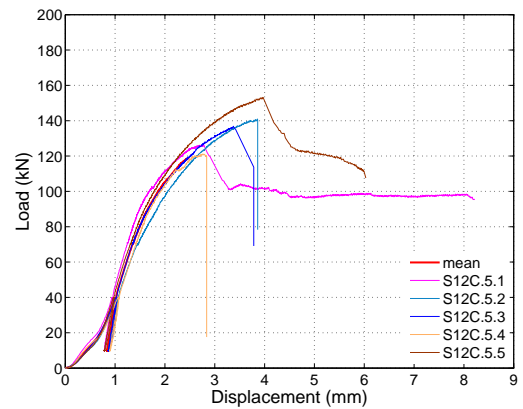


**Figure B-30: Spruce, five 12 mm hss dowels**

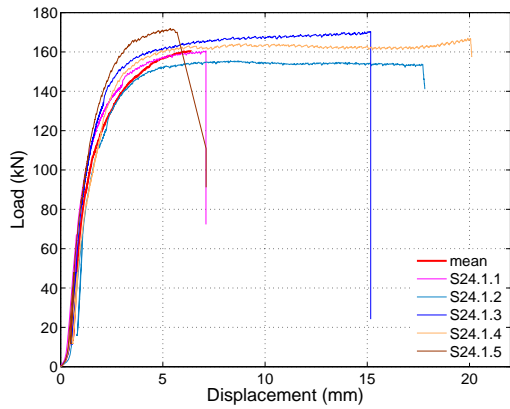


Figure B-31: Spruce, one 24 mm v-hss dowel

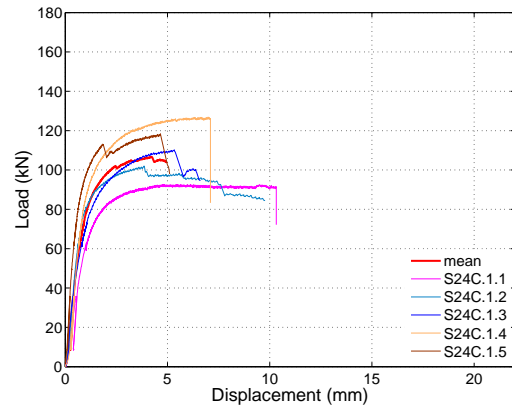


Figure B-34: Spruce, one 24 mm hss dowel

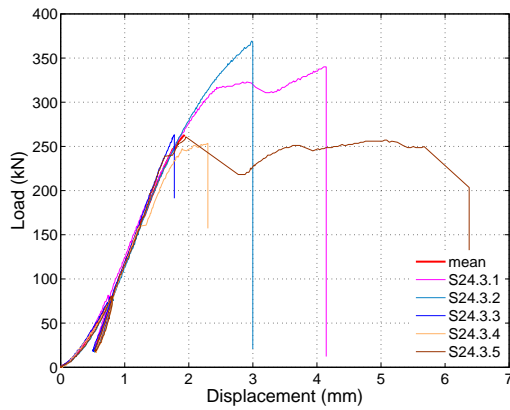


Figure B-32: Spruce, three 24 mm v-hss dowels

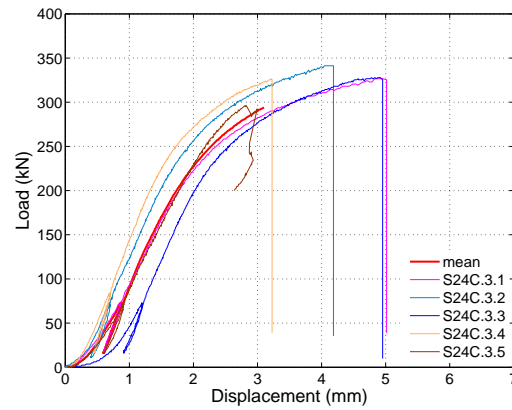


Figure B-35: Spruce, three 24 mm hss dowels

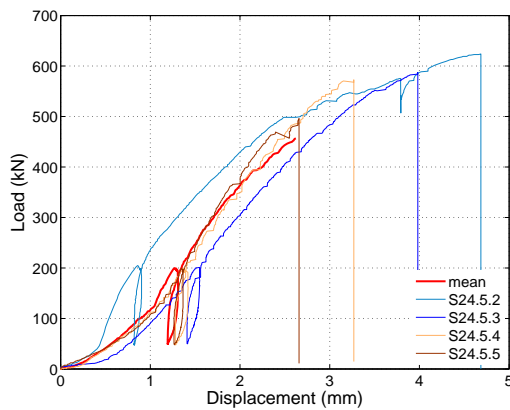


Figure B-33: Spruce, five 24 mm v-hss dowels

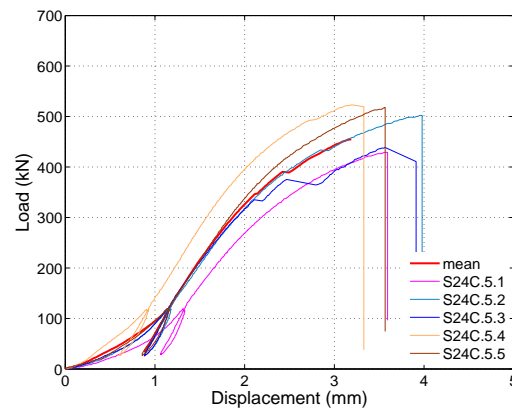


Figure B-36: Spruce, five 24 mm hss dowels

## B.4 SINGLE TESTS

### Legend:

- Test = nomination of specimens according to section B.1, red nominations indicate measuring problems
- Diameter dowel = measured diameter, mean value
- Density = density at test
- m.c. = moisture content at test
- Density at 12 % m.c. = measured density adjusted to 12% moisture content
- T = mean thickness of timber members
- $D_{LVDT}$  = measuring distance of LVDTs (see Figure 7-5). For double tests with identical upper and lower joint, the upper LVDTs were always fastened 5mm under top edge of timber members. Unfortunately, the fastening on the steel plates changed, but it can be assumed that no elongation occurred in the steel plate
- $F_{test}$  = measured maximum force = load carrying capacity
- $F_{test,12\%}$  = measured maximum force adjusted to 12% m.c.
- $v(F_{test})$  = displacement at maximum force
- FM = failure mode of tested specimens according to Johansen (N.B. not always symmetric):  
1 = no plastic hinge; 2 = one plastic hinge per shear plane; 3 = two plastic hinges per shear plane
- Angle dowel FM2 = measured angle of deformation in failure mode 2, mean value
- Wood at final deformation piece 1/piece 2 = indicates how piece 1/piece 2 of specimen have failed ('brittle' covers all brittle failures such as splitting or row shear out – often, brittle cases showed both failure modes and could not be assigned clearly to one FM):  
emb = embedment failure; brittle incl. = inclined brittle behaviour indicating grain deviation; tension = tension rupture; (knot) = failure at location of knot; support = support and not tested joint splitted which means tested joint showed only embedment
- $F_{pred}$  = prediction according to section 7.4.6 with measured values, **with  $n_{ef} = n!$**
- $F_{pred,12\%}$  = prediction according to section 7.4.6 with measured values and adjusted to 12% m.c., **with  $n_{ef} = n!$**
- $K_{ser,pred}$  = prediction of stiffness per joint, with measured values
- $K_{ser,pred,12\%}$  = prediction of stiffness per joint, with measured values and adjusted to 12% m.c.
- $K_{ser,test}$  = stiffness at test per joint

Only azobé with 12 mm dowels (piece 1/piece 2):

- Orig. beam = number of the strength-graded beams (only tropical hardwood) from which the test specimens were sawn (properties see Table B-16)

**Table B-10: Azobé with 12 mm dowels, single test results**

test	dia. dowel	density [kg/m <sup>3</sup> ]	m.c. [%]	density at 12% m.c. [kg/m <sup>3</sup> ]	t [mm]	D <sub>LVD</sub> [mm]	F <sub>test</sub> [kN]	F <sub>test,12%</sub> [kN]	v(F <sub>test</sub> ) [mm]	FM	angle dowel	wood at final deformation 1/piece 2	F <sub>pred</sub> [kN]	F <sub>pred,12</sub> % [kN]	K <sub>Ser,pred</sub> [kN/mm]	K <sub>Ser,pred,12</sub> % [kN/mm]	K <sub>Ser,test</sub> [kN/mm]	orig. beam
A12_1_1	11.87	1083	21.8	995	64	108	72.9	86.0	9.44	2	9	brittle incl./emb	73.6	68.9	74	65	44	45
A12_1_2	11.88	1093	21.6	1006	64	108	73.3	86.5	8.63	2	8	brittle incl./brittle incl.	74.2	69.5	75	66	54	45
A12_1_3	11.90	1123	22.5	1027	64	108	71.7	84.6	7.12	2	10	brittle incl./brittle	76.0	70.8	78	68	50	47
A12_1_4	11.85	1131	21.9	1039	64	108	73.5	86.7	8.41	2	9	emb/brittle incl.	76.0	71.0	78	69	54	47
A12_1_5	11.88	1144	22.0	1050	64	108	68.8	81.2	6.01	2	6	brittle incl./emb	77.0	71.9	80	70	62	47
A12_3_1	11.91	1063	22.1	975	63	108	191.2	225.6	5.99	2	5	emb/brittle	216.5	202.4	215	189	60	67
A12_3_2	11.90	1123	22.2	1029	63	108	158.1	186.5	3.10	2	4	brittle incl./brittle incl.	225.8	210.7	233	205	54	45
A12_3_3	11.89	1129	22.8	1029	64	108	187.8	221.6	4.86	2	4	brittle/brittle	226.5	210.6	235	205	73	67
A12_3_4	11.88	1156	23.5	1048	64	108	182.2	215.0	5.65	2	5	brittle incl./brittle incl.	232.9	215.4	244	210	65	66
A12_3_5	11.90	1184	23.6	1073	65	108	193.8	228.7	4.56	2	7	brittle incl./brittle incl.	237.9	219.8	253	218	66	66
A12_5_1	11.81	1087	17.9	1033	64	73	215.7	254.1	2.21	1	-	brittle/emb	370.3	355.4	368	341	145	50
A12_5_2	11.80	1099	17.2	1050	63	73	294.9	341.2	3.26	2	0.5	brittle/tension	367.9	354.8	374	349	124	62/61
A12_5_3	11.86	1130	16.9	1082	64	73	288.8	331.3	3.28	2	0.5	brittle/brittle	376.5	363.9	392	367	151	46
A12_5_4	11.84	1133	16.9	1085	64	73	297.4	341.5	3.04	2	0.5	brittle/brittle	380.5	367.6	393	368	217	47
A12_5_5	11.90	1200	17.1	1148	65	73	307.1	353.9	2.76	2	3	emb/brittle	400.9	386.8	430	402	151	34
A12C_1_1	12.01	1089	21.1	1008	66	108	56.5	66.7	8.51	3	11	brittle incl./brittle incl.	50.1	48.2	75	67	27	50
A12C_1_2	11.99	1096	21.1	1013	64	108	51.4	60.6	5.32	3	7	brittle incl./brittle incl.	50.1	48.2	76	67	42	64
A12C_1_3	12.00	1107	21.5	1020	64	108	59.9	70.6	15.38	3	17	emb/brittle incl.	50.4	48.4	77	68	64	48/61
A12C_1_4	12.00	1144	21.5	1054	64	108	60.9	71.9	15.96	3	14	emb/brittle incl.	51.3	49.2	81	71	46	48
A12C_1_5	12.00	1141	21.8	1049	63	108	58.1	68.6	10.22	3	10	emb/emb	51.2	49.1	80	71	48	48
A12C_3_1	12.00	1102	21.9	1013	64	108	140.4	165.6	5.91	3	5	emb/brittle	150.9	144.7	229	202	35	61
A12C_3_2	12.00	1104	21.6	1017	65	108	127.5	150.4	3.54	2	4	brittle incl./brittle incl.	151.2	145.1	230	203	40	52
A12C_3_3	12.00	1111	22.1	1019	64	108	120.2	141.8	2.66	2	4	brittle/brittle	151.7	145.3	232	204	41	59
A12C_3_4	11.99	1128	21.6	1039	64	108	133.8	157.9	3.73	2	4	brittle incl./brittle incl.	152.6	146.4	237	210	41	52
A12C_3_5	12.00	1139	21.7	1048	63	108	116.8	137.8	2.69	2	5	brittle incl./brittle incl.	153.5	147.2	241	212	41	59
A12C_5_1	12.00	1094	21.5	1009	64	108	255.4	301.4	5.84	3	5	brittle (knot)/brittle incl.	250.8	240.8	378	334	130	60
A12C_5_2	11.99	1105	21.8	1016	65	108	205.7	242.7	2.09	2	2	brittle incl./emb	251.8	241.4	383	338	143	64/50
A12C_5_3	12.01	1110	21.5	1023	64	108	222.0	262.0	2.79	3	4	emb/brittle	252.8	242.7	386	342	126	45
A12C_5_4	12.00	1128	21.8	1037	64	108	278.2	328.3	7.04	3	7	brittle/brittle	254.6	244.1	396	349	138	53
A12C_5_5	12.00	1139	21.7	1048	64	108	203.5	240.1	2.37	2	6	brittle incl./brittle incl.	256.0	245.5	401	354	124	49

**Table B-11: Azobé with 24 mm dowels, single test results; series A24\_1 and A24\_3 double tests**

test	dia. dowel	density [kg/m <sup>3</sup> ]	m.c. [%]	density at 12% m.c. [kg/m <sup>3</sup> ]	t [mm]	D <sub>1,0/20</sub> [mm]	F <sub>test</sub> [kN]	F <sub>test,12%</sub> [kN]	√(F <sub>test</sub> ) [mm]	FM	angle dowel	wood at final deformation 1/piece 2	F <sub>pred</sub> [kN]	F <sub>pred,12%</sub> [kN]	K <sub>ser, pred</sub> [kN/mm]	K <sub>ser, pred, 12%</sub> [kN/mm]	K <sub>ser, test</sub> [kN/mm]
A24_1_1	23.95	1186	22.7	1082	120	73	291.4	343.9	4.71	2	3	emb/emb	277.9	259.2	170	148	226
A24_1_2	23.99	1161	21.0	1074	120	73	323.0	381.1	5.06	2	2	emb/emb	274.0	258.4	165	147	179
A24_1_3	24.03	1144	21.2	1057	120	73	304.7	359.5	5.06	2	2	emb/emb	271.5	255.7	162	144	164
A24_1_4	23.97	1128	21.5	1039	120	73	282.7	333.6	3.74	2	2	emb/emb	267.7	251.8	158	140	189
A24_1_5	23.99	1153	20.9	1068	120	73	327.8	386.8	7.73	2	0.5	emb/emb	272.6	257.3	163	146	249
A24_3_1	23.99	1112	21.6	1025	120	123	654.5	772.3	4.36	1	-	brittle/brittle	795.8	748.2	464	411	261
A24_3_2	23.96	1088	19.3	1021	120	123	700.8	826.9	4.84	2	0.5	brittle/emb	779.1	743.1	448	408	275
A24_3_3	23.98	1105	20.1	1030	120	123	687.4	811.1	4.41	2	0.5	brittle/brittle support	791.1	750.4	459	413	197
A24_3_4	23.96	1141	23.0	1039	120	123	734.9	867.2	3.17	2	0.5	emb/emb	809.1	754.0	482	419	272
A24_3_5	23.99	1133	22.5	1036	120	123	753.2	888.7	4.37	2	1	emb/emb	807.0	754.3	477	417	225
A24_5_1	23.98	1096	18.8	1033	120	123	844.6	996.6	2.55	1	-	emb/emb (unfinished)	1311.0	1254.6	757	693	318
A24_5_2	23.97	1095	18.4	1036	120	123	1213.8	1432.3	5.02	2	0.5	emb/emb (unfinished)	1310.6	1257.2	755	695	231
A24_5_3	23.91	1123	13.6	1107	120	23	1055.4	1107.6	1.82	1	-	brittle/emb	1330.3	1315.6	783	766	610
A24_5_4	23.91	1087	14.5	1063	120	23	1261.4	1355.3	3.86	1	-	brittle/emb	1297.1	1275.8	745	721	274
A24_5_5	23.90	1103	14.1	1083	120	23	1265.0	1344.4	4.16	2	0.5	brittle/brittle	1311.3	1293.0	761	741	437
A24C_1_1	24.08	1103	20.8	1023	119	73	169.5	200.0	17.70	3	20	emb/emb	195.3	188.1	153	137	77
A24C_1_2	24.11	1106	19.8	1034	120	73	166.4	196.4	11.22	3	10	emb/emb	196.1	189.6	154	139	100
A24C_1_3	24.18	1150	21.5	1059	120	73	192.9	227.6	18.96	3	18	emb/emb	200.9	192.9	164	145	108
A24C_1_4	24.20	1167	23.6	1058	120	73	208.7	246.3	20.79	3	20	emb/emb	202.8	193.1	168	145	115
A24C_1_5	24.02	1087	21.7	1000	120	73	166.1	196.0	7.57	3	10	emb/emb	193.0	185.2	150	132	112
A24C_3_1	24.00	1109	20.4	1032	120	123	596.0	703.2	5.57	2	1	brittle/emb	583.9	563.1	463	415	249
A24C_3_2	24.00	1087	25.7	968	120	123	530.1	625.6	4.43	2	3	emb/brittle	577.8	545.3	449	377	184
A24C_3_3	23.99	1129	25.1	1011	120	123	553.3	652.9	6.60	3	4	emb/emb	588.9	557.1	475	402	163
A24C_3_4	23.99	1125	19.7	1052	120	123	522.8	616.9	3.32	3	0.5	emb/brittle	587.6	568.4	472	427	238
A24C_3_5	24.00	1069	22.2	979	120	123	491.1	579.6	4.88	3	4	brittle/emb	573.2	548.6	438	384	96
A24C_5_1	23.98	1134	24.0	1024	120	123	978.6	1154.8	5.52	3	2	brittle/tension	982.3	933.5	796	683	306
A24C_5_2	23.93	1119	21.1	1035	120	123	888.4	1048.4	4.02	2	2	brittle/brittle	971.9	934.8	778	693	241
A24C_5_3	23.92	1081	22.7	986	120	123	923.8	1090.1	5.65	2	5	brittle/emb	954.6	912.1	739	644	352
A24C_5_4	23.97	1106	20.5	1028	120	123	737.3	870.0	3.11	2	3	brittle/brittle	969.3	934.6	766	687	385
A24C_5_5	24.14	1152	24.4	1037	120	123	809.2	954.9	6.22	3	5	emb/emb	1002.6	951.3	820	701	319

**Table B-12: Beech with 12 mm dowels, single test results**

test	dia dowel	density [kg/m <sup>3</sup> ]	m.c. [%]	density at 12% m.c. [kg/m <sup>3</sup> ]	t [mm]	D <sub>LVDI</sub> [mm]	F <sub>test</sub> [kN]	F <sub>test,12%</sub> [kN]	v(F <sub>test</sub> ) [mm]	FM	angle dowel	wood at final deformation piece 1/piece 2	F <sub>pred</sub> [kN]	F <sub>pred,12</sub> % [kN]	K <sub>ser,pred</sub> [kN/mm]	K <sub>ser,pred,12%</sub> [kN/mm]	K <sub>ser,test</sub> [kN/mm]
B12_1_1	11.80	733	9.1	753	72	58	66.9	61.0	12.80	2	12	brittle/emb	57.5	58.7	41	42	29
B12_1_2	11.77	736	8.4	760	72	58	74.4	66.3	17.55	2	18	emb/brittle	57.5	58.9	41	43	44
B12_1_3	11.78	707	8.4	730	72	58	71.0	63.4	15.88	2	20	brittle/brittle	55.8	57.2	38	40	86
B12_1_4	11.82	700	8.8	720	72	58	64.4	58.2	14.49	2	15	brittle/emb	55.6	56.8	38	40	38
B12_1_5	11.79	737	8.8	759	72	58	73.2	66.1	18.56	2	18	emb/brittle	57.6	59.0	41	43	49
B12_3_1	11.83	765	8.6	788	72	58	165.7	148.9	4.58	2	3	brittle/emb	178.7	183.1	130	137	65
B12_3_2	11.82	719	8.6	742	72	58	182.8	164.0	7.14	2	6	brittle/brittle	170.4	174.5	119	125	69
B12_3_3	11.80	699	8.9	719	72	58	176.4	159.8	7.48	2	6	brittle/emb	166.2	169.9	114	119	70
B12_3_4	11.81	703	8.6	725	72	58	178.9	160.7	9.34	2	6	brittle/emb	167.2	171.2	115	120	71
B12_3_5	11.81	775	8.7	798	72	58	163.5	147.3	3.80	2	6	brittle/brittle	180.2	184.4	133	139	58
B12_5_1	11.87	696	8.4	719	72	108	288.8	257.6	5.40	2	2	brittle/brittle	278.7	285.7	190	199	105
B12_5_2	11.86	695	8.5	717	72	108	293.7	263.0	5.64	2	2	brittle/emb	277.9	284.7	189	198	139
B12_5_3	11.89	700	8.5	723	72	108	303.5	271.6	6.44	2	5	brittle/brittle	280.3	287.2	191	201	120
B12_5_4	11.85	691	8.3	714	72	108	298.6	265.8	5.27	2	3	brittle/brittle	276.3	283.4	187	197	150
B12_5_5	11.86	731	8.5	754	72	108	285.2	255.5	3.89	2	2	brittle/brittle	288.8	295.9	204	214	129
B12C_1_1	11.88	714	8.6	736	72	58	57.7	51.8	16.26	3	20	brittle/emb	49.5	49.5	39	41	49
B12C_1_2	11.90	712	8.2	737	72	58	59.3	52.4	14.54	3	15	emb/brittle	49.6	49.6	39	41	46
B12C_1_3	11.87	731	8.5	754	72	58	57.2	51.2	14.07	3	15	brittle/brittle	50.0	50.0	41	43	43
B12C_1_4	11.87	734	8.9	755	72	58	60.5	54.7	15.82	3	16	emb/brittle	50.1	50.1	41	43	19
B12C_1_5	11.92	709	8.9	730	72	58	62.5	56.6	16.67	3	19	emb/brittle	49.6	49.6	39	41	21
B12C_3_1	11.88	733	8.5	756	72	58	148.9	133.4	4.72	3	3	emb/brittle	150.4	152.8	123	129	46
B12C_3_2	11.90	736	8.4	760	72	58	152.4	136.0	5.39	3	4	emb/brittle	151.1	153.6	124	130	91
B12C_3_3	11.90	705	8.5	729	72	58	159.3	142.3	8.10	3	5	brittle/emb	148.1	150.5	116	122	54
B12C_3_4	11.89	749	8.6	773	72	58	167.6	150.3	6.11	3	4	brittle/emb	152.3	154.7	127	133	52
B12C_3_5	11.89	726	8.5	750	72	58	158.2	141.5	4.96	3	6	brittle/brittle	150.0	152.4	121	127	63
B12C_5_1	11.91	694	10.8	701	72	58	236.1	227.4	4.33	3	2	emb/brittle	245.1	246.5	189	192	109
B12C_5_2	11.90	711	8.4	735	72	58	233.8	208.3	4.47	3	2	brittle/emb	247.9	252.0	196	206	113
B12C_5_3	11.90	710	8.2	735	72	58	249.0	220.6	4.95	3	2	emb/brittle	247.7	252.0	196	206	112
B12C_5_4	11.90	753	8.3	779	72	58	238.9	212.4	4.70	3	2	brittle/brittle	255.1	259.4	214	225	102
B12C_5_5	11.91	721	8.3	746	72	58	243.4	216.5	3.91	3	2	brittle/brittle	249.7	253.9	201	211	114

**Table B-13: Beech with 24 mm dowels, single test results; series B24\_1 double tests**

test	dia dowel	density [kg/m <sup>3</sup> ]	m.c. [%]	density at 12% m.c. [kg/m <sup>3</sup> ]	t [mm]	D <sub>LVDT</sub> [mm]	F <sub>test</sub> [kN]	F <sub>test,12%</sub> [kN]	√(F <sub>test</sub> ) [mm]	FM	angle dowel	wood at final deformation piece 1/piece 2	F <sub>pred</sub> [kN]	F <sub>pred,12%</sub> [% [kN]	K <sub>ser,pred</sub> [kN/mm]	K <sub>ser,pred,12%</sub> [kN/mm]	K <sub>ser,rest</sub> [kN/mm]
B24_1_1	23.96	714	8.7	735	144	77	304.7	274.8	24.38	2	11	brittle/emb	207.9	212.6	79	79	143
B24_1_2	23.95	718	8.4	741	144	77	304.7	271.6	24.47	2	11	brittle/emb	208.6	213.8	80	80	167
B24_1_3	23.94	713	8.2	738	144	77	305.9	271.2	15.74	2	8	brittle/brittle	207.5	212.9	79	79	147
B24_1_4	23.95	704	8.5	727	144	77	291.3	261.0	15.71	2	6	brittle/brittle	205.7	210.6	78	78	170
B24_1_5	23.92	699	8.5	722	144	77	292.5	261.9	19.71	2	10	brittle/brittle	204.4	209.2	77	77	158
B24_3_1	26.93	727	8.3	752	144	23	669.1	594.0	4.22	2	0.5	brittle/brittle	738.8	756.8	275	275	205
B24_3_2	23.91	723	8.4	747	144	23	676.4	602.4	4.72	2	0.5	brittle/brittle	628.0	643.8	242	242	198
B24_3_3	23.90	733	8.1	760	144	23	619.1	546.8	4.15	2	0.5	brittle/brittle	634.6	651.7	248	248	208
B24_3_4	23.92	719	8.4	743	144	23	630.1	561.9	3.32	2	0.5	brittle/brittle	625.6	641.2	240	240	213
B24_3_5	23.93	718	8.1	744	144	23	700.8	619.8	4.35	2	0.5	brittle/brittle	625.6	642.2	240	240	201
B24_5_1	23.91	704	9.0	724	144	23	944.5	858.3	3.96	1	-	emb/brittle	1026.3	1047.6	388	388	195
B24_5_2	23.90	715	9.8	729	144	23	944.5	882.2	4.52	2	0.5	brittle/brittle	1037.3	1052.8	397	397	184
B24_5_3	23.91	689	9.0	708	144	23	925.0	840.5	4.77	1	-	brittle top/emb	1010.2	1031.1	376	376	178
B24_5_4	23.89	697	9.8	711	144	23	949.4	886.8	3.87	2	0.5	brittle/emb	1017.2	1032.3	382	382	192
B24_5_5	23.90	672	9.4	688	144	23	871.4	803.8	3.37	1	-	brittle/brittle	990.6	1007.9	362	362	209
B24C_1_1	23.92	722	10.0	735	144	77	203.0	191.0	21.87	3	16	emb/brittle	156.1	157.6	81	81	75
B24C_1_2	23.86	710	8.3	734	144	77	199.1	177.1	21.97	3	16	brittle/emb	154.1	156.7	78	78	134
B24C_1_3	23.97	701	8.3	724	144	77	211.1	187.8	29.52	3	22	brittle/emb	154.3	156.9	77	77	111
B24C_1_4	23.88	742	8.1	769	144	77	208.4	184.3	19.80	3	14	emb/brittle	157.8	160.6	84	84	128
B24C_1_5	23.94	717	8.5	741	144	77	218.2	195.3	25.77	3	25	brittle/emb	155.8	158.3	80	80	119
B24C_3_1	23.81	710	8.4	734	144	23	498.5	444.3	5.75	2	3	brittle/brittle	460.5	468.2	235	235	160
B24C_3_2	23.92	708	8.4	732	144	23	541.1	482.4	8.86	3	5	brittle/brittle	464.0	471.6	235	235	231
B24C_3_3	23.95	710	8.5	733	144	23	531.4	475.6	5.83	3	5	brittle/brittle	465.4	472.8	236	236	175
B24C_3_4	23.92	695	8.3	719	144	23	479.0	425.8	4.09	2	3	brittle/brittle	459.6	467.3	229	229	241
B24C_3_5	24.04	729	8.4	753	144	23	502.1	447.3	5.36	2	3	brittle/brittle	474.8	482.7	247	247	205
B24C_5_1	23.85	694	9.6	709	144	23	848.2	787.2	6.77	3	4	brittle/brittle	760.8	769.1	379	379	156
B24C_5_2	23.91	705	10.0	718	144	23	799.5	751.6	5.13	3	4	emb/brittle	770.8	777.7	389	389	191
B24C_5_3	23.91	705	9.4	722	144	23	769.0	708.7	5.23	2	3	brittle/brittle	770.5	779.7	389	389	172
B24C_5_4	23.88	707	10.1	719	144	23	814.1	768.5	6.48	2	3	brittle/brittle	770.4	776.9	391	391	167
B24C_5_5	23.88	692	10.0	704	144	23	882.4	830.5	8.98	2	5	brittle/brittle	761.8	768.5	378	378	170

**Table B-14: Spruce with 12 mm dowels, single test results**

test	dia dowel	density [kg/m <sup>3</sup> ]	m.c. [%]	density at 12% m.c. [kg/m <sup>3</sup> ]	t [mm]	D <sub>LVD</sub> T [mm]	F <sub>test</sub> [kN]	F <sub>test,12%</sub> [kN]	v(F <sub>test</sub> ) [mm]	FM	angle dowel	wood at final deformation piece 1/piece 2	F <sub>pred</sub> [kN]	F <sub>pred,12%</sub> [kN]	K <sub>ser,12%</sub> [kN/mm]	K <sub>ser,12%</sub> [kN/mm]	K <sub>ser,12%</sub> [kN/mm]
S12_1_1	11.77	422	12.2	421	92	108	42.7	43.0	17.68	2	7	brittle/emb	42.8	42.7	18	18	13
S12_1_2	11.80	444	11.8	445	92	108	44.4	44.1	11.44	2	14	brittle/emb	44.4	44.4	19	19	22
S12_1_3	11.80	460	12.3	459	92	108	43.8	44.2	16.23	2	12	emb/brittle	45.9	45.8	20	20	13
S12_1_4	11.85	466	12.1	466	91	108	43.0	43.1	12.05	2	12	emb/brittle	46.3	46.3	21	21	29
S12_1_5	11.79	494	12.1	493	91	108	46.5	46.7	17.97	2	12	brittle/emb	47.8	47.8	23	22	21
S12_3_1	11.75	465	12.0	465	91	108	111.4	111.2	5.42	2	2	brittle/emb	137.0	137.1	61	61	46
S12_3_2	11.80	480	12.3	479	91	108	112.3	113.3	4.73	2	2	emb/brittle	141.4	141.1	65	65	47
S12_3_3	11.81	489	12.7	486	90	108	124.0	126.5	7.62	2	4	brittle/brittle	142.7	142.0	67	66	53
S12_3_4	11.80	494	12.6	492	90	108	122.2	124.5	6.95	2	4	brittle/brittle	143.7	143.1	68	67	53
S12_3_5	11.78	496	12.6	494	90	108	107.4	109.2	3.53	1	-	emb/brittle	143.8	143.3	68	67	56
S12_5_1	11.79	469	12.3	467	90	108	148.1	149.5	2.69	1	-	brittle/brittle	229.6	229.1	104	104	62
S12_5_2	11.79	471	12.5	468	90	108	172.9	175.7	3.61	2	0.5	emb/brittle	230.2	229.3	105	104	65
S12_5_3	11.76	477	12.5	475	90	108	136.7	138.6	2.68	1	-	brittle/emb	232.1	231.3	107	106	70
S12_5_4	11.80	481	12.8	477	90	108	189.1	193.6	4.23	2	0.5	brittle/emb	234.5	233.2	108	107	70
S12_5_5	11.82	492	12.7	489	91	108	199.6	203.8	4.69	2	0.5	brittle/brittle(knot)	239.8	238.6	112	111	72
S12C_1_1	12.03	441	12.1	441	92	108	28.8	28.9	12.03	3	13	brittle/emb	34.2	34.2	19	19	32
S12C_1_2	11.99	446	11.7	447	92	108	31.0	30.7	8.61	3	6	brittle/emb	34.2	34.2	20	20	22
S12C_1_3	12.02	447	11.8	448	92	108	30.7	30.6	16.19	3	13	brittle/brittle	34.4	34.4	20	20	12
S12C_1_4	12.00	464	11.8	465	91	108	35.7	35.5	3.61	3	6	brittle (knot)/emb	34.9	34.9	21	21	18
S12C_1_5	11.99	481	12.4	480	91	108	33.7	34.0	8.33	3	7	brittle/emb	35.5	35.4	22	22	24
S12C_3_1	12.01	418	12.4	416	90	108	77.7	78.7	4.95	2	4	brittle/emb	99.5	99.4	53	53	47
S12C_3_2	11.99	447	12.5	445	90	108	88.0	89.4	5.28	2	4	brittle/brittle	102.7	102.4	59	59	42
S12C_3_3	12.02	463	12.7	460	91	108	89.4	91.4	4.84	2	4	brittle/emb	105.0	104.6	62	62	42
S12C_3_4	12.01	486	12.8	483	91	108	91.9	94.0	5.36	3	5	emb/brittle	107.5	107.1	67	67	64
S12C_3_5	12.00	499	12.9	495	91	108	101.1	104.0	4.72	2	4	emb/brittle	108.6	108.2	70	69	62
S12C_5_1	12.01	430	12.1	430	91	108	126.3	126.8	2.78	2	6	brittle/brittle	168.3	168.2	93	93	49
S12C_5_2	12.01	440	12.4	438	91	108	141.0	142.8	3.86	2	2	emb/brittle	170.3	169.9	96	96	52
S12C_5_3	12.01	458	12.5	456	91	108	136.9	139.1	3.37	2	3	brittle/emb	173.8	173.4	102	102	52
S12C_5_4	12.01	479	12.4	477	91	108	121.2	122.6	2.76	2	2	brittle/emb	177.7	177.4	109	109	44
S12C_5_5	12.01	492	12.8	488	90	108	153.2	156.8	3.97	2	5	brittle/brittle(knot)	179.9	179.3	114	113	61

**Table B-15: Spruce with 24 mm dowels, single test results; series S24\_1 double tests and series S24\_3 reinforced**

test	dia dowel	density [kg/m <sup>3</sup> ]	m.c. [%]	density at 12% m.c. [kg/m <sup>3</sup> ]	t [mm]	D <sub>LVDt</sub> [mm]	F <sub>test</sub> [kN]	F <sub>test,12%</sub> [kN]	√(F <sub>test</sub> ) [mm]	FM	angle dowel	wood at final deformation piece 1/piece 2	F <sub>pred</sub> [kN]	F <sub>pred,12%</sub> [%]	K <sub>ser, pred</sub> [kN/mm]	K <sub>ser, pred,12%</sub> [kN/mm]	K <sub>ser, test</sub> [kN/mm]
S24_1_1	23.99	393	11.7	394	166	123	160.6	159.0	7.11	2	0.5	emb/brittle	144.1	144.4	32	33	124
S24_1_2	24.00	402	12.0	402	166	123	155.6	155.5	8.31	2	6	emb/emb	146.8	146.8	34	34	110
S24_1_3	24.02	412	11.8	412	165	123	170.4	169.6	15.09	2	5	brittle/brittle	149.0	149.1	35	35	130
S24_1_4	24.01	418	12.0	418	165	123	167.0	167.2	19.92	2	7	emb/emb	150.6	150.6	36	36	93
S24_1_5	23.98	439	12.2	438	165	123	172.0	173.2	5.37	1	-	brittle/brittle	155.7	155.5	38	38	133
S24_3_1	24.00	385	11.6	387	165	73	340.0	335.8	4.11	1	-	brittle/brittle	426.7	427.8	95	95	135
S24_3_2	24.01	411	11.6	412	165	73	369.3	364.5	2.99	1	-	brittle/brittle	445.7	446.9	104	105	123
S24_3_3	24.02	413	11.9	414	165	73	263.2	262.5	1.77	1	-	brittle/brittle	448.1	448.3	105	105	117
S24_3_4	23.98	417	11.7	417	166	73	253.5	251.5	2.30	1	-	brittle/brittle	450.1	450.9	106	107	113
S24_3_5	23.99	422	12.0	422	166	73	260.8	260.9	1.95	1	-	brittle/brittle	455.5	455.4	109	109	123
S24_5_2	23.99	418	12.3	417	166	123	624.0	630.5	4.69	1	-	brittle/brittle	753.5	751.9	178	178	410
S24_5_3	23.99	428	12.9	425	166	123	587.4	603.5	3.98	1	-	tension/brittle	764.9	760.5	185	182	200
S24_5_4	23.96	444	12.4	442	166	123	572.8	580.2	3.27	1	-	brittle/brittle(knot)	784.0	781.8	195	194	191
S24_5_5	23.96	465	12.3	464	165	123	496.0	500.0	2.66	1	-	brittle support(knot)/brittle	809.3	807.9	209	208	187
S24C_1_1	23.96	377	12.1	377	166	73	92.7	92.9	5.42	2	6	emb/brittle	112.0	111.9	30	30	81
S24C_1_2	23.97	381	12.2	380	166	123	102.0	102.5	3.85	2	4	emb/brittle	113.4	113.3	31	31	120
S24C_1_3	23.98	423	12.1	423	166	123	110.2	110.5	5.33	2	3	emb/brittle	119.7	119.7	36	36	116
S24C_1_4	23.97	466	12.2	465	166	123	126.9	127.8	6.98	2	4	brittle/emb	125.9	125.8	42	42	134
S24C_1_5	23.99	474	12.7	471	166	123	118.4	120.7	4.66	2	5	brittle/brittle	127.1	126.8	43	43	176
S24C_3_1	23.99	400	11.9	401	166	123	326.6	325.2	4.83	2	2	brittle(knot)/brittle	350.7	350.9	100	100	105
S24C_3_2	23.95	410	12.1	410	166	123	341.2	342.4	4.04	2	2	brittle support incl./brittle	353.9	353.7	104	104	151
S24C_3_3	23.95	419	11.9	420	166	123	327.8	326.5	4.78	2	2	brittle/brittle	357.7	357.9	107	107	108
S24C_3_4	23.95	420	11.8	421	166	123	326.6	324.9	3.22	2	0.5	brittle/brittle support(knot)	358.2	358.5	108	108	163
S24C_3_5	24.00	442	11.8	443	166	123	296.1	294.4	2.81	2	0.5	brittle/emb	368.6	368.9	116	117	105
S24C_5_1	23.97	411	12.4	410	165	123	429.0	433.8	3.56	2	0.5	brittle support/brittle support	591.5	590.5	174	173	126
S24C_5_2	23.96	425	12.5	423	165	123	502.1	509.8	3.95	2	0.5	brittle/brittle	600.4	599.0	182	181	141
S24C_5_3	23.96	435	12.1	435	165	123	438.7	440.3	3.57	2	0.5	brittle/tension support(knot)	608.1	607.8	189	189	135
S24C_5_4	23.97	451	12.7	449	165	123	522.8	533.2	3.18	2	0.5	brittle/tension support	619.6	617.7	200	198	149
S24C_5_5	23.97	459	12.3	458	165	123	518.0	522.6	3.57	2	0.5	brittle/tension support	624.9	624.1	205	204	136

**Table B-16: Four-point bending tests of original beams of series azobé with 12 mm dowels**

original beam	rho_beam [kg/m <sup>3</sup> ]	mc_beam	Edyn_wet	MoE_static global [MPa]	MoE_static local [MPa]	MoR [MPa]
34	1214	35.3	22809.9	16600.3	20918.2	90.2
45	1147	45.5	14579.5	10797.3	11883.1	69.3
46	1102	42.9	16631.5	12286.5	15536.1	65.8
47	1285	48.5	18058.2	12245.6	13918.0	58.1
48	1193	53.7	17617.7	13203.1	14717.5	87.6
49	1224	47.9	16934.7	13134.6	16864.6	84.0
50	1118	44.0	15967.8	12218.6	15922.3	92.0
52	1219	17.4	15224.0	11605.7	15039.1	61.9
53	1165	44.8	15342.1	11245.3	15729.2	56.3
59	1150	43.8	17829.5	13629.4	14056.7	74.9
60	1079	41.3	15416.5	11493.6	16079.4	73.3
61	1153	39.5	17259.7	13655.7	15585.0	66.9
62	1206	42.1	20257.1	16224.0	22325.3	89.1
64	1149	38.8	17751.5	13759.4	14771.8	72.8
66	1196	44.3	16485.8	12737.4	16246.0	75.9
67	1168	38.2	18051.6	12458.8	16699.6	72.2

Legend:

- rho\_beam = density at test
- mc\_beam = moisture content at test
- Edyn\_wet = dynamic MoE at test
- MoEstatic\_global = global MoE of four-point bending test
- MoEstatic\_local = local MoE of four-point bending test
- MoR = MoR of test



# C

## MISCELLANEOUS

### C.1 DERIVATION OF DAMAGE VARIABLES

#### Ductile Law

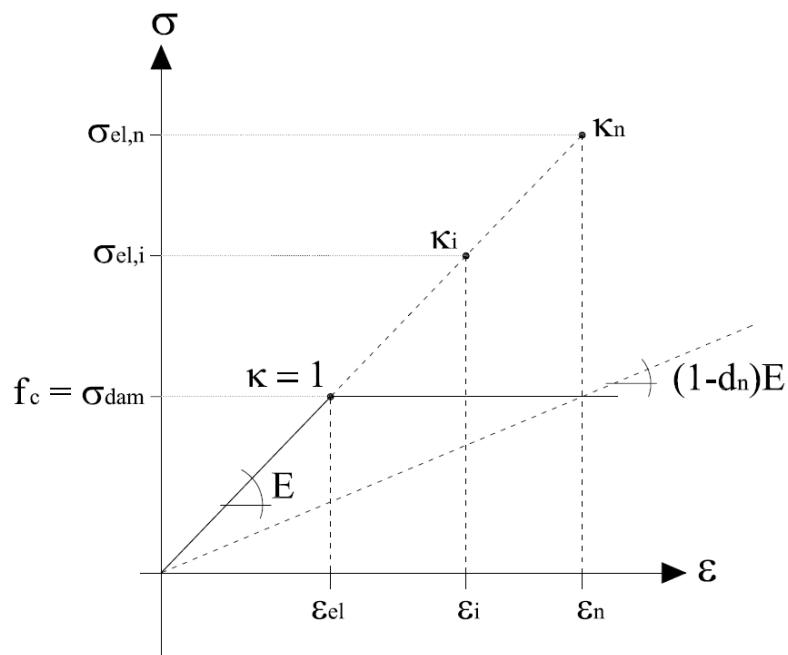


Figure C-1: Ductile damage evolution



Definitions of variables:

$$G_f = \frac{1}{2} f_t \varepsilon_{ult} \Leftrightarrow \varepsilon_{ult} = \frac{2G_f}{f_t}$$

$$\sigma_{el,ult} = E \varepsilon_{ult}$$

$$\kappa_{ult} = \frac{\sigma_{el,ult}}{f_t} = \frac{E \varepsilon_{ult}}{f_t} = \frac{2G_f E}{f_t^2}$$

$$\sigma_{el,n} = E \varepsilon_n$$

$$\sigma_{dam} = (1-d) E \varepsilon$$

Equation for line a:

$$\sigma(\varepsilon) = \frac{E f_t^2 \varepsilon - 2G_f E f_t}{f_t^2 - 2G_f E}$$

Equation for line b:

$$\sigma(\varepsilon) = (1-d) E \varepsilon$$

Derive intersection point of lines a and b and solve for d:

$$(iii) \quad d(\varepsilon) = 1 - \frac{f_t^2}{f_t^2 - 2G_f E} + \frac{2G_f f_t^2}{f_t^2 - 2G_f E} \varepsilon$$

The last step is to define  $d$  as a function of the history parameter  $\kappa$ :

At increment  $i$ :

$$\kappa_i = \frac{\sigma_{el,i}}{f_t}$$

$$\sigma_{el,i} = E \varepsilon_i = \kappa_i f_t$$

$$\Rightarrow \varepsilon_i = \frac{\kappa_i f_t}{E}$$

Insert in (iii):

$$d(\kappa) = 1 - \frac{1}{f_t^2 - 2G_f E} \left( f_t^2 - \frac{2G_f E}{\kappa} \right)$$

Check:

$$d(\kappa=1) = 0 \quad \text{AND} \quad d\left(\kappa = \frac{2G_f E}{f_t^2}\right) = 0$$

## C.2 DESIGNATION OF SOLUTION-DEPENDENT STATE VARIABLES

Damage variables (no viscous stabilisation):

$$\text{SDV1} = d_{t,0\_nr}$$

$$\text{SDV2} = d_{c,0\_nr}$$

$$\text{SDV3} = d_{t,90R\_nr}$$

$$\text{SDV4} = d_{c,90R\_nr}$$

$$\text{SDV5} = d_{t,90T\_nr}$$

$$\text{SDV6} = d_{c,90T\_nr}$$

$$\text{SDV7} = d_{vR\_nr}$$

$$\text{SDV8} = d_{vT\_nr}$$

$$\text{SDV9} = d_{roll\_nr}$$

Damaged stiffness matrix (is not needed for calculation and can be changed easily in the UMAT):

$$\text{SDV19} = C^{dam}(1,1)$$

$$\text{SDV20} = C^{dam}(2,2)$$

$$\text{SDV21} = C^{dam}(3,3)$$

$$\text{SDV22} = C^{dam}(4,4)$$

$$\text{SDV23} = C^{dam}(5,5)$$

$$\text{SDV24} = C^{dam}(6,6)$$

$$\text{SDV25} = C^{dam}(1,2)$$

$$\text{SDV26} = C^{dam}(1,3)$$

$$\text{SDV27} = C^{dam}(2,3)$$

Stabilised damage variables:

$$\text{SDV10} = d_{t,0}$$

$$\text{SDV11} = d_{c,0}$$

$$\text{SDV12} = d_{t,90R}$$

$$\text{SDV13} = d_{c,90R}$$

$$\text{SDV14} = d_{t,90T}$$

$$\text{SDV15} = d_{c,90T}$$

$$\text{SDV16} = d_{vR}$$

$$\text{SDV17} = d_{vT}$$

$$\text{SDV18} = d_{roll}$$

History parameter  $\kappa$ :

$$\text{SDV28} = \kappa_{t,0}$$

$$\text{SDV29} = \kappa_{c,0}$$

$$\text{SDV30} = \kappa_{t,90R}$$

$$\text{SDV31} = \kappa_{c,90R}$$

$$\text{SDV32} = \kappa_{t,90T}$$

$$\text{SDV33} = \kappa_{c,90T}$$

$$\text{SDV34} = \kappa_{vR}$$

$$\text{SDV35} = \kappa_{vT}$$

### C.3 NEEDED INPUT MATERIAL PARAMETERS - PROPS

#### *ELASTIC PROPERTIES*

$E_0$	=	<b>PROPS ( 1 )</b>	parallel-to-grain
$E_{90}$	=	<b>PROPS ( 2 )</b>	perpendicular-to-grain
$G$	=	<b>PROPS ( 3 )</b>	shear modulus
$G_{roll}$	=	<b>PROPS ( 4 )</b>	rolling shear modulus
$\nu_{12}$	=	<b>PROPS ( 5 )</b>	Poisson's ratios
$\nu_{13}$	=	<b>PROPS ( 6 )</b>	
$\nu_{23}$	=	<b>PROPS ( 7 )</b>	

#### *ULTIMATE STRENGTH PROPERTIES*

$f_{c,0}$	=	<b>PROPS ( 8 )</b>	Compression parallel-to-grain
$f_{t,0}$	=	<b>PROPS ( 9 )</b>	Tension parallel-to-grain
$f_{c,90}$	=	<b>PROPS ( 10 )</b>	Compression perpendicular-to-grain
$f_{t,90}$	=	<b>PROPS ( 11 )</b>	Tension perpendicular-to-grain
$f_v$	=	<b>PROPS ( 12 )</b>	Longitudinal shear
$f_{roll}$	=	<b>PROPS ( 13 )</b>	Rolling shear

#### *DAMAGE PROPERTIES*

$G_{f-t,0}$	=	<b>PROPS ( 14 )</b>	Fracture energy tension parallel-to-grain
$G_{f-t,90}$	=	<b>PROPS ( 15 )</b>	Fracture energy tension perpendicular-to-grain
$G_{f-v}$	=	<b>PROPS ( 16 )</b>	Fracture energy longitudinal shear
$G_{f-roll}$	=	<b>PROPS ( 17 )</b>	Fracture energy rolling shear

#### *VISCOSITY FOR VISCOUS STABILISATION*

$\eta$	=	<b>PROPS ( 18 )</b>	
--------	---	---------------------	--



Und natürlich auch für Stefanie

